

University of Bath



PHD

Nanostructured ZnO films for water treatment by photocatalysis

Ramirez Canon, Anyela M.

Award date:
2015

Awarding institution:
University of Bath

[Link to publication](#)

General rights

Copyright and moral rights for the publications made accessible in the public portal are retained by the authors and/or other copyright owners and it is a condition of accessing publications that users recognise and abide by the legal requirements associated with these rights.

- Users may download and print one copy of any publication from the public portal for the purpose of private study or research.
- You may not further distribute the material or use it for any profit-making activity or commercial gain
- You may freely distribute the URL identifying the publication in the public portal ?

Take down policy

If you believe that this document breaches copyright please contact us providing details, and we will remove access to the work immediately and investigate your claim.

Download date: 23. May. 2019

Nanostructured ZnO films for water treatment by photocatalysis

Anyela M. Ramírez Cañón

A thesis submitted for the degree of Doctor of Philosophy
University of Bath
Department of Chemical Engineering
May 2014

COPYRIGHT

Attention is drawn to the fact that copyright of this thesis rests with the author. A copy of this thesis has been supplied on condition that anyone who consults it is understood to recognise that its copyright rests with the author and that they must not copy it or use material from it except as permitted by law or with the consent of the author.

This thesis may be made available for consultation within the University Library and may be photocopied or lent to other libraries for the purposes of consultation.

Declaration

This thesis contains original work except for any collaboration acknowledged and highlighted within the text. The stainless steel flat plate batch photocatalytic reactor described in Chapter 6 Section 6.1.1 was designed in collaboration with Dr Massimiliano Vezzoli and Dr Davide Mattia. The tubular annular photocatalytic reactor described in Chapter 6 Section 6.2.1 was also designed with the help of Dr. Mattia. Partial TEM analysis was carried out by Dr Yina Guo in the Materials and Surface Science Institute of the University of Limerick in Ireland.

Abstract

The development of nanostructured materials for environmental applications has received considerable attention in recent years. The properties of nanoparticles or nanostructured materials, such as large surface areas or high aspect ratios, translate into large improvements in the performance of existing devices and in the discovery of novel applications. On the other hand, photocatalysis is an attractive technology for the elimination of organic pollutants in water due to its simplicity, ease of implementation and reasonable cost compared to other advanced oxidation processes. A key disadvantage of many photocatalysts is their use in powder form which makes their recovery from treated water costly. In addition, incomplete removal can lead to accumulation over time with adverse effects to the environment. As a result significant effort has been placed in immobilizing photocatalytic materials on different substrates. The immobilization of photocatalyst results in a decrease in photocatalytic performance mainly due to reduction of surface area; therefore, research is now focusing on developing nanostructured materials which combine the attributes of nanotechnology and photocatalysis.

In the present thesis, a systematic study of the relationship between properties of supported ZnO nanostructures and their photocatalytic activity was performed. Analysis was carried out by producing ZnO nanostructured films via anodization. The effects of voltage, temperature, reaction time and type of electrolyte on the morphology of ZnO nanostructures was studied. Results show that the type of electrolyte and its concentration determine the morphology and size of the nanostructures. Voltage, time and temperature affect the distribution and density of the nanostructures along the surface and affect the crystal size of the ZnO. The band gaps of the films were in the range of 3.27 and 3.50 eV. Although ZnO is a hydrophilic material, some of the films displayed hydrophobic and super-hydrophobic behaviour. The results obtained in this study and some data already published in the literature were correlated to the synthesis parameters, and were used to devise design guidelines to obtain ZnO films with specific nanostructures and macroscopic properties by controlling the anodization parameters.

The photocatalytic activity of the ZnO nanostructured films (ZnO-NFs) were studied using three different photocatalytic reactors, (i) a thermo-stated batch reactor, (ii) a recirculating flat plate reactor, and (iii) a recirculating tubular annular reactor. Phenol and methyl orange (MO) were used as a model compounds. It was found that crystal size does not affect the photocatalytic performance of the films while morphology has an important impact on the degradation of phenol. The stability of the ZnO nanostructures was tested under different levels of oxygen, degradation of phenol occurred even at anoxic conditions following the Mars-van Krevelen mechanism. The formation of new nanostructures produced during the photocatalytic reaction was studied and a mechanism of formation was proposed. The study of the photocatalytic performance in the flat plate reactor showed that there was a mass transfer limitation in the process. ZnO nanostructures showed higher photocatalytic activity and morphology stability in the tubular annular reactor. Degradation of MO and phenol was produced in darkness by the nanostructures supported in Zn foil. It was also demonstrated that oxygen plasma post-treatment enhances the photocatalytic activity of the ZnO-NF by 36% while making the photocatalyst more stable for the photocatalytic degradation of phenol compared to those treated with heat. An electrical current was applied to the photocatalyst in the tubular annular reactor, which improved the degradation of phenol and participated in the formation of nanostructures in the Zn wire surface.

Acknowledgements

I would like to express my truthful gratitude to my supervisor, Dr Davide Mattia, for his guidance throughout my PhD and for his constant support and advice.

Thanks to the academics from the chemical engineering department, in particular to Dr Dr Laura Torrente, Dr Petra Cameron, Dr Tom Arnot and Dr Will Lewis for the constructive discussions on some of this work. Also thank you to Dr Janet Scott who has always guided me and supported me since my arrival to the Doctoral Training Centre.

I thank my friends from the environmental nanotechnology research group namely David Miles, Maria de la Luz Medina Llamas, Dr Hannah Leese, Dr Kah Peng, Dr Daniel Minett and Dr Massi Vezzoli for the great team work and for making the work in lab an enjoyable experience.

Thanks to my friend Hendrik du Toit, and to the 2010 cohort of the Sustainable Chemical Technologies Institute, in particular to my good friends Sarah Abuo-Shehada and Jess Sharp.

All the analytical work would not have been possible without the technical support of Dr John Mitchells and Ursula Potter at the Microscopy and Analysis Suite. Dr Daniel Lou-Hing, Dr Alex Ciupa and Fernando Acosta from the technician team in the Chemical Engineering Department and Paul Frith and John Bishop for the manufacture of the reactors

Finally, I would like to say thanks to my entire family for their love, support, patience and constant encouragement. Thanks for being my strength, not only during my PhD but during my entire life.

Thanks to my dearest friends who support me in distance: Adriana Vivas, Ximena Amparo Velasco, Nicole Botero, Adriana Quintero, Rocio Torres and Carolina Ospina.

Special gratitude to Dr Craig Robert Owen who gives me a family here in England. Thanks also for teaching me the concept of social construction in life, which made me more critical and a better person and scientist.

This work would not have been possible without the support of COLFUTURO – Colombia, COLCIENCIAS–Colombia through the Francisco Jose de Caldas Scholarship and DTC founding through the EPSRC.

For the favourite people in my heart: Tatys, Nanis and Vancho

Contents

List of Figures	x
List of Tables	xviii
Nomenclature	xix
Abbreviations	xxi
.....	1
1. Chapter 1: Introduction.....	1
1.1 Aims and objectives	3
1.2 Thesis overview.....	5
2. Chapter 2: Literature review.....	7
2.1 Challenges of water for human consumption.....	7
2.1.1 Current technologies for water treatment.....	9
2.2 Heterogeneous photocatalysis, principles and determining factors	14
2.2.1 Photocatalytic mechanism.....	15
2.2.2 Kinetics of photocatalytic reactions	18
2.2.3 Light in photocatalytic processes.....	21
2.2.4 Photocatalytic reactors	22
2.2.5 Photocatalytic materials for heterogeneous photocatalysis.....	25
2.3 Zinc Oxide as a photocatalytic material	29
2.3.1 Nanostructures of ZnO	34
2.4 Electrocatalysis and Photoelectrocatalysis for water treatment	37
2.5 Summary	39
3. Chapter 3: Experimental – Material and methods.....	39
3.1 Fabrication of nanostructured ZnO films and nanostructured ZnO wire	40
3.1.1 Starting material pre-treatment	41
3.1.2 Anodization of Zn foil.....	42
3.1.3 Anodization of Zn wire	43
3.1.4 Post-annealing of ZnO-NFs and ZnO-NWs.....	44
3.2 Characterisation of the photo-catalytic materials	45

3.2.1	Morphology analysis.....	45
3.2.2	Wettability analysis.....	47
3.2.3	Analysis of chemical composition.....	49
3.2.4	Crystallography analysis.....	49
3.2.5	Band gap energy measurement.....	50
3.2.6	ZnO films profiles measurement.....	51
3.3	Photocatalytic setup.....	51
3.4	Light source.....	53
3.5	Analytical measurements of organic compounds.....	54
3.5.1	UV-Visible Spectrophotometric measurements.....	54
3.5.2	High performance liquid chromatography (HPLC).....	55
3.5.3	Total Organic Carbon.....	59
3.6	Dye and phenol absorption.....	60
3.7	Software used in analysis of data.....	60
3.8	Statistical Analysis and Reproducibility.....	60
3.9	Summary.....	61
	62
4.	Chapter 4: Results and Discussion.....	62
4.1	Pre-treatment of the starting material.....	62
4.2	Anodization process.....	64
4.2.1	Proposed formation mechanism of ZnO.....	64
4.2.2	Formation of nanowires by Anodization of Zn with KHCO_3	66
4.3	ZnO films composition.....	69
4.4	ZnO-NFs morphology. Effect of anodization conditions.....	71
4.4.1	Effect of type of electrolyte and concentration on film morphology.....	71
4.4.2	Effect of voltage on film morphology.....	74
4.4.3	Effect of temperature on film morphology.....	74
4.4.4	Effect of anodization time on film morphology.....	76
4.4.5	Nanostructures Sizes.....	78
4.5	Wetting Behaviour.....	80
4.6	Crystallinity of ZnO-NFs.....	84
4.7	ZnO-NFs profiles.....	87
4.8	ZnO-NFs band gap energy.....	87

4.9	Thermal Post-treatment	89
4.10	Rational design guidelines for controlled formation of ZnO nanostructures via anodization	95
4.11	Summary	99
	101
5.	Chapter 5: ZnO nanostructured films as a photocatalyst for water treatment in a batch reactor.....	101
5.1	Initial analysis: Degradation of phenol in the batch reactor.....	101
5.1.1	Adsorption and photolysis of phenol in the batch reactor.....	102
5.1.2	Photocatalytic degradation of phenol as a model compound in the batch reactor	104
5.1.3	Effect of external mass transfer on the overall degradation rates in the batch reactor.....	110
5.2	Correlation between ZnO-NFs morphology and their photocatalytic performance.....	111
5.2.1	Effect of Crystallinity on the photocatalytic performance of ZnO-NFs .	112
5.2.2	Effect of morphology on the photocatalytic performance of ZnO-NFs: nanostructure arrangement.....	114
5.2.3	Effect of Morphology on photocatalytic performance of ZnO-NFs: Different shapes of nanostructures	120
5.3	Stability of ZnO-NFs morphology during photocatalytic reactions.....	124
5.3.1	Effect of Oxygen level on the morphology of ZnO films during photocatalytic reactions	125
5.3.2	Formation of new ZnO nanostructures during photocatalytic reaction. .	130
5.3.3	Alternative post-treatments	135
5.4	Summary	141
	134
6.	Chapter 6: Alternative reactors to study the photocatalytic performance of ZnO nanostructures.	134
6.1	Photocatalytic reactors for ZnO-NF _(s) studies.....	135
6.1.1	Stainless steel flat plate batch photocatalytic reactor design	138
6.1.2	Preliminary experiments with FP-PCR - Photolysis of Methyl Orange .	142

6.1.3	FP-PCR used as a slurry photocatalytic reactor for the decomposition of MO.	148
6.1.4	ZnO-NFs as a photocatalytic material in FP-PCR.	149
6.1.5	Turning to a more stable model compound.	152
6.1.6	Epoxy acrylic flat plate batch photocatalytic reactor.	155
6.2	Exploring new shapes of photo catalyst substrate: From flat shape to cylindrical shapes	156
6.2.1	Tubular annular photocatalytic reactor (TA-PCR) design.	157
	160
6.2.2	Nano-structured photocatalytic wires (ZnO-NW) for photocatalytic applications	160
6.2.3	ZnO-NW as photocatalytic material TA-PCR	164
6.3	Deposition of ZnO on optical fibers	171
6.3.1	Preparation of the sol-gels	171
6.3.2	Coating of glass and optical fibers	173
6.4	Decolouration of MO by ZnO-NF in darkness	176
6.5	Summary	182
Chapter 7: Conclusions and future work.		193
7.1.	Conclusions	193
7.1.1.	Production of ZnO-NF for photocatalytic applications	193
7.1.2.	Mechanism of anodization of ZnO and formation of nanostructures	194
7.1.3.	Anodization conditions and its effect in ZnO properties	194
7.1.4.	Guidelines for controlled formation of ZnO nanostructures via anodization	195
7.1.5.	ZnO-NF as a photocatalytic material for the degradation of phenol in batch reactor	195
7.1.6.	Stability of ZnO-NF during photocatalytic reactions	196
7.1.7.	Effect of Post-treatment of ZnO-NF in photocatalytic activity	197
7.1.8.	Photocatalytic experiments with FP-PCR	198
7.1.9.	ZnO-NW and cylindrical reactor	198
7.1.10.	Decomposition of MO with ZnO-NF in darkness	199
7.1.11.	Deposition of ZnO on optical fibers surface.	199

7.1.12.	Concluding Remarks	199
7.2.	Future work.	200
7.2.1.	Mechanism of nanostructures formation via anodization of Zn.	200
7.2.2.	Further study of crystal size and crystal defects produced during anodization.....	200
7.2.3.	An alternative post-treatment to enhance the photocatalytic activity and morphological stability of ZnO nanostructures.	201
7.2.4.	Further analysis on the photocatalyst in anoxic photocatalytic reactions. 201	
7.2.5.	ZnO-NW and TA-PCR	201
7.2.6.	Further studies of the degradation of dyes by ZnO-NFs in darkness conditions.....	202
8.	References.....	203

List of Figures

Figure 1.1 Contextualization of the present work in different science and engineering fields.....	3
Figure 1.2 Scheme of the general aim of the research project	4
Figure 1.3 Summary flow chart of the thesis structure	6
Figure 2.1 Characteristics and classification of water treatment systems (Adapted from Metcalf and Eddy [35])	10
Figure 2.2 Classification of advanced technologies for water treatment (Adapted from Metcalf and Eddy [37] and Munter [7]).....	11
Figure 2.3 Particle size cut off for the different membrane filtration techniques (Adapted from Lenntech [41])	12
Figure 2.4 Classification of the advanced oxidation processes for water treatment (adapted from Andreozzi <i>et al</i> [51]).....	13
Figure 2.5 Number of publications per year related to photocatalysis studies and photocatalysis for water applications [55]	15
Figure 2.6 Mechanism of photocatalysis (adapted from Herrmann [53]; Cassano <i>et al</i> , [57] and Houas <i>et al</i> [59]).....	16
Figure 2.7 Types of heterogeneous photocatalytic reactors classified by the form of photocatalyst (Cassano <i>et al</i> [57]).....	22
Figure 2.8 Number of publications related to photocatalytic reactors since 2005 [55].	23
Figure 2.9 Scheme of two types of immobilized reactors (Ling <i>et al</i> [86]).....	24
Figure 2.10 Number of publications related to photocatalytic studies with ZnO and TiO ₂ since 2005 [55].	27
Figure 2.11 Proportion of publications related to the use of ZnO in photocatalysis compare to TiO ₂ and to other photocatalytic materials [55].	30
Figure 2.12 Crystal structures of ZnO. Grey dots refer to Zn atoms while black dots refer to oxygen (Morkoç <i>et al</i> [128])	30
Figure 2.13 Comparison of pores nanostructures obtained with anodization of alumina (a) [190] to porous morphologies produced with anodization of Zn (b) [189].	35
Figure 2.14 Schematic representation of photoelectrocatalytic process in an electrocell with TiO ₂ (Garcia Bessegato [198]).....	38
Figure 3.1 Three holes sample holder used in anodization of Zn foil.....	40

Figure 3.2 Set-up for electro-polishing of zinc foil and zinc wire.....	41
Figure 3.3 Anodization setup used for the fabrication of ZnO-NFs and ZnO-NWs.....	42
Figure 3.4 Two-electrode cell used in anodization process to obtain ZnO-NFs.....	43
Figure 3.5 Two-electrode cells used in anodization process to obtain ZnO-NWs.....	44
Figure 3.6 ZnO films cut with different techniques: scissors (a), wire cutters (b), immersion in liquid nitrogen and cut with scalpel (c), coated with resin and cut with scalpel (d).....	46
Figure 3.7 Difference between static contact angle and static effective contact angle..	48
Figure 3.8 Absorption spectra of ZnO-NF (Na(OH) [0.1M] / 1h / 40 V).....	50
Figure 3.9 Schematic of the profile measurements.	51
Figure 3.10 Schematic of the batch photocatalytic setup.....	52
Figure 3.11 External chamber used in the photocatalytic setup.....	52
Figure 3.12 Control of the UV light intensity produced by a Handheld UV lamp	53
Figure 3.13 Degradation of phenol with ZnO-NFs and different sources of light.....	54
Figure 3.14 Methyl orange absorbance spectrum (300 – 650 nm) at different concentrations	55
Figure 3.15 Chromatogram of phenol at different concentrations at 254 nm run for 200 seconds (a) and for 1200 seconds (b) (error: ± 0.01 ppm).....	56
Figure 3.16 Chromatogram of phenol [40 ppm] (a) and [2.5 ppm] (b) at different wavelength.	57
Figure 3.17 Calibration curve of phenol at 210 nm.	58
Figure 3.18 Detection of by-products of phenol decomposition by HPLC	58
Figure 3.19 TOC of different concentration of phenol ranged between 0.05 and 5ppm.	59
Figure 4.1 Speciation of zinc as a function of pH a) at fixed zinc concentration of 1×10^{-3} M (top) and b) as a function of zinc concentration at 25 °C showing only the dominant species (bottom) [242].....	65
Figure 4.2 Changes in a) current b) pH of the electrolyte, c) conductivity of the electrolyte and d) dissolved Zn on the electrolyte during anodization of Zn foil.....	67
Figure 4.3 Different stages of productions of nanowires analysed by changes in current during anodization of Zn with KHCO_3 [0.05M] at 10 °C, 1V and 1h. Inset: FESEM of nucleation of Zn	68
Figure 4.4 FESEM micrographs of the early stages of the formation of nanowires close to the pores produced by the nucleation of Zn during anodization.....	69

Figure 4.5 SEM micrographs of morphologies obtained with different electrolytes: a) H_3PO_4 (1 M, 40 V, 1 min, 10 °C); b) HNO_3 (1 M, 1 V, 1 h, 10 °C); c) HCl (0.1 M, 40 V, 1 h, 10 °C); d) $\text{H}_2\text{C}_2\text{O}_4$ (0.1 M, 1 V, 1 h, 10 °C); e) NaOH (0.1 M, 40 V, 1 h, 10 °C); f) KHCO_3 (1 M, 1 V, 1 h, 10 °C)	72
Figure 4.6 SEM micrographs of morphologies obtained at 1 V, 10 °C, for 1 minute, with different electrolytes at 0.1 M (left) and 1 M (right): a) $\text{H}_2\text{C}_2\text{O}_4$; b) KHCO_3 ; c) H_3PO_4 ; d) HCl	73
Figure 4.7 FESEM micrographs of morphologies obtained at 10 °C, for 1 hour, with different electrolytes at two different voltages 1 V (left) and 40 V (right): a) KHCO_3 (0.1M); b) HCl (0.1M); c) NaOH (0.1M); d) KHCO_3 (1M).	75
Figure 4.8 Speciation diagram of dominant zinc species as a function of pH, zinc concentration and temperature [242]	76
Figure 4.9 SEM micrographs of morphologies obtained at 10 °C and over two different time periods: 1 minutes (left) and 60 minute (right): a) HCl (1 M, 1 V); b) $\text{H}_2\text{C}_2\text{O}_4$ (0.1 M, 1 V); c) KHCO_3 (0.1 M, 1 V); d) KHCO_3 (1 M, 40 V).....	77
Figure 4.10 TEM micrographs showing beam damage over a ZnO nanowire	78
Figure 4.11 FESEM micrographs (left) and wire diameter distribution (right) of ZnO-NFs obtained with KHCO_3 (0.1M) : a) (5 V, 5 min); b) (12 V, 30 min); c) (10 V, 5 min); d) (1 V, 1 hour).....	79
Figure 4.12 SEM micrographs of morphologies obtained at 10 °C and over two different time periods: 1 minutes (left) and 60 minute (right): a) HCl (1 M, 1 V); b) $\text{H}_2\text{C}_2\text{O}_4$ (0.1 M, 1 V); c) KHCO_3 (0.1 M, 1 V); d) KHCO_3 (1 M, 40 V).....	81
Figure 4.13 Sliding angles of super-hydrophobic ZnO-NFs.....	83
Figure 4.14 XRD spectra of films obtained with NaOH. a) [0.1M], 1V, 1 min, 10°C. b) [0.1M], 1V, 1 hour, 10°C. c) [0.1M], 40V, 1 min, 10°C. d) [0.1M], 40V, 1 hour, 10°C	85
Figure 4.15 crystal size distribution of ZnO-NFs obtained with KHCO_3 (0.1M): (5 V, 5 min) (a) ; (12 V, 30 min) (b); (10 V, 5 min) (c) and (1 V, 1 hour) (d)	86
Figure 4.16 Types of ZnO films profiles: Convex profile (red line) HNO_3 (0.1M/1V/10°C/1min); flat profile (lilac line) $\text{H}_2\text{C}_2\text{O}_4$ (0.1M/40V/10°C/1min); concave profile (purple line) H_3PO_4 (0.1M/1V/10°C/60 min).....	87
Figure 4.17 UV-visible absorbance spectra (a) and differentiated absorbance spectra (b) of ZnO films produced with NaOH [0.1M] at different experimental conditions. (Red line 40V/1min/10°C; light purple line 40V/1min/0°C; blue line 40V/1h/0°C; dark purple line 40V/1h/10°C.....	88

Figure 4.18 TEM micrographs of nanowires before (a) and after (b) post-annealing at 350 °C, 1h, 1 °C/min and their magnification (bottom).....	90
Figure 4.19 XRD of ZnO films obtained with KHCO ₃ [0.05M], 1V, 10C, 1h and post-annealing under different temperatures.....	91
Figure 4.20 XRD of ZnO films obtained with KHCO ₃ [0.05M], 1V, 10C, 1h exposed to different times of post-annealing.	92
Figure 4.21 Crystal size distribution (a) and TEM micrographs of (b-c) crystals of samples post-annealed at 1h and 18h respectively.....	93
Figure 4.22 FESEM micrographs of ZnO-NFs (KHCO ₃ /1V/1h/10°C) (a) before and (b) after post-annealing at 300 °C for 1 hour with a rate temperature of 1 °C/min.	94
Figure 4.23 TEM micrographs of ZnO nanostructures; (b-c) wire of samples post-annealed at 1h and 18h respectively and (a) its crystal size distribution.	94
Figure 4.24 3D plot of the Morphology of ZnO-NFs obtained by anodization at different experimental conditions	96
Figure 4.25 Mirror-like plot of wetting behaviour of ZnO-NFs obtained by anodization at different experimental conditions.....	97
Figure 4.26 Mirror-like plots of the Surface profile analysis of ZnO layer obtained by anodization of Zn at different experimental conditions	98
Figure 5.1 Absorption spectra of phenol, p-nitrophenol and benzene [285].....	103
Figure 5.2 Degradation of phenol and by-products for 12 hours in a batch reactor using ZnO-NF as a photocatalyst	105
Figure 5.3 Proposed degradation pathway of phenol and by-products for a 12 hours batch reactor experiment using ZnO-NF as a photocatalyst (adapted from [68]).....	106
Figure 5.4 Plot of fractional life method (a) and integral rate method (b) used to determine the kinetic order reaction of the photocatalytic degradation of phenol.....	106
Figure 5.5 TOC variation during the photocatalytic degradation of phenol and by-products in a batch reactor using ZnO-NF as a photocatalyst.	108
Figure 5.6 Change in conductivity (a) and dissolved Zn(II) ions (b) during the photocatalytic degradation of phenol for 12 hours in a batch reactor using ZnO-NF as a photocatalyst	109
Figure 5.7 Photocatalytic degradation of phenol at different stirring velocities in a batch reactor using ZnO-NF as a photocatalyst (a). Correlation between the final degradation of phenol after 4 hours of reaction and stirring velocity	111

Figure 5.8 Photocatalytic degradation of phenol with ZnO-NFs exposed to no-post-annealing, and to 30min, 1h, 18h and 36h of post-annealing. Crystal size distribution of ZnO-NFs (inset)	113
Figure 5.9 Top: FESEM images of ZnO nanowires obtained with KHCO_3 [0.05M] at 10 °C (a) 1V/ 1 h; (b) 10V/ 5 min; (c) 1V/ 30 min; (d) 5V/ 15 min. Bottom: Degradation of phenol with the different arrangements of nanowires.....	115
Figure 5.10 Top: Adsorption of Mg by the ZnO-NFs. Bottom: Kinetic constant of photocatalytic degradation of phenol with ZnO-NFs obtained at different anodization conditions.	117
Figure 5.11 ZnO-NF light absorbance at different wavelengths.....	118
Figure 5.12 Top: ZnO-NFs light absorbance at 254 nm. Bottom: Kinetic constant of photocatalytic degradation of phenol with ZnO-NFs obtained at different anodization conditions.	118
Figure 5.13 a) Comparison of ZnO-NFs thickness with kinetic constants for photocatalytic degradation of phenol with films obtained with KHCO_3 [0.05M] at 10 C and 1V/ 1 h (a); 10V/ 5 min (b); 1V/ 30 min (c); 5V/ 15 min (d). b) FESEM of cross section of ZnO-NF.	119
Figure 5.14 Comparison between phenol degradation with ZnO-NFs obtained at different anodization conditions (left) and their respectively conductivities (right).....	120
Figure 5.15 FESEM micrographs of ZnO-NF used for photocatalytic studies (top) and their photocatalytic activity in the (bottom).....	121
Figure 5.16 Schematic of photo-active surface area and photo-active surface volume for immobilised photocatalysts.....	123
Figure 5.17 Changes in conductivity and final value of dissolved Zn produced during photocatalytic degradation of phenol with different ZnO-NFs. The nomenclature used in this figure is the same as Figure 5.10 and includes the electrolyte used during the production of the ZnO-NFs by anodization.	124
Figure 5.18 Set up of the photocatalytic experiment at anoxic conditions.	126
Figure 5.19 OD concentration measured throughout the photocatalytic reaction (a). Photocatalytic degradation of phenol under different oxygen dissolved conditions (b).	127
Figure 5.20 FESEM micrographs of ZnO morphologies before and after photocatalytic degradation of phenol. (a) Initial morphology; (b) reaction without Oxygen saturated with Argon; (c) unsaturated with oxygen; (d) saturated with oxygen.	128

Figure 5.21 Changes in conductivity measured along the photo catalytic reactions with different oxygen dissolved conditions.	130
Figure 5.22 FESEM micrographs of Zn foil exposed to different external environments. Zn foil exposed to air (a); Zn foil immersed in deionised water (b); Zn foil immersed in deionised water with UV irradiation (c).	131
Figure 5.23 FESEM micrographs of ZnO-NF before (left) and after (right) photocatalytic experiments, showing the formation of new nanostructures.	133
Figure 5.24 FESEM micrographs of ZnO-NF before (left) and after (right) photocatalytic experiments, showing the formation of new nanostructures.	134
Figure 5.25 FESEM micrographs of Zn-NF before (a) and after (b-e) deposition of new nanostructures on the surface of nanowires. (The new nanostructures are shown at different magnifications).....	136
Figure 5.26 Comparison of the photocatalytic performance of ZnO-NFs with and without deposition of new nanostructures on the surface of the nanowires (photocatalytic degradation of phenol).	137
Figure 5.27 FESEM micrographs of Zn-NF displaying cracks (a) and loose of the ZnO layer (b) due to thermal post-treatment.....	138
Figure 5.28 TEM micrographs of ZnO films obtained with KHCO_3 [0.05M], 1V, 10C, 1h exposed to different post-annealing: with not post treatment (a); thermal post-treatment at 350 °C for 1 h (b); oxygen plasma post-treatment (c).....	138
Figure 5.29 Comparison of the photocatalytic performance of ZnO-NFs exposed to thermal post-treatment and oxygen plasma post-treatment	139
Figure 5.30 FESEM micrographs of Zn-NFs (post-treated with oxygen plasma) before (a) and after (b-c) photocatalytic degradation of phenol.....	139
Figure 5.31 XRD of ZnO films obtained with KHCO_3 [0.05M], 1V, 10C, 1h exposed to different post-annealing: with not post treatment; thermal post-treatment at 350 °C for 1 h; oxygen plasma post-treatment.	140
Figure 5.32 Changes in conductivity measured along the photo catalytic reactions with different post-treatment. (Colour font show the final concentration of dissolved Zn in the phenol solution).....	140
Figure 6.1 Reservoir and multi-meter used in the photocatalytic setup.....	136
Figure 6.2 Schema (top) and picture (bottom) of the FP-PCR setup	137
Figure 6.3 schema and picture of stainless steel flat plate batch photocatalytic reactor. Section AA (a); lateral view (b); Section BB (c); upper view (d). Top figure shows	

different parts of the reactor: top plate (1), bottom plate (2), outlet tubing (3) and quartz window (4)	139
Figure 6.4 Photolysis of MO at different initial concentration (a). Final Photodecomposition of MO after 240 min for different flows and light absorbance at the different MO concentrations (b) (<i>lines in Figure 6.4-a are used as a guide to facilitate visualization of the trends</i>).....	143
Figure 6.5 Schema of light absorbance at different concentrations on the model compound in the illuminated zone of the FP-PCR.....	144
Figure 6.6 MO absorbance (a) and MO transmittance (b) of light at different optical thickness in the illuminated zone of the FP-PCR.....	145
Figure 6.7 Photolysis of MO at different flows (a). Final photodecomposition of MO after 240 min at different flows (b) (<i>lines in Figure 6.6-a are used as a guide to facilitate visualization of the trends</i>).....	146
Figure 6.8 Reactor modelling of the FP-PCR for photolysis	146
Figure 6.9 Photocatalysis of MO [2.5 ppm] with ZnO powder (Flow: 27.2 ml/min)..	148
Figure 6.10 Degradation pathway for methyl orange (adapted from L. Gomathi Devi <i>et al</i> [322] and Wang <i>et al</i> [323]).....	149
Figure 6.11 Pictures of the ZnO-NF placed in FP-PCR. General view of the reactor (a); non-levelled ZnO-NF (b), levelled ZnO-NF (c)	150
Figure 6.12 Photolysis and photocatalysis of MO [2.5 ppm] with ZnO-NFs at the highest and lowest tested flow.	151
Figure 6.13 Photocatalysis at different concentration of MO at 27.2 mL/min. (Inset: enlarged Figure)	152
Figure 6.14 Photolysis and photocatalysis of phenol [20 ppm] at different flows	153
Figure 6.15 Photocatalysis of phenol at two different initial concentration and two volumes of solution in the FP-PCR at flow rate of 700 mL/min (Inset: enlarged Figure)	154
Figure 6.16 CAD-drawing (a) and picture (b) of the epoxy acrylic flat plate batch photocatalytic reactor.	156
Figure 6.17 Tubular annular batch photocatalytic reactor (TA-PCR)	157
Figure 6.18 Schematic (top) and picture (bottom) of the TA-PCR setup	158
Figure 6.19 Photometric data, UVC lamps 6 W phillips used for the TA-PCR [337].	160
Figure 6.20 FESEM micrographs of 1 mm wire. Zn wire (a,d); annealed Zn wire (b,e) and electro polished Zn wire in Perchloric acid – Ethanol [1:2] at 20v, -70C for 15 min (c,f).....	161

Figure 6.21 FESEM micrographs of ZnO-NW showing area with and without ZnO layer.....	161
Figure 6.22 Anodization of Zn wire at 0.1M, 1 V, 10 C and 1 min (a), 5 min (b), 15 min (c,e,f) and 45 min (d,g).	162
Figure 6.23 Cracks formed as a result of anodization of Zn wire at 0.1M, 1 V, 10 C and 70 min (a-b).....	163
Figure 6.24 Schema of ZnO-NF and ZnO-NW showing radial tension.	163
Figure 6.25 Photolysis of phenol [5 ppm], at two different flow rates and 10 °C.	164
Figure 6.26 Photolysis, photocatalytic and electrical assisted photocatalysis (EAPC) degradation of phenol [5 ppm], 10 °C, in the TA-PCR.....	166
Figure 6.27 changes in conductivity (a) and concentration of dissolved Zn (b) in the TA-PCR	167
Figure 6.28 FESEM of Zn wire after photocatalytic (a-b) and EAPC (c-d) reaction. .	168
Figure 6.29 FESEM of Zn-NW before (a,b) and after (c,d) photocatalytic reaction...	169
Figure 6.30 Proposed schema of the dissolution and precipitation of Zn(II) in the FP-PCR and TA-PCR.	170
Figure 6.31 Schema of the set-up for the production of Sol-gel.....	172
Figure 6.32 Sol-gel depositions over glass slides	174
Figure 6.33 PCF2 coated with SGA and SGB	175
Figure 6.34 FESEM micrographs of PCF2 coated with SGA1 (a), SGA2 (b), SGA3 (c), SGB4 (d), SGB5(e).....	175
6.35 XRD of ZnO powder (a), SGA (b), SGB (c).	176
Figure 6.36 Changes in colour produced by ZnO-NF in darkness after 24 hours. Initial samples (a), samples after 24 hours (b), Changes in MO absorbance (c).The anodization conditions of the ZnO-NF were: HCl [0.1M], 1h, 1V, 10 °C and HKCO ₃ [0.1M], 1min, 40V, 10 °C.....	177
Figure 6.37 Final decolouration of MO produced by ZnO-NF in darkness after 48 hours and their respective ZnO-NFs. The anodization conditions of the ZnO-NF were: HCl [0.1M], 1h, 1V, 10 °C and HKCO ₃ [0.1M], 1min, 40V, 10 °C.	177
Figure 6.38 Final decolouration of MO produced by ZnO powder and by ZnO-NF with different morphologies and obtained at different anodization conditions.	178
Figure 6.39 Comparison between final decolouration of MO produced by different ZnO-NFs and their morphology.....	181

List of Tables

Table 1.1 Comparative cost of some AOPs (Adapted from Munter [7])	2
Table 2.1 Bandgap energy and λ_{Ebg} of catalyst (Dhananjay at al [110]).....	26
Table 3.1 Experimental conditions of anodization of Zn.	43
Table 3.2 Experimental conditions of post-annealing study.	45
Table 4.1 Composition of ZnO-NFs obtained by EDX analysis.....	69
Table 4.2 Solubility of potential compound formed during anodization of Zn.....	70
Table 4.3 XPS composition of films obtained with different electrolytes	70
Table 4.4 Matrix summarising the results obtained from the rational design guidelines	99
Table 5.1 Phenol and common by-products produced during photocatalytic degradation [286]......	104
Table 5.2 Kinetic constant of photocatalytic degradation of phenol in different studies	107
Table 5.3 Composition of ZnO films after photocatalytic degradation of phenol under different dissolved oxygen conditions	129
Table 6.1 Entrance length for the FP-PCR calculated at different Reynolds numbers.	140
Table 6.2 Residences times for the FP-BR calculated at different Reynolds numbers.	141
Table 6.3 Head loss and pressure drop for the FP-PCR calculated at different Reynold number.....	142
Table 6.4 Total head loss and pressure drop for the photocatalytic setup calculated at different Reynolds number.....	142
Table 6.5 Entrance length and retention times for the TA-PCR.	159
Table 6.6 Composition of the Sol-Gel samples for ZnO deposition experiments.....	172
Table 6.7 PCF internal configurations[342].....	174

Nomenclature

A	Cross sectional area (m^2)
C	Speed of light ($\text{m}\cdot\text{s}^{-1}$)
C_e	Concentration in the liquid phase at equilibrium (mg l^{-1})
C_i	Concentration of the substrate ($\text{mol}\cdot\text{l}^{-1}$)
C_o	Initial concentration of the compound or pollutant (mg l^{-1})
D_h	Hydraulic diameter (m)
E	Band gap energy (eV)
F	Darcy friction factor (-)
G	Gravity ($\text{m}\cdot\text{s}^{-2}$)
h_f	Head loss for the reactor (m)
h_{fa}	Friction losses along the photocatalytic set up (m)
I	Light intensity (candela - Cd)
$k_{app,v}$	Pseudo-first-order reactor volume based reaction rate constant
k_i^k	Reaction kinetic constant ($\text{mol}\cdot\text{g}_{\text{cat}}^{-1}\cdot\text{min}^{-1}$)
K_i^A	Adsorption constant ($\text{mol}\cdot\text{l}^{-1}$)
Le	Entrance length (m)
l_{ch}	Total length of the channel (m)
l_p	Length of the photolysis area (m)
M_{cat}	Mass of the catalyst (mg)
Nr	Number of recirculation times (-)
Q_e	Amount of compound per unit weight of catalyst ($\text{mg}\cdot\text{g}_{\text{cat}}^{-1}$)
Q_{max}	Maximum amount of organic chemical species that forms a monolayer on the surface of the catalyst ($\text{mg}\cdot\text{g}_{\text{cat}}^{-1}$)
Re	Reynolds number (-)
r_i	reaction rate ($\text{mol}\cdot\text{g}_{\text{cat}}^{-1}\cdot\text{min}^{-1}$)
S	Illuminated surface area of the catalyst (m^2)
t_{le}	Total light exposition (s)
t_{r-t}	Total residence time of the fluid in the reactor (s)

t_{r-p}	Residence time in the irradiation area of the reactor (s)
V_s	Total volume of pollutants solution (m ³)
V_r	Reactor volume (m ³)
v	Flow velocity (m.s ⁻¹)
ΔP_r	The Pressure drop in the channel (N.m ²)
ΔP_a	the pressure drops of the segments (Equation 6.10) and the pressure drop in the reactor or channel (ΔP_r) (N.m ²)
ϵ	Molar absorption coefficient (m ² .mol ⁻¹)
$\phi_{overall}$	Quantum yield (number of moles of pollutant degraded. Number of moles photons absorbed ⁻¹)
γ_{sv}	Solid-vapour interfacial tension (J.m ⁻²)
γ_{sl}	Solid-liquid interfacial tension (J.m ⁻²)
γ_{lv}	Liquid-vapour interfacial tension (J.m ⁻²)
λ	Cut off wavelength – Plank Equation (nm)
λ_{Ebg}	Minimum wavelength band gap energy (nm)
μ	Dynamic viscosity (kg.m ⁻¹ .s ⁻¹)
ρ	Density of water (mg/mL)
σ	Scattering coefficient (μ_s .cm ⁻¹)
τ	Optical thickness (m)
ω	Scattering albedo
ϕ	Solid fraction of the surface (-)
ξ	Photon efficiency (number of moles of pollutant degraded. Number of moles photons absorbed ⁻¹)

Abbreviations

AOP	Advanced oxidation processes
BET	Brunauer Emmett Teller surface area
BOD	Biological oxidation demand
COD	Chemical oxidation demand
DO	Dissolved oxygen
EAPC	Electric assisted photocatalysis process.
EDX	Energy dispersive X-ray spectrometer
FESEM	Field emission scanning electron microscope
FP-PCR	Flat plate photocatalytic reactor
FWHM	Full width at half maximum
HLB	Hydrophilic-lipophilic balanced
HPLC	High-performance liquid chromatography
JCPDS	Joint committee on powder diffraction standards
LVRPA	Local volumetric rate of photon absorption”
MBRs	Membranes bio-reactors
MO	Methyl orange
MvK	Mars-van Krevelen mechanisms
NPOC	Non-purgeable organic carbon
PCA	Photocatalytic activity
PCF	Photonic crystals fibers
pH _{PZC}	pH of point of zero charge
PK _a	Point off association constant
PTFE	Polytetrafluoroethylene
PVP	Polyvinylpyrrolidone
PZC	Point of zero charge
R6G	Rhodamine 6G
RO	Reverse osmosis
RTE	Radiative transfer equation
SDR	Spinning disk reactor
SEC angle	Static effective contact angle
SEM	Scanning electron microscope
SG	Sol Gel
TA-PCR	Tubular annular photocatalytic reactor
TC	Total carbon
TEM	Transmission electron microscopy
TIC	Total inorganic carbon

TOC	Total organic carbon
UNESCO	United nations educational, scientific and cultural organization
UNICEF	United nations children fund
UV	Ultra violet
VOC	Volatile organic carbon.
WP	Wet perimeter
WHO	World health organization
XPS	X-ray photoelectron spectroscopy
XRD	X-ray diffraction
ZnO-NFs	ZnO nanostructured films
ZnO-NWs	ZnO nanostructured wires

*“Somewhere, something incredible is
waiting to be known.”*

Carl Sagan

Chapter 1: Introduction.

Scarcity of water sources and the constant pollution of fresh water sources have increased concern about the availability of sufficient water supplies for human consumption. Furthermore, emerging water pollutants impose new challenges for developing highly efficient, compact and inexpensive systems for the safe reuse of waste water [1], [2]. Conventional water treatment systems are capable of removing suspended solids, oil and fat, degrading organic matter and, depending on the technologies, removing nitrogen and phosphorus from urban waste water. However, these systems display low efficiency for removing organic compounds and pollutants that are present in small concentrations (micro-pollutants). They also require sequential processes in order to reach the minimal standards of water quality increasing the cost of the treatment due to high energy consumption, and high maintenance and operating costs [3]. Existing technologies such as reverse osmosis (RO), micro and nanofiltration display high efficiency in removing pollutants, but have issues related to fouling, which increase the cost of energy for pumping and replacement of the membranes. On the other hand, advanced oxidation processes (AOPs), are highly efficient at degrading organic compounds and have the potential of total mineralisation of pollutants *in situ* rather than requiring subsequent processing as is the case with filtration or absorption using activated carbon. However, the potential generation of by-products, non-selectivity, interfering compounds, and cost of some of the equipment limit their extensive use as a tertiary treatment. The strength and drawbacks associated with the current technologies have prompted studies to develop compact and efficient systems that combine high degradation with inexpensive technology [4].

Photocatalysis is an AOP which uses light as a source of energy to activate the catalyst forming highly reactive species. Photocatalytic oxidation is an attractive technology for

the elimination of organic pollutants in water due to its simplicity, ease of implementation and reasonable cost compared to other AOPs (Table 1.1). In addition, it does not require the use of hazardous materials such as hypochlorite, peroxide or ozone [5]. Finally, photocatalytic reactions have the potential to contribute not only to the oxidation of organic pollutants but also to the mitigation of fouling when used in combination with filtration [6].

Table 1.1 Comparative cost of some AOPs (Adapted from Munter [7])

Process	Cost of oxidant	Cost of UV
O ₃ /UV	High	Medium
O ₃ /H ₂ O ₂	High	0
H ₂ O ₂ /UV	Medium	High
Photocatalytic oxidation	Very low	Medium

Until now, the majority of photocatalytic reactors and treatment plants have used dispersed photocatalyst due to the following advantages: Low pressure drop through the reactor, high photocatalyst surface area and good mass transfer of the pollutants from the water to the photocatalyst. The major disadvantage of slurry systems though is the removal of the photocatalyst from the cleaned water after treatment by sedimentation or filtration. These extra steps make the process expensive and treating very large volumes of water is almost impossible [8]. Photocatalytic systems using a supported photocatalyst do not require catalyst separation step. However, it has frequently been reported that the process efficiency is reduced and that for the same catalyst loading, slurry reactors are more effective than fixed-bed systems due mainly to a decrease in surface area in the latter [9].

The application of nanotechnology in photocatalysis have contributed to the development of novel photocatalysts and the enhancement of existing ones [10]. This technology has been applied to the development of nanostructured supported photocatalysts, improving the surface area on a fixed-bed. As a result, new techniques to support photocatalytic materials on different substrates have been also developed [11]–[13]. One of the most used photocatalytic materials in water treatment is TiO₂ which has a band gap of 3.2 eV, is stable, and highly photoactive. A substitute for this material is ZnO, which also show high photoactivity. Its band gap is 3.2 eV, and it is less expensive than TiO₂ [14].

Based on the need for compact systems that mix the advantages of different technologies, this project aims to exploit the physical properties of ZnO, the advantages of nanostructured materials and the benefits of photocatalysis, in order to develop nanostructured ZnO photocatalytic films, and to study their properties as a photocatalytic material for the degradation of organic pollutants. As shown in Figure 1.1, this project involves three main science and engineering fields, namely, water treatment, material science and nanotechnology.

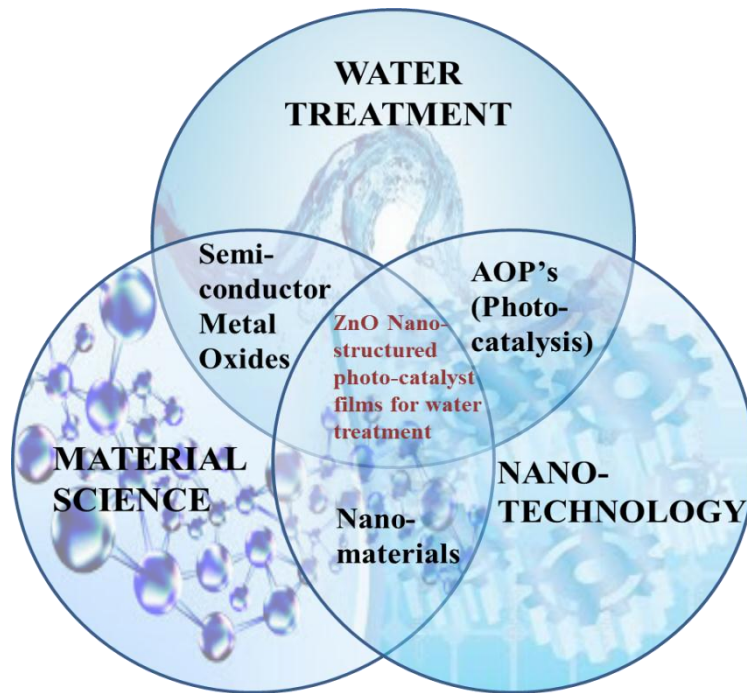


Figure 1.1 Contextualization of the present work in different science and engineering fields

1.1 Aims and objectives

Anodization of Zn is an easy and inexpensive way to produce ZnO nanostructures. The possibility of producing different morphologies by changing the experimental conditions makes anodization an attractive method for research at laboratory scale, and for the potential scaling up for industrial applications. Anodization of Zn has been reported in different studies, however, no systematic study correlating anodization variables with the obtained morphology has been conducted before.

In terms of environmental applications, ZnO has been reported as an effective photocatalyst for the degradation of organic pollutants in water. The majority of the studies have used ZnO in a powder form without considering the technical and economic implications of the separation of the ZnO from the water. On the other hand, studies of supported ZnO nanostructures for photocatalytic degradation of pollutants are limited compared to the ones with powders. Although some studies have mentioned the limitation of ZnO as a photocatalytic material due to its photocorrosion, only few studies have included experimental analysis about its stability during photocatalytic reactions. For this project, anodization of Zn was selected as method to produce ZnO nanostructured films, and the overall aim of this work was to conduct a systematic study of the correlation between anodization variables, the physicochemical properties of the obtained ZnO nanostructured films and their photocatalytic activity. Considerable attention was paid to morphology and films stability during degradation reactions of pollutants in water (Figure 1.2).

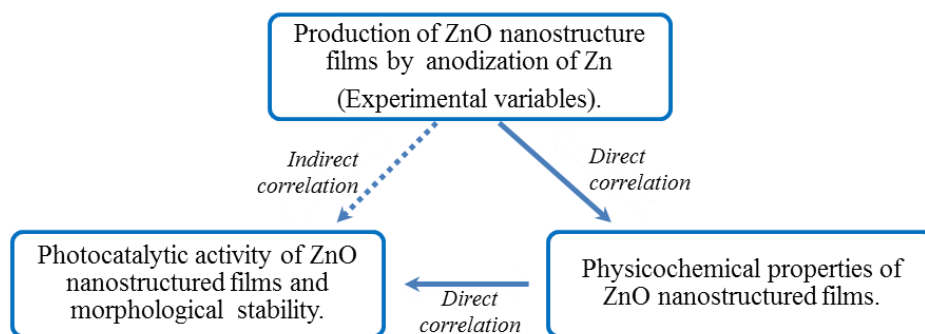


Figure 1.2 Scheme of the general aim of the research project

To meet this aim, the following specific objectives were established:

- Conduct a systematic study on the production of nanostructured ZnO films (ZnO-NFs) using anodization of Zn.
- Characterise the ZnO nanostructures films as a photocatalytic material.
- Assess the correlation between the anodization variables and physical properties of the ZnO-NFs. (i.e. Morphology, wettability behaviour, ZnO layer profile, particle size distribution and crystal size distribution).
- Test the photocatalytic performance of the ZnO-NFs in the degradation of an organic model pollutant in a batch reactor.

- Analyse the effect of some physical properties of the ZnO-NF on their photocatalytic performance.
- Asses the morphological stability of the ZnO-NFs under photocatalytic reactions and different types of mixing given by the type of reactor.

1.2 Thesis overview

The present chapter has (i) provided an overview of the situation of use of nanotechnology and photocatalysis in water treatment, (ii) highlighted this research project as a cross-road between three scientific and engineering fields (i.e. Water treatment, nanotechnology and material sciences) and (iii) discussed the aims and objectives of the present work. The following Chapter (#2) presents a summary of literature review in water quality, heterogeneous photocatalysis and ZnO as a photocatalytic material. Methods, materials and experimental procedures used throughout this research project are discussed in Chapter 3.

Chapter 4 presents in detail the production of the ZnO nanostructured films (ZnO-NFs) and their physicochemical characterisation. It also shows results obtained from the study of the correlation between anodization parameters with surface morphology and the effect of thermal post-treatment on morphology and crystallinity. The study of the ZnO-NFs photocatalytic properties during the degradation of phenol in a batch reactor is presented in Chapter 5. This chapter has three sections covering: (i) an initial analysis of phenol in the batch reactor, (ii) the effect of morphology and crystallinity of the ZnO-NF in photocatalysis and (iii) a study of ZnO-NF morphology stability during the photocatalytic reaction with phenol.

The final result chapter (Chapter 6) presents the design of a recirculating flat plate reactor, and a recirculating tubular annular reactor (TA-PCR). The former reactor was designed with the aim of studying the photocatalytic activity and stability of the ZnO-NFs at different flow regimes. For the TA-PCR, ZnO nanostructured wires were obtained by anodization and used as a photocatalyst. Taking advantage of the configuration of the TA-PCR, a current was applied to the Zn wire during a photocatalytic process and results are also discussed. Finally, the decolouration of methyl orange and initial degradation of phenol using ZnO-NFs under dark conditions (in absence of light during the reaction), and the deposition of ZnO layer on optical

fibers are also presented in this chapter. Conclusions of the present research project and future work are presented in Chapter 7. Figure 1.3 displays a summary flow chart of the thesis structure.

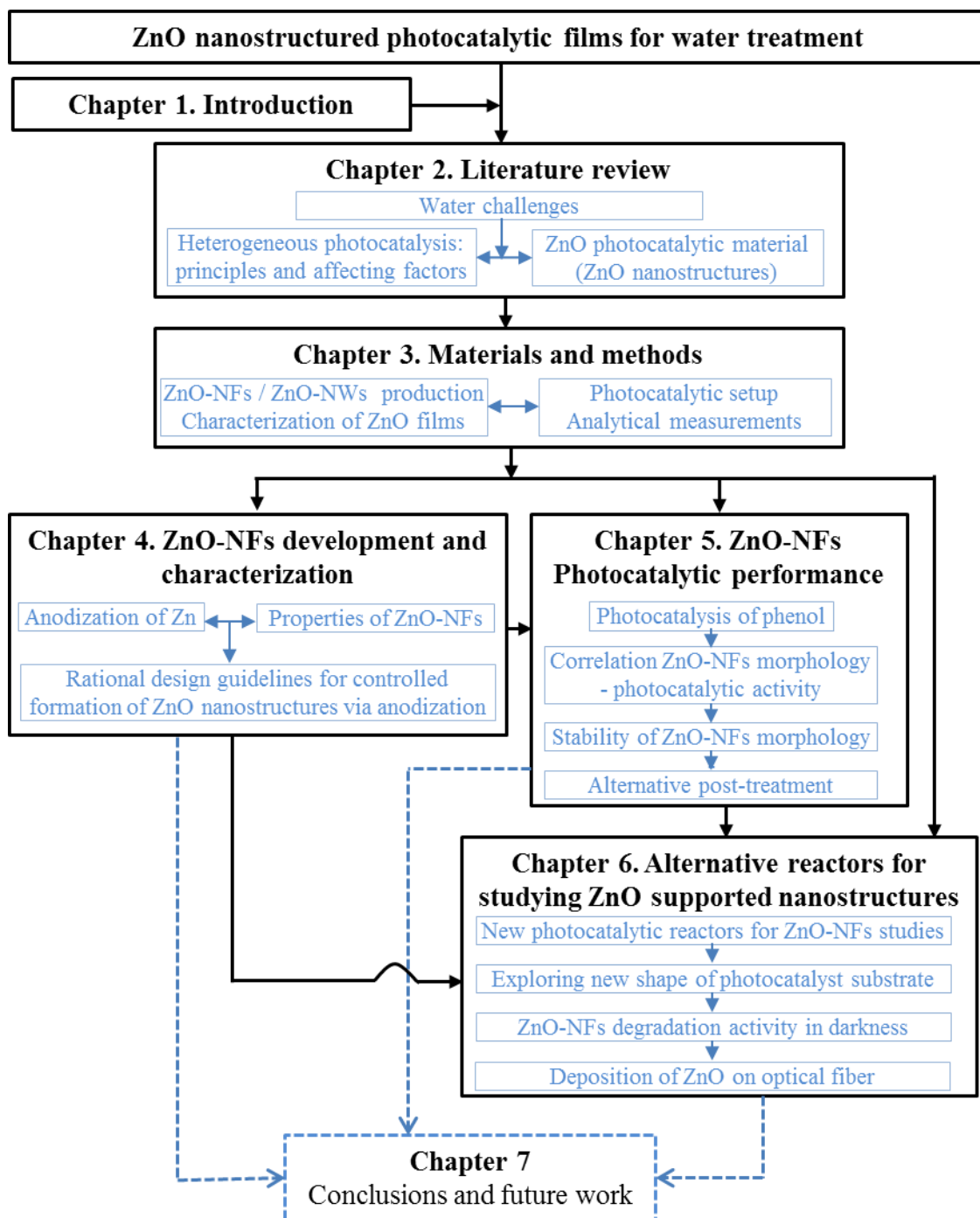


Figure 1.3 Summary flow chart of the thesis structure

“The literature of science is filled with answers found when the question propounded had an entirely different direction and end”

John Steinbeck

Chapter 2: Literature review.

In Chapter 1, this thesis was defined at the nexus of three science and engineering fields: Water treatment (i.e. Advanced Oxidation Processes /photocatalysis), Nanotechnology (i.e. Nano-materials) and materials science (metal oxides semiconductors). This chapter will present a general overview of concepts, theories and studies related to photocatalysis and the use of ZnO nanostructures as a photocatalyst in water treatment. The first section will provide a summary about the current situation of water pollutants and a brief discussion about existing technologies for water treatment. The Second section will present the fundamentals theories of photocatalytic reactions, mechanisms, kinetics and photocatalysts, introducing the use of ZnO as a photocatalytic material. It also will summarise some characteristics of photocatalytic reactors used in research. The last section discusses aspects related to ZnO as a photocatalyst including properties, uses in water treatment and ZnO nanostructures. Additionally, the last section will present a background on anodization as a technique for manufacturing ZnO nanostructures. Throughout the chapter, statistical data about the research in photocatalysis and about the use of ZnO in water treatment will also be presented.

2.1 Challenges of water for human consumption

Some of the UN Millennium Development Goals, such as reducing child mortality, combating malaria and other diseases, and ensuring environmental sustainability, are directly associated to water concerns [15]. Water issues can be analysed from different perspectives: One is the inadequate access to clean water and sanitation. This situation is directly linked to water quality and to the complexity of transporting water from natural sources to settlements in order to satisfy the basic needs of the population. Another perspective is water scarcity, which is related to the fact that the amount of water available for human consumption has decreased in the last decades [16]. Along

with domestic needs, this scarcity affects other sectors such as agriculture and industry as well.

The total amount of water on the Earth is estimated to be about $1.4 \times 10^6 \text{ m}^3$ but only 2.5% of this volume is fresh water. The sources of freshwater are distributed as follows: 0.3% in rivers and lakes, about 30% underground and approximately 70% in the glacial regions and permanently snow covered areas [17]. This distribution shows the limitation of water sources available for human consumption. According to the World Health Organization (WHO) and United Nations Children Fund (UNICEF) one in six people do not have access to “improved water sources” around the world [18].

Water scarcity affects different aspects of the life and economy. 8% of the total amount of water used around the world is for domestic purposes, 70% is used in irrigation, and 22% in industry and energy production [19]. According to the intergovernmental panel on climate change, due to the decrease in the amount of fresh water, it is predicted that by 2050 only 50% of crops will be irrigated with rainfall while the rest will require new sources of water [20].

Access to water resources is expected to become scarcer due to water shortages, erratic rainfall, glaciers melting and sea level rise resulting from global warming. One consequence of these phenomena is the salinity of coastal potable water sources will increase, affecting approximately a third of the world’s population [21]. These water shortages are predicted to affect developing countries more than developed ones [22]. More densely populated cities, where water demand is extremely high and water sources are limited, will be the worst affected. For instance, in 60% of European cities with a population higher than one hundred thousand, the rate of use of underground water is faster than the rate of replenishment [23].

Water quality, on the other hand, is mainly affected by anthropogenic activities with around two million tons of waste produced by humans disposed every day in water courses [24]. As a result, people who use this water without previous treatment are exposed to acquired illness. Although there are well established treatment systems, the access to them is limited, in particular in developing countries [24].

Among the issues related to water quality, emerging pollutants have caught the attention of environmental organization and research institutes due to their toxic effects and recalcitrant properties [25]. The most common emerging pollutants are pharmaceuticals and household cleaning products, endocrine-disrupting compounds (e.i. steroids and hormones), flame retardants, gasoline additives and industrial additives [26]. The presence of industrial pollutants in water sources is a common situation, in particular in countries with a weak environmental legislation. According to the World Water Assessment Program of the United Nations and UNESCO[24] in developing countries 70% of industrial wastes are discharged in water sources without treatment.

In terms of domestic activities, the mass use of cosmetic, cleaning and pharmaceutical products increases the level and variety of water pollutants. These compounds are discarded in the sewage system, passed through waste water treatment without successful removal, and discarded in water courses affecting aquatic ecosystems[27]. Additionally, as they are not removed during the drinking water treatment, they have also been found in drinking water sources as reported in different studies [28], [29]. Among the different types of emerging pollutants, drugs have received high public and scientific attention due to their potential toxicity and to their mass use and production [30], [31], accounting more than 3000 types of pharmaceuticals in the market [32]. Drugs are usually found in concentrations of nano-grams per litre, have toxic effects, are persistent in the environment, and are bioactive, which means that they can produce biochemical and physiological changes in natural species [33].

Due to the limited water sources, the potential scarcity of water, low efficiency for organic compounds removal in conventional water treatment systems, and emerging pollutants, new technologies with high performance in the degradation of organic pollutants, low use of chemicals and energy efficient are needed. The initiative to develop highly efficient and compact systems involves minimizing the use of chemical and residual products in order to minimize the exposure of humans to toxic chemicals [34] .

2.1.1 Current technologies for water treatment

Water treatments are classified in primary, secondary and tertiary treatment depending of the type of pollutants removed during the process and the quality of the effluent obtained as shown in Figure 2.1. Conventional water treatment systems include: (i)

sedimentation, coagulation and flocculation for the removal of suspended solids, (ii) activated sludge systems or trickling filters to remove some organic compounds and nutrients by using suspended microbes, (iii) aeration for oxidation of organic compounds; and (iv) disinfection for elimination of pathogens. The integration of those processes in a water treatment facility is the most common primary and secondary treatment nowadays, producing effluents that are suitable for some reuses such as restricted irrigation, industrial applications or for discharge in water courses [3]. For unrestricted irrigation and for drinking water, on the other hand, higher quality standards are established, thus a tertiary treatment is usually needed. Furthermore, the presence of recalcitrant compound in water sources has brought the development and use of highly efficient advanced technologies.

Treatment	Characteristic	Technologies
Preliminary	Removal of rags, sticks, floatables, grit and grease.	Screening, Grit removal, comminution, flotation.
Primary	Partial removal of suspended solids and organic matter.	Sedimentation, decantation, coagulation, flocculation.
Secondary	Removal of biodegradable organic matter and suspended solids, it can involve the removal of nutrients.	Secondary sedimentation, flocculation, Biological degradation, sludge processes.
Tertiary	Removal of residual suspended solids, nutrients and disinfection.	Nitrogen removal, phosphorous removal, chemical coagulation, deep and surface filtration.
Advanced	Removal of dissolved and suspended materials remaining after normal biological treatment.	Membrane filtration, Ion exchange, Adsorption, chemical oxidation, AOPs.

Figure 2.1 Characteristics and classification of water treatment systems (Adapted from Metcalf and Eddy [35])

Advanced technologies have been studied for oxidation of different water pollutants showing remarkable results in the degradation of complex compounds. The classification of these technologies is shown in Figure 2.2 and includes UV light, ozone, membrane filtration and advanced oxidation processes (AOPs). The use of UV light in water treatment allows the photochemical inactivation of pathogens and photodegradation of chemical compounds, these techniques are efficient but require that the light penetrate the whole water column and also some waterborne pathogens show high resistance to UV light [36].

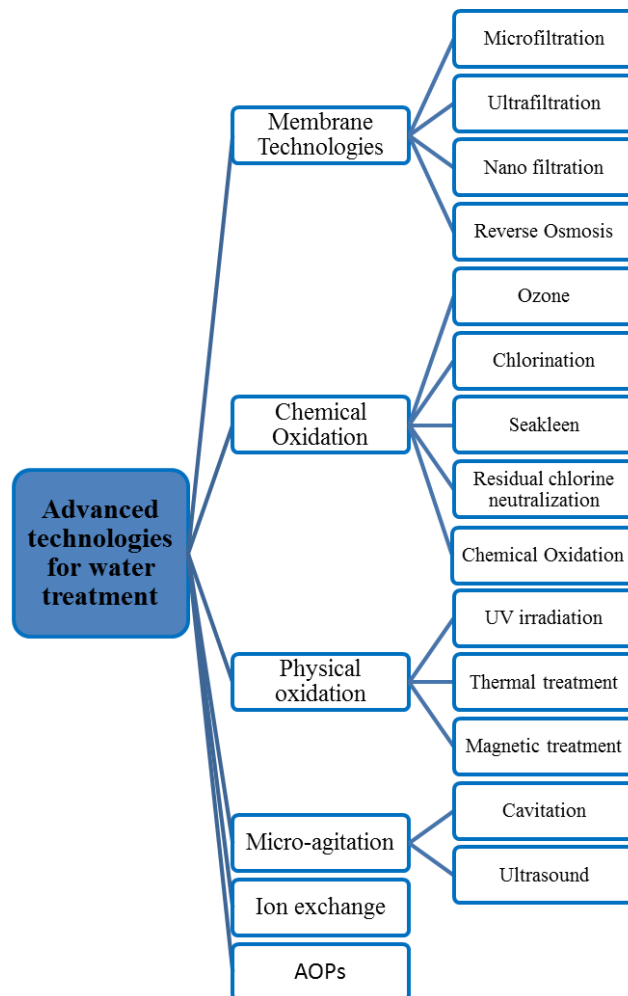


Figure 2.2 Classification of advanced technologies for water treatment (Adapted from Metcalf and Eddy [37] and Munter [7])

Membrane technologies for water treatment include reverse osmosis (RO) and filtration (microfiltration, ultrafiltration and nanofiltration). Figure 2.3 shows the cut offs of the different membranes techniques. Filtration uses straining to separate particles from the media and its mechanism is size exclusion. RO uses pressure to separate large

molecules and salts from water by using selective membranes [38]. The main application of RO is desalination where water from the sea is used as a fresh water source, in fact, 50% of the worldwide desalination plants include a RO process [39]. The main drawback of filtration and RO is fouling which occurs when membrane pores are clogged by pollutants such as salt and suspended solids. The development of robust membranes, new materials, and more efficient energy recovering systems have moved RO towards extraordinary improvements in terms of reduction in energy consumption and higher efficiency [40].

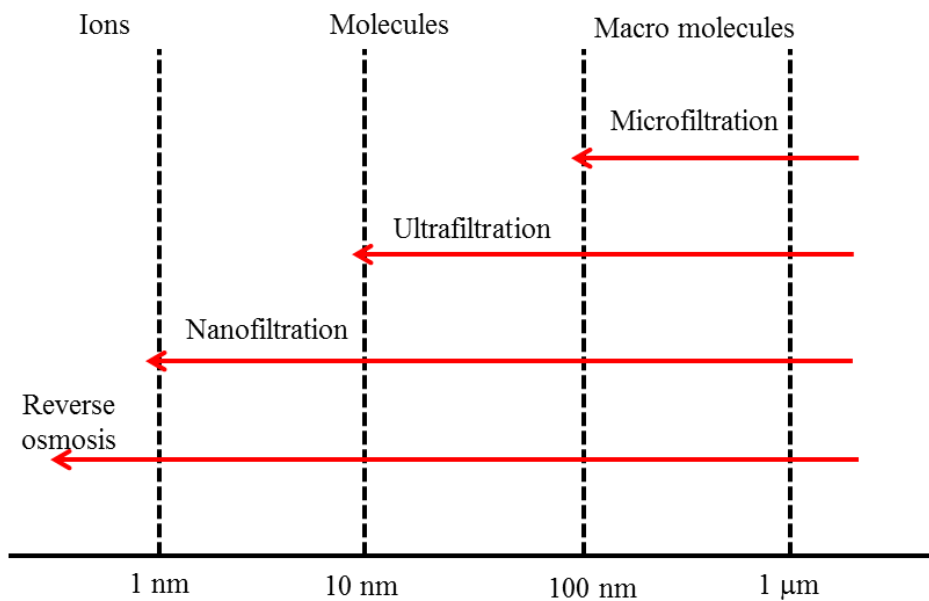


Figure 2.3 Particle size cut off for the different membrane filtration techniques (Adapted from Lenntech [41])

A combination of technologies that include filtration and degradation of pollutants are the membrane bio-reactors (MBRs), which nowadays is one of the most used methods for wastewater treatment. In the MBRs, the wastewater is mixed with activated sludge (liquor) and the liquor is filtrated through an immersed or sidestream membrane. In this process biodegradation of pollutants occur producing high quality permeates. Costs associated to these systems involve the pumping of water and sludge, the cleaning and replacement of membranes and the energy required to maintain a homogeneous mixture of the liquor. As mentioned before, control of fouling in membranes is one of the issues associated with these systems and its reduction still remains a challenge [42].

Finally, AOPs for water treatment are based on the generation of hydroxyl radicals (OH•). The oxidation potential of the OH• radicals (2.8 V) is higher than other species

used in water treatment, such as ozone (2.07 V), H₂O₂ (1.78 V), HOCl (1.49 V) and chlorine (1.36 V) [43]. It is therefore it is considered a highly oxidant species capable of degrading a wide range of organic pollutants into CO₂, water and mineral acids [44]. Due to its high reactivity, OH• radical is unstable and it must therefore be produced *in situ* inducing its formation by chemical or photochemical reactions [45]. The main advantage of this technology is the potential total mineralisation of the organic compounds. Additionally, there is a degradation of the pollutants instead of only a separation process as occur with membrane technologies where pollutants are transferred from water to another media. As shown in figure 2.4, the formation of OH• can be obtained through different methods, namely, ozone with UV light, hydrogen peroxide and UV light, cavitation, E-beam irradiation, reaction via Fenton, and photocatalysis [45]. Among these methods, photocatalysis has been recognised for its high capability to mineralize organic compounds until CO₂, water and simple inorganic acids. This property makes photocatalysis an attractive method for the destruction of toxic and recalcitrant pollutants. For instance, photocatalysis has successfully used to degrade a variety of organic compounds such as dyes [46]–[48], endocrine disrupting chemicals [49] and phenolic compounds [50].

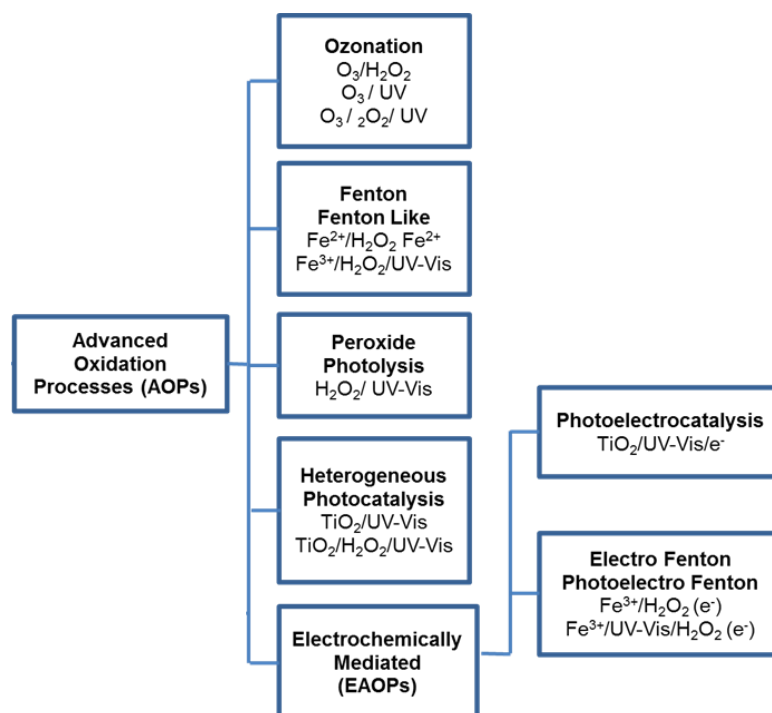


Figure 2.4 Classification of the advanced oxidation processes for water treatment (adapted from Andreozzi *et al* [51])

2.2 Heterogeneous photocatalysis, principles and determining factors

Photocatalysis is defined by different authors as the catalytic acceleration of photoreactions [43]. However, in this definition it is not clear the role of the light in the activation of the catalyst leading to confusion between different processes that occur in a photoreactor and that are activated by light. Othashi [52] has defined photocatalysis as ‘the chemical reaction induced by photo-absorption of a solid material, or photocatalyst, which remains unchanged during the reaction’. This definition appears to be more accurate since it not only specifies the light activation of the photocatalyst but also gives information about the state of the photocatalyst and its participation on the reaction.

According to Herrmann *et al* [53], photocatalytic research projects started in different European catalytic laboratories in the 1960s and 1970s. Some of the studies carried out in England at that time include: (i) The study of photo-adsorption/desorption of oxygen on ZnO in 1960 and with TiO₂ in 1973, (ii) the photocatalytic oxidation of CO on ZnO (1960) and (iii) the selective isopropanol oxidation in acetone. Another study about oxidation of CO on ZnO carried out in Germany in 1964 is recognised as the first reference to include the word “photocatalysis” in its title [53]. However, the expansion of photocatalytic research is commonly attributed to the publication in English of Fushima and Honda’s work on the splitting of water into hydrogen and oxygen, using a titania-base anode illuminated with UV light in 1972 [54].

Since 1972, the number of publications about photocatalysis has increased dramatically. In the last decade, the numbers of publications about photocatalysis have increase from 1100 to 3800 publications in averall (Figure 2.5). This trend not only aligns with the increase in the number of research projects about photocatalysis itself, but also to the multidisciplinary applications of this technology in a variety of fields such as semiconductors physics, surface science, photo-chemistry material science and chemical engineering [53].

In terms of environmental applications, photocatalytic studies have been focused on using semiconductor materials as photocatalyst for the depuration of pollutants in gas and liquid phases. In this area, the number of publications in the last decade accounts a total of 6500 publications including papers, reports and reviews. As shown in Figure 2.5, between 2013 and 2014, 25% of the total photocatalytic studies were related to water treatment.

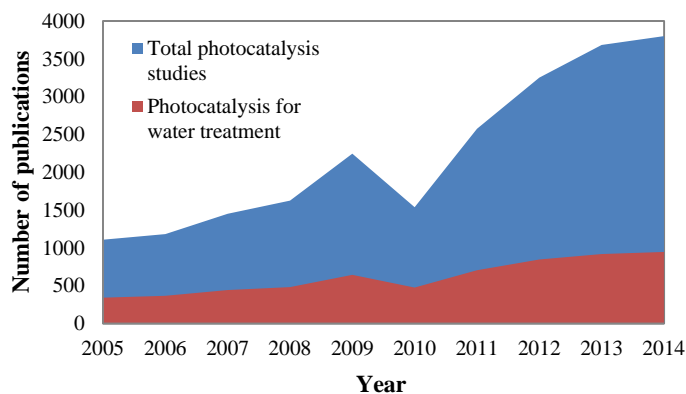


Figure 2.5 Number of publications per year related to photocatalysis studies and photocatalysis for water applications [55]

2.2.1 Photocatalytic mechanism

In water treatment, photocatalytic reactions follow the heterogeneous catalysis principles where the process occurs at the interface of the solid (catalyst) and the media (water) [46]. It has been suggested that heterogeneous photocatalysis occurs in seven general steps [56]: (i) External mass transfer (diffusion) of reactants from the bulk fluid phase to the external surface of the solid photocatalyst, (ii) Internal mass transfer (internal diffusion) of the reactants from the external surface of the photocatalyst through the pores to the interior surface of the photocatalyst, (iii) adsorption of reactants, (iv) reaction in the adsorbed phase, (v) desorption of products, (vi) Internal counter-diffusion of the products through the pores to the external surface of the photocatalyst and (vii) external counter-diffusion of products from the external surface of the photocatalyst to the fluid media. The reaction in the adsorbed phase (step iv) consists on a multiple sub-steps as shown in Figure 2.6. The reaction in the adsorbed phase starts with the excitation of the catalyst by photons at certain wavelength where electrons absorb energy reaching conduction band and creating an electron-hole pair. These species (electron-hole pair) move to the surface of the catalyst where adsorbed species act as scavengers. The hole reacts with adsorbed water (or another electron donor such as OH^- which can be present on the catalyst material) producing the $\text{OH}\cdot$ radical; while the electron reacts with oxygen (or another electron acceptor) forming $\text{O}_2\cdot^-$. The latest ion is a superoxide radical which can further react either with hydrogen ions (H^+) from the water splitting process forming $\text{HO}_2\cdot^-$ or react directly with another species. Both $\text{OH}\cdot$ and $\text{O}_2\cdot^-$ are the main responsible for the degradation of the pollutants in the oxidation–reduction reactions. During the reaction, a recombination of

the electron-hole pair occurs [57]. Furthermore, some compounds absorbed on the catalyst surface can be directly degraded by the hole or the electron before their recombination [58].

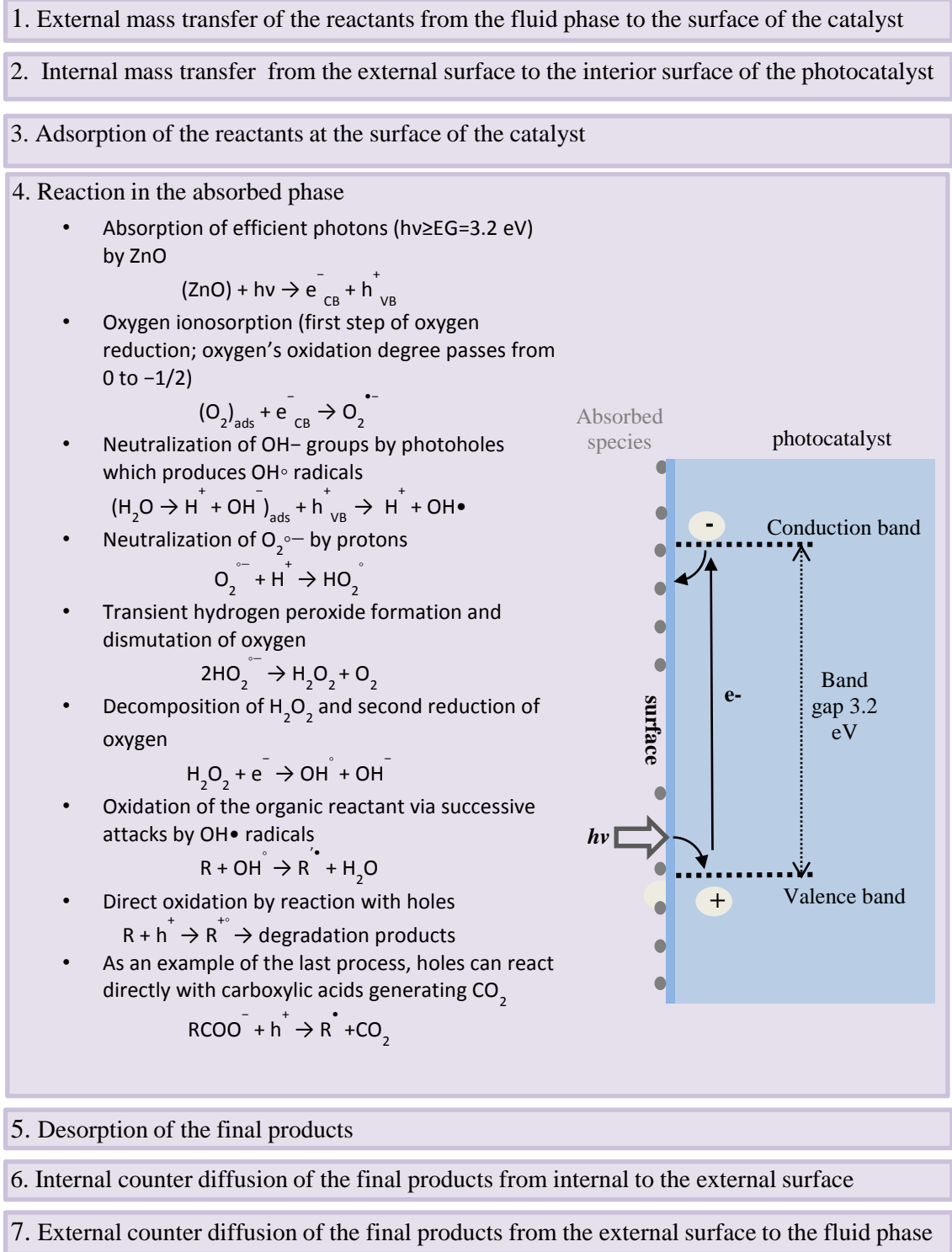
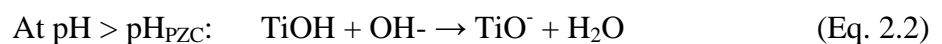
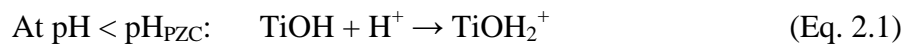


Figure 2.6 Mechanism of photocatalysis (adapted from Herrmann [53]; Cassano *et al*, [57] and Houas *et al* [59])

Photocatalysis is considered a first order reaction where the degradation rate is proportional to the concentration of the substrate or pollutant. The most common model to estimate kinetic parameters in photocatalytic process is the method of initial rate [60] which is a model based only on one component, ignoring intermediates products and making it difficult to predict and to study photocatalytic reactions through theory. Another factor that makes the study of photocatalytic reactions difficult is the multiple variables involved in the process such as light intensity, mass transfer, and adsorption process.

Photocatalysis occurs on the surface of the catalyst and involves adsorption of pollutants. The main factors that affect the adsorption of pollutants are: (i) The mass transfer mechanisms, which is related to fluid mechanics, and directly influenced by the type of reactor and mixing process, (ii) the physical-chemical properties of the photocatalyst surface and (iii) the properties of the pollutant. The adsorption of chemical species is influenced by the pH of the media due to its effect on the chemical form of the pollutants (depending on its PKa) and on the charge of the solid catalyst (based on its point of zero charge PZC). The pH value where the photocatalyst is not charged is known as pH_{PZC} and is used in surface characterisation [61].

When the pH of the media is similar to the pH_{PZC} , the total charge of the surface is zero and the interaction of the photocatalyst with water molecules and other chemical species is minimal due to the absence of electrostatic forces. Changes in the pH of the media induce changes on the surface charge density of the photocatalyst. When the photocatalyst surface is charged, electrostatic forces attract ions. As shown in the water equilibrium equation for titanium dioxide (Equation 2.1 and 2.2), when the pH of the media is higher than the pH_{PZC} , the surface is charged negatively. On the other hand, positive surface charge occurs at pH lower than the pH_{PZC} [44].



In water treatment, the pH is given by the dissolved chemical species. During photocatalytic reactions, the pH can vary due to the production of by-products and therefore the adsorption of the pollutants change through the reaction [62]. Additionally, when the photocatalyst is dispersed in water, changes in pH during the

reaction might change the catalyst particle size as agglomeration can occur due to the electrostatic interactions produced by changes in the surface charge [63].

The adsorption rate is strongly influenced by the concentration of the pollutant, high adsorption is produced at high pollutant concentrations. However, the effect of high pollutant concentrations in photocatalysis has been discussed from two different perspectives: Richard *et al* [58] suggested that by increasing the concentration of the pollutants, their absorption is higher and, therefore, they are more likely to be degraded by photocatalysis and through direct oxidation by positive holes. In opposition of that, it has been suggested that high concentrations of pollutants no longer increase the rate of photocatalytic reaction, additionally it can affect the process in two ways, (i) by saturating the photocatalyst surface and (ii) by absorbing fractions of light [44].

2.2.2 Kinetics of photocatalytic reactions

For heterogeneous catalysis, different mechanisms have been proposed to explain the interaction between the catalyst and the adsorbed molecules or ions, namely the Mars-van Krevelen (MvK), Eley-Rideal (ER) and Langmuir-Hinshelwood (L-H) mechanisms. The latter is the most accepted and used mechanism for photocatalysis, however new photocatalytic kinetic models (related or unrelated to the Langmuir-Hinshelwood rate equation) are still under analysis [64], [65].

The Mars-van Krevelen mechanism suggests that during the reaction one or more components of the catalyst's lattice are taken by the reactants. Doornkamp and Ponc [66] reviewed this mechanism and observed that it occurs during different photocatalytic reactions. They suggested that a combination of Mars-van Krevelen and Langmuir-Hinshelwood occur frequently during catalytic reactions and both mechanisms result either in similar or different products. Since photocatalytic processes require oxygen for the oxidation-reduction reactions, oxygen is directly taken from the media and used in the radical initiation. Under limited oxygen conditions, the reaction follows the MvK mechanism and the oxygen is taken directly from the catalyst lattice, which is later replaced with oxygen from the media if possible [67]. A high steady-state concentration of oxygen vacancies in the catalyst appears to promote the MvK mechanism as oxygen from the adsorbed substrates can bond into the catalyst [66].

The main reaction mechanism defining the full degradation (mineralisation) of organic compounds by photocatalyst is the Langmuir-Hinshelwood (L-H). Equation 2.3 is the general form of the L-H reaction rate (r_i) for compound “ i ” ($\text{mol}\cdot\text{g}_{\text{cat}}^{-1}\cdot\text{min}^{-1}$) and monochromatic light, where LVRPA refers to the “local volumetric rate of photon absorption”, k_i^k is the reaction kinetic constant ($k_i^k = \text{LVRPA} * k_i^l$) ($\text{mol}\cdot\text{g}_{\text{cat}}^{-1}\cdot\text{min}^{-1}$), K_i^A the adsorption constant ($\text{mol}\cdot\text{l}^{-1}$), C_i the concentration of the substrate ($\text{mol}\cdot\text{l}^{-1}$) and the subscript “ j ” denote each component involved in the photocatalytic reaction [68].

$$r_i = \text{LVRPA} \frac{k_i^l K_i^A C_i}{1 + \sum_{j=1}^n K_j^A C_j} = \frac{k_i^k K_i^A C_i}{1 + \sum_{j=1}^n K_j^A C_j} \quad (\text{Eq. 2.3})$$

L-H model describes the reaction as a multiple component system and explicitly displays the influence of photon absorption. However, the majority of the kinetic studies for photocatalytic reactions for different types of pollutants have used simplified L-H models. Some of the assumptions made by these models are: (i) Photocatalysis is a single component system (when only one chemical species is present), (ii) the influence of by-product on the reaction rate is minimal, (iii) the effect of photon absorption is not considered or it is coupled with other parameters. Furthermore, kinetic parameters found in literature are strongly related to the reactor configuration (i.e. size and geometry), rather than the kinetic degradation of a given compound. As a result, there is a limitation when comparing kinetic data between different studies and to scale up the process [69].

The calculation of the adsorption constant (K_i^A) needed in the analysis of the reaction rate (Equation 2.3) requires special attention, in particular for photocatalytic reactions with supported catalyst (as the one developed in this thesis). Normally, K_i^A is calculated using the classical L-H isotherm given by Equation 2.4, where Q_e ($\text{mg}\cdot\text{g}_{\text{cat}}^{-1}$) is the amount of compound per unit weight of catalyst, Q_{max} ($\text{mg}\cdot\text{g}_{\text{cat}}^{-1}$) is the maximum amount of organic chemical species that forms a monolayer on the surface of the catalyst and C_e (mg l^{-1}) is the concentration of the compound “ i ” in the liquid phase at equilibrium. As the constant Q_{max} and K_i^A are specific for each compound and varies with the type of photocatalyst used, they usually are calculated from experimental data where Q_e and C_e are correlated in adsorption experiments in dark.

$$Q_e = \frac{Q_{\text{max}} K_i^A C_e}{(1 + K_i^A C_e)} \quad (\text{Eq. 2.4})$$

By definition, Q_e is expressed as a function of the mass of the catalyst (M_{cat}) (Equation 2.5) where C_o is the initial concentration of the compound or pollutant, and V_s is the total volume of the solution. Using Equation 2.5, the value of Q_e can be determined, in particular for catalysts in powder form. For supported photocatalyst, on the other hand, the amount of photocatalyst cannot be easily determined. Furthermore, the total mass of catalyst present in a film does not necessarily represent the amount of catalyst available for the photocatalytic reaction. These conditions make the analysis of either adsorption and photocatalysis of organic pollutants difficult with supported photocatalysts. Similar limitations occur with the calculation of the LVRPA (usually calculated from the radiative transfer equation (RTE)), where the experimental analysis has been well developed for powder photocatalyst as it has been reported in several studies [68], [70], [71].

$$Q_e = \frac{(C_o - C_e)V_s}{M_{cat}} \quad (\text{Eq. 2.5})$$

During photocatalysis, high concentrations of the organic compound result in a pseudo-zero order reaction. At low concentration, with not oxygen limited, the reaction is pseudo-first order as describe by equation 2.6, where $k_{app,v}$ is the ‘pseudo-first-order reactor volume based reaction rate constant’ which comprises light absorption, oxidant concentration and catalyst concentration. $k_{app,v}$ can be calculated using equation 2.7 where S is the illuminated surface area of the catalyst, V_r is the reactor volume and k_i^k is the pseudo-first or second order reaction rate constant [72].

$$r_i = k_{app,v}C_i \quad (\text{Eq. 2.6})$$

$$k_{app,v} = \frac{S}{V_r} k_i^k \quad (\text{Eq. 2.7})$$

The efficiency of the photocatalytic reaction can be expressed either by the quantum yield ($\phi_{overall}$) or by the photon efficiency (ξ) given by equations 2.8 and 2.9 respectively. Due to the difficulty in measuring the rate of photon absorption, the latter parameter is preferred and defined as the relation between the number of transformed molecules and the number of incident photons [72].

$$\phi_{overall} = \frac{\text{reaction rate}}{\text{rate of photon absorption}} \quad (\text{Eq. 2.8})$$

$$\xi = \frac{\text{reaction rate}}{\text{incident monochromatic light intensity}} \quad (\text{Eq. 2.9})$$

2.2.3 Light in photocatalytic processes.

Photocatalytic reactions are initiated by the absorption of photons by the photocatalyst; the effect of the light in photocatalytic reactions depends on the type of photocatalyst, the light wavelength and the light intensity. Electron-holes pairs in a photocatalyst are produced when the energy absorbed is equal or higher than the band gap of the photocatalyst. The light wavelength determines the energy given to the system. UV-A light is in the wavelength range of 315 to 400 nm (3.10 – 3.94 eV); for UV-B the wavelength range is 280 to 315 nm (3.94–4.43 eV) while for UV-C the range is 100 to 280 nm (4.43–12.4 eV). Although UV-A light provides enough photonic activation energy for most of the frequently used photocatalyst (see Section 2.2.5), different photocatalytic studies have also used UV-B and UV-C sources including sunlight [73].

The photocatalytic reaction rate (r_i) is directly dependent on the light intensity (I), as is expressed by Equation 2.10 where k_i^k is a rate constant, C_i is the concentration of the substrate or pollutant and n is the kinetic order given by the light intensity. At light intensity lower than 25 mW/cm², the production of electron-holes pairs is limited and they are totally consumed during the photocatalytic reaction, therefore, the reaction is considered a first order with a value of n equal to 1. Light intensity higher than 25 mW/cm², on the other hand, generates excess of electron-hole pairs with a high rate of recombination, and as a result, the reaction is a half order, and the value of the kinetic order in this case is 0.5 ($n=0.5$) [74], [75].

$$r_i = k_i^k C_i I^n \quad (\text{Eq. 2.10})$$

The amount of light absorbed by the catalyst is affected by the optical properties of the solution (or waste water), i.e. molar absorption coefficient (ϵ), scattering coefficient (σ) and the phase function [76]. The absorption coefficient is defined as the fraction of incident radiant energy that is absorbed by a molecule or a particle per unit mass. Scattering coefficient is also known as dissipation coefficient and is defined as ‘The fractional decrease in intensity of a beam of electromagnetic radiation or particles per unit distance traversed, which result by scattering rather than absorption’, while phase function refers to the angular distribution of light intensity scattering by a particle at a given wavelength [77].

Although absorption coefficient and scattering coefficient are important variables in photocatalysis and, in particular, in the design of the photocatalytic reactor, the

calculation of them separately is a complex process. Therefore, the extinction coefficient, which is the addition of the scattering and absorption coefficients at similar wavelength, is used as an experimental parameter of analysis calculated by photometric measurements [76], [78]. High values of extinction coefficients, given by high absorption and/or high scattering of light, minimize the amount of light absorbed by the photocatalyst resulting in a low generation of electron-hole pairs and reactive species, and therefore in a decrement of the reaction rate.

2.2.4 Photocatalytic reactors

A large variety of photocatalytic reactors have been designed and reported for water treatment. Based on the distribution of the catalyst within the reactor, conventional photocatalytic reactors can be classified as a slurry reactors, fixed or supported catalytic bed and fluidised catalytic bed reactors [57]. Figure 2.7 displays a general scheme of these types of photocatalytic reactors. Furthermore, variations in geometry, type of mixing process, light source and location of the light are commonly found in literature. Other authors have classified the photocatalytic reactors according to the shape; for this type of classification, the most common reactors used in photocatalytic studies are flat plates reactors [79]–[81] and annular reactors [82], [83]. Photocatalytic reactors can operate either in batch, batch with recirculation, or in continuous mode.

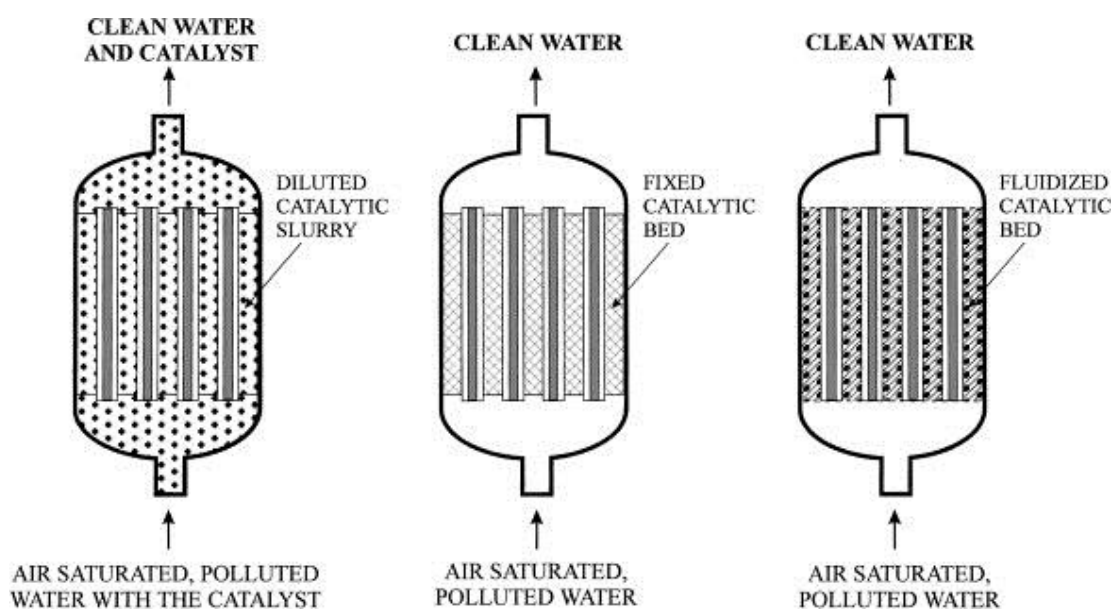


Figure 2.7 Types of heterogeneous photocatalytic reactors classified by the form of photocatalyst (Cassano *et al* [57])

The number of research publications (i.e. papers, reports and reviews) focused exclusively on the design and optimization of photocatalytic reactors has slowly increased in the last decade (Figure 2.8). For instance, in 2005 the number of publications related to photocatalytic reactors was 135 while in 2010 the number increased to 140 publications and to 167 publications in 2014.

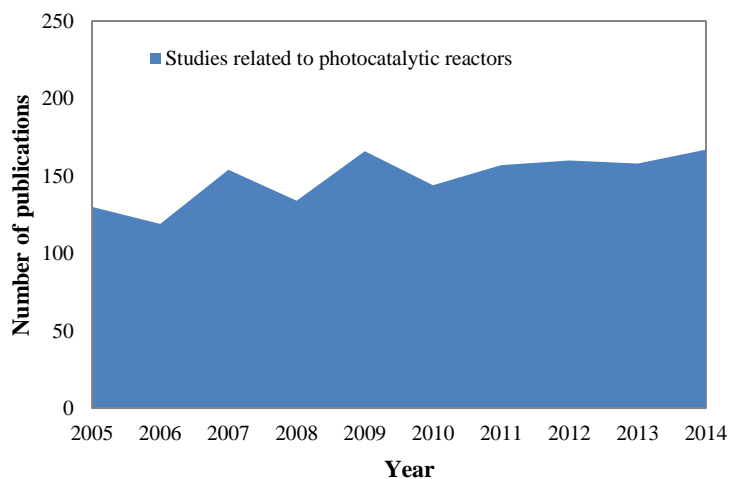


Figure 2.8 Number of publications related to photocatalytic reactors since 2005 [55].

For a dispersed photocatalyst, the most common photocatalytic reactors found in the literature and used for experimental studies for water treatment are (i) the batch reactor where the light source (usually UV lamps) is either immersed in the water or placed on the top of the reactor and (ii) the slurry annular reactor in which the light source is placed in the internal channel while the water with the dispersed catalyst flows through the annular space. Slurry reactors have high surface volume ratio and therefore the mass transfer between pollutants and photocatalyst is high resulting in high rates of degradation. On the other hand, slurry reactors require downstream separation to recover the photocatalyst [8]. Additionally, the increase of amount of photocatalyst that can be used in this type of reactors is limited due to the scattering produced by the particles that decrease the penetration of light [84], [85].

For an immobilised photocatalyst, Lin *et al* [8] identified three categories of photocatalytic reactors according to the location of the light source: (i) Reactors that use external lamps where the photocatalyst is coated on the reactor wall (Figure 2.9-a), (ii) reactors with internal lamps (*immersion reactors*) where the photocatalyst is immobilised on the lamp glass or on the reactor wall (Figure 2.9-b) and reactors that

use monolithic structures containing the photocatalyst, where internal light tubes or fiber optic bundles are used.

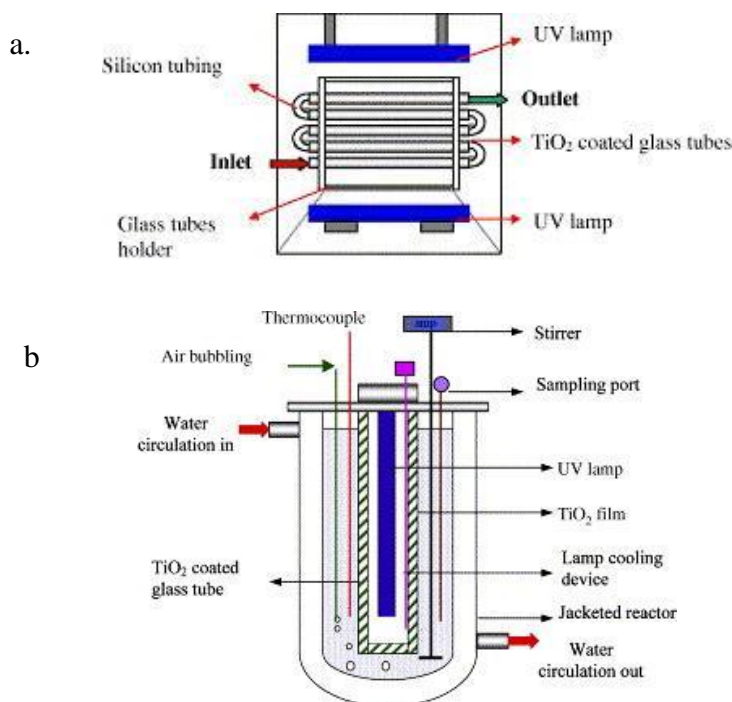


Figure 2.9 Scheme of two types of immobilized reactors (Ling *et al* [86])

Reactors with immobilised photocatalyst display lower efficiency compared to slurry reactors due to the decrease in the surface area of the photocatalyst and potential mass transfer limitations [9]. To minimise mass transfer limitations, supported photocatalysts have been used in fluidised reactors [87]–[90] which maintain high surface area to volume ratios with a high level of contact between the photocatalyst and the dissolved pollutants and beads. Another method to maximise the surface area is using a nanostructured photocatalyst, which will be discussed for ZnO in Section 2.3.1.

In addition to design, modelling and experimental validation play an important role in the development of photocatalytic reactors [91]–[99]. The biggest challenges in this area, is the complexity of the radiation absorption-scattering modelling. The two most important dimensionless parameters for the modelling of a photocatalytic reactor are (i) the optical thickness (τ) which is the relationship between the reaction space and the photons free path in the suspension (known also as the opacity of the photoreactor) and

(ii) the scattering albedo (ω) which is related to the optical properties of the photocatalyst in suspension [100].

Recently, other non-conventional configurations of reactors have been developed for photocatalytic studies. The new designs are based on a concept called “process intensification” where higher efficiencies and productivities are preferred [101]. Some of the alternative configurations of photocatalytic reactors that use suspended catalyst include: Rotating drum reactors, Taylor vortex reactors [102], and fountain photocatalytic reactors [94]. Non-conventional configurations of photocatalytic reactors that used immobilised catalyst include: swirl flow reactors [103], optical fiber photoreactors [104], and spinning disc reactors (SDR)[105]. The latter reactor, when used in batch mode, has been successfully used for the degradation of methyl blue, 4-chlorophenol and salicylic acid with titanium dioxide, showing its promise for use in processes with mass transport limitations such as photocatalysis [106].

Micro and nanofluidic devices have been developed and successfully used in engineering processes. This technology is now being used in the design of photocatalytic reactors. Since the recombination of the electron-hole pairs is in competition with the formation of reactive species and with oxidation-reduction reactions, the surface-to-volume ratio in the reactor strongly affects the reaction time. In reactors with a small volume, the photocatalytic reactions proceed rapidly, decreasing the probability of electron-hole recombination as is the case with micro reactors which have shown a remarkably large surface area to volume ratio compared with conventional batch reactors [107].

2.2.5 Photocatalytic materials for heterogeneous photocatalysis

Photocatalytic materials are usually pure or composites of metal oxides, metal sulphides, oxysulfides or oxynitrides [108]. According to their electronic configuration, photocatalysts can be classified as transition metal cations with empty d orbitals (d^0), metal cations with d filled orbitals (d^{10}) and lanthanide metal cation with empty d and f orbitals (f^0d^0). Since their ‘d’ orbitals are either empty or totally full, their conduction band orbitals are ‘d’ or ‘sp’, while their valence band orbitals are ‘O 2p’, ‘S 3p’ or ‘N 2p’. These electronic configurations are responsible for their photocatalytic properties

as hybridized orbitals with large dispersion are able to generate mobile photoelectrons once the material is exposed to light [108].

In a photocatalytic process, the activation energy depends on the photocatalyst band gap and on the wavelength of the light which also determines the energy applied [109]. The activation energy must be sufficient to move electrons from the valence band to the conduction band (see section 2.2.1). Table 2.1 displays the bandgap energy (E_{bg}) and the minimum wavelength ($\lambda_{E_{bg}}$) for the photoexcitation of different photocatalysts [108]. Since 40% of the solar light correspond to the wavelengths of infrared (1mm-750 nm), 50% to visible wavelength (750-400nm) and only 10% is UV wavelengths (400nm-10nm), the majority of photocatalysts listed in Table 3 are not suitable to use solar light due to their requirement of UV light to be activated. This limitation is one of the main drawbacks of photocatalysis and the base of many studies that are focused on modifying the band gap of photocatalysts in order to make them highly photoactive under solar light.

Table 2.1 Bandgap energy and $\lambda_{E_{bg}}$ of catalyst (Dhananjay et al [110])

Photocatalyst	Bandgap (eV)	$\lambda_{E_{bg}}$	Photocatalyst	Bandgap (eV)	$\lambda_{E_{bg}}$
Si	1.1	1127	α -Fe ₂ O ₃	3.1	400
WSe ₂	1.2	1033	ZnO	3.2	388
Fe ₂ O ₃	2.2	564	TiO ₂ (Anatase)	3.2	388
CuO ₂	2.2	564	SrTiO ₃	3.4	365
CdS	2.4	517	SnO ₂	3.5	354
WO ₃	2.7	459	ZnS	3.37	335
TiO ₂ (rutile)	3.0	413			

Figure 2.10 displays the trend of the number of publications in photocatalysis with TiO₂ and ZnO in the last decade. Regarding to the total number of publications about photocatalysis, TiO₂ has been a predominant material. As observed in Figure 2.10, until 2010 more than 50% of the total photocatalytic studies worked with TiO₂. From 2010 to the present, the proportion of publications with TiO₂ compared to the total photocatalytic publications has dropped due to the development and application of new photocatalytic materials for research. The use of ZnO for photocatalytic studies, on the

other hand, has increased especially in the last 5 years where the number of publications raised from 165 papers in 2009 to 417 publications in 2014.

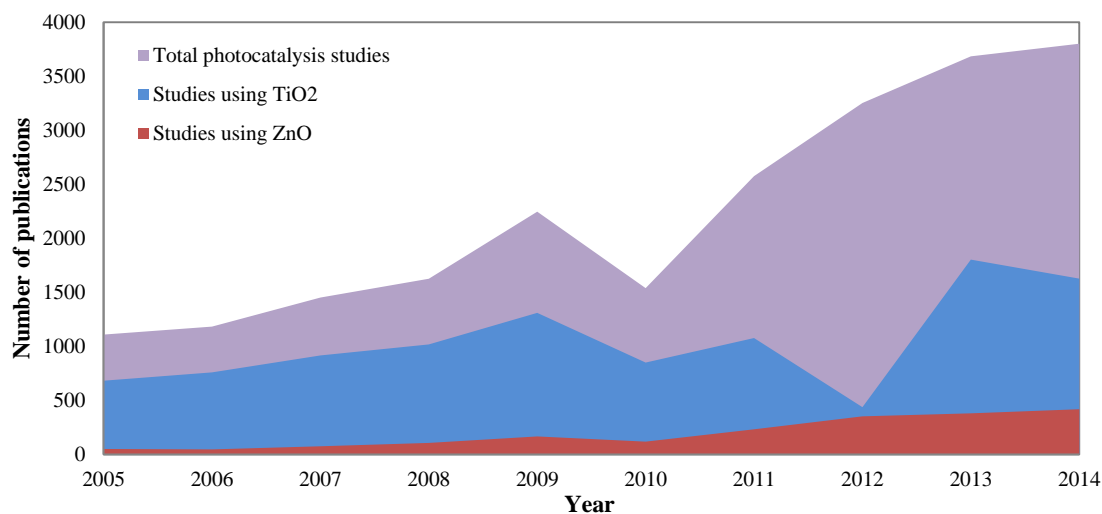


Figure 2.10 Number of publications related to photocatalytic studies with ZnO and TiO₂ since 2005 [55].

As previously mentioned, TiO₂ is one of the most used photocatalyst. Hence, this section presents a summary of this material and the main findings. TiO₂ has important properties such as being highly photo-reactive (usually up to 10% of photonic efficiency), economical, nontoxic, photo-stable and chemically and biologically inert. These properties have made this material ideal for environmental applications [111]. TiO₂ has been used for a large variety of studies, from the principles of photon absorption and formation of reactive species, to nanostructured photocatalyst studies. Some of the studies that have been carried with TiO₂ include:

a) Crystallinity studies. It is well known that high crystallinity reduces the recombination rate of photo-excited electrone-hole pairs. However, the effect of other crystal properties such as crystal orientation, crystal morphology and crystal size on photocatalytic activity are still under research. The effect of the crystalline phase on photocatalytic activity of the material has been studied using the different crystal structures of the TiO₂ (i.e. tetragonal (rutile), tetragonal (anatase), and orthorhombic (brookite))[112]. In general, the photocatalytic activity of the rutile phase (band gap 3.02 eV) is considerably lower than the anatase phase (band gap 3.2 eV). The increased photocatalytic activity of the anatase phase has been attributed to different properties such as: (i) higher Fermi level, (ii) lower capacity to absorb oxygen, (iii) higher capacity

of hydroxylation and, (iv) inherent surface band bending. [113]. The later property, which is formed in deep regions of the photocatalyst, allows a higher number of electron-hole pairs to migrate to the surface before recombination. On the other hand, for the rutile phase, only holes produced close to the surface can migrate successfully to the surface. In terms of crystal orientation, it has been reported that the (001) facet is more reactive than the (101) facet in an anatase crystal [114].

b) Synthesis of TiO₂ nanoparticles and nanostructured materials. In this area, dimensionality of the structures has been discussed in terms of its effect in photocatalysis. Some of the morphologies that have been synthesised studied included: (i) spheres with zero dimensionality which have usually displayed high surface area, resulting in higher photocatalytic activity for the degradation of organic pollutants. Additionally, this morphology displays large light absorption capacity; (ii) fibers and tubes that have shown high surface-to-volume ratio, resulting in lower electron-hole pair recombination (due to the short distance for charge carrier diffusion); (iii) two dimensional sheets (usually nanoflakes morphologies also with high aspect ratio) have displayed smooth surfaces and high adhesion to the substrates; (vi) three dimensional structures or monoliths (including interconnected structures) with high carrier mobility and large surface-to-volume ratios, which can result in efficient diffusion pathways for adsorbed species [115].

c) Preparation of visible light-responsive TiO₂, including preparation and studies of doped TiO₂ photocatalyst [111]. The main aim of doping is to improve the absorption of light in the visible region by decreasing the band gap or introducing an intra-band gap state. Studies with TiO₂ include doping with transition metal cations (e.g. Fe, V, Mo, Re), which can provide additional energy levels within the band gap of the TiO₂ [116]. Other types of dopants used with TiO₂ are noble metal such as Pt, Ag, Au, Pd, Ni, Rh and Cu. Due to the lower Fermi levels of the noble metals compared to the one of TiO₂, photo-excited electrons can move from the conduction band to the metal (deposited on the surface of the TiO₂). On the other hand, photo-generated holes in the valence band remain in the TiO₂. As a result, the electron-hole pair recombination is lower, enhancing the photocatalytic activity. Finally, doping with anions has been studied as an alternative to make TiO₂ photocatalytic active under visible light. Studies have included the substitution of oxygen in the lattice for N, S or C [112][117]. In this type of doping,

the mixing of p states of the anion with the O 2p states narrows the band gap energy of TiO₂ [112].

d) Photo-induced surface wettability changes. UV light reduces the wettability of the TiO₂ making it highly hydrophilic [118]. High contact angles in TiO₂ are mainly due to surface roughness. It has been suggested that under UV light, TiO₂ decomposed absorbed compound changing its initial surface composition [119]. In addition, the absorption of hydroxyl (OH) groups in the surface appears to be cause of hydrophilic surfaces.

e) Environmental applications. TiO₂ has been studied for a large variety of photocatalytic applications such as: (i) oxidation-reduction reactions, including photocatalytic degradation of pollutants, decomposition of NO; (ii) reduction of CO₂; (iii) application of visible light responsive TiO₂ for solar water splitting, solar cells and photo-fuel cells; (iv) degradation of pollutants in air and water. For the later application, and similar to ZnO, a large variety of pollutants have been used as model compounds including: aliphatic, aromatic, dyes, polymers and pesticides. A discussion about the photocatalytic performance of TiO₂ compared to ZnO is presented in the next section.

2.3 Zinc Oxide as a photocatalytic material

ZnO has become an attractive material for photocatalytic applications due to its unique combination of semiconducting and piezoelectric properties [12]. Additionally, ZnO is recognised for its excitonic stability, direct band gap of 3.2 eV, high electron mobility, good transparency and strong luminescence at room temperature [120]. Interest in ZnO as a photocatalytic material has increased recently, accounting for about 10% of the total photocatalytic research in the last 5 years (Figure 2.11) [55]. ZnO has been widely studied for different applications such as self-cleaning paints[121], cosmetics, sun creams, photo degradation of organic products [122], and as a potential candidate for light emission applications [123] and for developing optoelectronic and sensor devices [124]–[126]. On the other hand, two main factors have limited the widespread use of ZnO in research, namely, ZnO's difficulty with carrier doping and its vulnerability to photocorrosion [127]. The former condition has limited the use of ZnO in studies that are related to production of new doped photocatalysts while photocorrosion has decreased the extensive use of ZnO in water treatment.

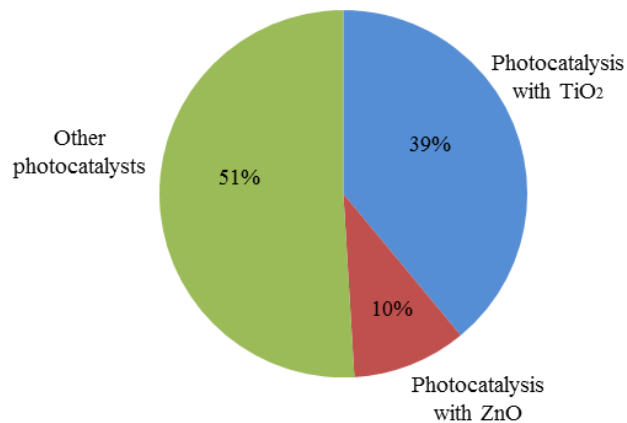


Figure 2.11 Proportion of publications related to the use of ZnO in photocatalysis compare to TiO₂ and to other photocatalytic materials [55].

ZnO is a natural and stable n-type semiconductor. The excess of negative electron charge carriers have been attributed to defects in the lattice, and in particular to oxygen vacancies and Zn interstitial [128]. The stability of ZnO as a n-type semiconductor has limited the production of ZnO-related materials for electronic and photonic applications where p-type semiconductor are preferred [129]. ZnO displays three types of crystal structures, namely, *zinc blend*, *rocksalt* and *wurtzite* (as shown in Figure 2.12). The latter is the most common structure where each anion is surrounded by four cations at the corner of the tetrahedron and vice versa [128].

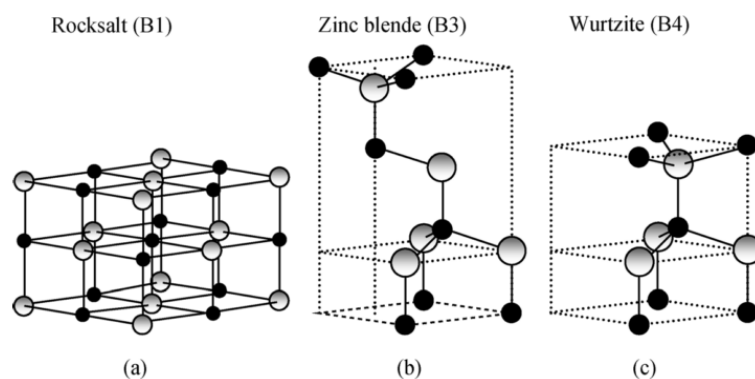


Figure 2.12 Crystal structures of ZnO. Grey dots refer to Zn atoms while black dots refer to oxygen (Morkoç *et al* [128])

ZnO is an amphoteric oxide, it can be dissolved in acid forming metal cations and in alkaline solutions forming oxyanions of Zn such as zincates [130]. The amphoteric properties make ZnO vulnerable to the effects of changes in pH. Meulenkamp *et al* [131] found a size dependence of the corrosion rate (etching) when ZnO particles in ethanolic solution were exposed to anhydrous acetic acid. It was suggested that changes of size during dissolution follows a random behaviour due to some properties such as surface area and polydispersion which may vary simultaneously with particle size. Furthermore, David *et al* [132] determined the dissolution kinetic of ZnO nanoparticles; results showed that particles with primary diameter of 71 nm and 20 nm have similar values of solubility to those for bulk ZnO; while particles with primary diameter of 6 nm displayed higher solubility than the bulk.

The exposition of ZnO to light induces photocorrosion on the surface and therefore increases the dissolution of ZnO in water [127]. The dissolution rate of ZnO in water is affected by the type of light used (i.e. wavelength and intensity) and by properties of the material such as thickness, structure, porosity and, in the case of supported materials, the adhesion of the ZnO to the substrate. For instance, Spathis *et al* [127], have reported that the photocorrosion of ZnO layers immersed in a 3.5% NaCl solution and exposed to white light (130 mW/cm^2) decreased as the oxide thickness increased [127]. They also suggested that the initial high production of by products during photocorrosion delayed the dissolution of ZnO.

In terms of uses of ZnO in water treatment, it was established that ZnO powder is the most common form used for water treatment [133]–[136]. In this form ZnO has been successfully used for treating organic pollutants such as alcohols, phenolic compounds [137]–[139], aromatics compounds[58] and dyes [140]–[146]. Some results have shown economic benefits and better performance over other photocatalytic materials such as titanium dioxide (TiO_2) [140]–[142], [147]. For instance, ZnO and TiO_2 powder were used to degrade a common fungicide 2-phenylphenol (OPP) using UV light wavelength higher than 300 nm [148]; in this study the reaction with ZnO was faster with a better overall conversion.

The most common model compounds used for photocatalytic studies in water treatment are dyes. Dyes are mainly selected due to their extensive use in industry and easy measurement in the laboratory. In general, ZnO displays good performance in the

degradation of dyes. For example, reactive blue-19 was 98% degraded using UV light at wavelength lower than 350 nm for 30 minutes [149], 100% decolouration of red-4b, yellow-3r and blue-5G was reached upon visible light for 30 minutes[48], acid Yellow-23 was treated with ZnO powder and the kinetic of this process were established in this study [150] and ZnO, TiO₂, SnO₂, ZnS and CdS in powder form were used to degrade Methyl orange (MO) and Rhodamine 6G (R6G) with UV light (365 nm) and solar light at different pH [47]. The latter study showed a maximum degradation (higher than 90% after 4 hours) using ZnO at basic pH, and a better performance was observed with ZnO and sun light compared to UV light. All those studies were performed with ZnO in a powder form. It is important to highlight that most of the studies with dyes mentioned herein have not considered photolytic effects and partial degradation (i.e. decolouration) and therefore some of the results about photocatalytic performance can be overestimated.

A considerable number of photocatalytic studies for water treatment applications have used supported ZnO, evaluating the general performance of the photocatalytic reactions in terms of surface area [151]–[157]. For instance, a comparison between photocatalytic activity (PCA) of ZnO nanorods and nanoparticles films for the degradation of methylene blue (MB) with visible light showed that nanoparticle films have a lower PCA compared to the nanorods films; nanorods degraded 90% of the MO while only 60% was degraded by nanoparticles after 180 minutes of reaction [158]. In the latter study, the differences in PCA were attributed to the low surface area of the nanoparticles. Ultrafine ZnO particles were also produced to study their surface properties and PCA by using phenol as a model compound, in this study authors suggested that the PCA depends mainly on the surface properties including surface area and active species contained in the surface (i.e. oxygen deficiencies and hydroxyl species)[135].

Besides surface area, other factors play an important role in photocatalytic reactions [159]. Different authors have stated that properties such as morphology, aspect ratio, particle size and orientation of crystals have strong effect in the properties of ZnO and therefore in its photocatalytic properties [12], [160], [161]. However, no systematic research has carried out in this field and properties such as surface morphology, wetting behaviour, and ZnO crystallinity and their effect on photocatalysis have not been extensively studied [133]. The influence of surface morphology and nanostructure size

on the PCAs has been described using ZnO nanoflake array films for degrading methyl orange with UV light [162]. Another study [155] also reported changes in PCA due to different morphologies, this research included the effect of oxygen concentration in photocatalysis using Methyl blue (MB) as a model compound. Authors suggested that ZnO films with aligned structures showed better PCA, and also that adding oxygen resulted in higher degradation of most of the films with more stable nanostructures. A further study conducted by the same research group included a complete study of the kinetics, studying MB by-products produced during photocatalytic degradation at two different wavelengths [153].

Different authors agree about the properties of an “ideal catalyst” including its low cost, stability and sustained photoactivity, photoactivation with visible and near UV light, high conversion efficiency and quantum yield, high adaptability to react with a variety of pollutants, biologically and chemically inert, and low toxicity [163]. ZnO displays some of these properties; it is an inexpensive material, has high PCA to degrade a variety of pollutants and is not toxic for human use. Additionally, ZnO is capable of absorbing pollutants even at extremely low concentrations through hydrogen bonds, which can be used in the treatment of nanopollutants via photocatalysis [164].

On the other hand, there are some drawbacks that restrict the extensive use of ZnO as a photocatalyst for water treatment, among them are: The requirement of UV irradiation equal or lower than 388 nm which limits the use of solar energy as a source of light, photocorrosion and its potential toxicity in aquatic environments, in particular at the nanoscale size. Although ZnO shows the best photocatalytic performance under UV light, some studies have used visible light illumination to obtain satisfactory results [165]–[167]. For instance, a photocatalytic reactor based on ZnO nanorods and solar light was developed showing 99% removal of *Escheritia coli* and *Staphylococcus aureus* [168]. Another study showed that phenol was degraded by ZnO under solar light with a negligible photocorrosion [169].

ZnO is considered a non-toxic compound [170] and therefore it has been used in different products that are in contact with humans (i.e. sun creams, painting, and food additives). However, ZnO represents a risk once it reaches natural aquatic environments. Some studies have reported the antibacterial activity of ZnO on Gram-positive bacteria even in dark conditions [171]. Furthermore, at nanoscale, the toxicity

of ZnO is expected to be higher due to its larger surface area and the facility to be absorbed by aquatic specimens [172]. The causes of the toxicity of ZnO nanoparticles in aqueous environments are still under research, though it has been attributed to either the reactivity of the Zn(II) ion itself, to the nanoscale properties of the ZnO or to a combination of the Zn ion with the size of the particles [173]. Therefore, the use of ZnO in powder for water treatment requires a special management in order to minimize ZnO discharges in the natural environment. As mentioned before, separation of ZnO from the water increases the cost of the water treatment and therefore a stable fixed photocatalyst would be more convenient from this perspective.

2.3.1 Nanostructures of ZnO

In general, reduction of a materials size to the nanoscale level, induces changes in the electrical, mechanical, chemical and optical properties [12]. Nanostructures are expected to be more efficient at photocatalysis due to the quantum size effect at nanoscale in which means the valence band and conduction band change into a discrete level enhancing the oxidation-reduction capability [10]. Additionally, nanoparticles display higher surface areas which allow for absorbing higher amounts of pollutants onto the photocatalyst surface and increasing the exposition light surface area in the photocatalyst [174].

Different methods have been used for the production of nanostructures, amongst them: vapour [12], [175], [176], epitaxial growth [177], electrodeposition [178], and anodization [179]–[183]. Through these methods diverse nanostructures such as nanowires, nanorings, nanoflakes, nanoneedles, nanocages and nanospheres [184] have been produced. The vapour-phase synthesis used for the production of nanostructures requires high temperatures (500 – 1400 °C) and low pressures. These inflexible conditions make this method expensive. Methods that use solution chemical approach work at lower temperatures (< 200 °C); but the long reactions times (from few hours to days) make them impractical. Electrochemical processes, on the other hand, do not require high temperatures and the reaction times are less than 1 hour. Based on the variety of nanostructures [179]–[183], including nanoporous structures produced by anodization of aluminium and titanium, anodization was selected as a process for obtaining the ZnO nanostructured films in this project.

Anodization of zinc has been widely used for the formation of ZnO layers and ZnO nanostructures. Although this electrochemical process is extensively used, the understanding of the mechanism that controls the formation of the ZnO nanostructures and the relationship between anodization conditions and nanostructure's properties is still limited. It is common to find publications about the anodization of Zn that have either used well-developed theories for anodization of alumina or cited previous studies without considering differences in anodization conditions and, in particular, the type of electrolyte used.

Unlike anodization of Zn, the mechanism for the anodization of alumina has been extensively studied and a large amount of literature about it can be found. The first major study about correlation between structure and anodization parameters was reported in 1940s [185]. Since then, different mechanisms for the formation of porous and non-porous structures have been proposed [186], [187]. In alumina the formation of porous structures occur when there is a balance between the growth and the dissolution of the oxide layer, while non-porous structures are formed when the oxide layer is resistant to the dissolution by the electrolyte [188]. This theory about anodization of alumina is not suitable for zinc, as during the anodization of zinc, the balance between growth and dissolution usually results in shapeless surfaces rather in the formation of pores. In fact, ZnO pore structures, similar to those produced by anodization of alumina (Figure 2.13-a), have not been reported up to now. Studies that have claimed the production of ZnO pores structures have shown a porous surface instead (Figure 2.13-b) [189].

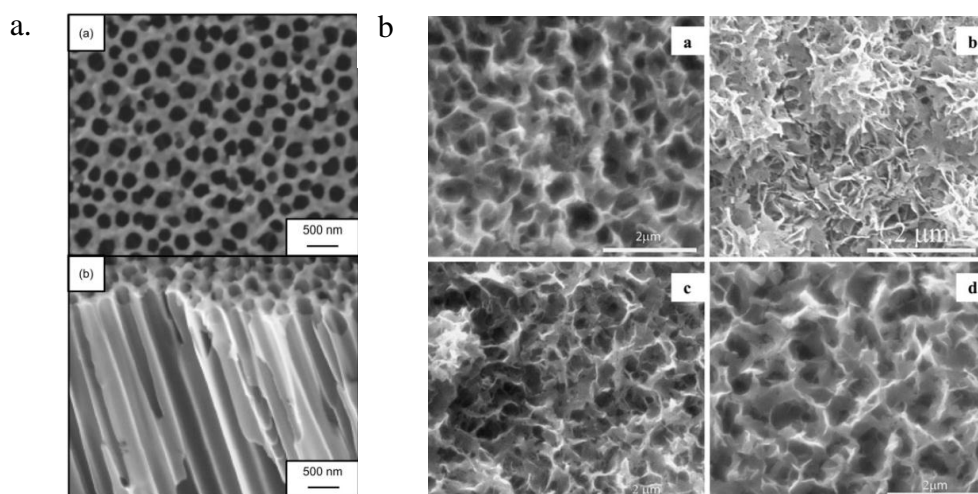


Figure 2.13 Comparison of pores nanostructures obtained with anodization of alumina (a) [190] to porous morphologies produced with anodization of Zn (b) [189].

Similar to the anodization of alumina, anodization of zinc has two main mechanisms for shaping Zn into ZnO nanostructures. Equations 2.11 to 2.15 describe the generic reactions that occur in an electrochemical-cell during anodization of Zn. Hydrogen is formed during the anodization reaction (Equation 2.11) while the formation and etching of the ZnO takes place at the Anode. The first mechanism is the formation of Zn ion complex (Zn^{2+}) (Equation 2.12) and its further oxidation which leads to the formation of ZnO (Equation 2.13 and Equation 2.14); the second mechanism is an etching process that dissolves the formed ZnO (Equation 2.15). Both mechanisms coexist during the reaction time and are strongly affected by the type of electrolyte and its concentration, current density, temperature and reaction time. As will be discussed in Chapter 4, the different reactions that take place during anodization depend on the type of the electrolyte used.

Anodization

At the cathode:



At the anode:



Etching



* X represent the negative ion of the electrolyte (eg. PO_3^{2-}) which may form a zinc salt (e.i. Zn_3PO_4) for etching process during anodization process.

Some of the nanostructures obtained through different studies by anodizing Zn include: producing nanoporous-like structures at room temperature by using oxalic acid [0.3, 0.5 and 1M] as a electrolyte at 10V [163], where it was determined that the crystal size is proportional to the concentration of oxalic acid. In another study [125], nanocrystals were produced using the same voltage (10V) and electrolyte (Oxalic acid) at lower concentrations [0.3, 0.1, 0.05 M]. Striped nanostructures were obtained with a mixture of sulphuric acid (H_2SO_4) and ethanol (OH-Et) at 5 °C, and 40 V and at room

temperature at between 5 V to 40 V [183], [191]. The latter study also investigated the anodization of zinc with an electrolyte containing fluoride ions obtaining ZnF_2 structures which can be converted into ZnO by thermal annealing. Nanoparticles, nanoneedles and nanoflowers were obtained with sodium hydroxide (NaOH 4M) by modifying the anodization time from 15 min to 60 min at 25 °C and a current density of 8.33 mA/cm^2 [192]. Similar nanoparticles were obtained at a lower concentration (NaOH 0.1M) at 20, 30 and 40V for 60 minutes [193]. Nanoneedles were obtained using a basic solution of Zn(OH)_4^{2-} at a current density of 0.3 mA/cm^2 and at room temperature [181], and KHCO_3 was used to produce ultralong ZnO nanowires, it was found that in reactions of 2 hours the length of the nanowires decrease from 35 μm to 20 μm when the temperature is reduced from 25 to 5 °C, and high temperatures ($> 50 \text{ }^\circ\text{C}$) lead to smaller nanostructures [194].

2.4 Electrocatalysis and Photoelectrocatalysis for water treatment

Other processes that use catalytic material and have been used in water treatment are electrocatalysis and photoelectrocatalysis. The term electrocatalysis refers to the process that combines electrochemistry and catalysis. This process is the base of large number of new technologies such as energy storage, fuel cells, solar fuels, and electro-synthesis [195]. Electrocatalysis uses a catalyst in order to increase the rate of electrode reactions that have low exchange current density. In this process, reactions occur either on the electrode surface (which usually is the photocatalyst itself) or in the solution [196]. Although metals, alloys, semiconductors (especially oxides) and complexes have displayed catalytic properties, catalysts used in electrocatalysis are typically based on transition metals [196].

In photoelectrocatalysis, on the other hand, a catalyst is activated by light and the increase of the electrode reaction rate is induced by an electrical potential [197]. Similar to photocatalysis, electrophotocatalysis involves the generation of electron-hole pairs which react with adsorbed species to produced hydroxyl radicals (see section 2.2.1). By applying an electrical potential, electrons are induced to the counter electrode minimizing the electron-hole pair recombination [198]. A scheme of photoelectrocatalysis with TiO_2 is displayed in Figure 2.14.

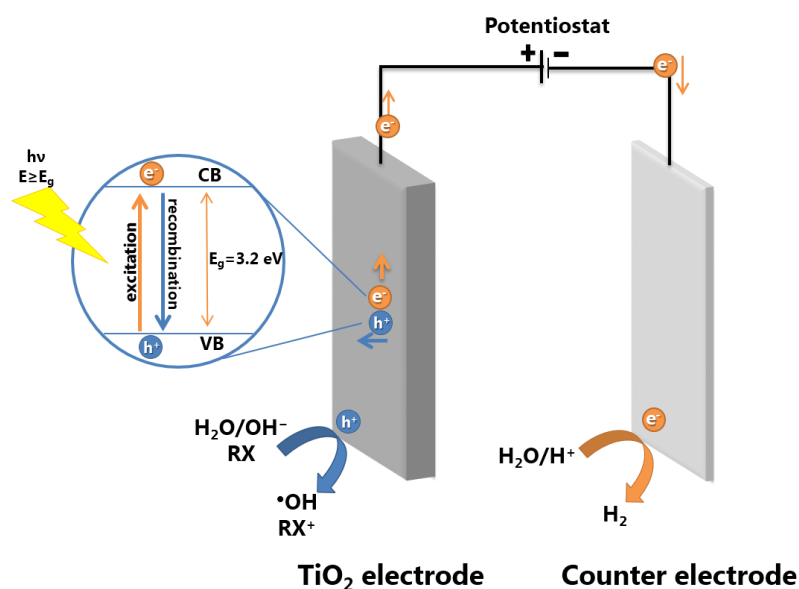


Figure 2.14 Schematic representation of photoelectrocatalytic process in an electrocell with TiO_2 (Garcia Bessegato [198])

Electrocatalysis and photoelectrocatalysis have been used as technologies for water treatment. In both processes, the elimination of the pollutants is caused by a reactive species. Electrocatalysis requires the addition of an electrolyte that promotes the generation of oxidants (ClO_2 , O_3 , H_2O_2) and reactive radicals ($\text{OH}\cdot$, $\text{O}\cdot$, $\text{ClOH}\cdot$) [199], while in photoelectrocatalysis, the formation of reactive species follows the mechanism of conventional photocatalysis as mentioned in section 2.2.1.

The most common catalysts used in electrocatalysis are platinum and ruthenium which are recognised for their catalytic properties. However, other catalysts have also been used for water treatment. For instance, Murphy [200] described the degradation of phenol and surfactants using rhodium as a catalyst. Another study used titanium electrodes with electrodeposited metals (Ti/Pt) in the degradation of textile industrial effluent adding NaCl as a electrolyte [199]. $\text{TiO}_2/\text{carbon}$ was studied for the degradation of oily water using Na_2SO_4 as electrolyte in an electrocatalytic membrane reactor [201]. For photoelectrocatalysis, on the other hand, studies with TiO_2 or ZnO have reported the degradation of a variety of organic compounds including hormones [202], pesticides [203] aromatic compounds [204]–[206], dyes [205], [207] and organochlorinates [208].

2.5 Summary

This chapter has introduced and discussed concepts and technics that will be used throughout this thesis. An overview of water-related issues and, in particular, to water availability and quality water was presented in the first section. In this section the impact of emerging pollutants in water quality and some of the current technologies for water treatment were discussed, introducing photocatalysis as a highly effective technology to degrade toxic and recalcitrant pollutants. The second section presented the fundamental theories about photocatalysis followed by a brief discussion about general properties of photocatalytic materials. ZnO was identified as a unique photocatalytic material due to its semiconducting and piezoelectric properties. Therefore, ZnO properties, its use in photocatalysis for water treatment and some studies about ZnO nanostructures were discussed in the last section. Additionally, the last section presented a background of anodization as a technique for making ZnO nanostructures.

Throughout this chapter, some still open gaps in researching were identified and discussed:

- In terms of anodization of zinc, there is still no clear understanding of the mechanism for the production of nanostructures. Additionally; there is not a systematic study on the production of ZnO nanostructures by anodization that provides an approach about the relationship between experimental parameters of anodization and the properties of the ZnO nanostructures.
- Although ZnO has been used in several photocatalytic studies with water, there is a deficient in understanding on changes produced in the morphology of nanostructures during photocatalytic reactions.
- The number of studies about the effect of ZnO properties, such as surface morphology, wetting behaviour, and ZnO crystallinity, in photocatalysis for water treatment is limited. Furthermore, the effect of oxygen on the photocatalyst stability has been explained by some authors who have performed reactions under low levels of dissolved oxygen; however, anoxic conditions have not been extensively studied.
- Large numbers of studies that have analysed photocatalysis of organic pollutants (in particular dyes) have measured photolysis as a control. However, limited

kinetic analysis of the effect of photolysis on these compounds and its effect on photocatalysis has been reported.

The following chapters will present the techniques, methods and equipment used to (i) obtain nanostructured ZnO films (ZnO-NFs) and nanostructured ZnO wires (ZnO-NWs), (ii) characterise the ZnO-NFs as a photocatalytic material and (iii) test them in a photocatalytic reaction with phenol as a model compound (Chapter 3). This will be followed by Chapter 4 which discusses the production and characterisation of ZnO-NFs. In this chapter the study of anodization as an electrochemical technique to obtain ZnO-NFs and the relationship between anodization conditions and properties of the photocatalyst is presented. In Chapter 5, ZnO-NFs were tested as a photocatalytic material and their morphological stability during photocatalytic reactions was studied. Chapter 6 displays alternative configuration of reactors used for the study of supported ZnO nanostructures and ZnO-NFs. Additionally, the development of ZnO nanostructured wire and its performance in the photocatalytic degradation of phenol; and the deposition of ZnO layer on optical fiber surface is discussed in Chapter 6. In this chapter the degradation obtained under darkness conditions is also discussed.

Learn from yesterday, live for today, hope for tomorrow. The important thing is to not stop questioning.”
Albert Einstein

Chapter 3: Experimental – Material and methods.

Electrochemical anodization is extensively used for commercial and industrial applications such as electronics, automobiles, buildings and architecture, medical and dental equipment and home furnishings. The first industrial use of anodization was in 1923 to protect an aircraft from corrosion made with Duraluminun (an alloy of aluminium, copper, manganese and magnesium) using chromic acid as the electrolyte. Later, new electrolytes where implemented in the process. For instance, the use of sulphuric acid was patented by Gower and O’brian in 1927 [209]. Later, in 1932, anodization with oxalic acid was patented in Japan. In 1953 Keller *et al* [210] conducted studies about the anodization of aluminium and the relationship between anodization conditions and porous and nonporous structures. Since then, a significant number of researches have focused on using this technique to produce different nanostructures with a large variety of electrolytes and for different applications. The use of anodization has been extended to other metals and materials such as titanium, zinc, magnesium, zirconium, niobium, hafnium and tantalum [211]. In terms of zinc, anodization holds great promise in that it allows a large variety of morphologies to be obtained as discussed in Section 2.3.1.

In the present thesis, two configurations of ZnO films were developed through anodization. ZnO nanostructured films (ZnO-NFs) were obtained using flat Zn foil while ZnO nanostructured wires (ZnO-NWs) were produced with Zn wire. The first part of this chapter discusses in detail the production of the ZnO-NFs and ZnO-NWs and the different methods of analysis used for their characterisation. The second part describes the methodology and materials used during the study of the photocatalytic performance of ZnO-NFs in the degradation of organic pollutants in water. The description includes the setup of a batch reactor system and the analytical techniques used to quantify

changes in the concentration of the model organic compounds and their by-products. Three other reactors were fabricated to study the photocatalytic activity of ZnO-NWs and ZnO-NFs, which will be discussed in Chapter 6.

3.1 Fabrication of nanostructured ZnO films and nanostructured ZnO wire

ZnO-NFs and ZnO-NWs were produced through the anodization of zinc; this electrochemical method was described previously in chapter 2 and reported in literature [178], [212]. For the fabrication of a single ZnO-NF, high purity zinc foil (99.98%, 0.25 mm thickness, Alfa Aesar) was cut in pieces of 1.0 cm by 1.5 cm and used as starting material. The film was placed in a polytetrafluoroethylene (PTFE) holder; copper tape was used to connect the Zn foil to the electrodes. In order to be able to produce multiple ZnO-NFs, a three-hole Teflon holder was designed with an exposed area of 1.2 cm in diameter for electro-polishing and 1.1 cm for anodization (see Figure 3.1). These types of holders allowed simultaneous production of three ZnO-NFs. To produce three films at once, the zinc foil was cut in pieces of 1.5 cm by 7.0 cm, and the copper tape was held along the Zn foil providing a better flow of electrons.

For the production of ZnO-NWs, on the other hand, Zn wire was used as a starting material. Two different wire diameters were used: 0.1 mm (Alfa Aesar 99.9%) and 1 mm (Good fellow 99.9%). The Zn wire was directly immersed (without holders) into the electrolyte for electro-polishing and anodization processes.

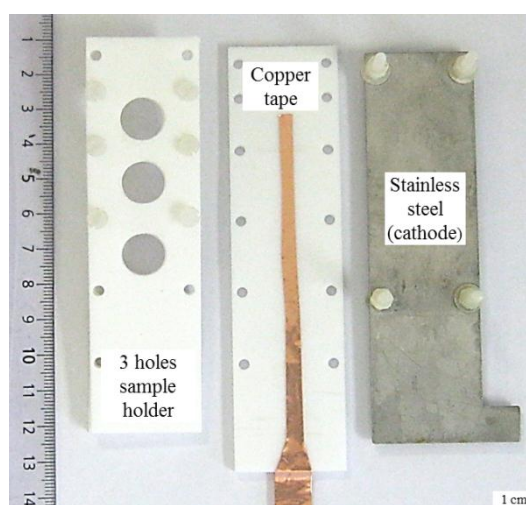


Figure 3.1 Three holes sample holder used in anodization of Zn foil.

3.1.1 Starting material pre-treatment

The zinc foil and zinc wire were annealed in air at 300 °C (CWF 1100, Carbolite) at 1 °C/min for one hour, followed by a degreasing process with acetone (HPLC grade, 99.5+%, Fisher) in an ultrasonic bath (Fisher Scientific, FB 15048) for 10 minutes, and rinsing thoroughly with ethanol and deionised water. The annealing process allowed the material to release the internal stress, produce recrystallization, and improve the microstructure of the zinc by removing crystal defects and grain boundaries[213], while the cleaning process removed all external contamination that can affect the electro-polishing process or the formation of the nanostructures during anodization [214].

Before anodization, the annealed materials were electro-polished in a solution of ethanol (>99.8%, *Sigma Aldrich*) and perchloric acid (60-62%, *Alfa Aesar*) in a volumetric ratio of 1:2 at -70 ± 2 °C and 20 V for 15 minutes; the electro-polishing treatment ensured a smooth and clean surface free of the natural oxide layer, leaving the Zn surface ready for the formation of the nanostructures[215]. As shown in Figure 3.2, the PTFE holder with the Zn foil was placed in a stainless steel beaker filled with the electro-polishing solution. The metallic beaker was externally covered with a mixture of dry ice and acetone to keep the temperature constant. The electro-polishing treatment was performed using a power supply (Agilent, E3620A) at constant voltage where the Zn foil was connected as anode and the stainless steel beaker was used as cathode. For the electro-polishing of the wire, the wire was immersed directly into the solution avoiding any contact with the metallic beaker.

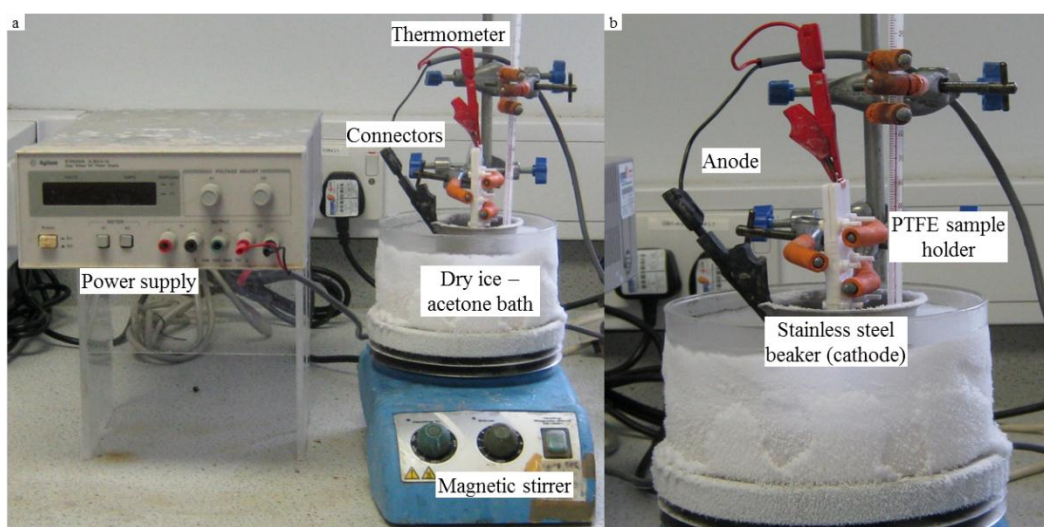


Figure 3.2 Set-up for electro-polishing of zinc foil and zinc wire.

3.1.2 Anodization of Zn foil

As shown in Figure 3.3, the anodization process was performed using a DC power supply to control the current applied to the system (Agilent, E3634A). To keep the temperature constant during the reaction, a water cooled cell with constant recirculation of the coolant was used (Thermo Scientific HAAKEC 10-K10, DC10-K20 or DC50-K35). Additionally, a magnetic stirrer was used to mix the electrolyte solution in the anodization reactor.

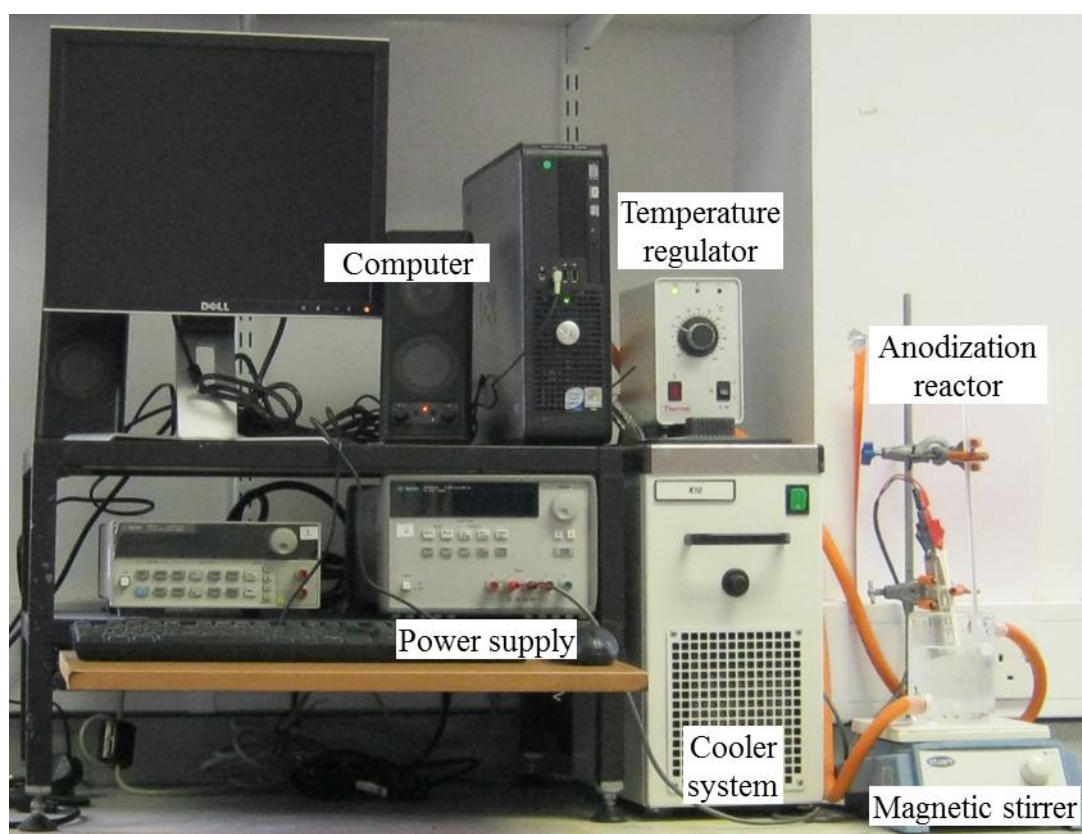


Figure 3.3 Anodization setup used for the fabrication of ZnO-NFs and ZnO-NWs.

Anodization was performed in a two-electrode cell spaced 8 mm apart using the electro-polished zinc foil as anode and a stainless steel plate (SS316 grade) as cathode, as shown in Figure 3.4. The Zn foil anode was held in the PTFE holder which allowed the Zn foil to be anodized only in one face. Different ethanolic solutions (0.1 M and 1 M) were used as electrolytes i.e. Hydrochloric acid HCl (37% solution, *Across Organic*), nitric acid HNO₃ (65%, *Sigma Aldrich*), orthophosphoric acid H₃PO₄ (85%, *Alfa Aesar*), oxalic acid H₂C₂O₄ (98%, *Across Organic*), sodium hydroxide NaOH (1 M volumetric solution, *Fisher*), and aqueous solution of potassium bicarbonate KHCO₃ (99.99% Powder, *Sigma Aldrich*). For each electrolyte, the anodization of the Zn was performed

at different experimental conditions of concentration, voltage, temperature and reaction time as displayed in Table 3.1. After anodization, the obtained ZnO-NFs were thoroughly rinsed with ethanol and deionized water; followed by a drying process in a vacuum desiccator at 2×10^{-3} millibars for 36 hours. All ZnO-NFs were stored in a desiccator cabinet.

Table 3.1 Experimental conditions of anodization of Zn.

Electrolyte	HCl; HNO ₃ ; H ₃ PO ₄ H ₂ C ₂ O ₄ ; NaOH; KHCO ₃
Concentration	0.1M; 1M
Temperature	0°C; 10°C
Voltage	1V; 5V
times	1 minutes; 60 minutes

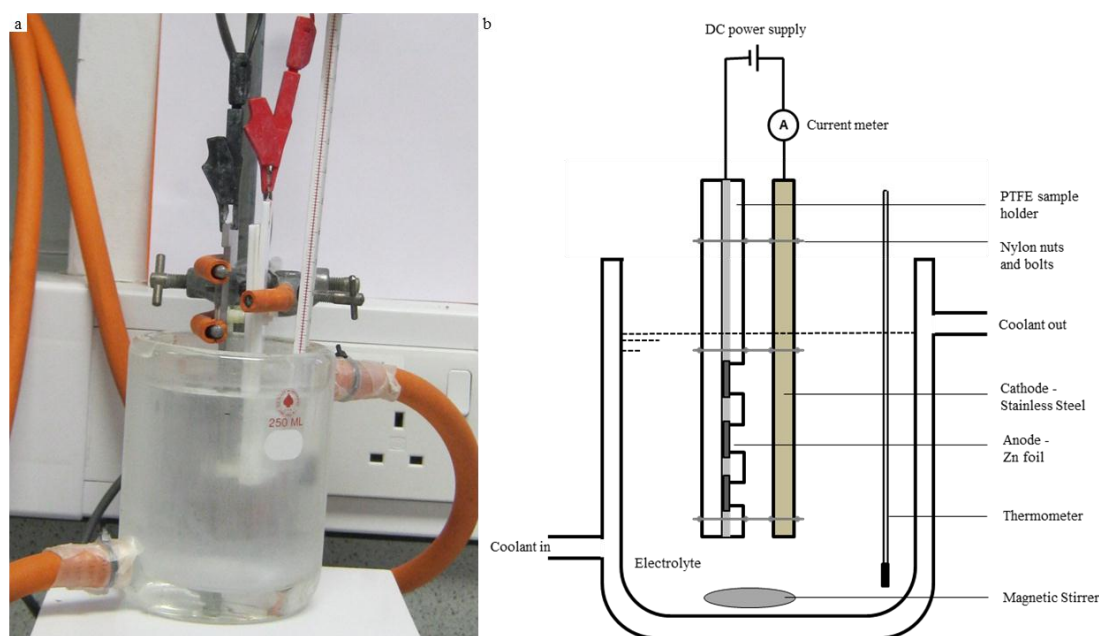


Figure 3.4 Two-electrode cell used in anodization process to obtain ZnO-NFs.

3.1.3 Anodization of Zn wire

Anodization of the zinc wire was performed in a two-annular electrode system using a stainless steel tube as an external cylinder, as shown in Figure 3.5. The electro-polished wire was placed with a constant radial distance of 1.5 cm along the tube. The Zn wire was connected as anode while the external stainless steel tube was used as cathode. Both, anode and cathode were connected directly to the power supply (Agilent, E3634A). The annular electrodes allowed the outer surface of the wire to be equally

exposed to the electrolyte and to the current flow. Aqueous solution of potassium bicarbonate KHCO_3 (99.99% Powder, *Sigma Aldrich*) were used as electrolyte. The anodization conditions were carried out at different voltages (1 V and 5 V), concentration of electrolyte (0.01M, 0.05M and 0.1M) and times (1, 5, 15 and 45 minutes); while the temperature of the electrolyte was kept constant throughout anodization at 10 °C using a water cooled cell. Once anodization was completed, the samples were thoroughly rinsed with ethanol and deionized water and dried with air. Subsequently, the wires were stored in a desiccator cabinet for further analysis and post-treatment.

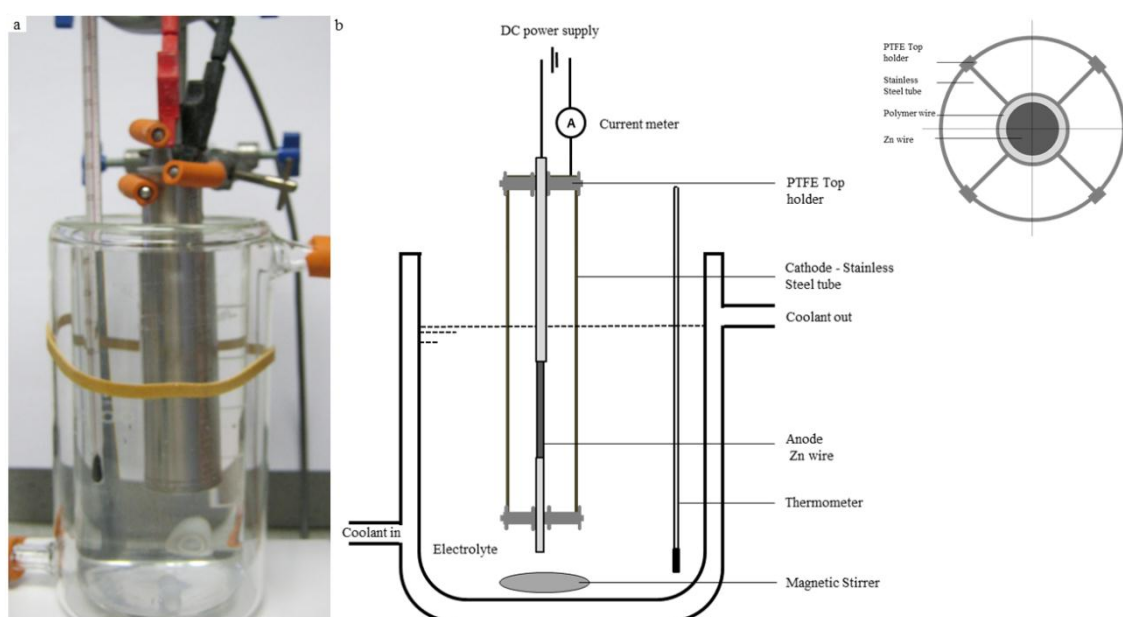


Figure 3.5 Two-electrode cells used in anodization process to obtain ZnO-NWs.

3.1.4 Post-annealing of ZnO-NFs and ZnO-NWs

The initial study about the formation of nanostructures by anodization of Zn foil involved the characterisation of the samples without any further post-treatment after anodization. Post-annealing of ZnO in air can modify the crystallite size and increase the O/Zn atomic ratio [216]. Additionally, a release of stress and change in packing density of ZnO crystals occur when ZnO is exposed to thermal post-treatments [217]. Therefore, the effect of post-annealing on the crystallinity of the nanostructures and on the photocatalytic activity of the ZnO nanostructures was investigated. The study involved the post-annealing of selected ZnO-NFs at different temperatures over

different time periods as is shown in Table 3.2. After post-annealing, samples were stored in darkness in a desiccator cabinet.

Table 3.2 Experimental conditions of post-annealing study.

ZnO-NFs code*	Anodization conditions	Post-annealing conditions
AR-an-0064	[0.1M] NaOH / 1h / 40v / 10 °C	No post-annealing
AR-an-114A	[0.1M] NaOH / 1h / 40v / 10 °C	200 °C – 1h
AR-an-114B	[0.1M] NaOH / 1h / 40v / 10 °C	350 °C – 1h
AR-an-114C	[0.1M] NaOH / 1h / 40v / 10 °C	350 °C – 10h
AR-an-0064	[0.1M] NaOH / 1h / 40v / 10 °C	300 °C – 24h
AR-an-113A	[0.1M] KHCO ₃ / 1h / 1v / 10 °C	No post-annealing
AR-an-099A	[0.1M] KHCO ₃ / 1h / 1v / 10 °C	200 °C – 1h
AR-an-113B	[0.1M] KHCO ₃ / 1h / 1v / 10 °C	350 °C – 1h
AR-an-113C	[0.1M] KHCO ₃ / 1h / 1v / 10 °C	350 °C – 10h
AR-an-104C	[0.1M] KHCO ₃ / 1h / 1v / 10 °C	350 °C – 1h
AR-an-113A	[0.1M] KHCO ₃ / 1h / 1v / 10 °C	300 °C – 24h

(*)production code assigned to each film during anodization.

3.2 Characterisation of the photo-catalytic materials

The characterisation of the supported nanostructures used in this project (i.e. ZnO-NFs, ZnO-NWs) was focussed on establishing the relationships between material properties and photocatalytic behaviour.

3.2.1 Morphology analysis

Before morphological analysis, ZnO-NFs were dried in a vacuum desiccator at 2×10^{-3} millibars for at least 24 hours. No special preparation or coating was used for this analysis. The surface morphology of ZnO-NFs and ZnO-NWs were observed using a Hitachi S-4300 field emission scanning electron microscope (FESEM) and a JEOL JSM6480LV scanning electron microscopy (SEM) equipped with an energy dispersive X-ray spectrometer (EDX, Oxford, ONCA x-ray analyser, Oxfordshire, UK). The microscope was set up in the range of 2.0 and 3.0 kV (accelerating voltage) and the working image distance was 15 mm. Micrographs were taken at different magnifications (usually 1 K, 5 K, 10 K, and 20 K). Since ZnO is a non-conductive material, the acquisition of images using FESEM has some limitations in terms of magnification and resolution. One of the main problems with this method of analysis is a phenomenon called charging that is produced by the build-up of electrons and their uncontrolled discharge [218]. Once the surface of the material is charged, there is a distortion of the image such as abnormal contrast, image deformation or shift that limit

the analysis of the morphology; this alteration is more evident at high magnification. Nonetheless, high quality micrographs have been obtained allowing to study the relationship between morphology and photocatalytic behaviour, as discussed in Chapter 5.

Thickness measurements of the ZnO layer were included in the morphology analysis. Due to the ductility and hardness of the Zn foil substrate, different methods were attempted to cut the films and expose the cross section of the ZnO layer. However, only in few cases it was possible to obtain high quality cross sectional micrographs of the ZnO films. ZnO films that were sectioned using scissors, wire cutters or immersed in liquid nitrogen and then cut with scalpel, showed damage of the ZnO nanostructures as shown in Figure 3.6(a-c). Other samples were coated with resin to protect the structure of the ZnO nanostructures; once the resin was dry, the ZnO films were cut with a scalpel. However, the latter method did not allow obtaining high resolution SEM micrographs (Figure 3.6-d). Consequently, the analysis of the ZnO thickness was limited to ZnO-NFs obtained with KHCO_3 which displayed thick ZnO layers and nanowire morphology. It was found that by bending the Zn foil substrate for this type of films, the ZnO layer was detached from the substrate allowing the measurement of the ZnO layer.

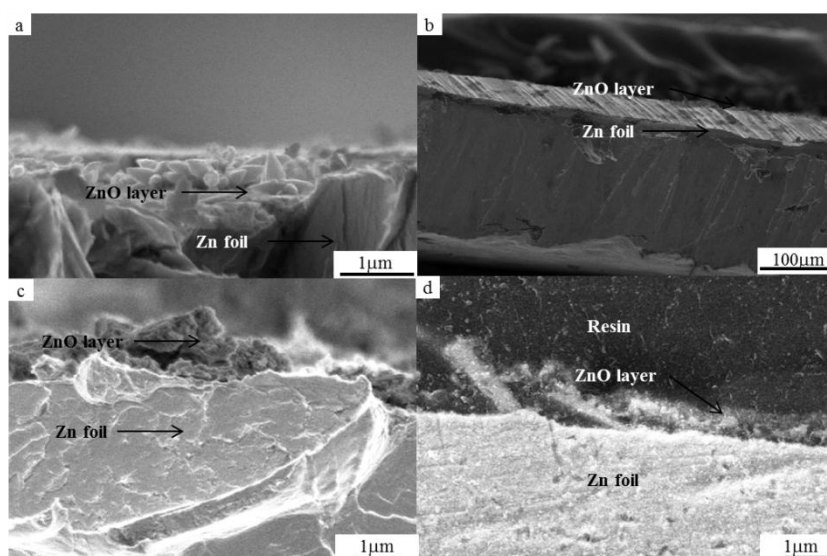


Figure 3.6 ZnO films cut with different techniques: scissors (a), wire cutters (b), immersion in liquid nitrogen and cut with scalpel (c), coated with resin and cut with scalpel (d).

3.2.2 Wettability analysis

The static contact angle is defined as the measurable angle ($0^\circ - 180^\circ$) that a liquid forms once it is in full contact with a solid. Young's equation (Equation 3.1) describes the contact angle of a liquid with a flat-homogeneous surface correlating the surface tension of (i) the solid-vapour interface (γ_{sv}), (ii) the solid-liquid interface (γ_{sl}) and (iii) the liquid-vapour interface (γ_{lv}). Hydrophilic surfaces have static contact angles in the range of 0° - 90° ; hydrophobic surfaces display static contact angles between 90° and 180° ; while surfaces with contact angles higher than 150° are considered super-hydrophobic [219]. A contact angle of 90° is obtained when $\gamma_{sv} = \gamma_{sl}$; liquids spread on surfaces when the difference between γ_{sv} and γ_{sl} is equal or higher than γ_{lv} ; while liquids "bead up" on a solid surface when γ_{sv} is lower to γ_{sl} .

$$\cos \theta = \frac{\gamma_{sv} - \gamma_{sl}}{\gamma_{lv}} \quad (\text{Eq. 3.1})$$

Young's equation applies only when the surface of the solid is flat and chemically homogeneous. For rough and chemically homogeneous surface, Wenzel proposed an equation that involves the roughness factor (r) and it is used when the liquid is in full contact with the solid or substrate (Equation 3.2).

$$\cos \theta_e = r \cos \theta_s \quad (\text{Eq. 3.2})$$

In the case that penetration of the liquid does not occur, it is assumed that a layer of air is beneath; this phenomenon is called a Cassie-Baxter state and the contact angle in that case can be calculated using equation 3.3 using the solid fraction of the surface (ϕ).

$$\cos \theta_e = \phi \cos \theta_s - (1 - \phi) \quad (\text{Eq. 3.3})$$

For smooth and chemically heterogeneous surfaces, Cassie equation (3.3) correlated the static contact angles (θ_{s1} and θ_{s2}) with the area fraction of the component surfaces. To distinguish between static contact angles measured in flat surfaces and those measured on rough surfaces, some authors used the term effective contact angle for the latter case (Figure 3.7) [220].

$$\cos \theta_e = \lambda \cos \theta_{s1} + (1 + \lambda) \cos \theta_{s2} \quad (\text{Eq. 3.4})$$

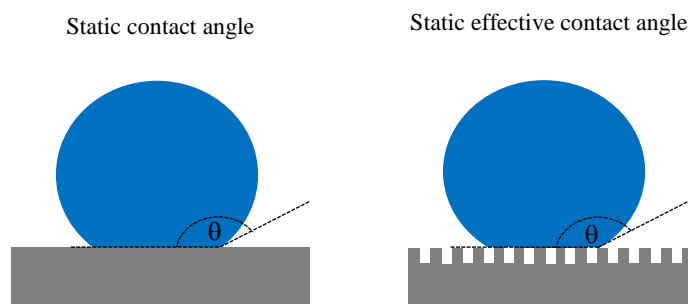


Figure 3.7 Difference between static contact angle and static effective contact angle.

The wetting behaviour of rough and non-homogeneous surfaces is still under discussion [221]–[223]. Theoretical studies have worked on the derivation and validation of Wenzel and Cassie equations under different scenarios[10][220], [224]–[227], while other authors have proposed more complex and sophisticated models [223][228]. One of the reasons for the absence of a unified model is the different hypothesis about the interfacial areas that take part in the calculation of contact angles. For instance the experimental study conducted by Gao and McCarthy [221] suggested that the behaviour observed during measurements of advancing and receding contact angles is caused by “interactions of the liquid and the solid at that three-phase contact line alone” and therefore, the interfacial area within the contact perimeter is not relevant.

In this study, static effective contact angle (SEC angle) measurements were used to analyse the wetting behaviour of the ZnO-NFs and to determine differences of hydrophobicity between them. The analysis was carried out using an Optical Contact Angle Measuring device with automated dosing system MD unit (OCA-5, Dataphysics, Gerhard UK). The sessile method in air at 20 °C was used [219]: 2 μ L of deionised water was dropped on the surface of the ZnO-NFs and the contact angles were measured at three different points for each film, within the error $\pm 2^\circ$.

Advancing and receding contact angles were measured in selected films following the Drelich’s guidelines [229]. For this measurement, films were placed in a plastic holder and deposited in a quartz cuvette with deionized water so that the films and water were not in direct contact. The top of the cuvette was sealed with Parafilm® and left them for 15 minutes obtaining liquid-vapour saturated air within the cuvette. An initial drop of 2

μl of deionised water was deposited onto the surface of the ZnO-NFs and the SEC was measured, 2 μl of deionised water was added to the drop and the advancing contact angle was measured. Finally 2 μL of deionised water was removed from water drop and the receding contact angle was measured.

Selected ZnO-NFs were exposed to UV light at 254 nm for 6 hours in order to determine changes in the contact angle upon UV irradiation as it has been reported previously [230]. For this experiment a dark chamber equipped with a UV light source (UVG-54 Handheld UV lamp, 6 watts) was used, the ZnO-NFs were spaced 10 cm from the UV light. Contact Angles of the ZnO films were measured before and after 3 hours and 6 hours of UV irradiation. The contact angles were measured at 3 different points for each film, within the error $\pm 2^\circ$.

3.2.3 Analysis of chemical composition

The composition of ZnO-NFs and Zn-NWs was analysed using energy dispersive X-ray spectrometry (EDX, Oxford, ONCA x-ray analyser, Oxfordshire, UK) and X-ray photoelectron spectroscopy (XPS, VG Escalab 250) equipped with a high intensity monochromated Al Ka source. For the EDX analysis, samples were previously kept in a vacuum desiccator at 2×10^{-3} millibars for 36 hours and the analysis was carried out simultaneously with SEM analysis. XPS analysis involved a first qualitative scan for 10 minutes followed by a second and final scan for 2 hours. The final analysis was run only for the elements that were found during the first scan and it involved a quantitative elemental composition analysis of the elements.

3.2.4 Crystallography analysis

To analyse the crystal structure of the ZnO-NFs and ZnO-NWs two techniques were used: X-ray diffraction (XRD) and transmission electron microscopy (TEM). XRD patterns were obtained at room temperature using an X-ray diffraction system (Philips X-ray generator – PW 1710 diffractometer) set in a flat mode and the measurements were carried out between 2θ values of 0° and 100° where θ is the incident angle of the beam. Selected samples were also rotated 90° in the holder and then scanned between 2θ values of 20° and 50° .

Transmission electron microscope (TEM) micrographs were obtained using a TEM from the University of Leeds, UK (Philips CM200 FEGTEM field emission gun TEM/STEM with super-twin objective lens, cryoshielding, and Oxford Instruments UTW EDX detector) and a transmission electron microscope from the Materials and Surface Science Institute of the University of Limerick in Ireland (JEOL JEM-2100F with a field emission source with scanning TEM (STEM) attached). For this analysis, ZnO powder from the ZnO-NFs was obtained by scratching the ZnO layer. The powder was dispersed in ethanol (>99.8%, *Sigma Aldrich*) and ultra-sonicated for 2 minutes. A drop of the suspension was placed on a TEM grid (Lacey Carbon 400 mesh copper – Agar Scientific) and let dry at room temperature. The TEMs were operated at 80-200 kV with resolution to 0.14 nm and micrographs were taken at different magnifications.

3.2.5 Band gap energy measurement

Band gap energies were calculated using the UV-Vis absorbance spectra obtained with a UV-Vis photospectrometer set in reflectance mode (Ocean Optics, USB2000+UV-Vis, Florida, USA). Electro-polished Zn foil was initially used as a blank, but the natural ZnO layer (formed once the material is exposed to air) altered the measurement, therefore a mirror was used as a base line or blank. The energy was calculated using the Plank equation $E = \frac{hc}{\lambda}$ where E is the band gap energy, h is the Plank constant, C the speed of light and λ is the cut off wavelength obtained from the absorbance spectra for each ZnO-NFs (Figure 3.8).

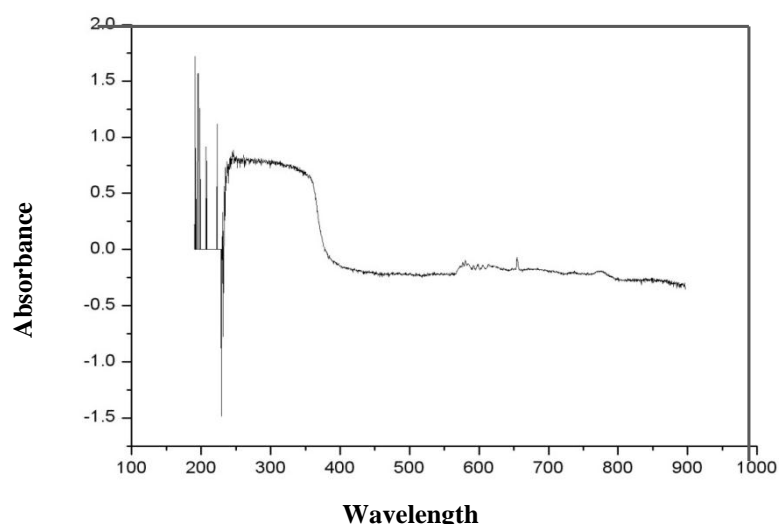


Figure 3.8 Absorption spectra of ZnO-NF (Na(OH) [0.1M] / 1h / 40 V).

3.2.6 ZnO films profiles measurement

As an alternative method to measure the thickness of the ZnO-NFs, profiles of the ZnO layer were obtained using a surface profiler (Veeco Metrology – Dektak 6M). The equipment was set to measure a total length of 11 mm. During the analysis, the sensor was initially placed on the Zn foil area and automatically moved toward the ZnO layer. Subsequently, the sensor was moved lineally along the ZnO surface until the total diameter of the ZnO film was reached as shown in Figure 3.9.

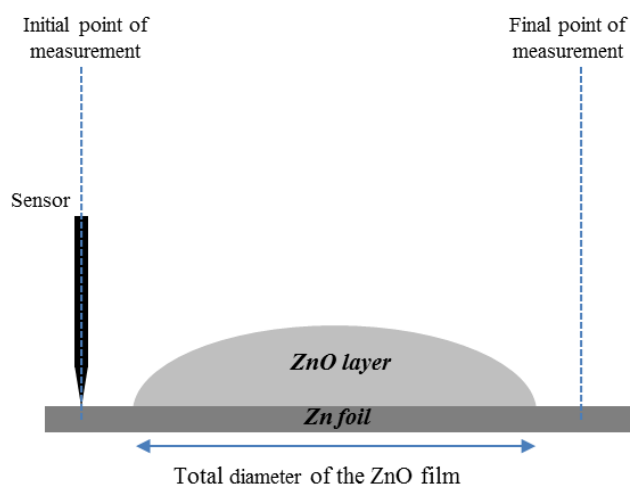


Figure 3.9 Schematic of the profile measurements.

3.3 Photocatalytic setup

This study covered two parts where the properties of the photocatalyst were tested. The first part was mainly focused on the relationship between physicochemical characteristics of the ZnO-NFs and their photocatalytic performance during the photocatalytic degradation of phenol in a batch reactor system. The second part included testing the ZnO-NFs and ZnO-NWs using alternative photocatalytic systems that might improve the degradation of organic pollutants using the immobilised ZnO. For the latter part, three different reactors were designed and tested in the photo-degradation and photocatalytic degradation of methyl orange and phenol, the design of these reactors and the photocatalytic experiments will be described in Chapter 6.

The performance of ZnO-NFs as a photo-catalyst was studied using a batch system with a total volume of 100 mL. The model compound solutions (25 mL) were deposited in a jacketed beaker (reservoir) provided with a magnetic stirrer where temperature was controlled using a water cooled cell (Thermo Scientific HAAKEC 10-K10, DC10-K20 or DC50-K35). For some experiments, oxygen or argon was supplied by flowing them

into the reservoir. Additional measurements such as pH, conductivity and Dissolved oxygen (DO) were conducted using a benchtop multimeter (Meter set Versa Star®). A Handheld UV lamp providing light at 254 nm was placed on the top of the beaker at 4.5 cm above the solution surface (Figure 3.10).

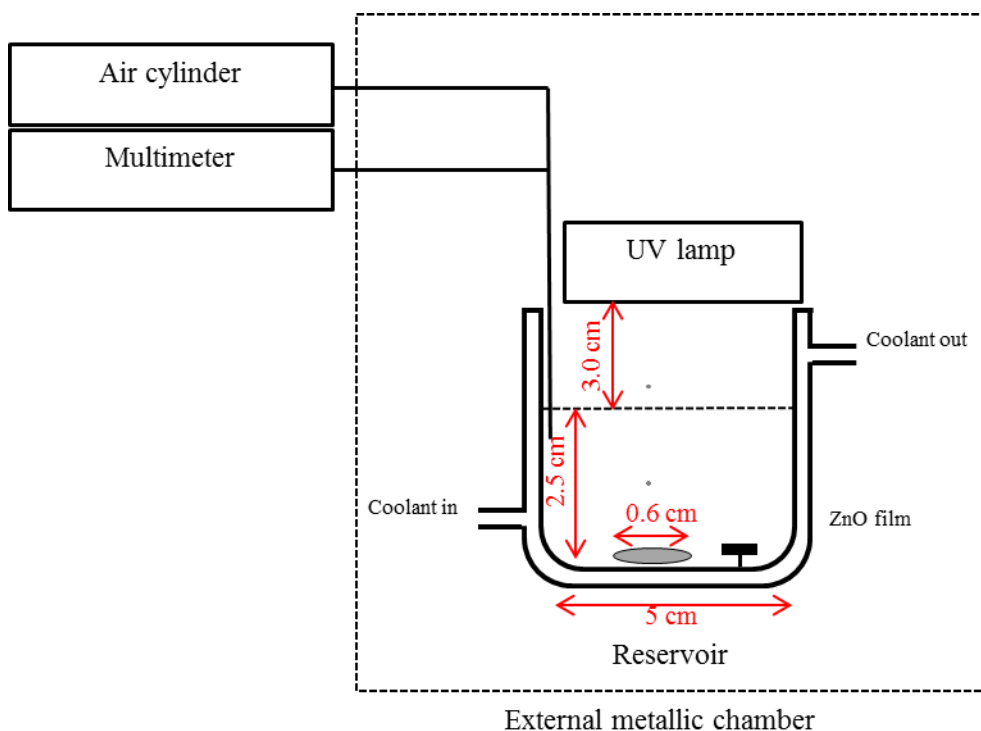


Figure 3.10 Schematic of the batch photocatalytic setup.

To protect people working in the lab from UV-C light exposure and protect the experiment from external contamination, the photocatalytic set up was installed in a metallic container with two chambers (Figure 3.11).

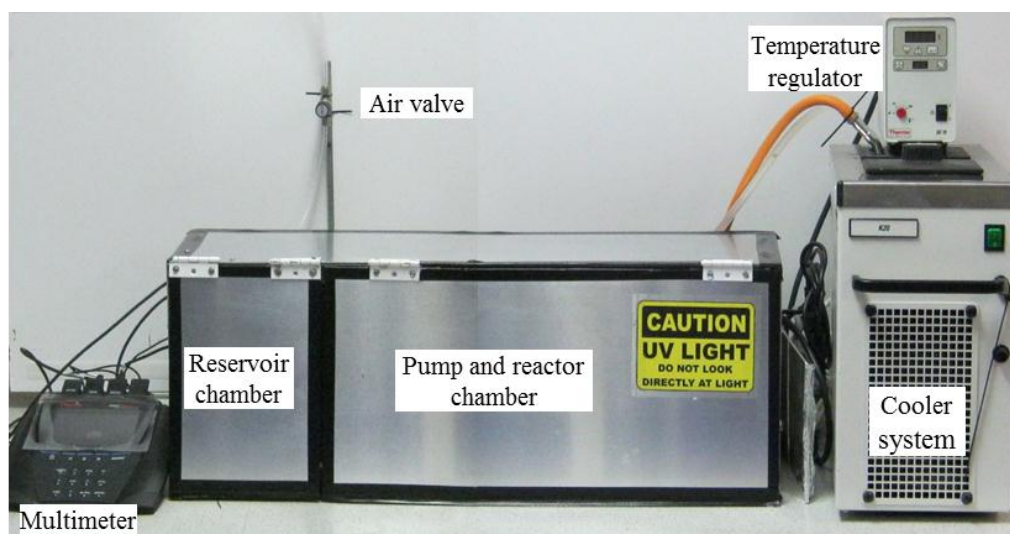


Figure 3.11 External chamber used in the photocatalytic setup.

3.4 Light source

Light plays an important role by providing the initial energy for the formation of an electron-hole pair. Ideally the light provided in a photocatalytic process should have a uniform radiation field with a constant light intensity; thus a uniform flow of electrons can be absorbed by the catalyst along the reaction time [73].

The band gap wavelength for ZnO, and thus the minimal energy to activate it as a photocatalyst, is 387 nm. However, a large number of photocatalytic studies with ZnO have used light with a wavelength of 254 nm [153], [155], [231]–[233]. To facilitate further comparison with other photocatalytic studies, in this project, a Handheld UV lamp providing light at 254 nm was selected. The light was monitored using a UV light meter (HHUV254SD – OMEGA engineering INC) connected to a UV-C and UV-A probe. Direct measurements indicated that the intensity of the light was 0.863 mW/cm²; using quartz on the top of the reactor, the intensity was reduced to 0.824 mW/cm².

Changes in light intensity were monitored as shown in Figure 3.12. It was found that at the beginning of the process the intensity of the light increases with time, followed by a stable irradiation after 3 minutes. As a result, for each experiment the lamp was pre-heated for 5 minutes before starting the photocatalytic experiments. The irradiation was checked at different times during the study verifying similar values in all the measurements.

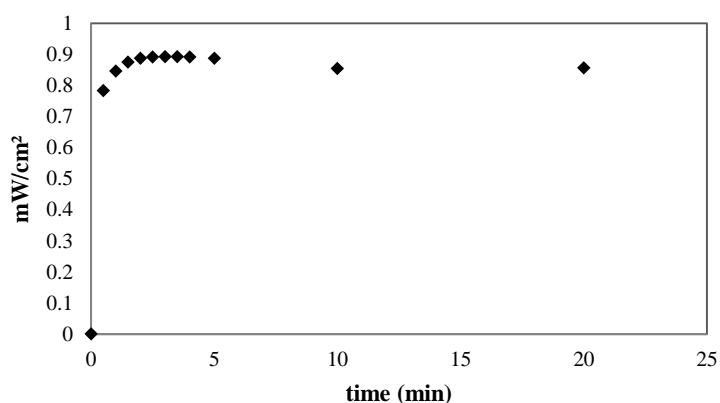


Figure 3.12 Control of the UV light intensity produced by a Handheld UV lamp (error ± 0.01 mW/cm²).

Three illumination scenarios were taken into account as a preliminary test for the degradation of phenol with ZnO-NFs: Total darkness (with no pre-exposition to light),

visible light and UV light. As shown in Figure 3.13, there was not considerable reduction in the concentration of phenol in the absence of light or with visible light.

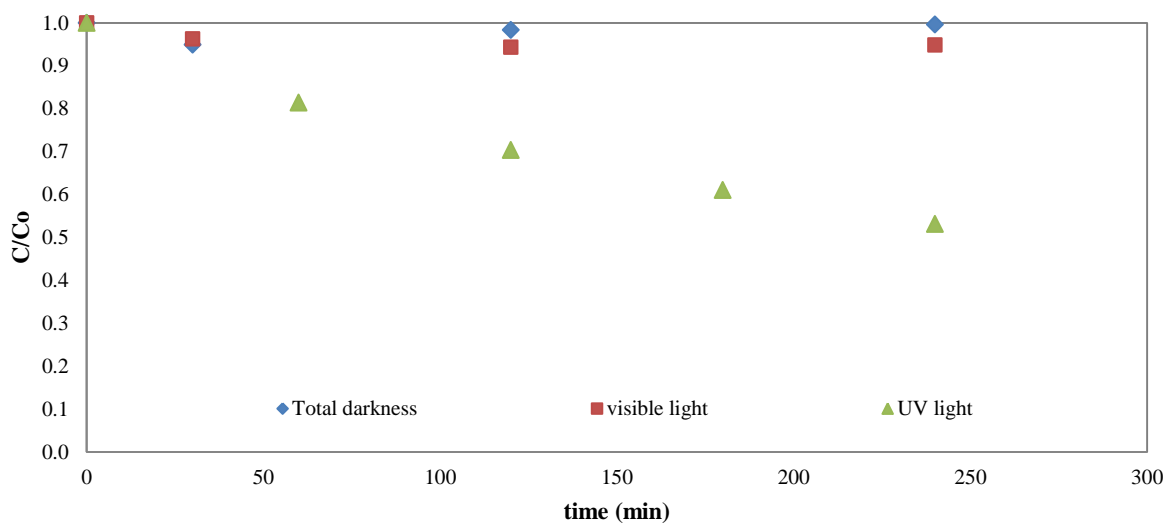


Figure 3.13 Degradation of phenol with ZnO-NFs and different sources of light.

3.5 Analytical measurements of organic compounds

Phenol p.a. ACS reagent 99-100.5% (Sigma Aldrich); methyl orange (MO) (Across Organic); and acetonitrile $\geq 99.9\%$ HPLC grade (Sigma-Aldrich - CHROMASOLV) were used as received without further purification.

3.5.1 UV-Visible Spectrophotometric measurements

Changes in MO concentration were measured during the experiments using a UV-Vis spectrophotometer (UV-1601 Shimadzu UK) in UV absorbance mode at a wavelength between 300 and 650 nm. Deionised water was used to establish the baseline and the calibration curve was obtained by measuring the absorbance of 5 different concentrations of MO at 464 nm as shown in Figure 3.14.

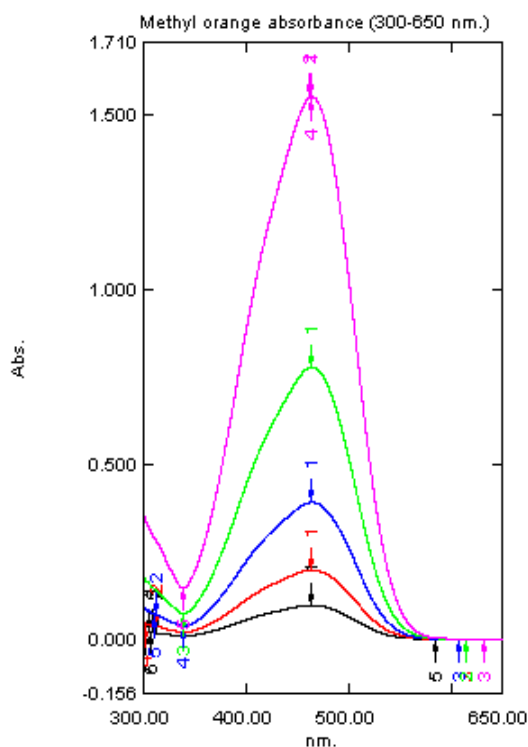


Figure 3.14 Methyl orange absorbance spectrum (300 – 650 nm) at different concentrations

3.5.2 High performance liquid chromatography (HPLC)

A series of preliminary measurements were carried out at different concentrations of phenol, mobile phase and wavelengths reported in literature [68], [81], [234]. As a result of the preliminary measurements, the method and conditions selected to measure changes in the concentration of phenol was established. A Shimadzu HPLC system (SCL-10A) equipped with an isocratic pump (Shimadzu Co, Japan, Model LC-10-ATVP), an auto sampler (Shimadzu, Japan, model SIL-10AD), and a UV-Vis detector (SPD-10AV) was used. The reverse phase chromatography was performed with Stainless steel, 150 mm X 2.0 mm, C18 column (Thermo, Germany). Aqueous solutions of acetonitrile [75:25] and [60:40] were used as a mobile phase.

The chromatographic conditions were established by a series of runs at different concentrations of phenol and wavelengths. Concentrations of phenol at 40, 20, 10, 5 and 2.5 ppm were prepared with deionized water. These solutions were used to determine the sensibility and detection limit of the equipment and to identify the peaks and retention times of the phenol. The chromatogram of phenol for each concentration was obtained at 254 nm, with a running time of 20 min, and an injection volume of 20 μ l (Figure 3.15 a). Additionally, only one peak obtained at 180 seconds was detected

(Figure 3.15 b); therefore further peaks formed during the photocatalytic reaction might be attributed to by-products of phenol.

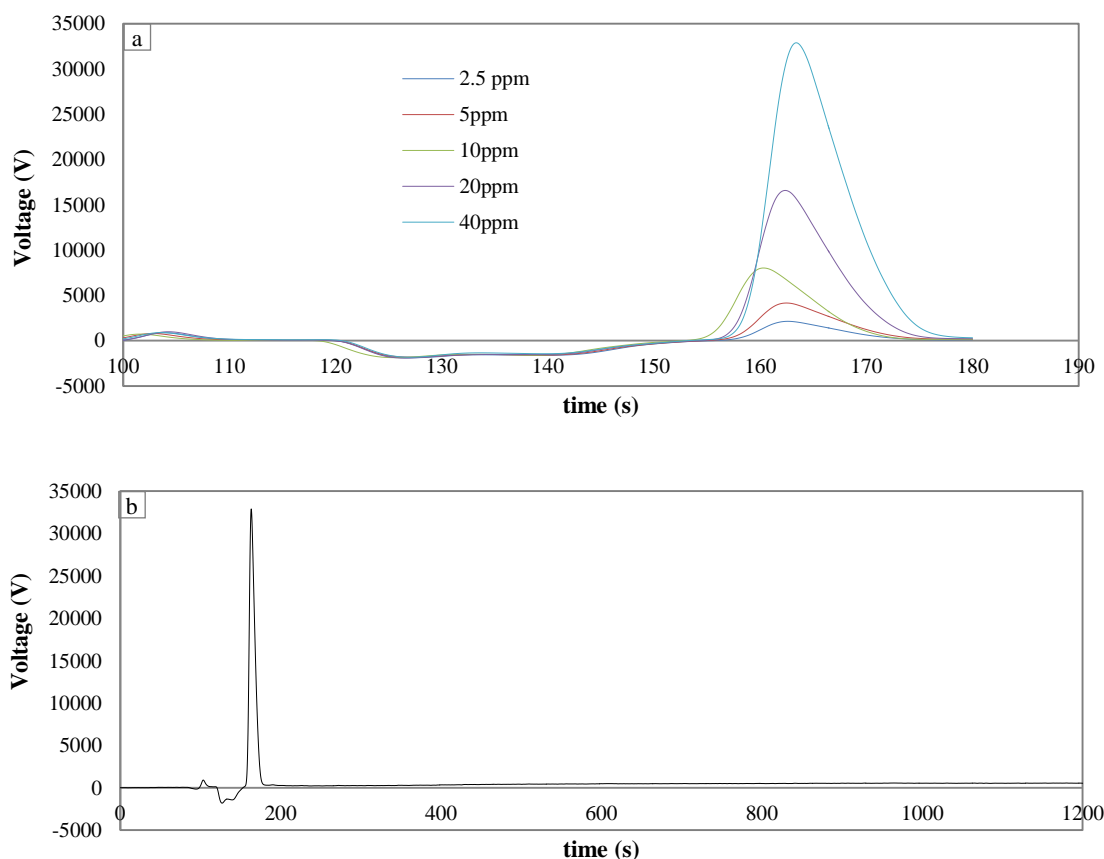


Figure 3.15 Chromatogram of phenol at different concentrations at 254 nm run for 200 seconds (a) and for 1200 seconds (b) (error: ± 0.01 ppm).

A series of chromatograms of phenol were obtained at the different detection wavelengths (i.e. 280 nm, 270 nm, 254 nm, 210 nm), for two concentrations of phenols (2.5 ppm and 40 ppm), running time of 5 min, and an injection volume of 20 μ l. Results showed that the wavelength in which the detection of phenol is highest for the selected method is at 210 nm (Figure 3.16). Once the range of concentrations and the wavelength were selected, the calibration curve was performed as shown in Figure 3.17.

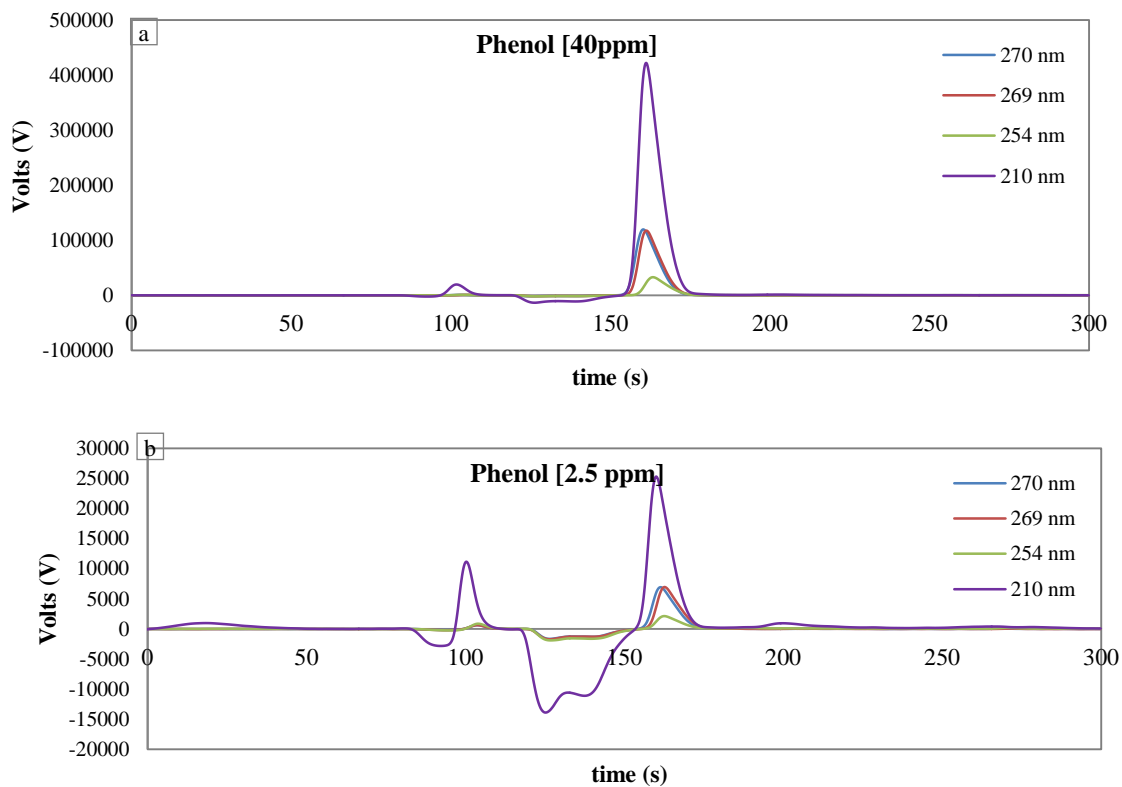


Figure 3.16 Chromatogram of phenol [40 ppm] (a) and [2.5 ppm] (b) at different wavelength.

Samples were collected every hour during the photocatalytic degradation of phenol, filtered by using a 0.22 μm syringe filter unit (Millex-GV, Merck Millipore), kept in glass vials (Fisher, VG-100-020c) in a cold room at 4 $^{\circ}\text{C}$ until HPLC analysis were carried out at room temperature.

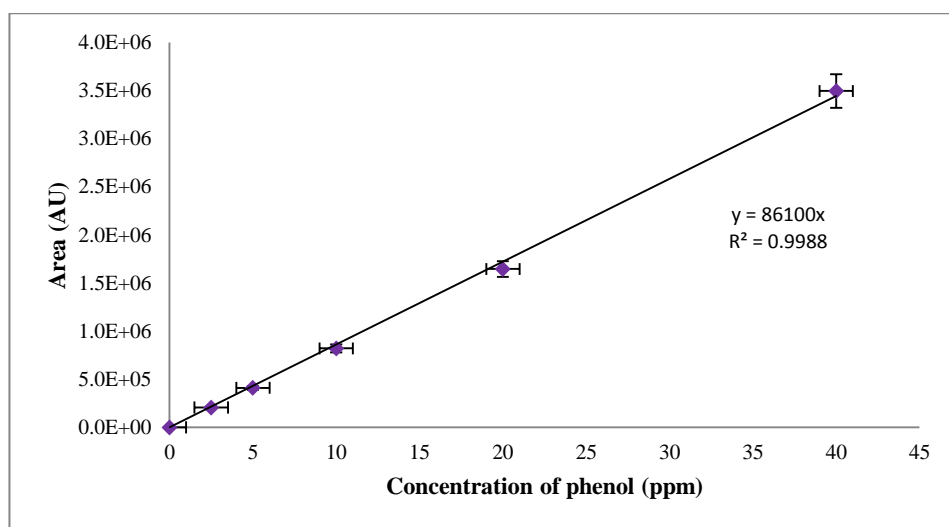


Figure 3.17 Calibration curve of phenol at 210 nm.

To identify the by-products of the photocatalytic degradation of phenol, 3 compounds, commonly generated during the degradation of phenol, were selected and analysed by HPLC, namely catechol, hydroquinone and benzoquinone [235]. For this analysis the mobile phase used was an aqueous solution of acetonitrile [50:50] and wavelengths of 210 nm and 270 nm were chosen (Figure 3.18). Once the retention time for each by-product was determined, a calibration curve at different concentrations was developed. Selected samples from the photocatalytic degradation of phenol with ZnO-NFs were analysed with the same method.

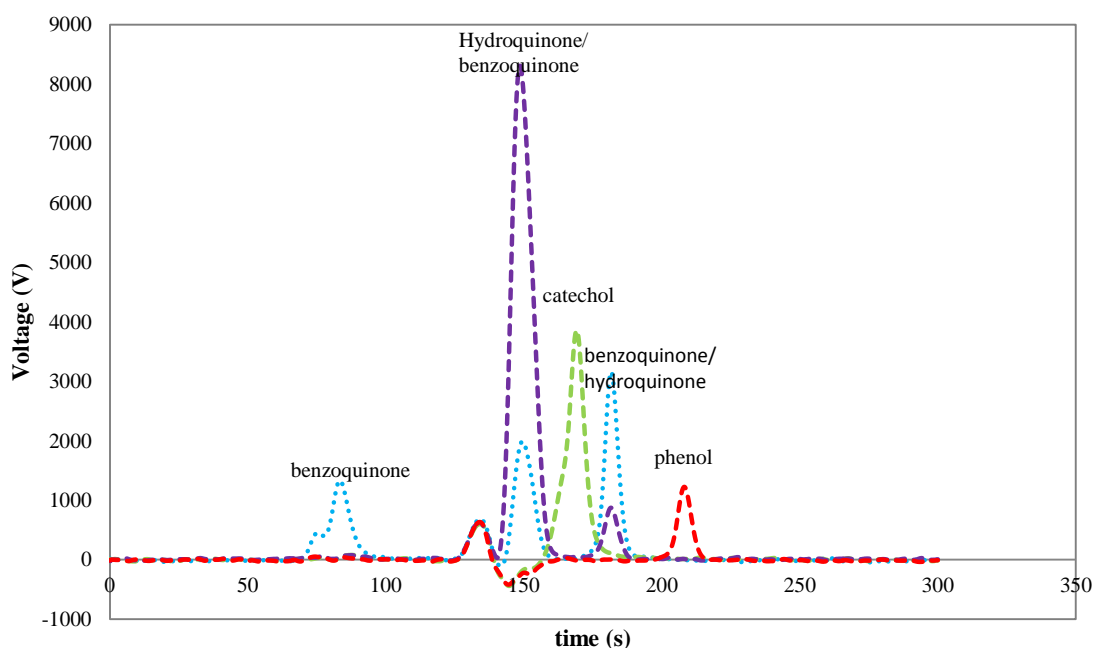


Figure 3.18 Detection of by-products of phenol decomposition by HPLC

3.5.3 Total Organic Carbon

Total organic carbon (TOC) was measured using a TOC-V CPN Shimadzu analyser. The system was initially calibrated with dissolutions of phthalate and sodium carbonate (Na_2CO_3) for measurements of total carbon (TC) and total inorganic carbon (TIC) respectively. The flame was set at $680\text{ }^\circ\text{C}$ and the injection volume was 20 ml. The TOC was calculated based on the results obtained from TO and TIC as following

$$\text{TC} - \text{TIC} = \text{TOC} = \text{NPOC} + \text{VOC},$$

Where NPOC is the non-purgeable organic carbon and VOC is the volatile organic carbon.

Prior to the TOC measurements of the phenol samples taken from the photocatalytic reaction, an analysis of sensitivity was performed in order to determine the limit of detection. Different solutions of phenol ranging between 0.05 ppm and 5 ppm were used. Results showed that the system was able to detect the minimal concentration tested (0.025 ppm of phenol) with a TOC of 0.01 mg/L as shown in Figure 3.19.

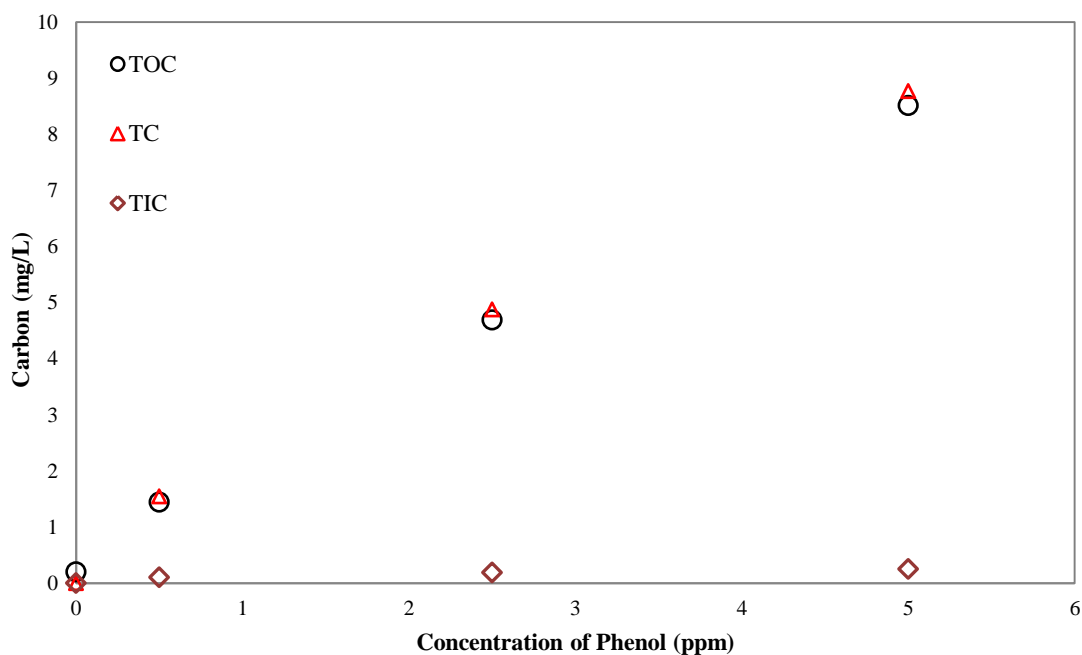


Figure 3.19 TOC of different concentration of phenol ranged between 0.05 and 5ppm.

3.6 Dye and phenol absorption

The absorption of MO and phenol onto the ZnO-NFs was compared with the absorption of these compounds onto commercial ZnO powder. Different amounts of ZnO powder (99.9%, Alfa Aesar) were mixed with 50 ml of 0.1 M methyl orange and with 50 ml of 0.1 M phenol with a constant stirring for 30 minutes and left for 12 hours in darkness. The mixtures were then centrifuged at 5000 rpm for 10 minutes and the initial and final concentration of MO and phenol were recorded by UV-Vis spectrophotometry and HPLC respectively. The Brunauer Emmett Teller (BET) surface area of the ZnO powder was previously measured. With the BET results a relationship between the amount of MO and phenol absorbed by the ZnO powder and the total surface area were correlated.

Selected ZnO films were cut into circular shapes of 0.8 mm diameter leaving only the supported ZnO layer exposed and then cut in half. Half of each film was immersed in 50 ml of 0.1 M methyl orange solution and the other half in 50 ml of 0.1 M phenol for 12 hours in darkness with stirring. The initial and subsequent concentrations of MO were measured using a UV-Vis spectrophotometer in UV absorbance mode at a wavelength of 464 nm, while the changes of phenol concentration were measured by HPLC following the procedure described in section 3.5.2.

3.7 Software used in analysis of data

For this project the following software were used in the collection of data and their analysis: Microsoft Word and Microsoft Excel ®, Matlab®, Class VP 5.02®, Image J ®, and Lab View 210 ®.

3.8 Statistical Analysis and Reproducibility

All the ZnO-NFs made by anodization in this study were produced following the protocols described in Section 3.1. Films that did not show a homogeneous layer by visual inspection were not used and therefore not used for characterisation or for photocatalytic applications. The characterisation of the ZnO-NFs and ZnO-NWs (i.e. contact angle and morphology) was performed in at least three areas of the films and differences were reported. For some analysis such as XRD and band gap measurements, a set of ZnO-NFs were selected and the analysis were repeated at least three times in order to verify results and determine the error.

For the preliminary experimental part of the photocatalytic study, single experiments were done in order to find the optimal experimental conditions and to determine the sensitivity of the equipment. During the photocatalytic experiments involving ZnO-NFs and ZnO-NWs, the selected experimental conditions were verified through the reaction time. Some experiments were repeated in order to verify reproducibility. Additionally, samples of phenol and MO exposed to photocatalytic degradation were randomly selected to be reanalysed by HPLC and UV-Vis absorption respectively.

Data from the experiments and analysis that were repeated was analysed using the software Excel®. Standard deviation was calculated and reported during the analysis of the results. The statistical analysis of the error generated by calibration of the equipment is also registered throughout the analysis.

3.9 Summary

This chapter described materials, methods and experimental systems used throughout the following chapters. The production of ZnO-NFs and ZnO-NWs and their characterisation were explained during the first and second section. The setup employed in photocatalytic experiments were described in section three, followed by the description of the analytical methods used for measuring the models organic compounds. Finally, information about software employed throughout the study and about statistical analysis and reproducibility was exposed in the last sections. The following chapter will discuss the results and findings of this study and the last chapter will provide the conclusion of the study and the proposed future work.

““Nothing in life is to be feared, it is only to be understood. Now is the time to understand more, so that we may fear less.”

Marie Curie

Chapter 4: Results and Discussion

This chapter presents in detail the production of nanostructured zinc oxide films (ZnO-NFs), the physicochemical properties of the ZnO-NFs obtained at different experimental conditions, and the effects of thermal post-treatment on the composition and crystallinity of the films. Additionally, design guidelines for controlling morphology, wetting behaviour and surface profile of the ZnO-NFs are discussed. Part of this work has been published in *RSC advances Journal* [212].

4.1 Pre-treatment of the starting material

Before anodization, a pre-treatment consisting of annealing and electro-polishing the zinc foil took place. During the annealing process, a partial restoration of the microstructure of the metal and its initial properties is expected. This process, called recrystallization, involves the removal of the dislocations, the formation and growth of new grains within the structure and the reconfiguration of the new grain structure [236]. Therefore, defects produced during the production of the Zn foil can be minimized, improving the quality of the starting material before electro-polishing, and the regularity of nanostructures produced by anodization. Zn foil used for fabricating ZnO-NFs was annealed at 350 °C for 1 hour.

Electro-polishing is an electrochemical method that improves the surface of metals by removing the natural oxide layer remnant layers and surface irregularities, creating a smoother surface. Different voltages and reaction times result in diverse qualities of electro-polished surfaces due to the variation of the electro-polishing mechanisms. By varying voltage, the initial step of electro-polishing (anodic-levelling) is affected. During the anodic-levelling irregularities are preferentially dissolved. This dissolution is

induced by a differential local charge distribution and occurs on the natural oxide layer and on the outer layers of the zinc foil. Once the surface defects are minimal, a second mechanism named micro-smoothing takes place. Micro-smoothing involves the formation of a thin ionic salt on the surface of the anode that is susceptible to be removed by diffusion given to the material a mirror-like aspect [237]. Electro-polishing has a significant impact on the production of homogeneous nanostructures [238].

In order to determine the optimal conditions for electro-polishing of the Zn foil, ethanolic solutions of phosphoric acid (H₃PO₄) and perchloric acid (HClO₄) were used in different volumetric proportions. HClO₄ in the volumetric ratio of 1:2 produced mirror-like surfaces and therefore this concentration was used for further tests. Higher volume ratios of HClO₄ resulted in corrosion of the Zn foil.

Pieces of Zn foil that were electro-polished with HClO₄ [1:2] for 15 minutes at 10, 15, 20 and 25 volts displayed no pitting; however at low voltages a white layer remains on the material. In order to obtain an optimal electro-polished surface, the voltage applied had to be strong enough to guarantee “anodic levelling” without resulting in corrosion of the material. The absence of a mirror-like finish on the Zn foil indicated that the anodic-levelling stage only occurred partially, thus a natural oxide layer remained or the irregularities were not dissolved. On the other hand, high voltages can lead to a rapid and non-homogeneous dissolution of the metal resulting in pitting [215].

During the electropolishing of zinc foil at different reaction times, it was observed that after 15 minutes similar surface textures were obtained but with a higher loss of Zn mass. After 15 minutes the surfaces were already smoother and further treatment was not needed. Based on these results, the Zn foil used for anodization were electro-polished with HClO₄ in the volumetric ratio of 1:2 with ethanol at 20V for 15 min and -70 °C. It is important to mention that zinc reacts naturally with oxygen forming ZnO directly (Equation 4.1). To prevent the formation of a new oxide layer, once the electropolishing was carried out, the electro-polished zinc foil was used immediately for anodization.



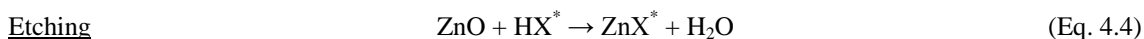
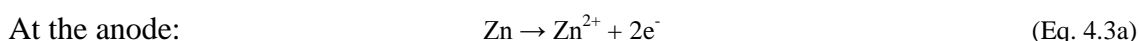
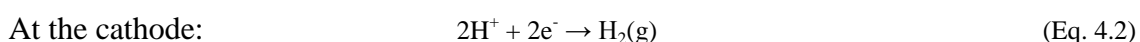
4.2 Anodization process

As it was discussed in Chapter 2, anodization of Zn is not a well understood process. In general, it is assumed that Zn nanostructures are formed by the competition between the formation of Zn ion complex (Zn^{2+}) that oxidise into ZnO and an etching process that dissolves the formed ZnO layer. However, the exact mechanisms for the formation of the Zn ion complex and the dissolution of ZnO have not been extensively studied. Furthermore, the mechanisms that lead to the formation of different nanostructures are still unknown.

4.2.1 Proposed formation mechanism of ZnO.

The majority of the literature about ZnO nanostructures and anodization of zinc have described the mechanism for the formation of ZnO nanostructures using equations 4.2 - 4.4, regardless of the type of electrolyte that was used. The main issue with using these general equations is that they do not take in account the effects of each electrolyte on the pH of the media, and the different species that are formed with the dissociation of the electrolyte. Herein, a mechanism based on the Zn(II) speciation is proposed, and therefore, the effect of pH and the concentration of Zn on the electrolyte solution has been taken into account.

Anodization



* X represent the anion of the electrolyte (e.i. PO_3^{2-}) which may form a zinc salt (e.i. Zn_3PO_4) during anodization process.

The different reactions that occur during the anodization process might vary depending on the pH of the electrolyte as it controls the predominant Zn(II) species and the dissolution of the ZnO. The speciation of Zn(II) as a function of pH (Figure 4.1) shows that at low zinc concentrations, the Zn^{2+} ion is the dominant Zn(II) species up to pH 8.7, while $Zn(OH)_2$ dominates from pH 8.7 to pH 11.4. A pH higher than 11.4 results in the formation of $Zn(OH)_3^-$. At high concentrations, on the other hand, stable $Zn(OH)_2$ in a

solid phase is present from neutral to high pHs, while at low pH values, Zn^{2+} ion turn into $Zn(OH)^+$ electropositive Zn(II) complex [239]–[241].

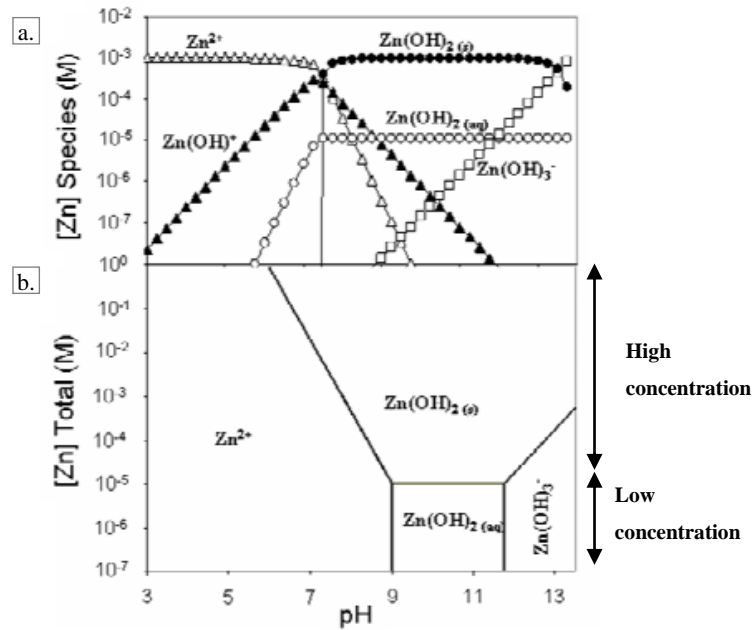


Figure 4.1 Speciation of zinc as a function of pH a) at fixed zinc concentration of 1×10^{-3} M (top) and b) as a function of zinc concentration at 25 °C showing only the dominant species (bottom) [242]

A percentage of the $Zn(OH)_2$ and $Zn(OH)_3^-$ produced turns into ZnO (Equation 4.3c) while it is likely that a large amount of $Zn(OH)_{(s)}$ precipitates either on the surface of the Zn foil or on the anodization reactor (as it was observed during the production of ZnO-NFs). Simultaneously, once the ZnO is formed, it is exposed to conditions that dissolve it in different ways depending on the electrolytes. Under acidic conditions, ZnO turns back into Zn ion (Zn^{2+}) following the reaction displayed in equation 4.5 [5]. A less likely reaction can also occur due to the attack of protons (from the acidic electrolyte) on Zn-O bonds followed by the dissociation of Zn (Equation 4.6) [243].



At alkaline pHs, ZnO tend to form hydroxide species. In particular ZnO could dissolve by forming hydroxo-complexes with OH (Equations 4.7 – 4.10) [5][243]. At neutral pH, on the other hand, ZnO reacts directly with water forming $Zn(OH)_2$. Since the solubility of $Zn(OH)_2$ is minimal in water a high precipitation of this product is expected.





Some of the soluble species produced during the dissolution of Zn and the dissolution of ZnO can react with dissociated ions from the electrolyte (for instance: HCO_3^- , PO_4^{3-} , Na^+) to form salt or Zn complexes. Additionally, ions can be attracted by the electrodes and be trapped by the newly formed layers of ZnO. The latter phenomenon has been discussed for the formation of alumina via anodization [244].

Although the different Zn species that can be formed during the anodization can be predicted by chemical and thermodynamic analysis, the actual formation of the ZnO nanostructures still remains a not well-known process. The anodization of Zn using KHCO_3 as electrolyte and the formation of nanowires was therefore analysed in detail to elucidate the nanostructure formation.

4.2.2 Formation of nanowires by Anodization of Zn with KHCO_3

Similar to the mechanism for the formation of ZnO by anodization, the mechanism that controls the shaping of ZnO nanostructures during anodization is still not clear. Herein, the pH, conductivity and concentration of dissolved Zn were measured during the anodization of Zn with KHCO_3 [0.05M] at 10 °C, 1V and for 1h. This data was correlated with the current density diagram obtained during the anodization of Zn and compared to the current density diagram for the anodization of aluminium. With this information, FESEM micrographs and based on the analysis made in Section 4.2.1, a mechanism of the shaping for the formation of ZnO nanostructures is proposed.

During 1 hour of anodization, the pH of the electrolyte was stable at 9.1 ± 0.1 (Figure 4.2-b). Conductivity, on the other hand, increased during the first 30 minutes and then it drops indicating a precipitation of Zn(II) (Figure 4.2-c). According to the speciation of Zn (Figure 4.1), three Zn(II) species coexist at pH of 9.1, namely, Zn^{2+} , $\text{ZnO}_{(\text{aq})}$, and $\text{ZnO}_{(\text{s})}$. The latter species is insoluble and precipitates. Since the pH values were stable during anodization, precipitation of $\text{ZnO}_{(\text{s})}$, observed during the reaction, is attributed to the increment on the Zn concentration produced by the dissolution of Zn foil and the formed ZnO.

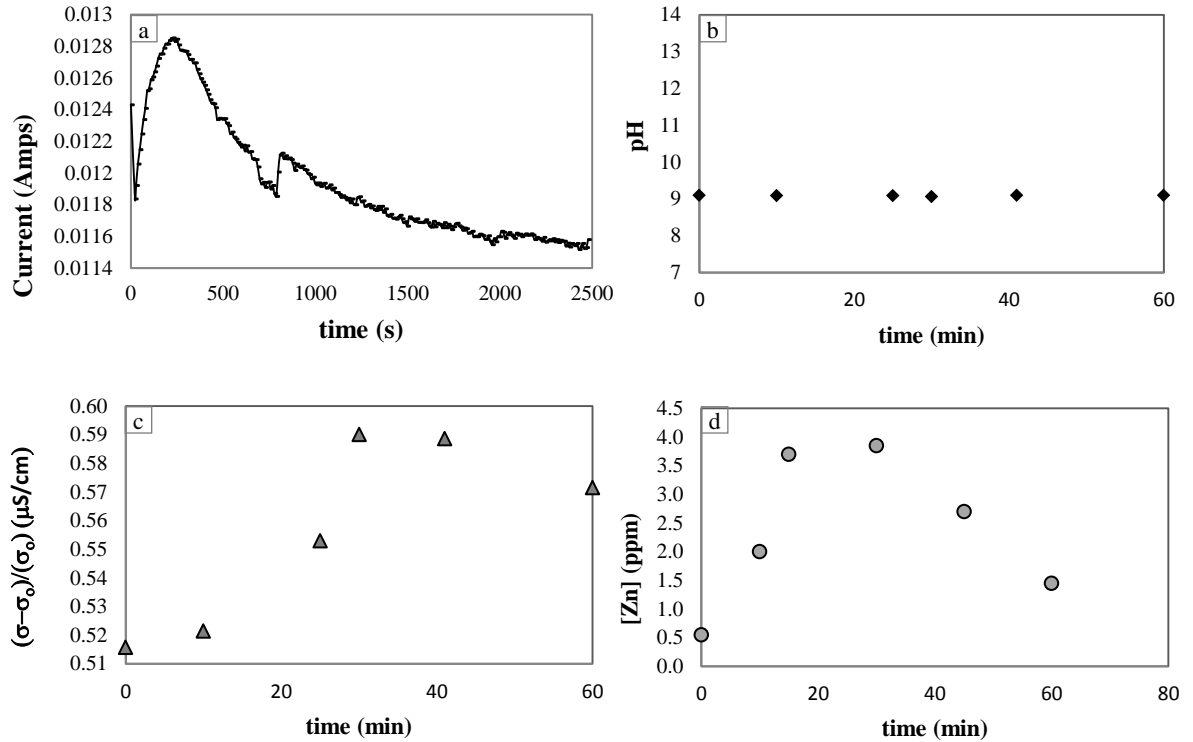


Figure 4.2 Changes in a) current b) pH of the electrolyte, c) conductivity of the electrolyte and d) dissolved Zn on the electrolyte during anodization of Zn foil.

The concentration of Zn dissolved in the electrolyte varied during the anodization reaction. As it can be observed in Figure 4.2-d, the dissolution of Zn is higher at the beginning of the reaction, between 20 and 30 minutes the concentration of dissolved Zn reaches a peak, followed by a drop. This behaviour coincides with the one observed during conductivity measurements (Figure 4.2-c). The concentration of zinc increases for the dissolution of zinc foil and ZnO (explained in detail in section 4.2.1). It appears that under these anodization conditions, after 20 minutes the concentration of Zn(II) reaches a maximum value where the predominant Zn(II) species becomes the non-soluble $\text{Zn}(\text{OH})_{2(s)}$.

The plot of the current vs. time obtained during anodization varied with each electrolyte. Figure 4.2-a displays the current's plot for KHCO_3 ; changes in current at the beginning of the process are similar to those obtained for alumina [244]. As depicted in Figure 4.3, the anodization starts with a value of current (A_0). An initial drop of current (from A_0 to A_1) occurs for the formation of a ZnO layer on the surface of the zinc foil, followed by a recovery on the current value to A_2 . The increase in the current suggests the exposure of small areas of Zn to the electrolyte or nucleation of the ZnO. Those

fresh areas of Zn become exposed to the electrolyte due to the formation-dissolution mechanism discussed earlier.

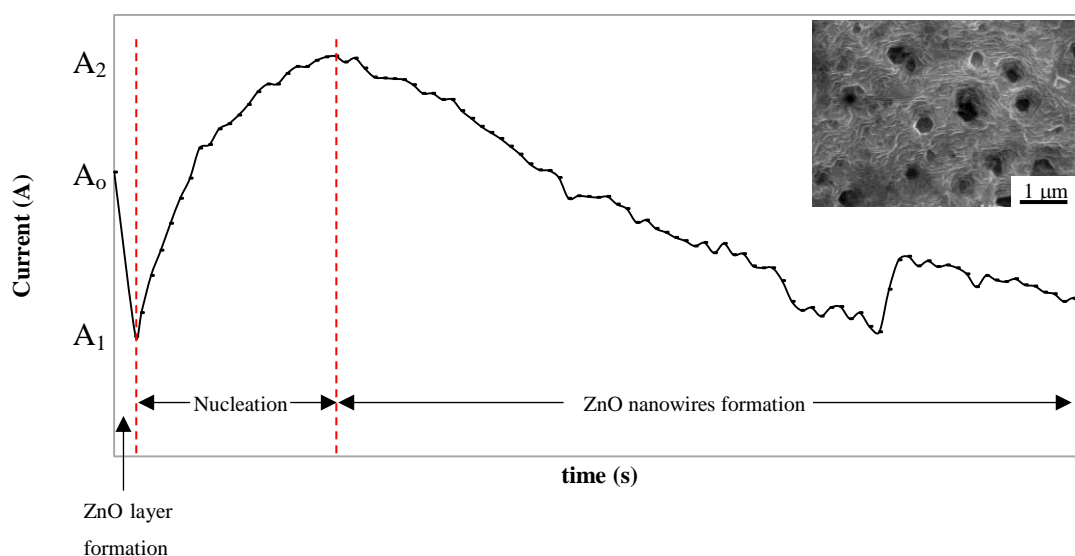


Figure 4.3 Different stages of productions of nanowires analysed by changes in current during anodization of Zn with KHCO_3 [0.05M] at 10 °C, 1V and 1h. Inset: FESEM of nucleation of Zn

FESEM micrographs of anodization carried out for a short period of time (Figure 4.3 – inset) revealed a nucleation of the ZnO similar to that of alumina [244]. Unlike alumina, after the nucleation there is no formation of pores; instead, the formation of nanowires takes place onto or nearby the nucleation sites (Figure 4.4). The formation of the nanowires produces a general failure on the current due to the formation of a ZnO layer. Slight increases and changes in the current in this stage, are caused by the constant dissolution and formation of ZnO and other Zn(II) species following the mechanism described in section 4.2.1. It is still unclear whether the formation of the ZnO nanostructures occurs from the base of the Zn outward (where the new layers are close to the Zn foil) as it occurs with alumina, or if it occurs by deposition of ZnO on the top of external layers. Some authors have suggested that in the initial state of the process ZnO nanoparticles are formed from the spontaneous nucleation of Zn(OH)_2 on the Zn foil, and those nanoparticles act as the foundation of more complex nanostructures [192], [245].

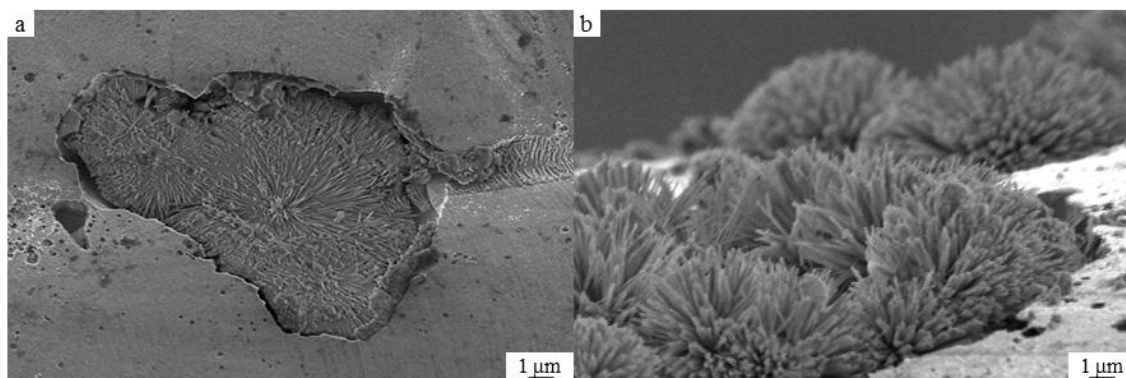


Figure 4.4 FESEM micrographs of the early stages of the formation of nanowires close to the pores produced by the nucleation of Zn during anodization.

4.3 ZnO films composition

Initial analysis of the composition of the ZnO-NFs by EDX revealed that the main compounds present in the film were zinc and oxygen. The film produced with H_3PO_4 at 1V contained a negligible amount of oxygen, thus indicating a minimal formation of the ZnO layer. Since the substrate of the films was zinc foil, this compound was found in a major proportion in all the samples. The presence of carbon was initially attributed to deposition from the beam during FESEM analysis. Some ZnO-NFs additionally showed traces of electrolyte ions (Table 4.1).

Table 4.1 Composition of ZnO-NFs obtained by EDX analysis.

Anodization conditions	Estimated composition					
	C	O	S	P	Zn	total
H_2SO_4 / [0.1M] / 40 V / 1 h / 10 °C	2.6	23.4	2.94	-	71.06	100
H_3PO_4 / [0.1M] / 1 V / 1 h / 10 °C	4.09	2.27	-	0	93.64	100
H_3PO_4 / [0.1M] / 40 V / 1 h / 10 °C	2.93	16.83	-	5.75	74.49	100
H_3PO_4 / [1M] / 40 V / 1 h / 10 °C	5.04	36.07	-	13.58	45.31	100

Among the electrolytes used in anodization, phosphorus (from the H_3PO_4 electrolyte) was found in a high proportion. As the dissociation of H_3PO_4 produces the ion PO_4^{3-} , it can either be attracted by the anode or react forming insoluble $\text{Zn}_3(\text{PO}_4)_2$, and then deposited on the surface of ZnO-NFs (Equation 4.11).

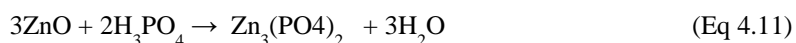


Table 4.2 displays the solubility constant of some Zn(II) compounds formed during anodization with different electrolytes. The formation of insoluble compounds and their subsequent deposition affects the purity of the ZnO films. Therefore, an extensive rinse of the ZnO-NFs surface with ethanol and deionised water was included as a part of the protocol of production of ZnO-NFs to minimize the presence of electrolyte traces.

Table 4.2 Solubility of potential compound formed during anodization of Zn.

Zn species	Solubility in water (25 °C)	K _{sp} (25 °C)
ZnO	0.16 mg/100 ml	3.86x10 ⁻¹⁰
Zn(OH) ₂	-	3.86x10 ⁻¹⁷
Zn ₃ (PO ₄) ₂	-	9.0x10 ⁻³³
Zn(NO ₃) ₂	327 g/100 ml	No data found
ZnC ₂ O ₄	-	9.0x10 ⁻⁸
Zn(SO ₄)	53.8 g/100ml	No data found

(-) means negligible data

Further analysis of the composition of ZnO-NFs obtained with different electrolytes was performed using X-ray photoelectron spectroscopy (XPS) (Table 4.3). The main elements found were Zn(2p) and O(1s). Despite the new rinsing protocol after anodization, samples still contained traces of the electrolyte confirming the ZnO composition that were found by EDX.

Table 4.3 XPS composition of films obtained with different electrolytes

	C (1s)	Cl (2p)	F (1s)	Fe (2p)	Na (1s)	O (1s)	P (2s)	Zn (2p)
	%	%	%	%	%	%	%	%
KHCO₃	9.2	-	-	1.8	-	55.0	-	34.0
NaOH	10.0	-	-	1.7	4.0	52.1	-	32.2
Ox. Ac.	34.6*	-	-	0.8	-	49.2	-	15.5
H₃PO₄	17.0	0.6	2.2	1.1	-	53.0	9.8	16.4
HCl	22.0	2.7	-	1.3	-	47.7	-	26.3

(-) means negligible values

As previously mentioned, it is believed that, in addition to the deposition of low soluble traces of electrolyte (i.e. salts of zinc) on the surface of the ZnO-NFs, anions from the dissociation of the electrolyte are incorporated into the ZnO barrier. This phenomenon has been described and quantified for anodization of aluminium[244]. The electric potential differences might be responsible for this incorporation, where anions negatively charged are attracted by the anode. Carbon (initially attributed to deposition from the beam during FESEM analysis) is likely to be present due to traces of ethanol (used as a solvent during anodization). Traces of Na(1s) found in the ZnO-NFs obtained with NaOH are attributed exclusively to deposition of low soluble traces rather than to incorporation for electric potential differences. Since sodium is found as cation in the electrolyte solution, it is unlikely that it can be attracted by the anode.

4.4 ZnO-NFs morphology. Effect of anodization conditions

As discussed in previous sections, formation of ZnO and its dissolution are directly affected by the electrolyte type and its concentration. During anodization, the applied current, temperature and reaction time can also modify the thermodynamic conditions of the reaction, and affect the formation of the nanostructures. Herein, the first systematic study about the effects of these parameters on the ZnO-NFs morphology is presented. Experimental conditions for anodization of Zn foil for 6 types of electrolytes were investigated and their effect on morphology was studied.

4.4.1 Effect of type of electrolyte and concentration on film morphology

FESEM micrographics obtained from the surface of the ZnO-NFs revealed that the shape of the nanostructures is determined by the electrolyte (Figure 4.5). Anodization performed using H_3PO_4 as electrolyte results in the formation of flake-like nanostructures; HCl , NaOH , HNO_3 , $\text{H}_2\text{C}_2\text{O}_4$ generated nano-flowers-like shapes; whereas nanorods and nanowires were obtained with KHCO_3 . The sizes of the nanostructures varied from about 100 nm obtained using HNO_3 and KHCO_3 at 0.1M to 20 nm found in the films made with NaOH and H_3PO_4 , also at low concentration (0.1M).

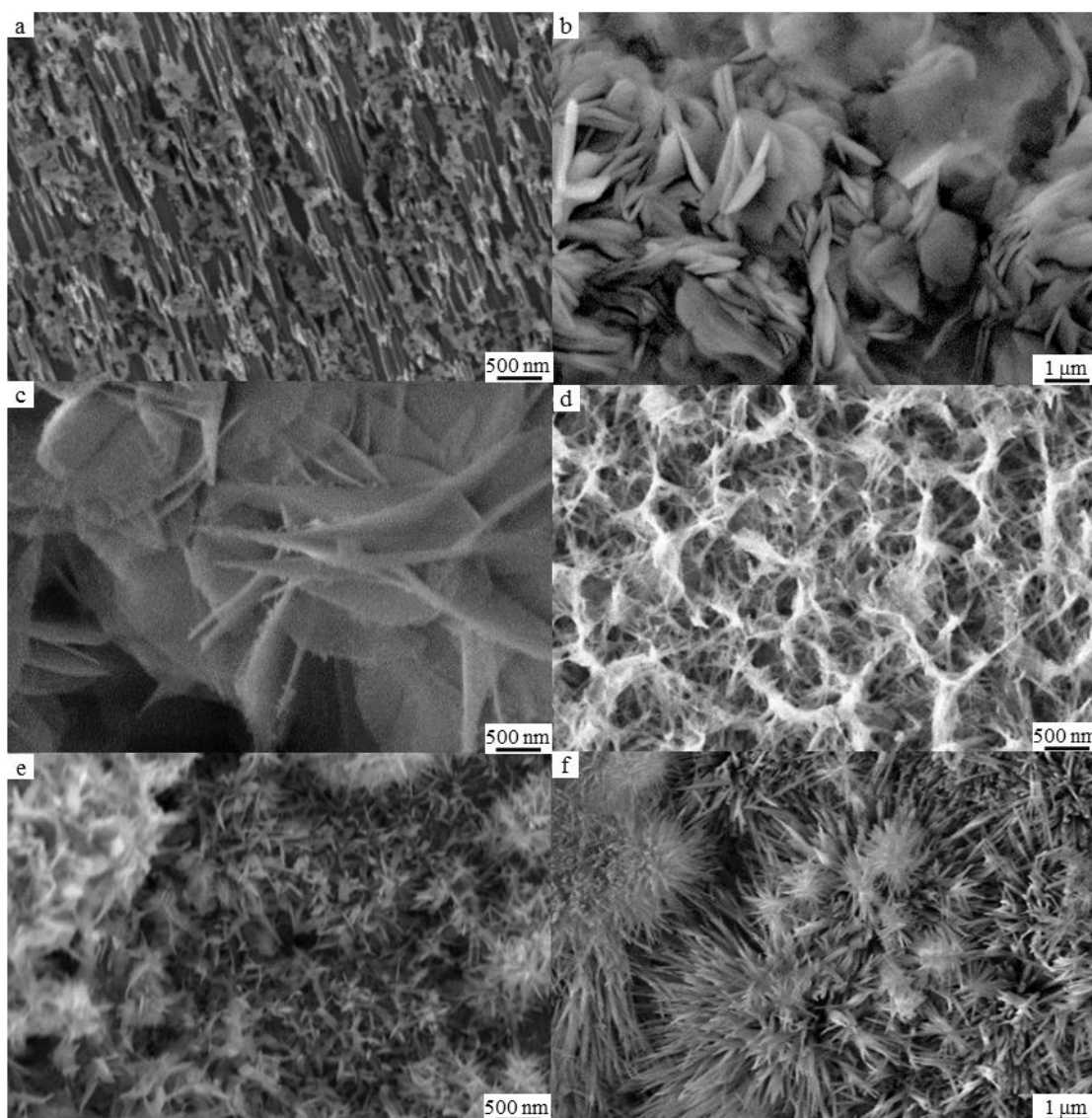


Figure 4.5 SEM micrographs of morphologies obtained with different electrolytes: a) H_3PO_4 (1 M, 40 V, 1 min, 10 °C); b) HNO_3 (1 M, 1 V, 1 h, 10 °C); c) HCl (0.1 M, 40 V, 1 h, 10 °C); d) $\text{H}_2\text{C}_2\text{O}_4$ (0.1 M, 1 V, 1 h, 10 °C); e) NaOH (0.1 M, 40 V, 1 h, 10 °C); f) KHCO_3 (1 M, 1 V, 1 h, 10 °C)

While the type of electrolyte defines the shape of the nanostructures, it appears that concentration of the electrolyte affects their size and their aspect ratio. For all the electrolytes used, increasing the concentration results in a higher surface density of nanostructures (Figure 4.6). High concentrations of electrolytes lead to an increase in the number of nanostructures per unit area and to thicker ZnO layers. For instance, in Figure 4.6-a (left), individual nanostructures can be observed, while in the film obtained at a higher concentration (Figure 4.6-a (right)) the number of nanostructures appears to be higher and therefore no individual nanostructures are visible. Similarly, Figure 4.6-c (left) shows a featureless surface, by increasing the concentration of H_3PO_4 more nanostructures and denser arrangements were obtained (Figure 4.6-c (right)). Usually,

nanostructures formed at low electrolyte concentrations are well-defined configurations where single nanostructures can be observed, as can be observed in Figure 4.6-b (left). Regardless of the type of electrolyte, high concentrations of electrolyte involves higher concentrations of Zn(II) species (ions) in the solution and, therefore, a higher precipitation of Zn(OH)₂ and ZnO, following the mechanism postulated in Section 4.2.1.

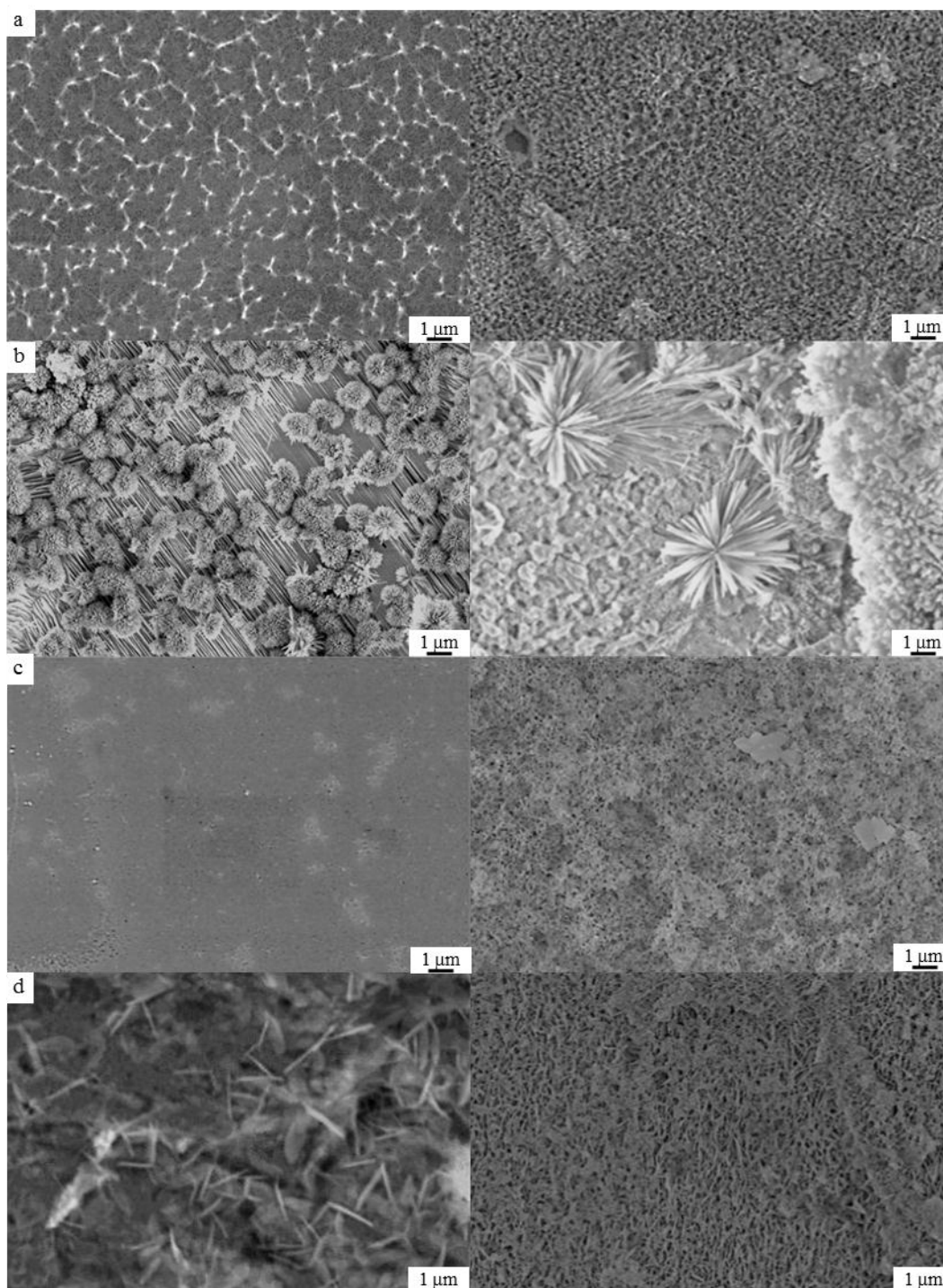


Figure 4.6 SEM micrographs of morphologies obtained at 1 V, 10 °C, for 1 minute, with different electrolytes at 0.1 M (left) and 1 M (right): a) H₂C₂O₄; b) KHCO₃; c) H₃PO₄; d) HCl.

4.4.2 Effect of voltage on film morphology

Figure 4.7 shows FESEM micrograph of ZnO-NFs surfaces obtained at 1 V and 40 V for similar concentrations of electrolyte. The effect of voltage appears to be similar to the effect of concentration: A high voltage leads the production of dense nanostructures where the number of nanostructures per unit area is high, additionally, nanostructures tend to be larger. For instance, in the FESEM micrograph of the ZnO-NF obtained with KHCO_3 at 1 V (Figure 4.7-a (left)) single nanowires can be observed, at higher voltages (Figure 4.7-a (right)), on the other hand, the film appears to have more nanostructures per unit area and no single nanowires are visible, instead nanowires appear in clusters.

In acidic conditions and at high voltage, the rapid generation of Zn^{+2} (Equation 4.5) results in pitting of the Zn foil. This phenomenon was observed during the anodization of Zn with $\text{H}_2\text{C}_2\text{O}_4$, H_3PO_4 and HCl specially at high concentrations. Anodization with KHCO_3 at 40 V resulted in the formation of linked or interpenetrated structures such the one shown in Figure 4.7-d (right). Those configurations might be produced once the nanowire reaches a certain length, bend and tangle with adjacent wires. This phenomenon might not be observed with other nanostructures due to their short length.

4.4.3 Effect of temperature on film morphology

Temperature affects the dissolution rate of the ZnO and the flow of ions through the electrodes. The effect of temperature on the morphology of the ZnO-NFs varied with the electrolyte used and the voltage applied. It was found that for acidic electrolytes the effect of temperature is more evident when low values of voltage and low concentrations of electrolyte were used. Films obtained with H_3PO_4 at 0 °C showed dense morphologies with undefined shapes. Anodization with HNO_3 at a low voltage (1 V) and a low temperature (0 °C) resulted in smaller sizes compared to those produced at 10 °C with a small increase of the amount of nanostructures per unit area. With HCl, low temperature (0 °C) induced the formation of denser nanostructures.

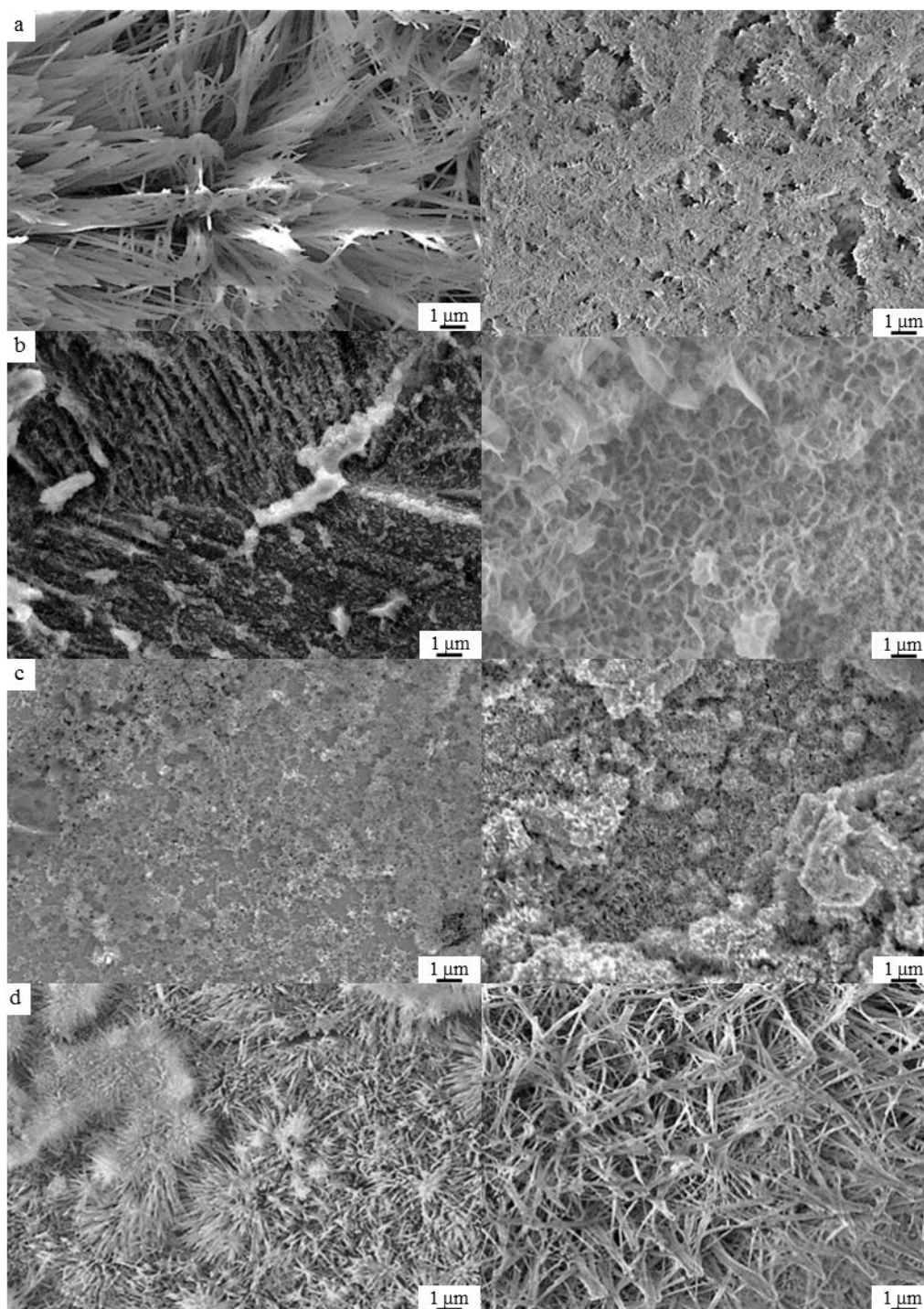


Figure 4.7 FESEM micrographs of morphologies obtained at 10 °C, for 1 hour, with different electrolytes at two different voltages 1 V (left) and 40 V (right): a) KHCO_3 (0.1M); b) HCl (0.1M); c) NaOH (0.1M); d) KHCO_3 (1M).

Nanostructures produced with $\text{C}_2\text{H}_2\text{O}_4$ (1 V, 40 V) and with NaOH at 1 V were not affected by changes in temperature. However, at 40 V the reduction of temperature limits the formation of nanostructures. Since the solvent used in anodization with KHCO_3 was water instead of ethanol, nanostructures obtained with this salt were more susceptible to changes in temperature: films obtained at 0 °C with KHCO_3 and at 1 V

displayed thicker configurations of nanowires than those produced at 10 °C. For this electrolyte, anodization at high voltage, high temperature and long periods of time resulted in complete dissolution of the Zn substrate, this suggests that, at these conditions, the etching process of the Zn (Equation 4.4) predominates.

From Figure 4.8, it can be observed that by increasing temperature, the diagram of species of Zn(II) shifts to the left direction (toward to lower pH) [239]. Therefore, at higher temperatures, Zn(OH)_2 in a solid form is more likely to be present at low pH and at higher concentrations of Zn. Increasing the temperature during the production of the ZnO-NFs, might also have an effect on mechanical properties such as micro-hardness and wear resistance [190].

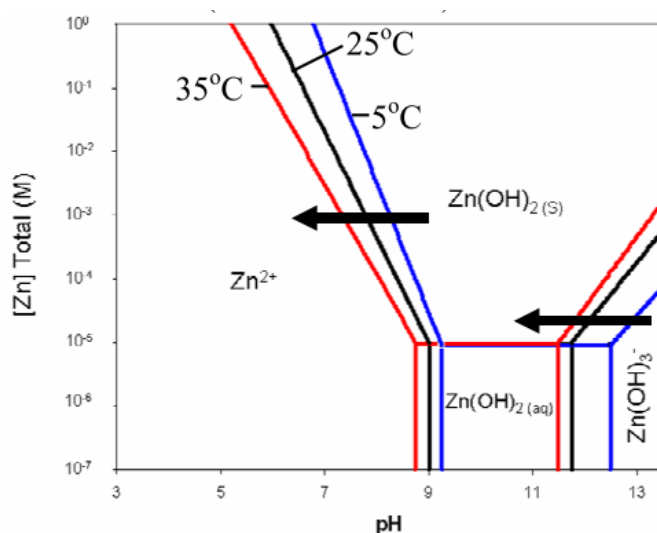


Figure 4.8 Speciation diagram of dominant zinc species as a function of pH, zinc concentration and temperature [242]

4.4.4 Effect of anodization time on film morphology

The effect of time during anodization varied with the initial morphology of the nanostructure (Figure 4.9). In general, nanostructures formed over a longer time period tend to be denser with more nanostructures per unit of area. Nanostructures that grow in one direction, like the nanowires shown in Figure 4.9-c (left), seem to be longer when produced for longer time (Figure 4.9-c (right)). On the other hand, nanostructures that grow in two directions, similar to the ones shown in Figure 4.9-a (left), appear to be thicker (Figure 4.9-a (right)). Similar to high voltages, longer times contribute to the formation of interpenetrated structures (Figure 4.9-b (left) and 4.9-d (left)) due to the

formation of longer nanostructures that tend to tilt. This phenomena occurs in particular at high concentrations where there are more soluble Zn(II) ions available for the formation and precipitation of ZnO as discussed earlier.

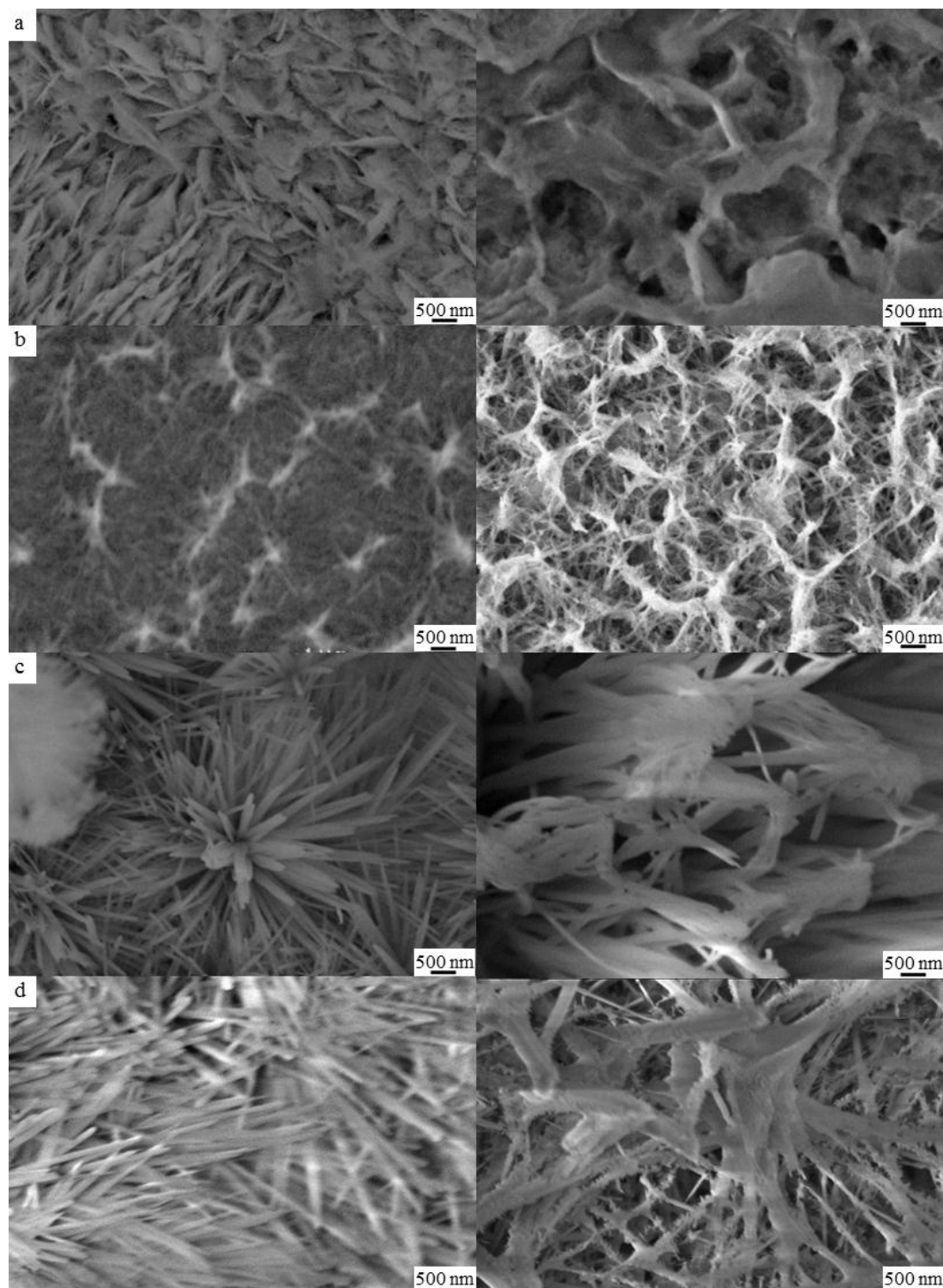


Figure 4.9 SEM micrographs of morphologies obtained at 10 °C and over two different time periods: 1 minutes (left) and 60 minute (right): a) HCl (1 M, 1 V); b) H₂C₂O₄ (0.1 M, 1 V); c) KHCO₃ (0.1 M, 1 V); d) KHCO₃ (1 M, 40 V)

4.4.5 Nanostructures Sizes

As it has been discussed, anodization conditions have an effect on the final morphology of the ZnO-NFs, in particular on the configuration of the ZnO nanostructures over the Zn foil surface. The study of nanostructures supported on a substrate limits the observation of individual nanostructures and therefore important characteristics such as particle size are difficult to determine. In order to evaluate the effect of anodization conditions on the particle size itself, nanowires obtained with KHCO_3 applying different voltages and varying anodization times were collected and examined by TEM.

During the TEM analysis, nanowires obtained by anodization without any post treatment showed instability of the ZnO layer. Once the wires were exposed to the beam, the surface started to react as it can be observed in Figure 4.10. The radiation damage during TEM and SEM analysis has been discussed in the literature [246]. It was not possible to establish either the reason of these instabilities or the type of damage caused by the beam on the ZnO nanowires. It is speculated that a potential conversion from $\text{Zn}(\text{OH})_2$ to ZnO might occur due to the thermal heating from the beam's energy. In order to make the nanowires more stable, before the nanowires were removed from the Zn substrate, all the ZnO-NFs were exposed to a thermal post-treatment at 350 °C with a rate of temperature increase of 1 °C/min for one hour as discussed in section 3.1.4. The diameters of the wires measured were used to obtain a diameter size distribution. An extensive study of the effect of post-annealing on the nanoparticles is covered in section 4.10.

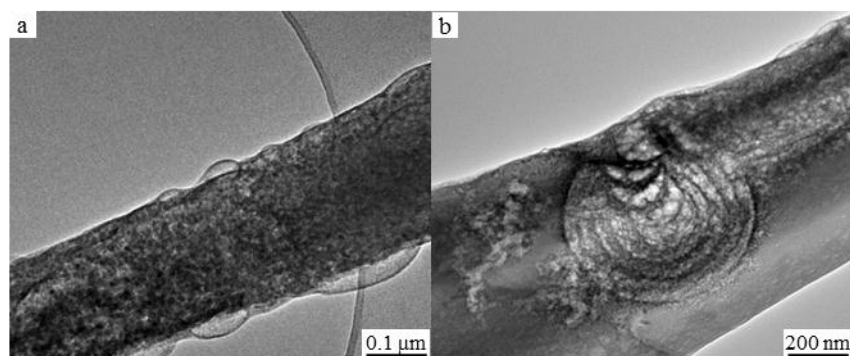


Figure 4.10 TEM micrographs showing beam damage over a ZnO nanowire

The size distribution analysis (Figure 4.11) revealed that time and applied voltages during anodization do not have a significant effect on the diameter of the individual nanowires. Although small differences in the diameters were observed, all analysed samples displayed comparable size distribution and the range of nanorods diameter was similar.

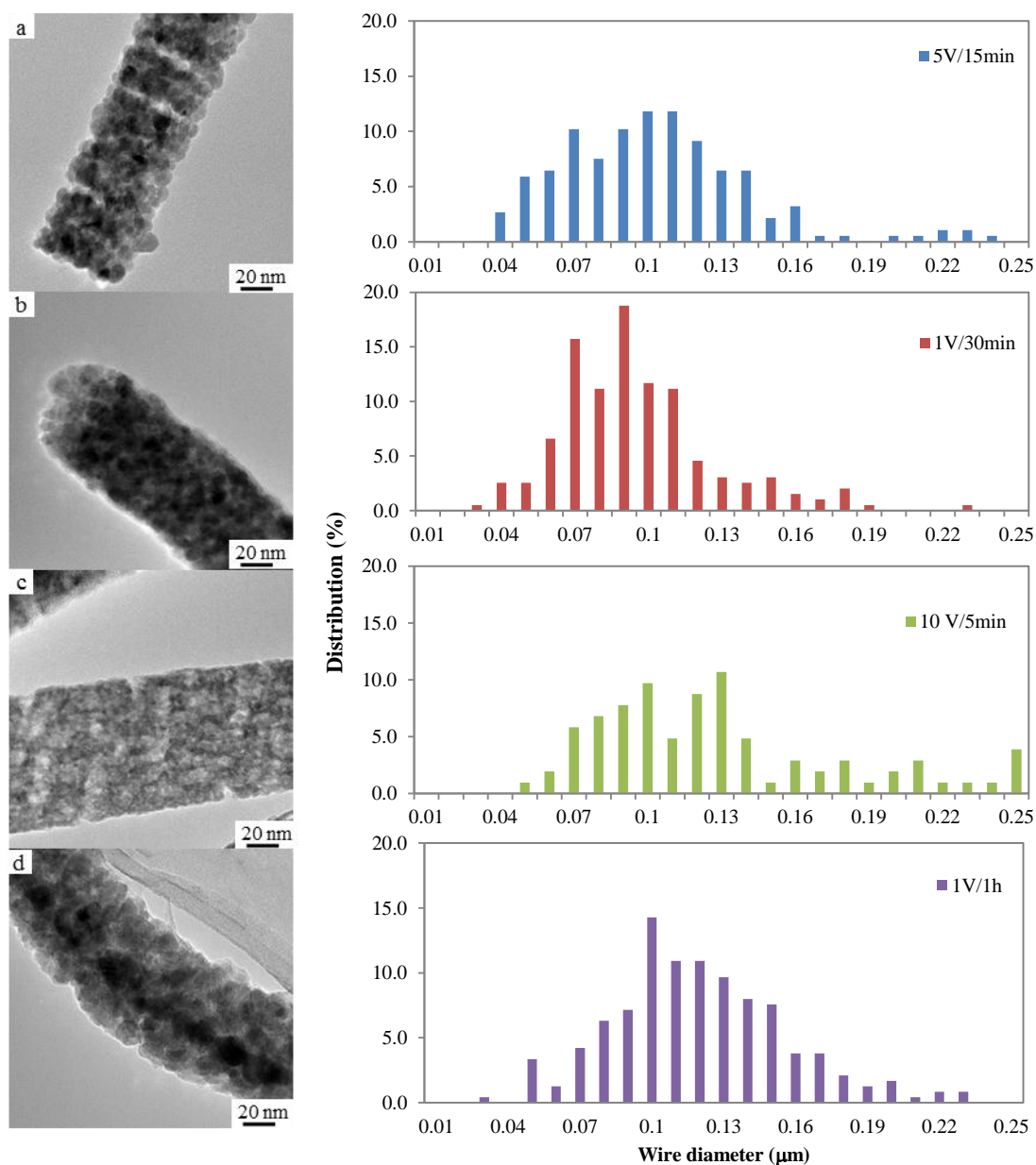


Figure 4.11 FESEM micrographs (left) and wire diameter distribution (right) of ZnO-NFs obtained with KHCO_3 (0.1M) : a) (5 V, 5 min); b) (12 V, 30 min); c) (10 V, 5 min); d) (1 V, 1 hour)

4.5 Wetting Behaviour

Although the compositional analysis of the ZnO-NFs showed slight differences between ZnO-NFs produced at different conditions, the main composition found was a combination of zinc and oxygen for all samples. Therefore, for the wettability analysis, it was assumed that surfaces of each film were chemically homogeneous. The ZnO-NFs obtained by anodization without post-treatment showed a wide range of static effective contact angles (SEC angles) from 20° to 157° (error $\pm 2^\circ$).

At ambient conditions, ZnO is a non-hydrolytic material with a good chemical stability and hydrophobic behaviour with static contact angles of 110° for smooth ZnO surfaces [247]. ZnO-NFs that displayed SEC angles lower than 110°, in particular those with hydrophilic surfaces, might contain considerable amounts of Zn(OH)₂ which can form ligands with the water molecules increasing hydrophilicity [248]. These results emphasize the importance of a thermal post-treatment to guarantee a full ZnO conversion.

The highest SEC angle values, (with a maximum of $152^\circ \pm 2^\circ$ and a minimum of $125^\circ \pm 2^\circ$), were found for nanorods and nanowires produced with KHCO₃. It appears that nanorod-like structures are likely to display hydrophobic and super-hydrophobic surfaces as it has been reported in other studies where these nanostructures were produced by different methods [249]. SEC angles higher than 120° were also obtained with other electrolytes at certain conditions, i.e. HCl [0.1M] and [1M] at 10 °C, 1h, 40V and 1V; HNO₃ [0.1M] and [1M] at 10 °C; H₃PO₄ [0.1M] and [1M] at 0 °C, 1h and 40V; 1min and 1V and NaOH [0.1M] at 40V, 10 °C and 0 °C. For hydrophobic and super-hydrophobic ZnO-NFs, differences on the SEC angles were produced by two main factors: the morphology of the ZnO-NFs (usually high surface aspect ratio) and the ZnO surface energy (typically low surface energies) [250].

For comparative analysis and given the large variety of structures of the ZnO films produced, their wetting behaviour will be analysed using the Cassie-Baxter and Wenzel models [251], [252] (see section 3.2.2). As shown in Figure 4.12, dense and vertically aligned nanostructures with a high aspect ratio, such as nanowires and nanorods obtained with KHCO₃, result in high SEC angles. For that configuration, it is assumed that the liquid that flows through interstices is minimal, trapping more air between the nanostructures and forming a solid-air-liquid interface.

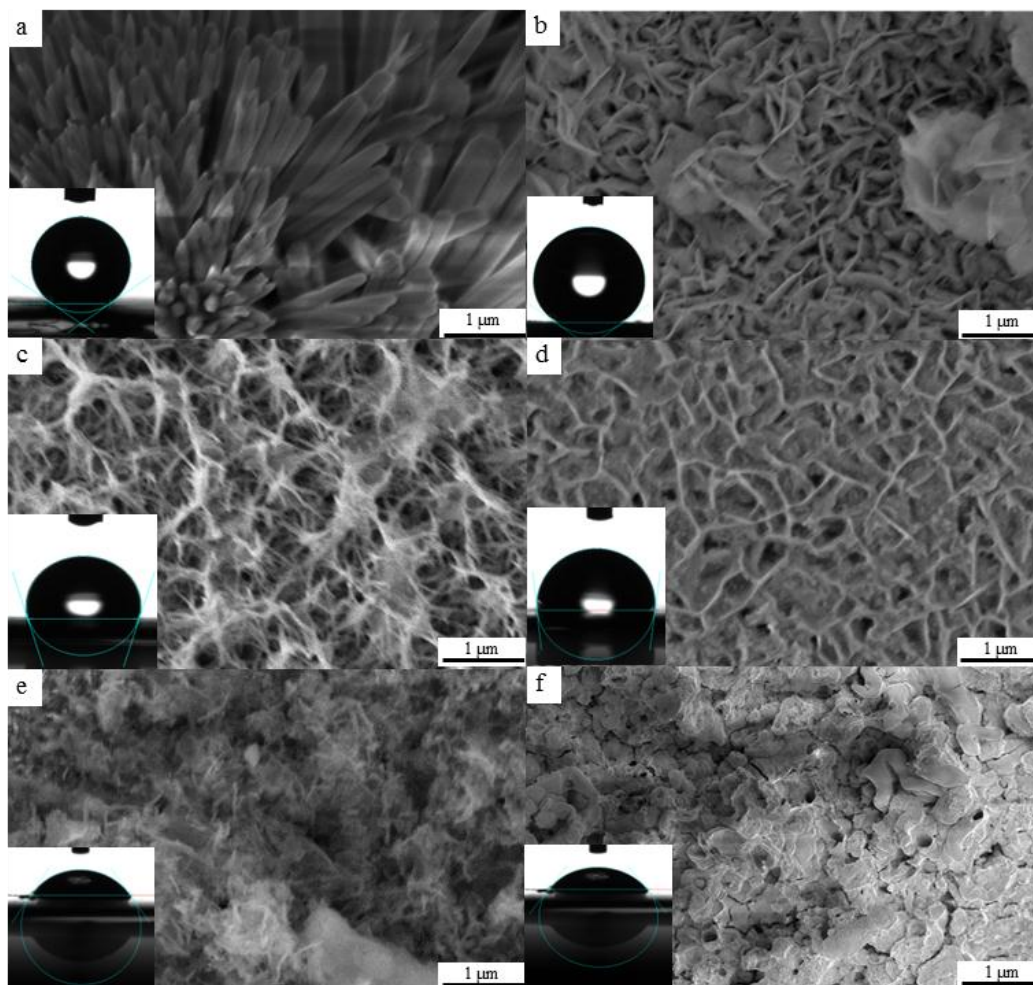


Figure 4.12 SEM micrographs of morphologies obtained at 10 °C and over two different time periods: 1 minutes (left) and 60 minute (right): a) HCl (1 M, 1 V); b) H₂C₂O₄ (0.1 M, 1 V); c) KHCO₃ (0.1 M, 1 V); d) KHCO₃ (1 M, 40 V)

On the other hand, less organized or less well-defined nanostructures, displayed lower SEC angles with values similar to those obtained on smooth ZnO films[181]. Within this study it was not possible to establish a difference of contact angle based on the size of the nanostructures. Similar studies of ZnO nanostructures obtained through the reaction of Zinc powder and hydrogen dioxide (H₂O₂) suggested that nanostructures displayed higher SEC angles than microstructure [247].

During the measurements of advancing and receding contact angles of ZnO-NFs with hydrophobic and super-hydrophobic surfaces, a barrier to the motion of the liquid on the contact line (Liquid – Solid interface) was observed. As a result, the observed contact angle was higher during the advancing motion (when the volume of the drop was

increased), while for receding motion (where the volume of the drop decreased) the observed contact angle was lower.

Although the Cassie-Baxter and Wenzel models fit most of the nanostructures obtained in this study, some ZnO-NFs with disorganised and unaligned structures displayed hydrophobic behaviour. Films produced with H_3PO_4 at 40 V, 0 °C for 1 hour and films produced with $\text{H}_2\text{C}_2\text{O}_4$ at 40 V for 1 hour exhibited contact angles higher than 125° despite of their irregular conformity and surface abnormalities.

During the characterisation of super-hydrophobic ZnO-NFs, sliding angle (critical angle at which a drop of water starts sliding in a tilted surface) was aimed to be measured. It has been reported that a water drop on a super-hydrophobic surface trend to slide down following a caterpillar-like rolling motion with or without slippage at the solid-liquid boundary) [253]–[256]. For ZnO nanostructures, a study conducted by Sakay *et al* [257] discussed the acceleration motion, sliding acceleration and resistance force caused during the sliding of a droplet on a tilted ZnO nanorods films. The super-hydrophobic ZnO-NFs obtained in this study, did not show the rolling motion as the water droplet never slides or drops regardless the sloped angle of the film as it is shown in Figure 4.13. Similar phenomena was also observed during the measurement of the sliding angle of super-hydrophobic ZnO nanorods [258]. In this study, the water droplet began to slide only when the surface was tilted to 70°. This behaviour was attributed to low surface free energy (which give hydrophobic properties) and high work of adhesion values.

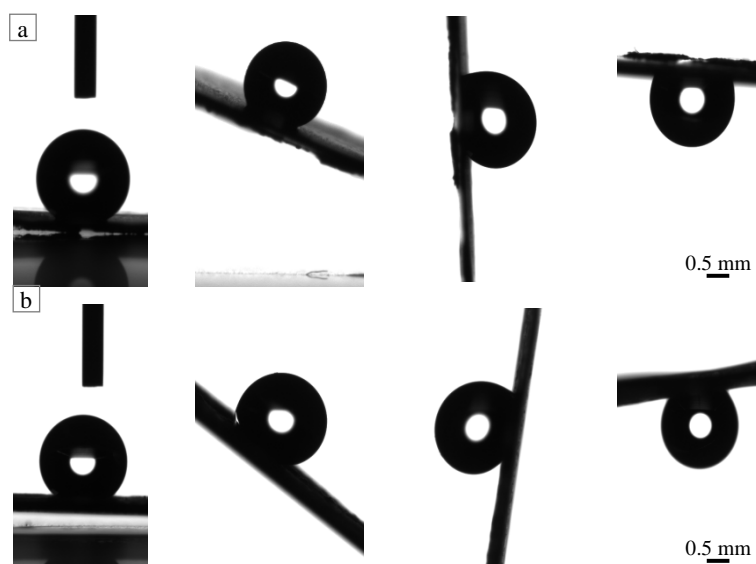
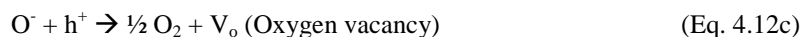


Figure 4.13 Sliding angles of super-hydrophobic ZnO-NFs

Changes in the contact angles of ZnO layers upon exposure to light have been reported before [230]. Under long term darkness conditions, the wettability of a surface can vary from hydrophilic to hydrophobic [259], [260]. Under UV light, on the other hand, there is a transition from a hydrophobic to a hydrophilic nature that occurs at different transition rates. It is assumed that subsequent to the generation of electron-hole pairs, (produced by UV irradiation of the ZnO surface), some of the holes can react with lattice oxygen forming surface oxygen vacancies. These vacancies might attract either oxygen or hydroxyl groups from water molecules. Additionally, crystalline defects are kinetically more favourable to hydroxyl adsorption as described in Equations 4.12(a-c) [230]. These changes on the ZnO surface might also affect the photocatalytic activity as discussed in Chapter 5.



ZnO-NFs that were kept in a dry box for several days maintained a constant contact angle. On the other hand, ZnO-NFs exposed to air and humidity from the environment displayed lower contact angles due to the absorption of moisture from the atmosphere [261]. The hydrophobicity of ZnO nanostructures obtained through a hydrothermal

synthesis method [257], [262]; magnetron sputter deposition [230], [247], [249], [259] and anodization [179] has been reported before, but the analysis of superhydrophobicity and comparative analysis between morphologies and wettability are still limited.

4.6 Crystallinity of ZnO-NFs

For this analysis, crystallinity has been interpreted as the content fraction of crystal phase compared to amorphous material. The crystallinity of the ZnO-NFs obtained by anodization without any post treatment was examined by XRD. XRD patterns were compared to the JCPDS XRD for ZnO and Zn. Results revealed that films contained ZnO in the crystal phase. However, it was assumed that samples also contained fraction of amorphous ZnO that are not detected by XRD. Similarly to other studies [181], [193], [194], XRD patterns revealed that the crystal phase of the ZnO-NFs consist of wurtzite-type crystals. The peaks with the strongest intensity were (101), (100) and (002); while (102), (110) and (103) peaks were not detected.

Differences in the XRD patterns imply that anodization conditions affect the crystallinity of the ZnO. Figure 4.14 displays the XRD spectra of ZnO-NFs obtained with NaOH [0.1M] at different voltages and times. Differences in the intensity of the peak at [002] and [100] indicate that the amount of crystal phase and the preferential orientation of those crystallites are different between the films. Additionally, small differences in the full width at half maximum (FWHM) suggested that the crystal size of the ZnO-NFs varied with anodization conditions.

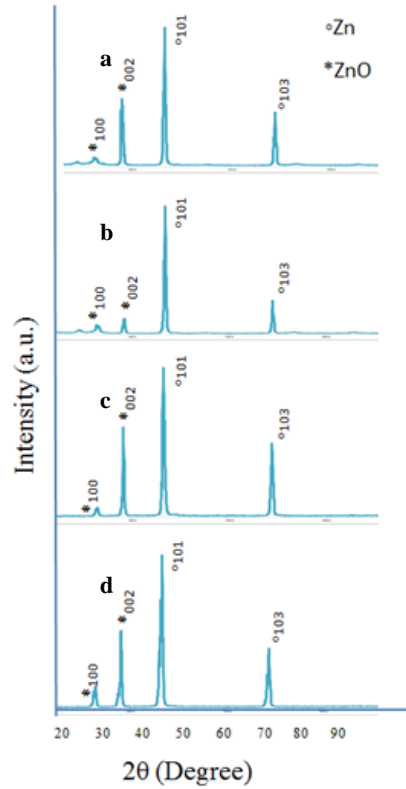


Figure 4.14 XRD spectra of films obtained with NaOH. a) [0.1M], 1V, 1 min, 10°C. b) [0.1M], 1V, 1 hour, 10°C. c) [0.1M], 40V, 1 min, 10°C. d) [0.1M], 40V, 1 hour, 10°C

The use of Scherrer equation is one of the most established ways to calculate the crystal size (D) using XRD patterns (Equation 4.13). This equation correlates the wavelength of X-ray radiation (λ), the diffraction angle (θ) and the full width at half maximum (FWHM). However, this method is only suitable to estimate ‘*the sizes of particles in the direction vertical to the corresponding lattice plane*’ and also do not include changes in the FWHM produced by distortion of the crystalline lattice [52]. Therefore, crystal size measurements were performed using TEM.

$$D = \frac{0.9\lambda}{FWHM \cdot \cos\theta} \quad (\text{Eq. 4.13})$$

Crystal size distribution obtained from the analysis of TEM images (Figure 4.15), revealed that the crystal size of nanowires varied with anodization conditions. The crystal size of samples obtained at 10 V and 1 hour was in the range of 5-10 nm, while for samples produced at 5 V for 15 minutes the range was between 9 and 16 nm. Changes in the size of the ZnO crystals obtained by anodization have also been reported

by Basu *et al* [125], [163]. In this study, the crystal size was calculated based on the XRD patterns and the Scherrer equation; crystal sizes were in the range of 2.41– 5.22 nm and were obtained by varying the concentration of the electrolyte (oxalic acid). Unlike Basu’s study, in this project different crystal sizes were obtained using the same concentration of electrolyte but varying voltage and anodization time.

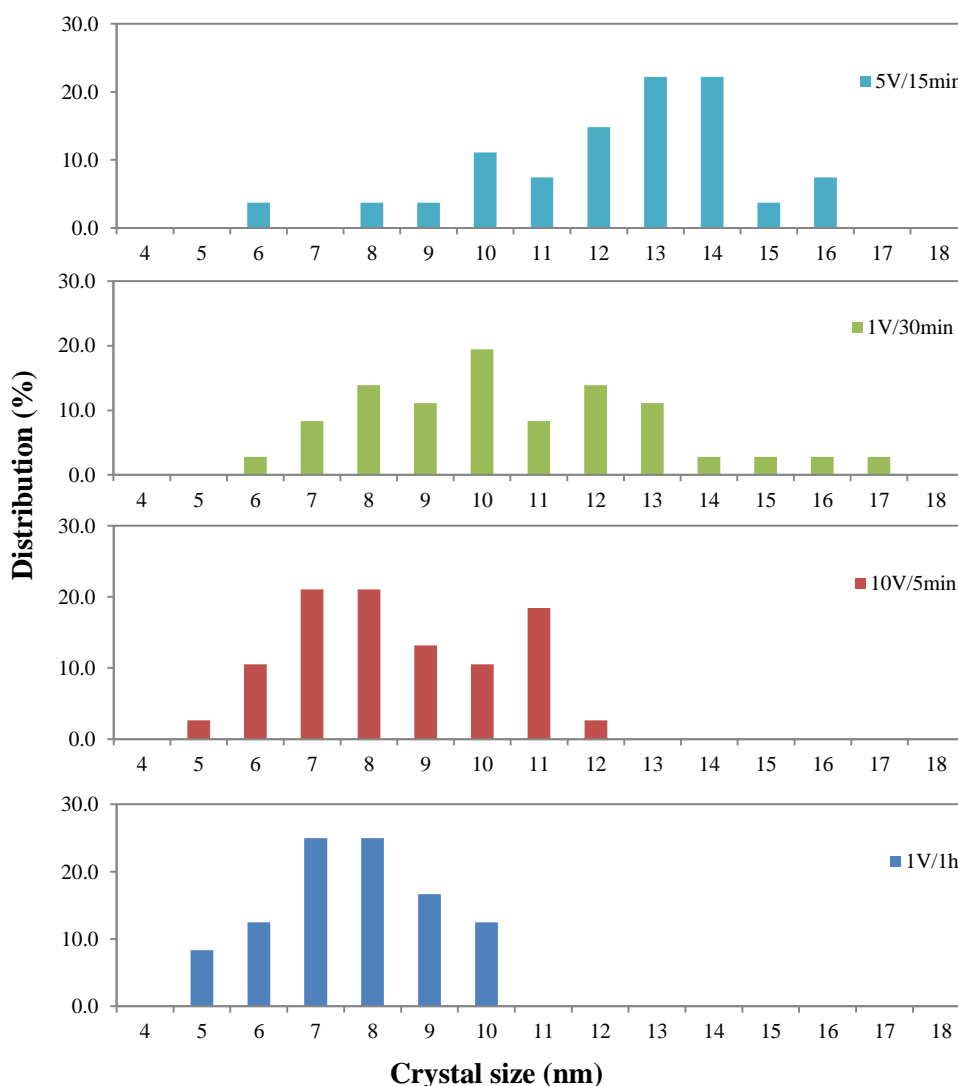


Figure 4.15 crystal size distribution of ZnO-NFs obtained with KHCO_3 (0.1M): (5 V, 5 min) (a) ; (12 V, 30 min) (b); (10 V, 5 min) (c) and (1 V, 1 hour) (d)

The growth of ZnO crystallites using different synthesis methods such as solution-based chemistry and chemical bath deposition has been extensively discussed [263], [264]. However, a systematic study of the growth of ZnO crystallites during anodization has not yet been reported in the literature.

4.7 ZnO-NFs profiles

ZnO films showed different profiles that vary from convex to concave (Figure 4.16). ZnO-NFs obtained with KHCO_3 tend to be convex, indicating that for this electrolyte the predominant process during anodization was the formation of the ZnO and $\text{Zn}(\text{OH})_2$ nanostructures. The thickest layer was about $260\ \mu\text{m}$ and it was obtained with KHCO_3 [0.1M] at 40 V, $10\ ^\circ\text{C}$, and 1 hour. On the other hand, acid electrolytes such as HCl and HNO_3 tend to form films with concave profiles. Anodization with NaOH and $\text{H}_2\text{C}_2\text{O}_4$ result mainly in the formation of ZnO-NFs with flat profiles.

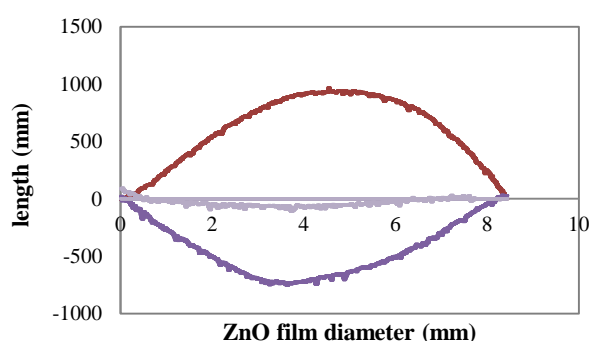


Figure 4.16 Types of ZnO films profiles: Convex profile (red line) HNO_3 (0.1M/1V/10 $^\circ\text{C}$ /1min); flat profile (lilac line) $\text{H}_2\text{C}_2\text{O}_4$ (0.1M/40V/10 $^\circ\text{C}$ /1min); concave profile (purple line) H_3PO_4 (0.1M/1V/10 $^\circ\text{C}$ /60 min).

The formation of concave profiles can be produced when, at certain conditions of anodization, the dissolution of Zn and etching process predominates over the formation of ZnO nanostructures. As a result, the high rate formation of (i) Zn^{+2} and ZnOH^+ ions (in acid media) and (ii) $[\text{Zn}(\text{OH})_4]^{2-}$; $\text{Zn}(\text{OH})_3^-$; $\text{Zn}(\text{OH})_2$ (in alkaline media), result in thinning of the zinc foil. Additionally, it was found that the growth of the nanostructures is not homogeneous along the Zn foil surface, indicating that the formation of the ZnO layer can be affected by external factors such as stirring. For ZnO-NF with convex profiles, on the other hand, the predominant process is the formation of nanostructures, while for flat profiles both mechanisms (formation and dissolution) occur at similar rates.

4.8 ZnO-NFs band gap energy

Band gap was measured through UV-Vis absorption spectroscopy. Absorbance and band gap energies were plotted and the differential of absorbance was calculated as

shown in Figure 4.17. The energy absorbed for each film appears to be affected by the morphology and the thickness of the ZnO-NFs. Higher values of absorbance were found in the ZnO-NFs obtained with Na(OH) and with HNO₃; both films showed low surface density with flower-like morphology (see Figure 4.5-b and 4.5-e). The lowest absorbance intensity was displayed by nanowire morphologies produced with KHCO₃, which were also the thickest films in this study (Figure 4.5-f).

In addition to the scattering of light produced by the nanostructures, slight variation of the chemical composition of the ZnO-NFs might be the responsible for the differences in absorbance intensity found in this study.

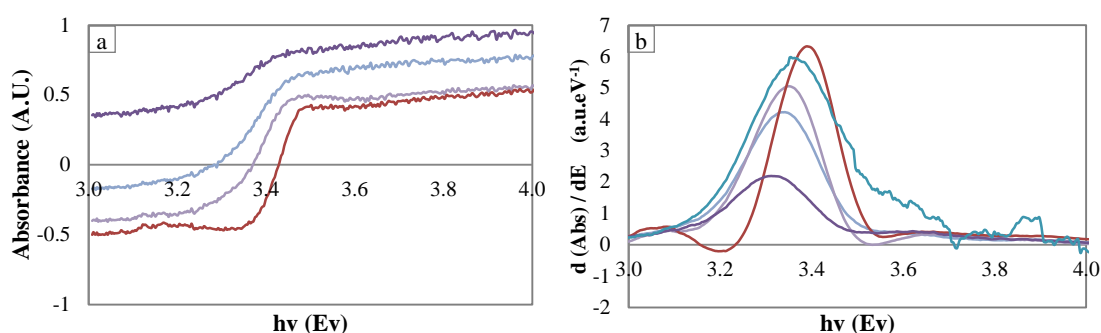


Figure 4.17 UV-visible absorbance spectra (a) and differentiated absorbance spectra (b) of ZnO films produced with NaOH [0.1M] at different experimental conditions. (Red line 40V/1min/10°C; light purple line 40V/1min/0°C; blue line 40V/1h/0°C; dark purple line 40V/1h/10°C).

Although band gap energy is a material and crystal structure property,[125] it has also been suggested that morphology factors such as nanostructuration [265]–[267] and particle size [268] modify the band gap emission. While bulk ZnO exhibits a band gap energy of 3.37 eV, films obtained in this study displayed band gap energies in a wider range from 3.27 to 3.50 eV. The largest band gap energies were found on films with the largest and denser nanostructures obtained with H₂C₂O₄ and KHCO₃. Small nanostructures tend to have lower band gap energies with some exceptions. Similar to the absorbance intensity, differences in band gap values can be produced by variation on morphology and composition of the ZnO-NFs.

Changes in band gap energies produced by differences in morphology not only involve the nanostructuration of the ZnO but also the potential scattering of light produced by the different shapes of the ZnO-NFs. Additionally, crystalline defects such as oxygen

vacancies have been recognised to have an enhancement in the band gap emission [269], [270]. In other studies, the variation on band gap in ZnO films have been attributed to the quantum confinement effect [163]. However, given the exciton Bohr radius for ZnO particles (2.34 nm) [271] and the nanostructure size of the ZnO-NFs (larger than 20 nm), the quantum effect is likely not to occur in this case.

4.9 Thermal Post-treatment

Results shown up to now refer to ZnO-NFs without any post-treatment. In this section, the results of ZnO-NFs exposed to thermal post-treatment will be discussed. ZnO-NFs were also exposed to alternative non-thermal post-treatments and these results will be discussed in Chapter 5. For the thermal post-treatment or post-annealing, ZnO-NFs produced with KHCO_3 under similar anodization conditions were exposed to different temperatures for different times. A slow heating and cooling rate was maintained (1 °C/min) to minimize stress and strain on the nanostructures. Samples were analysed before and after the post-treatment in order to identify changes produced during this process.

TEM micrographs (Figure 4.18) of single nanowires show changes in the crystallinity of the material. Nanowires that were not exposed to thermal post-treatment displayed a smooth surface (Figure 4.18-a) while the surface of post-annealed wires showed superficial and interstitial cracks (Figure 4.18-b) that affect the surface roughness of the wires. It is assumed that post-annealing affected the crystallinity of the ZnO-NFs in four ways [217]: (i) Some of the Zn(OH)_2 formed during anodization turned into ZnO; (ii) amorphous ZnO turned into wurtzite structures increasing the total amount of crystallites in the films; (iii) initial ZnO crystallites formed during anodization became larger and (iv) crystal defects decreased.

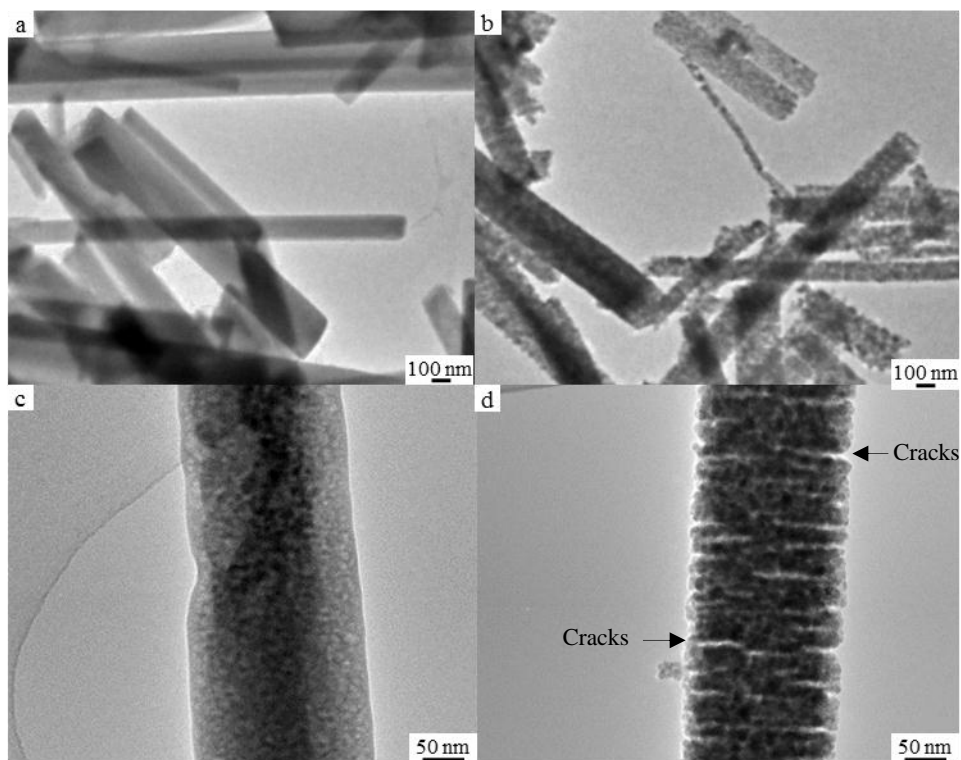


Figure 4.18 TEM micrographs of nanowires before (a) and after (b) post-annealing at 350 °C, 1h, 1 °C/min and their magnification (bottom)

At high temperature, the high diffuse activation energy of the ZnO atoms allow them to be relocated in the crystal lattice, thus grains with lower surface energy fuse into larger grains [272]. It is also been suggested that during the crystal growth, small crystallites merge together in a process called “coalescence” and amplify the boundaries of the grains making larger crystallites. Additionally, it has been observed that due to post-annealing, an increase in porosity and surface roughness occur [217].

XRD patterns confirm the changes in crystallinity produced when the ZnO-NFs are exposed to post-annealing treatment at different temperatures (Figure 4.19) and different time periods (4.20). Changes in the intensity of the XRD peaks revealed that the material became more crystalline once it was exposed to the thermal post-treatment; additionally, the peaks become broader indicating an increase in the grain size. Due to the overlap of the (101) peak with the (002) Zn peak it was difficult to determine the preferential orientation of the crystallites. However, it was observed that regardless of the time or temperature of the post-annealing, once the material became crystalline, the orientation of the structure remained constant maintaining a constant peak ratio. In addition, a small shift of the position of the diffraction peaks was observed indicating

that the post-annealing conditions produced a minimal tensile stress on the ZnO wires [272].

As shown in Figure 4.19, samples post-treated at 300 °C and 350 °C displayed an increase in the intensity of the (100) and (002) peaks. The similarity between the diffraction patterns obtained at 300 °C and 350 °C indicates that any post-annealing beyond 300 °C will result in similar changes in the crystallinity of the material. Post-treatment of ZnO-NFs obtained by anodization of Zn are limited to a maximum of 350 °C due to the melting point of the zinc substrate (400 °C).

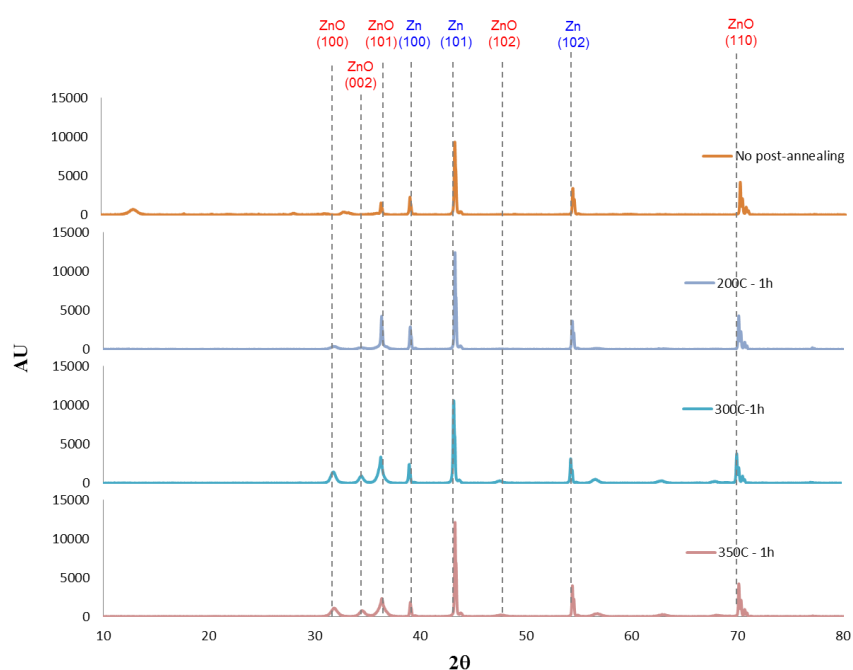


Figure 4.19 XRD of ZnO films obtained with KHCO_3 [0.05M], 1V, 10C, 1h and post-annealing under different temperatures

It is important to mention that the range of temperatures used during the post-treatment of ZnO-NFs is narrow and therefore no representative changes in the XRD peaks were observed. However, similar studies on thermal post-treatment on ZnO have reported large changes in crystal size and surface roughness [217]. Additionally, the magnitude and direction of the tensile and compress stress of the ZnO crystal lattice is significant only at higher temperatures (> 600 °C).

Post-annealing time appears to produce more notable changes in the crystallinity of ZnO-NFs compared to the temperature. From Figure 4.20 it can be observed that the intensity of the diffraction peaks for the (100), (002) and (101) planes increase with time. Reductions in the width full half maximum (WFHM) distance suggest that the sizes of the grains increase in the post-treated samples. TEM images were used to calculate the crystal size distribution and to analyse the effect of the post-treatment in the crystal size.

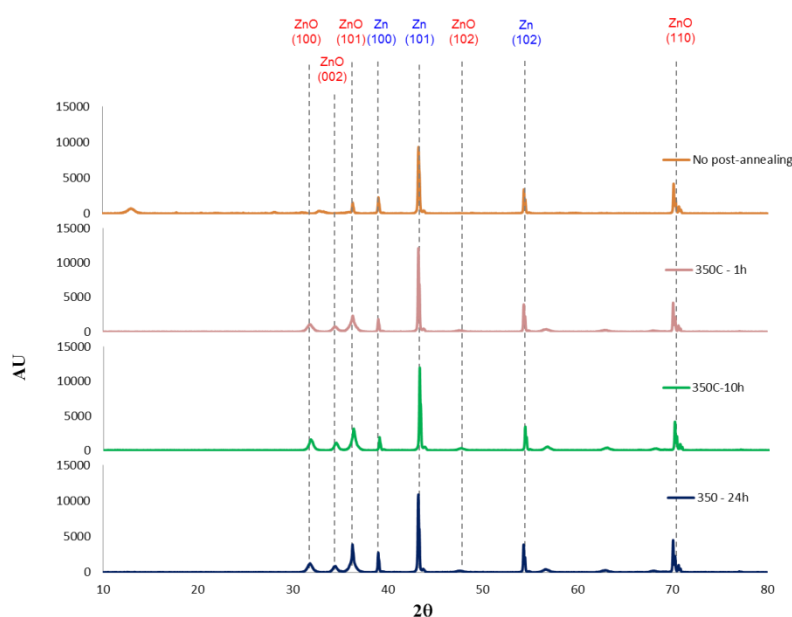


Figure 4.20 XRD of ZnO films obtained with KHCO_3 [0.05M], 1V, 10C, 1h exposed to different times of post-annealing.

The crystal size distribution of ZnO-NFs post-annealed at 350 °C for different periods of time show that crystal size is affected by the post-annealing time. Samples exposed to 18 hour and 36 hour of post-annealing displayed bigger crystallites compared to those exposed for only 1 hour (Figure 4.21 b-c). The crystal size distribution revealed a doubling of the initial crystal size going from a range of 5-10 nm to a range of 10-20 nm (Figure 4.21-a). Although the range of crystal size was similar for the films exposed to 18 and 36 hours, the distribution of crystal size in this range were slightly different. Films exposed to 18 hours post-treatment displayed higher number of crystal in the range of 15 and 16 nm, while ZnO-NF post-annealed for 36 hours had the higher number of crystal with sizes of 12, 14 and 16 nm.

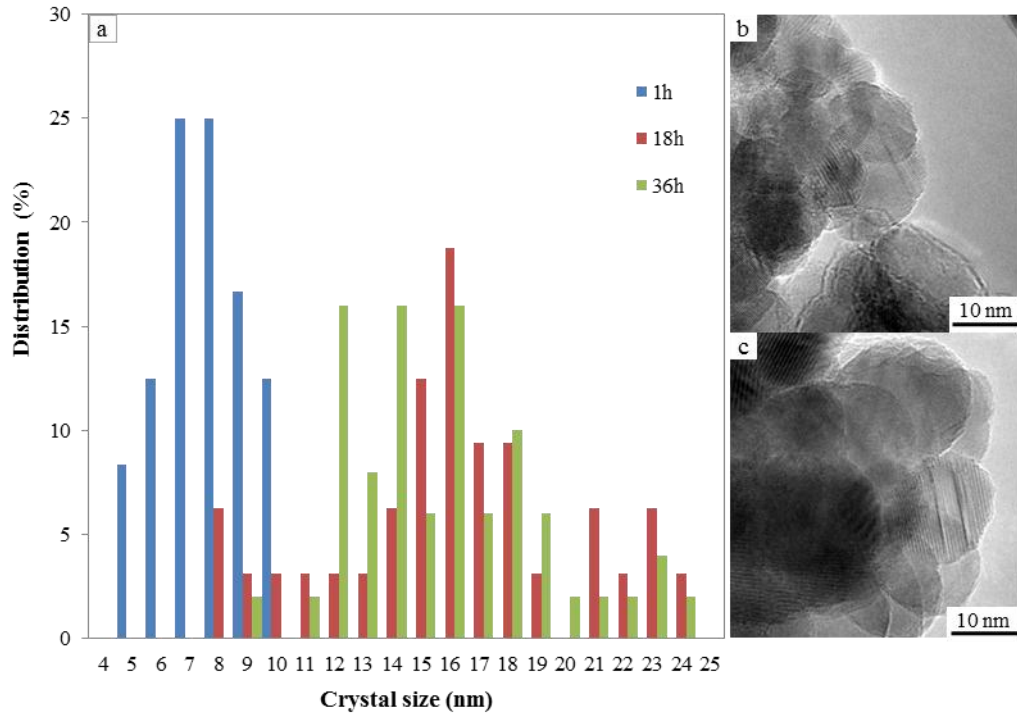


Figure 4.21 Crystal size distribution (a) and TEM micrographs of (b-c) crystals of samples post-annealed at 1h and 18h respectively

Since post-annealing led to an increase the crystal size and to a change in the surface of the nanowires (cracks) (see Figure 4.18), similar analysis of the effect of post-annealing in the morphology of the ZnO-NFs was carried out using FESEM, TEM and wire size distribution analysis of ZnO-NFs samples post-annealed at 350 °C for different periods of time. Figure 4.22 displays FESEM micrographs of the surface of ZnO-NFs before and after post-annealing. Results revealed that changes produced at crystal scale are not reflected on the morphology of the ZnO-NFs where the initial configuration of the nanowires is preserved.

Unlike crystal size, post-annealing treatment had a minimal effect on the size of the nanostructures. Different post-annealing times resulted in obtaining a similar nanowire size distribution (Figure 4.23) with a range of sizes between 50 and 140 μm . Nanowires that were exposed to 1 hour post annealing have similar diameter to those exposed to 18 hours and 36 hours.

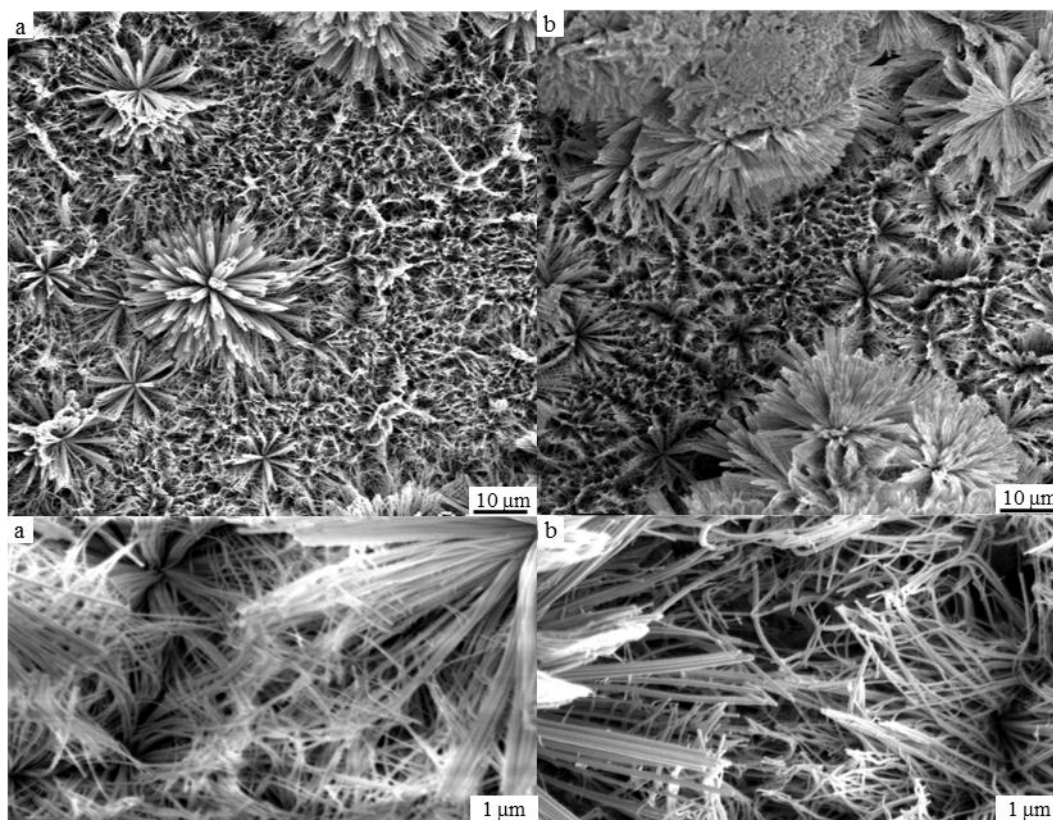


Figure 4.22 FESEM micrographs of ZnO-NFs ($\text{KHCO}_3/1\text{V}/1\text{h}/10^\circ\text{C}$) (a) before and (b) after post-annealing at 300°C for 1 hour with a rate temperature of $1^\circ\text{C}/\text{min}$.

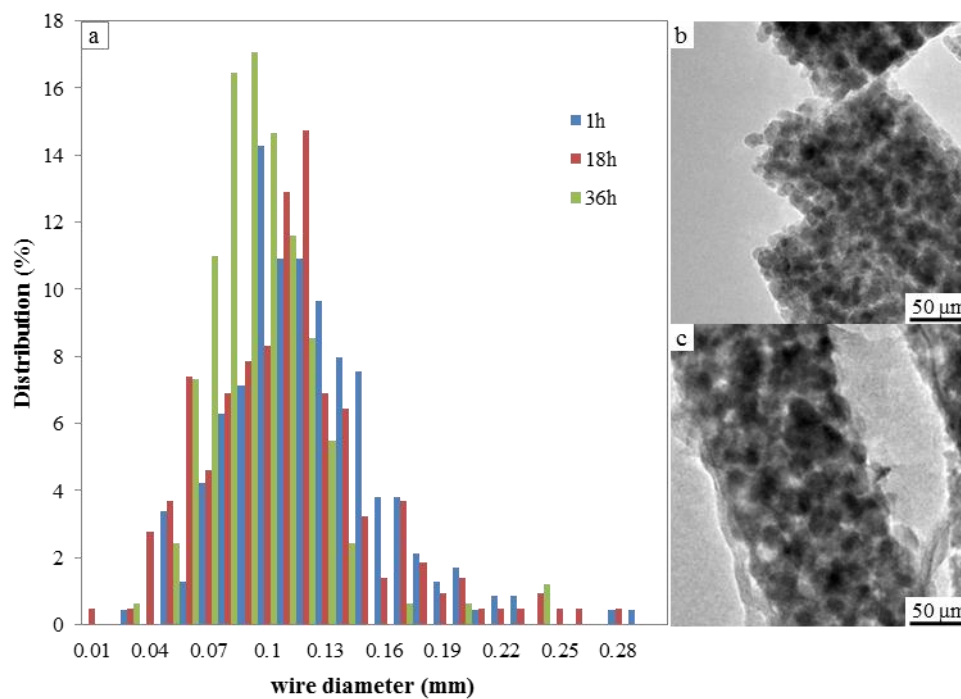


Figure 4.23 TEM micrographs of ZnO nanostructures; (b-c) wire of samples post-annealed at 1h and 18h respectively and (a) its crystal size distribution.

4.10 Rational design guidelines for controlled formation of ZnO nanostructures via anodization

As previously mentioned, anodization is a multi-parameter process controlled mainly by the type and concentration (C) of the electrolyte, the applied voltage (V) across the cell, the temperature (T) of the electrochemical bath and the anodization time (t). For the simultaneous analysis of these parameters and their effect in some properties of the ZnO-NFs, data collected in this project and from previous published studies were combined and analysed [212]. The main aim of this parametric analysis was to elucidate which combination of C , V , T and t will give a certain nanostructure. Temperature was excluded as a parameter from the analysis due to the lack of data from literature. Large numbers of publications have reported this parameter only as ‘room temperature’ rather than quantify it. Since different electrolytes at different concentrations have been used and reported for anodization of Zn, the pH of those solutions has been measured to offer a common analysis framework.

For the morphology analysis, ZnO nanostructures developed in this work and those already published in the literature have been classified in six groups. Additionally, each type of surface configuration or nanostructure was symbolized with a dot and a colour as follows:

- smooth – no nanostructure (dark blue dots)
- pitting – corrosion (light blue dots)
- aligned arrays of 1D nanostructures– nanowires, nanoneedles, nanorods (green blue dots)
- 2D – nanoplatelets, nanoflakes (orange blue dots)
- 3D arrangement – interpenetrated nanostructures (red blue dots)

For the wetting behaviour analysis, results of contact angles of the ZnO films obtained were classified into three large groups:

- Hydrophilic surface (contact angle $< 90^\circ$)
- Hydrophobic surface ($90^\circ \leq$ contact angle $\leq 120^\circ$)
- Super-hydrophobic surface (contact angle $> 120^\circ$)

For the profile analysis, ZnO films were classified as follows:

- ZnO layer predominantly concave
- ZnO layer predominantly flat
- ZnO layer predominantly convex

Figure 4.24 displays a 3D plot with morphologies of nanostructures (symbolized with dots) that were obtained with different electrolytes at different concentrations and, therefore, different pH. To simplify the analysis without omitting a third variable, Figure 4.24-a was rotated (Figure 4.24-b and 4.24-c) to better visualise the distribution of the different morphologies for different pHs, voltages and times.

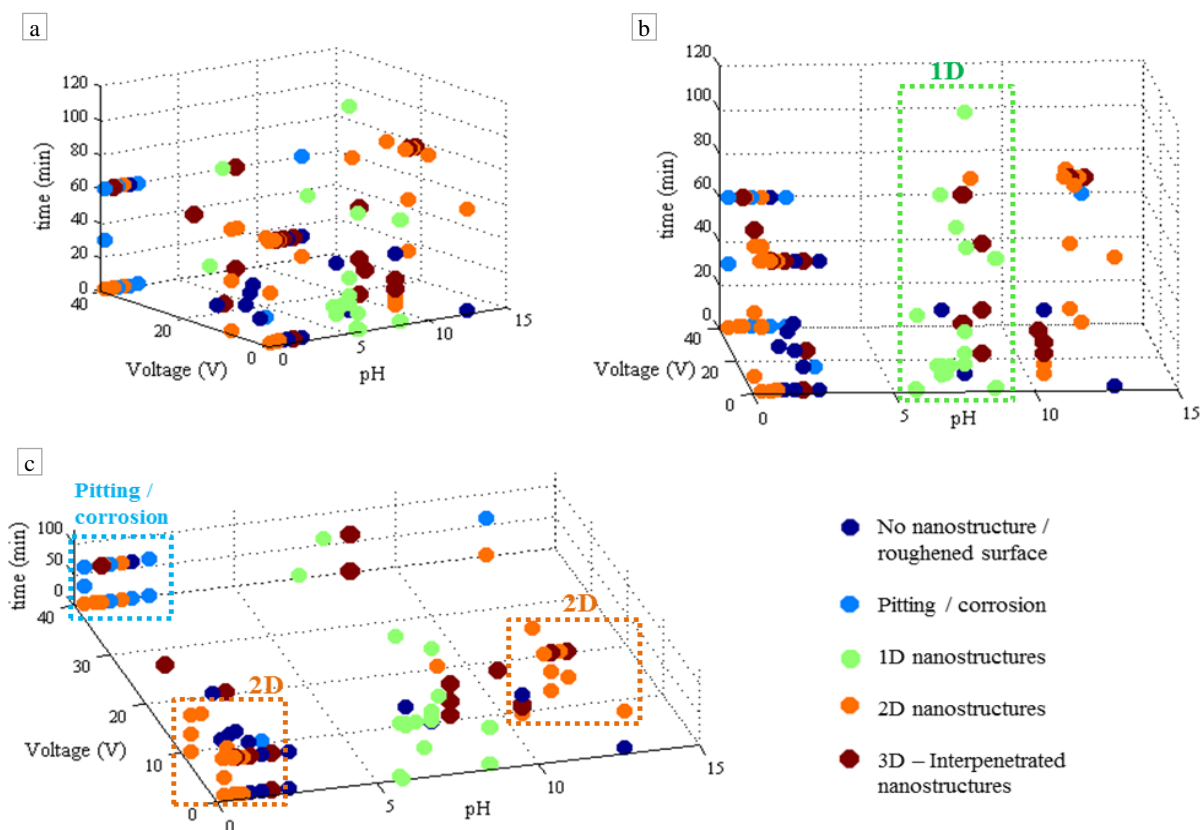


Figure 4.24 3D plot of the Morphology of ZnO-NFs obtained by anodization at different experimental conditions

From Figure 4.24-b and 4.24-c it is evident that the type of the electrolyte (analysed by pH) has the strongest influence over the morphology of nanostructures obtained by anodization. 2D nanostructures (orange dots) were obtained at low and high pH, while 1D nanostructures such as nanowires and nanorods (green dots) were obtained exclusively at neutral pH. Although these morphologies (1D and 2D) have been obtained with a variety of voltages and anodization times, most of the studies have used voltages lower than 20 V and periods of time shorter than 1 hour. Low pH and low voltage leads to the presence of featureless surfaces regardless of the reaction time (dark

blue dots). Pitting and corrosion (light blue dots) are more common at low pH and high voltage. Since 3D interpenetrated nanostructures (red dots) seems to be formed for the extensive growing of 1D and 2D nanostructures over time, they were mainly found in long term reactions regardless of the pH.

The parametric analysis of wetting behaviour was carried out using mirror-like plots with different dot colours symbolizing different wetting behaviour of the ZnO-NFs (Figure 4.25). With this type of plots it is possible to visualize eight possible combinations of experimental conditions, for instance, a simultaneous comparison of the effect of voltage, pH, and temperature (Figure 4.25-a); or voltage, pH, and time (Figure 4.25-b) can be made. Results revealed that, for all investigated temperatures, super-hydrophobic surfaces (red dots) are produced mainly at low pH and high voltage (40 V).

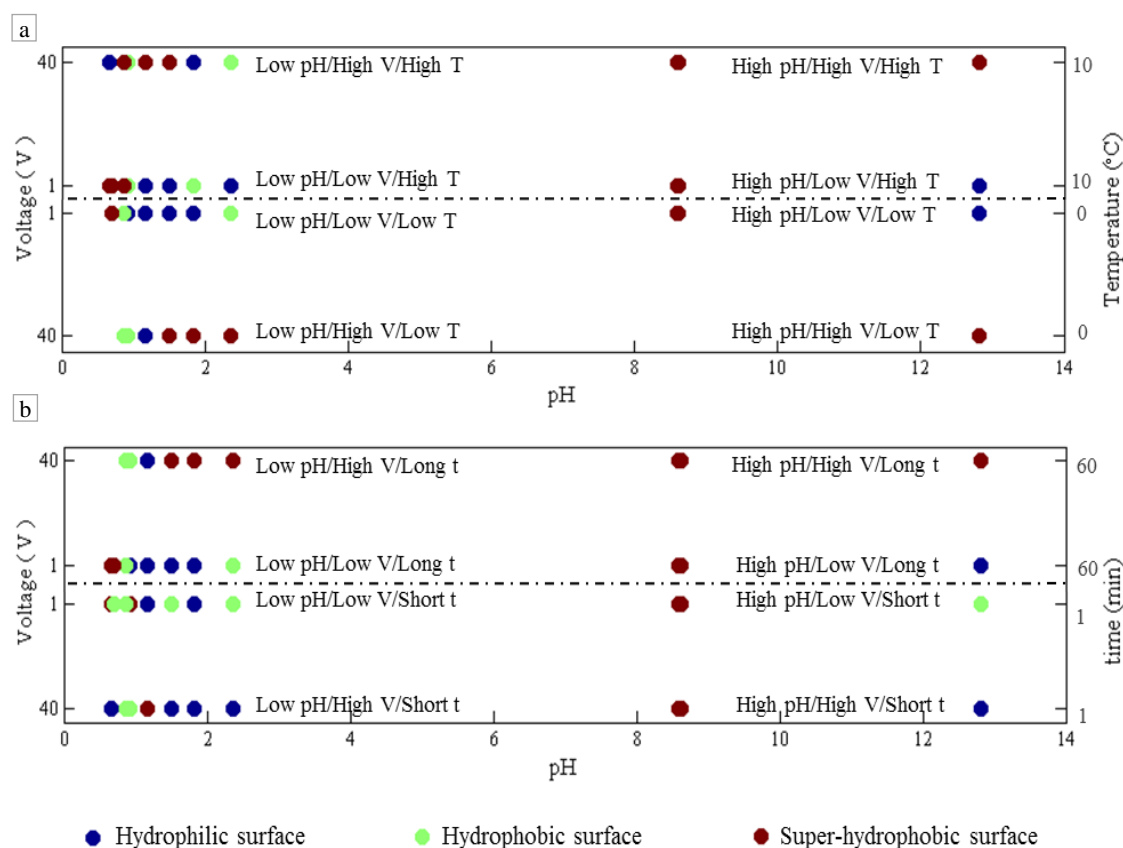


Figure 4.25 Mirror-like plot of wetting behaviour of ZnO-NFs obtained by anodization at different experimental conditions

Super-hydrophobic surfaces also predominate at neutral pH regardless of the voltage, time or temperature. It is important to mention that the morphologies that predominate at this pH are aligned 1D nanostructures which follow the Cassie-Baxter and Wenzel models for hydrophobic and super hydrophobic surfaces respectively as discussed in section 4.5. On the other hand, hydrophilic surfaces are produced mainly at low pH and low voltage (1 V). Similarities between dots from the lower middle row (Low V/High T) with the upper middle row of dots (Low V/Low T), revealed that, at low voltage (1 V), the wetting behaviour of the ZnO-NFs is not affected either by time or by temperature. High voltage and longer times lead to super-hydrophobic surfaces being formed (Figure 4.25-a, top row).

Figure 4.26 shows the mirror-like plot of profiles obtained in this study at two different temperatures (Figure 4.26-a) and two anodization times (Figure 4.26-b). No clear dependence of the profiles on voltage, temperature or time was found. Convex and flat profiles were more common at neutral and at high pH; while at low pH concave profiles predominate, in particular at low voltage (1 V).

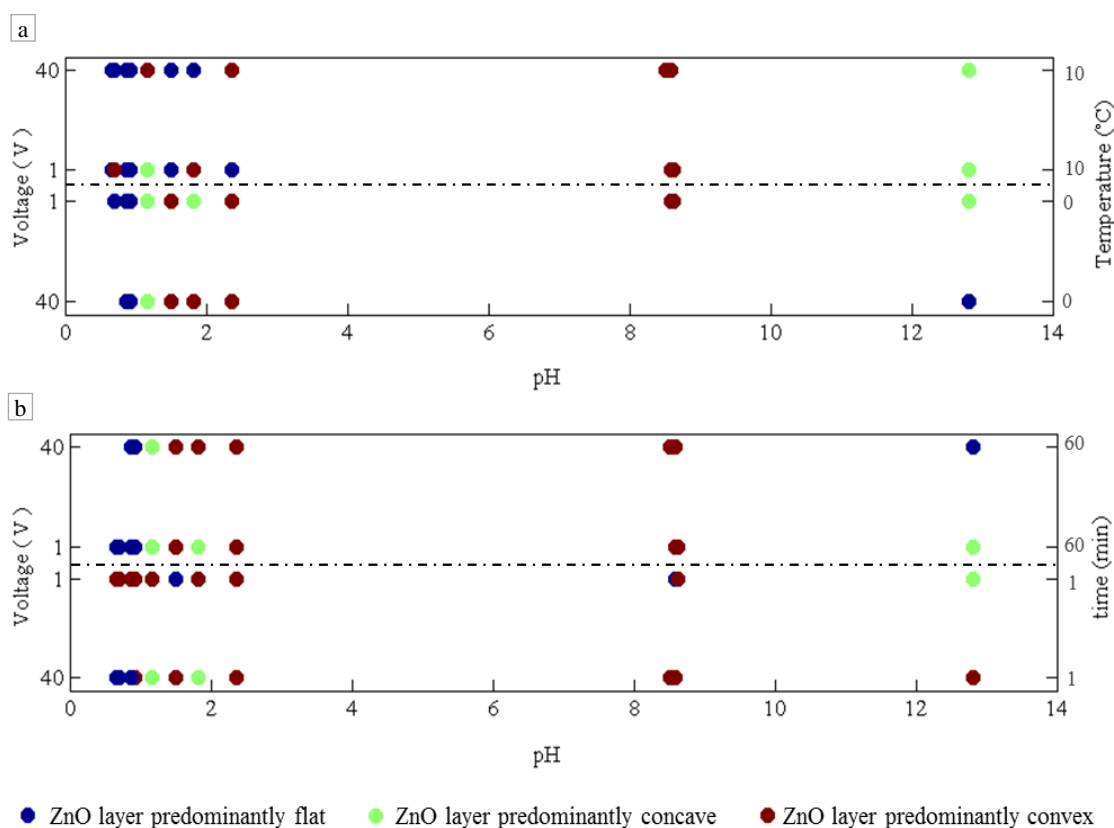


Figure 4.26 Mirror-like plots of the Surface profile analysis of ZnO layer obtained by anodization of Zn at different experimental conditions

Based on the ZnO-NFs analysed in this study, results of the rational design guidelines were summarized in a matrix (Table 4.4). The matrix compares the different combinations of anodization conditions with the more likely morphologies that can be formed. Green areas indicate that a correlation between the experimental parameters and the morphology was produced in this study or has been reported in the literature. For instance pitting and corrosion are more likely to occur at low pH with high voltage and long reactions. “1D aligned arrays – hydrophobic” have been obtained at neutral pH with a variety of voltages and times reaction. The lack of green areas in the “1D aligned arrays – Hydrophilic” row indicate that this combination have not been reported yet. 2D arrays (hydrophilic and hydrophobic) films have been obtained mainly at low pH regardless voltage and time. 3D arrays (either hydrophilic or hydrophobic) are produced exclusively at long time anodization regardless voltage and pH.

Table 4.4 Matrix summarising the results obtained from the rational design guidelines

Anodization conditions \ Nanostructures	Low PH	Low PH	Low PH	Low PH	Neutral	Neutral	Neutral	Neutral	High PH	High PH	High PH	High PH
	Low V Short t	Low V Long t	High V Short t	High V long t	PH Low V Short t	PH Low V Long t	PH High V Short t	PH High V long t	Low V Short t	Low V Long t	High V Short t	High V long t
No nanostructure												
Pitting - corrosion												
1D aligned arrays - Hydrophobic												
1D aligned arrays - Hydrophilic												
2D arrays - Hydrophobic												
2D arrays - Hydrophilic												
3D arrays - Hydrophobic												
3D arrays - Hydrophilic												

4.11 Summary

The mechanism of the formation of ZnO-NFs was analysed based on thermodynamic speciation of Zn(II) and comparing current plots from anodization of alumina with anodization of zinc. The band gap energies, crystallinity and profiles of the ZnO-NFs were discussed. The wettability of the ZnO-NFs was correlated to the morphology using Cassie-Baxter and Wenzel models. The effect of thermal post-treatment on ZnO-NFs also was studied.

From the analysis of the morphology of the ZnO-NFs and its correlation to anodization parameters the following conclusions were found: Anodization can be controlled through the synthesis conditions. The shape of the nanostructures is determined mainly

by the type of electrolyte, while the nanostructure surface density increases with concentration, voltage and time. The time also determines the size of nanostructures, leading to the formation of 3D interpenetrated nanostructures once the nanostructures reach a certain length. The effect of temperature varies with the electrolyte, where acids at low temperatures reduce the formation of nanostructures considerably. Time and applied voltage during anodization do not have significant effects on the diameter of the individual nanowires while crystal size of nanowires varied with anodization conditions. Dense and well-aligned nanostructures with high aspect ratios display high contact angles, while low aspect ratios and less ordered surfaces show lower contact angles, forming hydrophilic surfaces.

From these results the following design guidelines are devised:

- 1D aligned arrays, usually (super-) hydrophobic, are mainly obtained at near neutral pH regardless of voltage and time.
- 3D arrays (hydrophobic and hydrophilic) are formed for long reaction times, regardless of the pH and the voltage.
- 2D arrays can be formed at low and high pH regardless of the voltage and time. However, 2D arrays formed at high pH display hydrophobic behaviour only at high voltage.
- The anodization conditions where corrosion and pitting are more common are low pH, high voltage and for long-reaction times.

Finally, it was also found that thermal post-treatment does not affect the general morphology (shapes and arrangement of the nanowires) but modifies the surface of nanowires and increases the size of the crystallites.

“The scientist is not a person who gives the right answers; is the one who asks the right questions.”

Claude Lévi-Strauss

Chapter 5: ZnO nanostructured films as a photocatalyst for water treatment in a batch reactor.

The production and characterisation of ZnO-NFs has been described in detail in Chapter 4. This chapter will discuss the application of ZnO-NFs for the photocatalytic degradation of phenol (used as organic model compound) using an external jacketed batch reactor (see section 3.3). This chapter is divided in three parts: In the first section, the initial analysis of the degradation of phenol in the batch system is presented. The effect of ZnO-NFs morphology and crystallinity on the photocatalytic degradation of phenol is examined in the second section. Finally, the effect of dissolved oxygen on the degradation of phenol and changes in ZnO-NFs morphology caused by photocatalysis are reported in section three.

5.1 Initial analysis: Degradation of phenol in the batch reactor.

Phenol is an organic compound produced and used in different industrial sectors. Phenol is mainly produced at large scale in the petrochemical industry and used as a precursor for the production of polycarbonates, epoxies, Bakelite and nylon in the polymeric sector. It is also used to manufacture a range of pesticides and herbicides and a variety of pharmaceuticals compounds including salicylic acid [273]. As a result of its extensive use and the low control of its disposal, phenol has been widely found in both industrial effluents and natural streams [274], [275]. Due to its toxicity and recalcitrant properties, phenol has a strong negative impact on the environment and is considered a priority pollutant by the U.S. Environmental Protection Agency. Therefore, studies related to the degradation of this compound are interesting from an environmental point of view. Additionally, since the mechanism for the degradation of phenol is well understood, and its by-products are well defined, it is a practical model compound to be used when studying novel photocatalysts.

During photocatalysis, pollutants are simultaneously exposed to different processes that reduce the pollutant concentration in the source water, namely; adsorption of compounds on the catalyst surface, degradation due to the effect of light (photolysis) and degradation due to the effect of the catalyst once it is activated by light (photocatalysis). In photocatalytic studies for environmental applications, one of the challenges is to establish the real contribution of photolysis in the decomposition of pollutants during the photocatalytic reaction. In this study, preliminary experiments were carried out to determine the degree of both photolytic and photocatalytic degradation of phenol in the batch reactor under the selected conditions (a concentration of phenol of 5 ppm, stirring at approximately 1000 rpm and radiation using monochromatic UV-C light with a wavelength of 254 nm). Although high temperatures appear to be favourable for the photocatalytic reactions with organic compounds under UV-C light [276], the temperature for all the experiments was set at 10 °C to avoid potential evaporation produced by the UV lamp heating the water surface.

5.1.1 Adsorption and photolysis of phenol in the batch reactor

To measure the adsorption of phenol on the ZnO-NFs, prior to each photolytic and photocatalytic experiment, samples were immersed in the phenol solution in darkness for 30 minutes to ensure the adsorption equilibrium was reached. Phenol concentration was measured before and after adsorption. The concentration of phenol decreased by less than 2% for all experiments. Therefore, any further changes in concentration were attributed to degradation by photolysis and photocatalysis.

The degradation of phenol produced by photolysis was studied for 4 hours reaction in the batch reactor using UV-C light with a wavelength of 254 nm and without ZnO-NFs. Although the effect of light in photolysis and photocatalysis has been extensively discussed [276]–[281], there are still divergent opinions about the most suitable wavelength for photocatalysis with semiconductor metal oxides. Highly energetic short wavelength light has been recognised as being more effective in photocatalytic degradation of organic pollutants than longer wavelength light [276]–[278]. However, comparative studies have also reported better degradation of pollutants at longer wavelengths [279]–[281].

Chemical compounds exposed to UV light undergo photochemical reactions in which molecular bonds can be broken leading to simpler molecules [280]. Additionally, under UV light exposition, there is a small generation of hydroxyl radicals (Equation 5.1) that contributes to the degradation of the organic compounds [282].



The photolysis of the phenol in the batch reactor was minimal with only a reduction on the concentration of about 10%. Although the degradation of phenol by photolysis has been reported as negligible under similar UV-C wavelength irradiation [283], previous experiments, carried out in this project with different volumes of phenol in solution, showed that photodegradation in the range of 20-30 % can be reached when small volumes of phenol solution were irradiated by UV light. The molar absorption coefficient of phenol ($\epsilon = 2340 \text{ cm}^{-1}/\text{M}$) [284] and its absorbance spectrum (Figure 5.1) indicate that phenol has a strong tendency to absorb UV light in the range of 220 and 300 nm with a maximum absorption peak at 270.8 nm. Since the wavelength of light used in this project was 254 nm, a high photolysis of phenol was expected. The low oxidation of phenol by photolysis pointed out a potential irradiation constraint given either by the small irradiation area or by irregular irradiation along the water column.

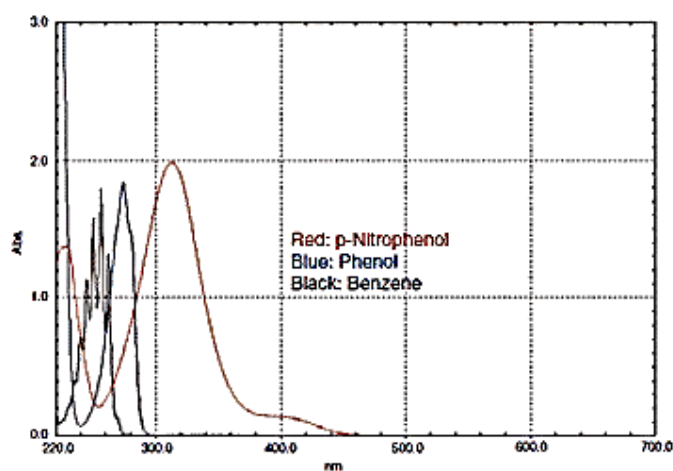


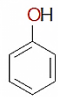
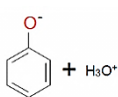
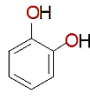
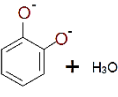
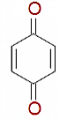
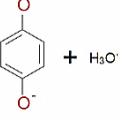
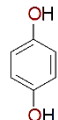
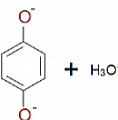
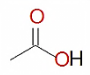
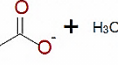
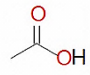
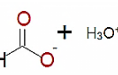
Figure 5.1 Absorbance spectra of phenol, p-nitrophenol and benzene [285]

Values of pH during the photolysis of phenol decreased from 6.2 to 5.9, indicating a slight acidification of the solution. The change in pH occurs due to the formation of acetic and formic acid during the decomposition of phenol and its by-products [68].

5.1.2 Photocatalytic degradation of phenol as a model compound in the batch reactor

During the photocatalytic degradation of organic compounds, the formation of multiple by-products (phenolate intermediates and acids) occurs. These reactions are therefore considered as multicomponent systems [286]. The most common by-products of phenol's degradation are catechol, benzoquinone, hydroquinone, acetic acid, formic acid and CO₂ [68]. Table 5.1 shows the solubility, pKa, molecular structure and dissociated form of phenol and its by-products. These properties will be used during the analysis of the phenol degradation throughout this chapter.

Table 5.1 Phenol and common by-products produced during photocatalytic degradation [286].

Species	Solubility in water (20 °C)	pKa in water	Molecular structure	Dissociated form
phenol	8.3 g/100 mL	9.0		
catechol	43 g/100 mL	9.5		
benzoquinone	1.0 g/100 mL	--		
hydroquinone	5.9 g/100 mL	9.9		
acetic acid	Miscible	4.8		
formic acid	Miscible	3.8		

In order to identify the kinetics of the degradation and mineralisation of phenol in the selected setup, 12 hour long experiments were carried out. Figure 5.2 displays the photocatalytic degradation of phenol and the evolution of phenolate by-products (i.e. catechol, benzoquinone and hydroquinone) as a function of time.

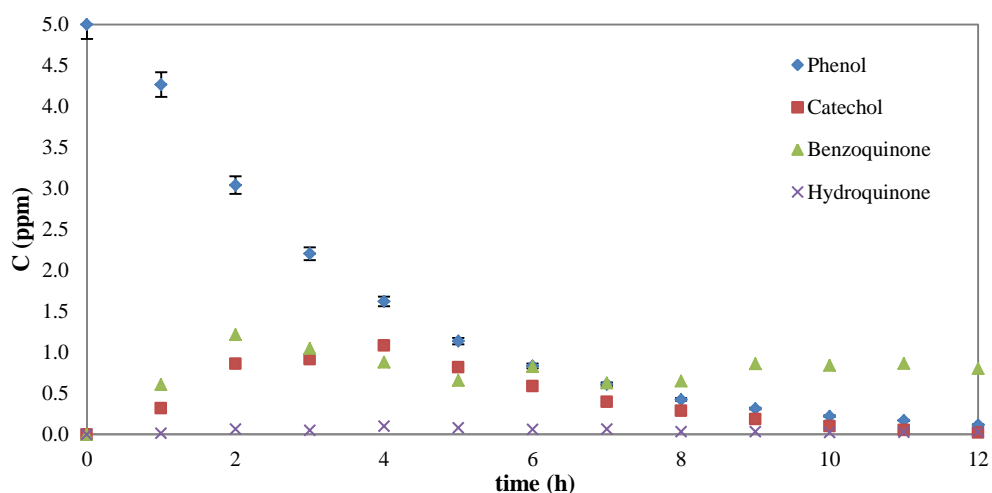


Figure 5.2 Degradation of phenol and by-products for 12 hours in a batch reactor using ZnO-NF as a photocatalyst

The formation of by-products affects the degradation rate of the phenol. Phenol and its by-products can be physisorbed through hydrogen bonds and chemisorbed through reactions with OH radicals producing ring alkylated intermediate products [287]. As observed in Figure 5.2, after 4 hours the concentration of catechol started to decrease while the concentration of benzoquinone remained quasi constant. Two factors might affect the degradation of benzoquinone; (i) its low solubility in water compared to the other phenolate intermediates (see Table 5.1) that limits its adsorption on the photocatalyst, and (ii) the potential formation of benzoquinone produced from the oxidation of phenol and catechol which maintains the concentration of benzoquinone quasi constant. A potential photodegradation pathway for phenol is shown in Figure 5.3, including the formation of acetic and formic acid [68].

Fractional life method was used to determine the kinetic order of the reaction [288]. The slope of the trend-line displayed in Figure 5.4a indicates that the order of the reaction is approximately one. Furthermore, by using the integration rate method, the kinetic order of the reaction was verified as shown in Figure 5.4b. The oxidation of phenol obeyed pseudo first-order kinetics in agreement with other photocatalytic studies with both powder and supported ZnO [137], [283] and with TiO₂ [68], [137]. First order kinetics are expected at low concentrations of phenol as the number of catalytic sites is not the limiting factor of the reaction rate (r_i), and therefore r_i is proportional to the phenol concentration.

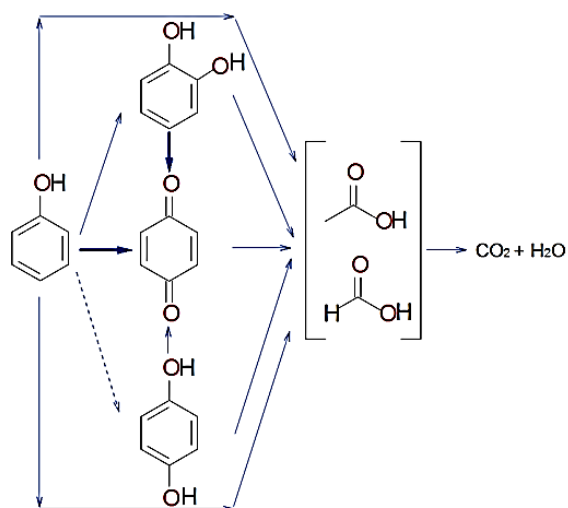


Figure 5.3 Proposed degradation pathway of phenol and by-products for a 12 hours batch reactor experiment using ZnO-NF as a photocatalyst (adapted from [68])

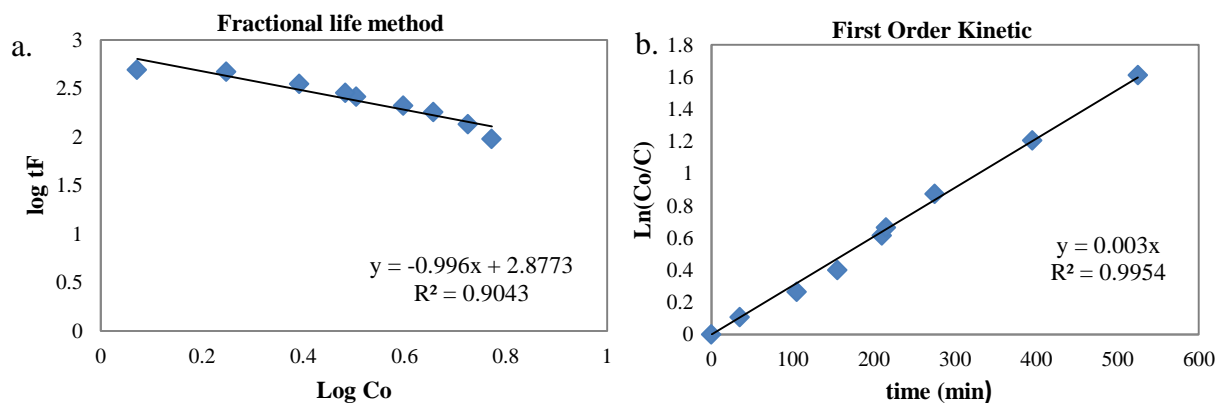


Figure 5.4 Plot of fractional life method (a) and integral rate method (b) used to determine the kinetic order reaction of the photocatalytic degradation of phenol.

Kinetic constants were calculated for all the photocatalytic reactions in this study using the integration rate method. Values of kinetic constant for the photocatalytic degradation of phenol in the batch reactor were found in the range of 0.10 to 0.44 h⁻¹. On the other hand, the range of kinetic constants in the tubular reactor were in the range of 0.59 to 1.60 h⁻¹. Table 5.2 displayed values of kinetic constant, reported in literature, for the photocatalytic degradation of phenol under different experimental conditions and types of reactors.

Table 5.2 Kinetic constant of photocatalytic degradation of phenol in different studies

Photocatalyst	Dose (g/L)	light	Reaction time (min)	Type of reactor	Co (ppm)	Final degradation	K (h ⁻¹)	Ref.
TiO ₂ (suspension)	0.5	Xe lamp (Simulating Solar spectrum)	150	Discontinuous cylindrical microreactors placed in a Solar Simulator	90	77%	0.582	[289]
Degussa P- 25 TiO ₂ .coated acrylic sheets	-	Low pressure mercury lamps. UV-A 400 nm	(0-300)	Batch photoreactor	100	-	0.096	[290]
Degussa P- 25 TiO ₂ .coated acrylic sheets	-	Low pressure mercury lamps. UV-A 400 nm	(0-300)	Batch photoreactor	10	-	0.27	[290]
ZnO (suspension)	2	254 nm	20	Batch reactor system	80	58.7%	1.2	[283]
ZnO (suspension)	2	254 nm	20	Batch reactor system	40	45%	1.99	[283]
Degussa P-25 (suspension)	1	HPA 400W lamp	360	Helical photoreactor (500mL) Flowrate: 0.11 l/min	10	97.3%	2.34	[235]
Degussa P-25 (suspension)	1	HPA 400W lamp 365 nm	360	Helical photoreactor (500mL) Flowrate: 0.23 l/min	10	99.8%	1.70	[235]
ZnO powder produced by sol-gel process (suspension)	1	Black light mercury HgV 125 W UV lamp	120	Batch reactor system	50	76%	0.9	[291]
ZnO powder produced by sol-gel process (suspension)	1	Black light mercury HgV 125 W UV lamp	120	Batch reactor system	100	70%	0.6	[291]
ZnO powder produced by sol-gel process (suspension)	1	Black light mercury HgV 125 W UV lamp	120	Batch reactor system	200	60%	0.42	[291]

It is difficult to compare the values of kinetic constant from table 5.2 due to the differences in experimental conditions. However, it is possible to establish that reactions performed with suspended photocatalyst showed higher rates than reactions with supported photocatalyst. Between the studies reported in table 5.3, the highest constant rate for the degradation of phenol (2.34 h^{-1}) was obtained in a helical photoreactor at a flow rate of 0.11 L/min with TiO_2 . On the other hand, in batch systems the highest flow rate obtained was 1.2 h^{-1} with suspended ZnO . The later kinetic constant is 2.7 times higher than the maximum constant found in this study with the batch reactor. Therefore, photocatalytic reactions at different stirring velocities were performed in order to evaluate the effect of external mass transfer resistance in the reaction. This experiment aimed to establish the best condition of mixing to assure high mass transfer between the solid photocatalyst and the liquid phase. This will be discussed in detail in section 5.3.1.

Total organic carbon (TOC) measurements confirmed the decomposition of phenol and its by-products (Figure 5.5). The TOC mineralisation was fitted to a zero order kinetic model ($r^{\text{TOC}} = k^{\text{TOC}}$). A similar behaviour has been reported for the degradation of phenol with TiO_2 [68]. TOC decreases due to the formation of CO_2 and its subsequent release from the solution. After 12 hours the TOC was reduced between 75 and 80 %, showing the elimination of the total organic matter present in the solution (i.e. Phenol and its by-products).

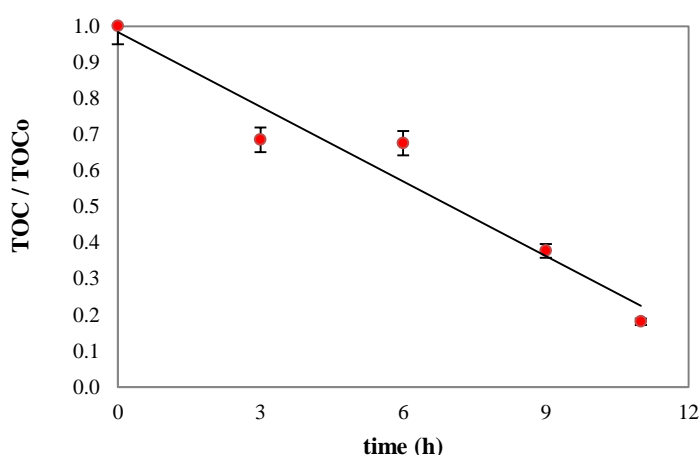


Figure 5.5 TOC variation during the photocatalytic degradation of phenol and by-products in a batch reactor using ZnO-NF as a photocatalyst.

During the 12 hour experiment, the pH and the conductivity of the phenol solution were recorded. Unlike photolysis, during the photocatalytic reaction there was a slight increase of the pH, with values changing from 6.2 to 6.5. A possible reason for this increase in pH is the dissolution of ZnO and formation of Zn(OH)₂ due to photo-corrosion of the ZnO-NFs. Since the pH affects the dissociation of the phenol and its by-products, and also determines the surface charge of the photocatalyst, changes in pH alter the adsorption of these compounds on the ZnO-NFs affecting the interfacial electron transfer and the photoredox process [292]. As the pH of point of zero charge (pH_{PZC}) for ZnO is 9.0 ± 0.3, and the pH of the phenol solution was in the range of 6.2-6.5, the surface of the ZnO-NFs was positively charged during the photocatalytic experiments. Therefore the adsorption of anions with negative charge, such as the phenolate intermediates, was more likely to occur.

It was observed that the conductivity increased throughout the photocatalytic reaction (Figure 5.6-a). Changes in conductivity can be attributed to multiple reasons, namely; the formation of ions produced from the degradation of phenol, the formation of CO₂ that remains soluble in the solution and the production of Zn(II) ions into the solution due to dissolution of the photocatalyst. The dissolution of the ZnO was confirmed by measuring the total concentration of dissolved Zn as shown in Figure 5.6-b. Changes in both conductivity and concentration of dissolved Zn did not follow the same trend, showing that the formation of by-products and CO₂ also contributes to the increase of conductivity. This was also confirmed during the photolysis experiments where conductivity always increased despite the absence of any ZnO-NF.

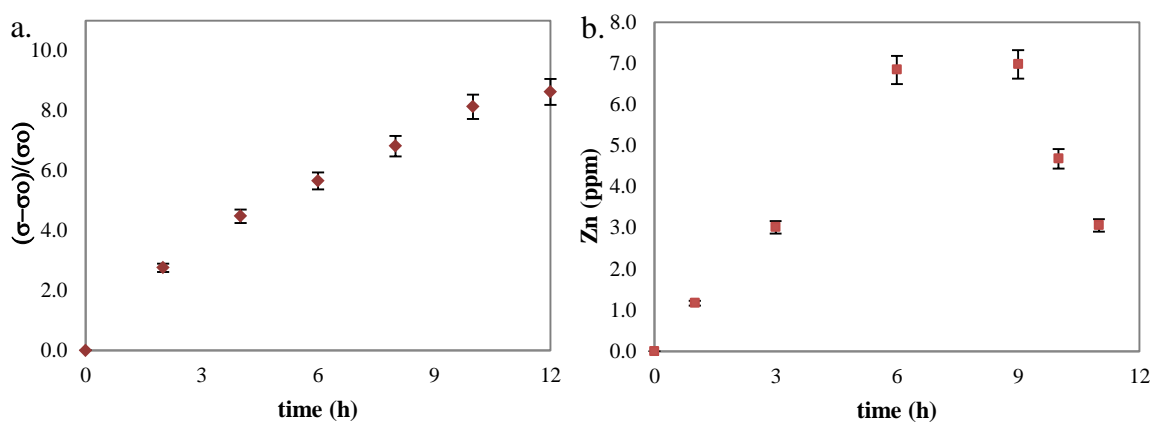


Figure 5.6 Change in conductivity (a) and dissolved Zn(II) ions (b) during the photocatalytic degradation of phenol for 12 hours in a batch reactor using ZnO-NF as a photocatalyst

A rise in the concentration of dissolved Zn might occur when ZnO is affected by photodegradation and is partially dissolved. A drastic drop in the concentration occurred after 8 hour of reaction, this is herein attributed to a re-precipitation of the Zn ions as will be discussed in detail in section 5.3.2. At this range of pH (6.2 – 6.5), the most likely Zn(II) species in solution was Zn^{2+} ; the accumulation of this ion in the solution affected the thermodynamic stability of the system favouring the production of insoluble $Zn(OH)_{2(s)}$ and producing a strong precipitation (see the thermodynamic speciation of Zn – Figure 4.1). As it will be discussed throughout this chapter, this phenomenon of “dissolution – re-deposition” occurs even during the early stages of the reaction.

A further detailed analysis of the kinetics of phenol degradation on ZnO-NFs is beyond the scope of this work, which is instead focused on understanding the relationship between ZnO-NFs properties and photocatalytic behaviour.

5.1.3 Effect of external mass transfer on the overall degradation rates in the batch reactor

Heterogeneous photocatalysis with supported photocatalyst can be affected by external mass transfer limitation. This condition is given by a slow diffusion of pollutants from the fluid boundary layer around the catalyst (liquid phase) to the external surface of the photocatalyst (solid phase). A study conducted by Chen *et al* [294] with immobilised photocatalyst (Degussa P25) in a semi-batch photoreactor, concluded that external mass transfer resistance can be considerably reduced by increasing the flow rate, leading to higher degradation rates. Internal mass transfer resistance, on the other hand, were difficult to assess directly as it is an intrinsic catalyst property and varies with the nature of the catalyst, coating method and thickness of the film [294]. In the present study, the effect of external mass transfer in the batch reactor was analysed during the degradation of phenol at different stirring velocities. By increasing the stirring speed, the fluid boundary layer is reduced, minimizing the mass transfer resistance. Once the mass transfer limitation is minimal, any increase in stirring speed does not affect the photocatalytic activity. At that point, the reaction is performing in the kinetically controlled regime rather than the mass transfer controlled regime. For this experiment, ZnO-NFs produced with $KHCO_3$ [0.05M] at 1 V for 1h and 10°C were used as a photocatalyst for the degradation of phenol [5ppm].

Figure 5.7a shows changes in phenol concentration during photocatalytic degradation at different stirring velocities and their kinetic constant. Low degradation of phenol (less than 20%) was observed in absence of stirring. Degradation in that experiment was produced mainly by photolysis, adsorption and “mass transfer limited” photocatalysis. Once the system was stirred, the degradation of phenol increased due to higher diffusion of the phenol in the system. As shown in Figure 5.7b, stirring velocities higher than 706 rpm result in similar final degradation of about 80% after 4 hours. The later result indicates that at high stirring velocities (higher than 706 rpm) the external mass transfer resistance becomes minimal and constant. Therefore, under similar experimental conditions (i.e. pollutant concentration, temperature, stirring velocity and illumination) changes in the photocatalytic degradation of phenol are caused by intrinsic photocatalytic properties. Further experiments were carried out at 1000 rpm.

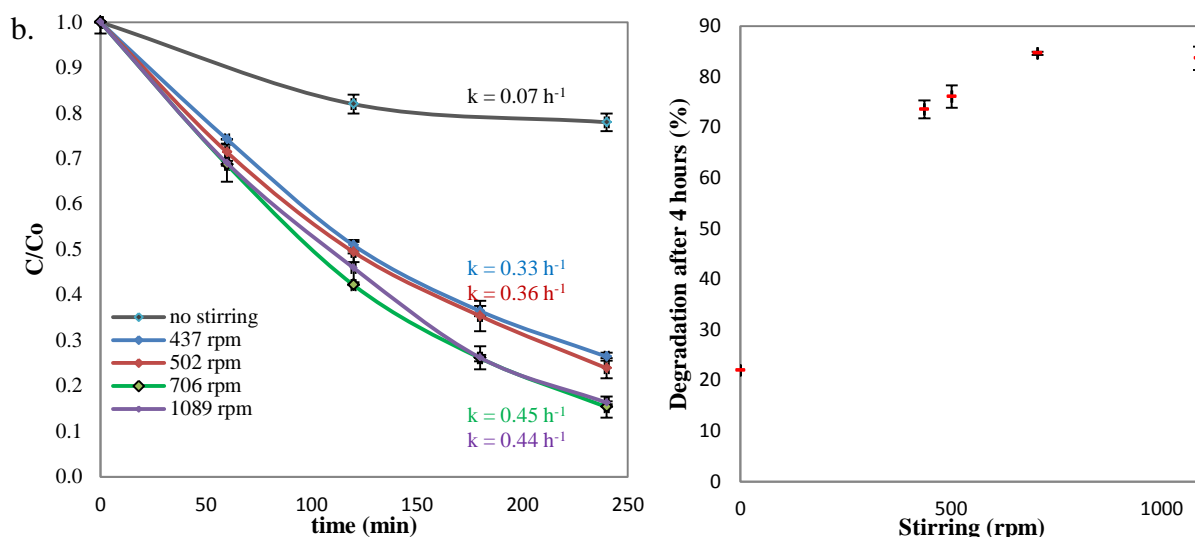


Figure 5.7 Photocatalytic degradation of phenol at different stirring velocities in a batch reactor using ZnO-NF as a photocatalyst (a). Correlation between the final degradation of phenol after 4 hours of reaction and stirring velocity .

5.2 Correlation between ZnO-NFs morphology and their photocatalytic performance.

As discussed in Chapter 4, different properties of the photocatalyst can affect its performance in the degradation of organic pollutants in water. It is widely recognised that surface area is one of the most important properties in photocatalysis [133], [135], [295], [296]. Some studies with ZnO powder and ZnO films have shown an enhancement of photocatalysis due to an increase in the surface area [134], [297], [298].

However, other authors [133], [299], [300] have suggested that surface morphology is even more important than surface area in photocatalysis since the former involves both the surface area and the active photocatalytic surface area (where photons reach the surface of the catalyst and activate it).

One of the most extensive studies into determining the predominant properties that affect the activity of a given photocatalyst, is the one carried out by Dr. Othani's research group, where 35 commercial TiO₂ powders were statistically analysed [301]. A correlation between six physical and structural properties of the catalyst (i.e. specific surface area, density of crystalline defects, primary particle size, secondary particle size and content of anatase and rutile phases) and photocatalytic activity was obtained through multivariable analyses. Although photocatalytic activity was fairly reproduced for five types of reactors, authors suggested that other properties such as morphology have important effect on the photocatalytic activity.

Herein a systematic study of the effect of ZnO-NF morphology and its photocatalytic behaviour is presented. Although preliminary experiments (see Section 5.1.2) showed that 12 hours were necessary for total degradation of phenol (TOC), shorter experiments of 4 hours were chosen as they are sufficient to show the impact of morphology on photocatalysis.

5.2.1 Effect of Crystallinity on the photocatalytic performance of ZnO-NFs

As discussed in Section 4.10, the thermal post-treatment in air applied to the ZnO-NFs affected the nanowire's roughness, increased its crystallite size, reduced the crystal defects and increased the content of ZnO in the films compared to the amount of Zn(OH)₂. Additionally, it was determined in Section 4.10 that the nanowires' diameter and morphology were unaltered during the post-annealing. For this analysis, ZnO-NFs with different post-annealing times and, therefore, different crystallinity were used in the photocatalytic degradation of phenol as is shown in Figure 5.8. Results show that changes produced by post-annealing have a considerable effect in the photocatalytic performance of the ZnO-NFs. All the experiments with post-treated ZnO-NFs resulted in higher phenol degradation after 4 hours compared to those films without post-annealing. However, no significant differences in the phenol degradation rate were observed between ZnO-NFs post-annealed at different times.

The size of the ZnO crystals does not appear to have a major effect on the degradation of phenol with all the experiments displaying similar kinetic constants in the range of 0.21 to 0.26 h⁻¹ regardless their crystal sizes. ZnO-NFs post-annealed for 1 hour (crystal sizes in the range of 5-10 nm) displayed similar photocatalytic performance to those post-annealed for 18 and 36 hours (crystal sizes in the range of 10-20 nm) despite having crystals that are almost double the size (Figure 5.8-inset). This result is in contrast to what was observed by Pardeshi *et al* [302], who have reported a direct relationship between crystallite size and photocatalytic performance of ZnO. However, in Pardeshi's study, the ZnO samples with different crystallite size also displayed different band gap energies, and thus differences in the photocatalytic performance can be related to crystal defects (that affect the band gap energy) rather than the crystallite size of the photocatalyst. Additional to the crystal's size, Wahi *et al* [303] proposed that the crystal orientation affects photocatalysis due to different water adsorption modes on ZnO powder. In the present study, this potential effect was not considered due to all the ZnO-NFs showed similar orientations (as analysed by XRD and discussed in Section 4.11.2).

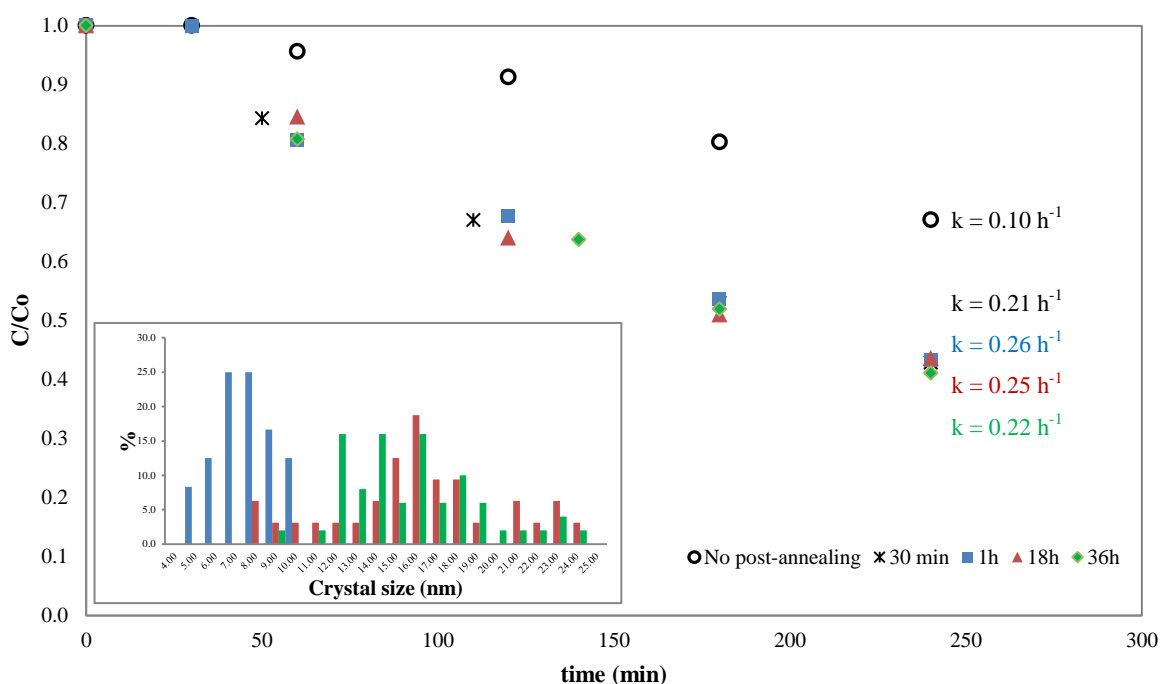


Figure 5.8 Photocatalytic degradation of phenol with ZnO-NFs exposed to no-post-annealing, and to 30min, 1h, 18h and 36h of post-annealing. Crystal size distribution of ZnO-NFs (inset)

The differences in photocatalytic performance between annealed and non-annealed ZnO-NFs are related exclusively to the increase of crystallinity. The formation of cracks

on the wires surface (and the potential increase in surface area) during post-annealing (see Figure 4.18) did not affect ZnO-NF photocatalytic performance. As will be discussed in Section 5.3.3, ZnO-NFs that were post-treated with oxygen plasma did not suffer changes of roughness and still displayed similar photocatalytic performance to ZnO-NFs that were post-annealed.

The differences between amorphous ZnO and crystalline ZnO, are attributed to the potential higher content of ZnO compared to Zn(OH)₂ and the reduction in crystal defects are responsible for the differences in photocatalytic performance between post-annealed and non-annealed ZnO-NFs. A higher purity of ZnO increases the effective number of electron-holes pairs, while less crystallite defects reduce the recombination of electron-hole pairs [304]. Additionally, these two factors have influence on the photocatalytic activity of the ZnO-NFs due to their influence on band gap energies [265]–[268].

5.2.2 Effect of morphology on the photocatalytic performance of ZnO-NFs: nanostructure arrangement

To study the effect of morphology on the photocatalytic performance of ZnO-NFs, two scenarios were considered: (i) Nanostructures (i.e. nanowires) with the same shape but different arrangement (e.g. single nanowires, flower-like nanowires, interpenetrated nanowires) and (ii) different shapes of the nanostructures. For the former case, ZnO-NFs obtained with KHCO₃ were produced at different anodization conditions and post-annealed at 350 °C for 1 hour. All ZnO-NFs displayed similar wire diameter distributions (see Figure 4.11) but different crystal sizes (see Figure 4.15). For this analysis, the effect of the crystal size was considered negligible as established before in Section 5.2.1.

Figure 5.9 (a-b) shows the FESEM micrographs of the ZnO-NFs surface morphologies with similar nanostructures i.e. nanowires, but in different arrangements. Based on visual observation of the FESEM micrographs and on the ZnO layer thickness, the films can be morphologically described as follows:

- Figure 5.9-a displays a ZnO-NF surface with high aspect ratio and a denser nanowire distribution (with more nanostructures per unit area). This film displayed a thick ZnO layer of $34.8 \mu\text{m} \pm 0.1 \mu\text{m}$.

- Figure 5.9-b shows the ZnO-NFs with a low density configuration where individual nanowires can be observed. The thickness of this ZnO-NF was $6.2 \mu\text{m} \pm 0.1 \mu\text{m}$.
- The ZnO-NF pictured in Figure 5.9-c displays low density configuration. This film displayed a ZnO film thickest of $14 \mu\text{m} \pm 0.1 \mu\text{m}$.
- The ZnO-NF shown in Figure 5.9-d had an interpenetrated structure with nano-wires growing in different directions. Additionally, this film displayed a thick ZnO layer of $34.8 \mu\text{m} \pm 0.1 \mu\text{m}$. This film was the thickest film with a average ZnO thickness of $47 \mu\text{m} \pm 0.1 \mu\text{m}$

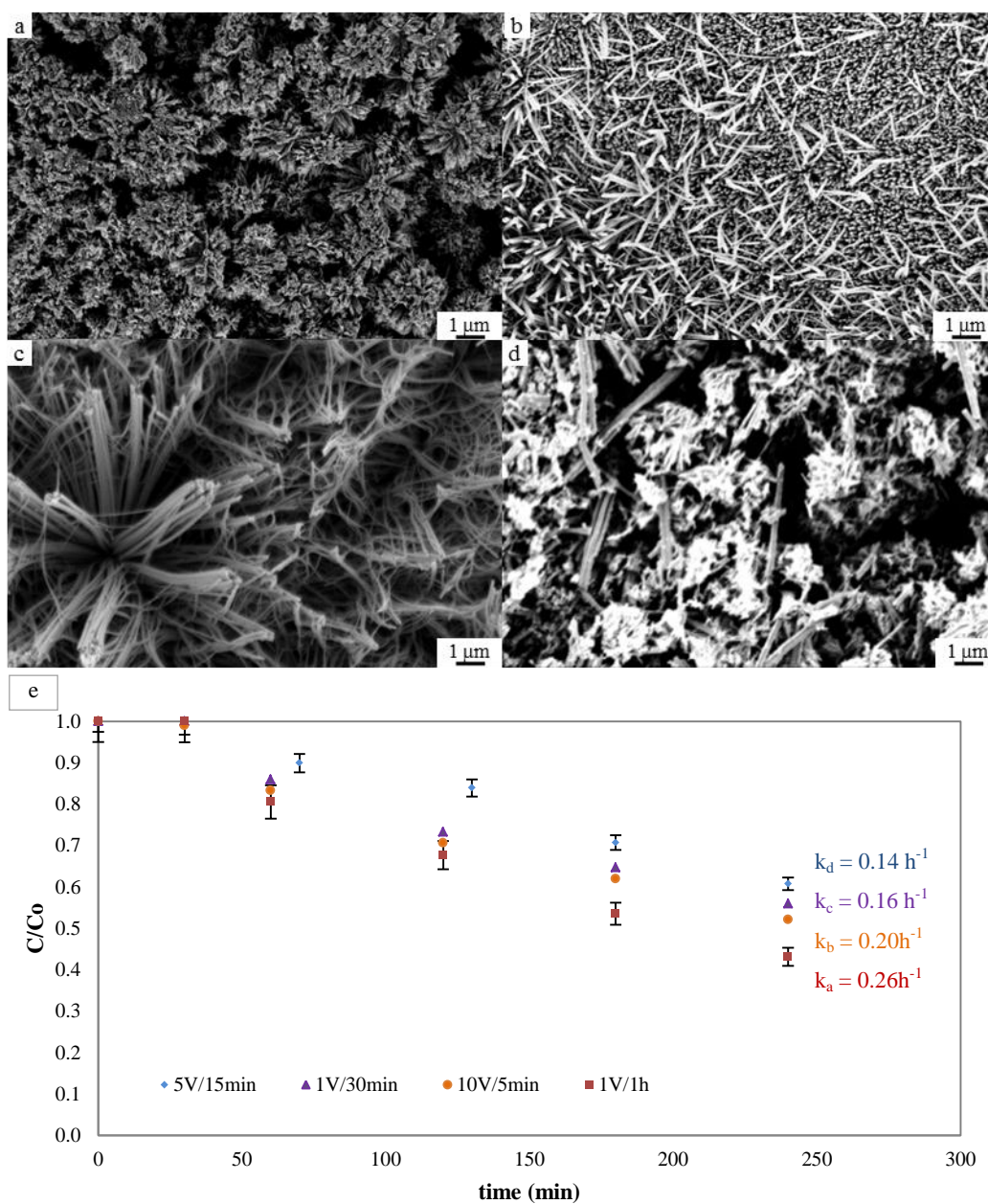


Figure 5.9 Top: FESEM images of ZnO nanowires obtained with KHCO_3 [0.05M] at 10°C (a) 1V/ 1 h; (b) 10V/ 5 min; (c) 1V/ 30 min; (d) 5V/ 15 min. Bottom: Degradation of phenol with the different arrangements of nanowires.

Different ZnO nanostructure arrangements resulted in different levels of phenol degradation (Figure 5.9-e). The highest degradation was obtained with the film that displayed the highest aspect ratio while the lowest degradation occurred with the interpenetrated nanowire film. It appears that the morphology not only determines the surface area where phenol can be adsorbed, but also the area that can be illuminated and activated by light (photo-active surface area).

As previously discussed in Chapter 2, the measurement of the surface area in films represents a challenge. Between the different methods used to measure total surface area of catalysts, BET, t-plot and a_s -plot method are the most well-recognised. These techniques are based on a mechanism of physical adsorption of gas molecules on the solid catalyst surface [305], which required specialised equipment set up in powder form that limits the study of supported photocatalyst. Herein, adsorption experiments with a metal were performed to compare the adsorption capacity of the films and therefore to establish differences in surface areas. Based on the study performed by Mahdavi *et al* [306], magnesium was absorbed on the surface of the ZnO-NFs.

Following the procedure reported by Mahdavi, the ZnO-NFs were immersed in 10 mL of $MgCl_2$ [150ppm] and left overnight, constantly shaken and at room temperature. After completing the adsorption experiment, films were removed from the solution and rinsed thoroughly with deionised water. Desorption was performed by immersing the ZnO-NFs in 10 mL of 0.01M $CaCl_2$ solution for 24 hours. The solutions were filtered and the concentration of Mg was measured by atomic absorption spectroscopy.

Figure 5.10 (top) shows the concentration of magnesium adsorbed by the ZnO-NFs and measured from the desorption experiments. The highest adsorption was achieved by the ZnO-NFs obtained at 10 V for 5 minutes. A comparison between the adsorption capacity of Mg (Figure 5.10 top) with the kinetic constant of the photocatalytic experiments (Figure 5.10 bottom) evidence that surface area is not the only controlling factor. The ZnO-NF with higher adsorption capacity for Mg displayed the lowest degradation of phenol by photocatalysis. On the other hand, the film with the higher kinetic constant had low adsorption capacity.

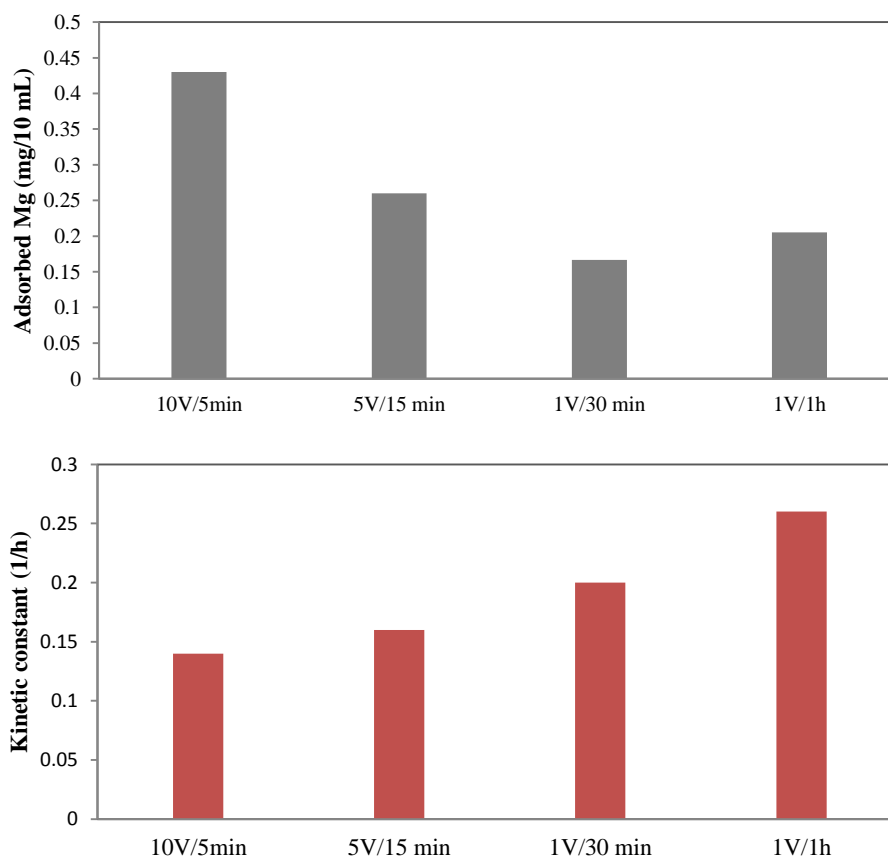


Figure 5.10 Top: Adsorption of Mg by the ZnO-NFs. Bottom: Kinetic constant of photocatalytic degradation of phenol with ZnO-NFs obtained at different anodization conditions.

An additional factor that can affect the photocatalytic performance of the films is their capacity to absorb light. It appears that dense morphologies with large number of nanostructures per unit area (forest-like morphologies) can be better at capturing light than bare thin films. Dense morphologies have higher ability to retain photons within the nanostructures. Additionally, light reflected by some nanostructures can be also absorbed by surrounding nanostructures. On the other hand, bare thin films or featureless films can reflect the light easier, resulting in a lower absorption of light. To analyse this aspect, the absorbance of light of the ZnO-NFs was measured. Figure 5.11 shows the absorbance of the films at different wavelengths. ZnO films show higher absorbance of light in the region of 380 to 200 nm. The film obtained at 1 V for 1 h displayed the highest absorbance of light followed by the film obtained at 1 V and 30 min of anodization reaction. A trend was found between the absorbance values at 254 nm (Figure 5.12 top) and the kinetic constants of the photocatalytic degradation of phenol (Figure 5.12 bottom). These results suggest that for the ZnO-NFs the absorbance

of light plays an important role in the photocatalytic performance. It is important to highlight that the light absorbance is directly related to the morphology of the nanostructures, which determine the capacity of the films for capturing photons, and therefore affect their photocatalytic activity.

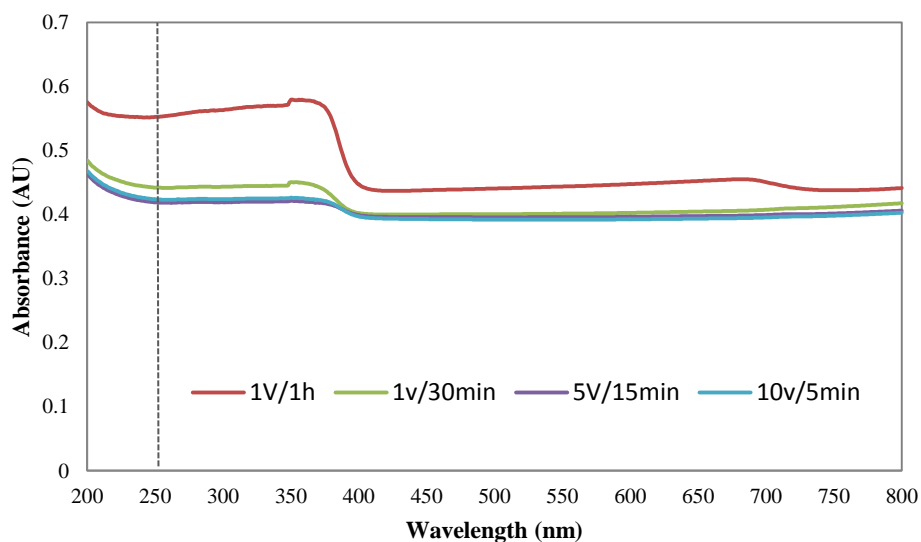


Figure 5.11 ZnO-NF light absorbance at different wavelengths.

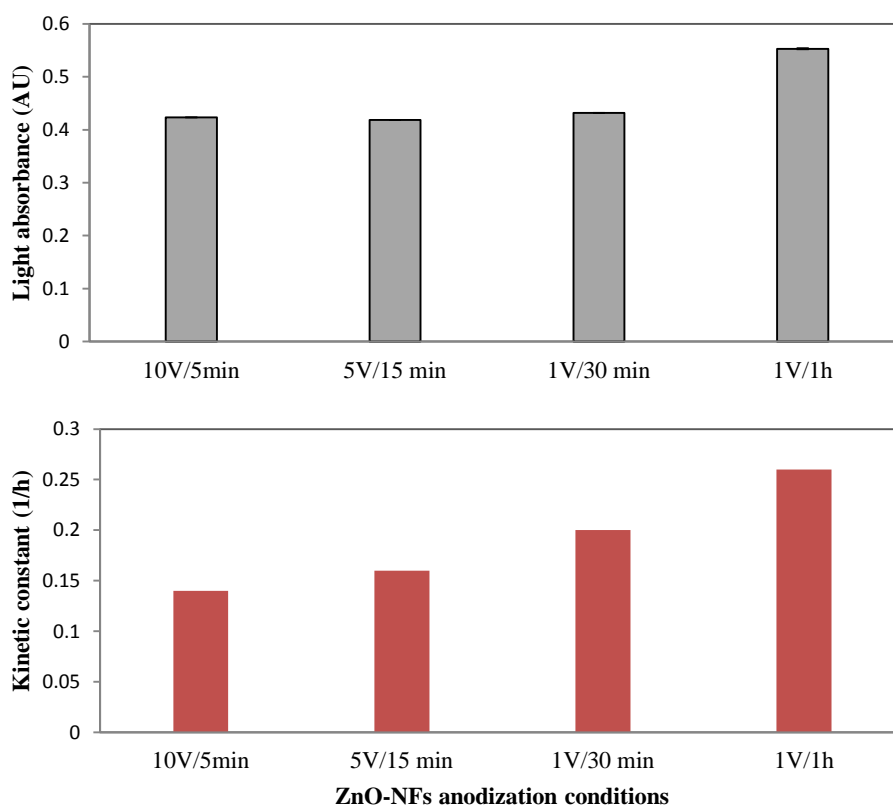


Figure 5.12 Top: ZnO-NFs light absorbance at 254 nm. Bottom: Kinetic constant of photocatalytic degradation of phenol with ZnO-NFs obtained at different anodization conditions.

Finally, to evaluate the hypothesis that the differences in phenol degradation would be due to the ZnO-NFs thicknesses, the kinetic constant of the photocatalytic degradation of phenol obtained after 4 hours of reaction was correlated with the thickness of each film. As shown in Figure 5.13, no direct relationship between ZnO layer thickness and photocatalytic performance was found. Different degradations of phenol (represented by the kinetic constant) were obtained regardless of the thickness of the ZnO-NFs, and the two thickest films displayed both the highest and the second lowest degradation.

Since the photon penetration depth for polycrystalline ZnO at 254 nm (about 0.13 μm) [307] is lower than the ZnO-NFs thickness (6.2 – 47.9 μm), it is assumed that the light penetration was similar for all of the tested ZnO-NFs. Therefore, the innermost ZnO layers were not exposed to UV light and therefore did not act in the photocatalytic reaction. As all the photocatalytic experiments were carried out under similar photon penetration depth, differences in photocatalytic degradation of phenol here are not related to the thickness of the ZnO-NFs.

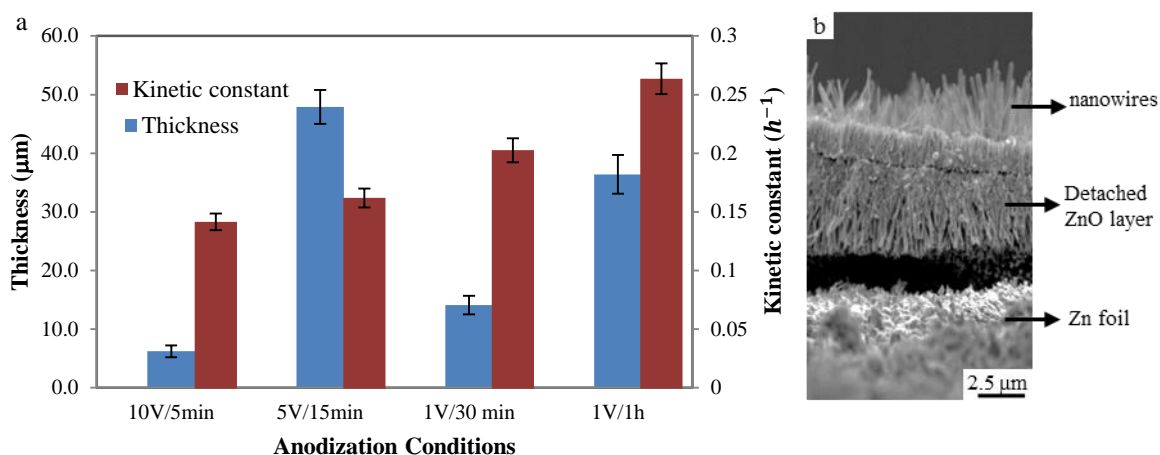


Figure 5.13 a) Comparison of ZnO-NFs thickness with kinetic constants for photocatalytic degradation of phenol with films obtained with KHCO_3 [0.05M] at 10 C and 1V/ 1 h (a); 10V/ 5 min (b); 1V/ 30 min (c); 5V/ 15 min (d). b) FESEM of cross section of ZnO-NF.

As discussed in section 5.1.2, changes in conductivity are due to multiple phenomena occurring in parallel during the photocatalytic reaction, such as the formation of ions (dissociation of by-products), the formation of soluble CO_2 and the dissolution of Zn(II) ions. For the set of photocatalytic experiments analysed in this section, no direct relationship was found between changes in conductivity and degradation of phenol (as shown in Figure 5.14-a and Figure 5.14-b). However, since different nanowire

arrangements displayed different rates of conductivity changes, it is asserted that (i) some morphologies tend to be more stable against photo corrosion than others and (ii) the rate of degradation of phenol and formation of by-products dissociated in water varies with the morphology of the ZnO-NF.

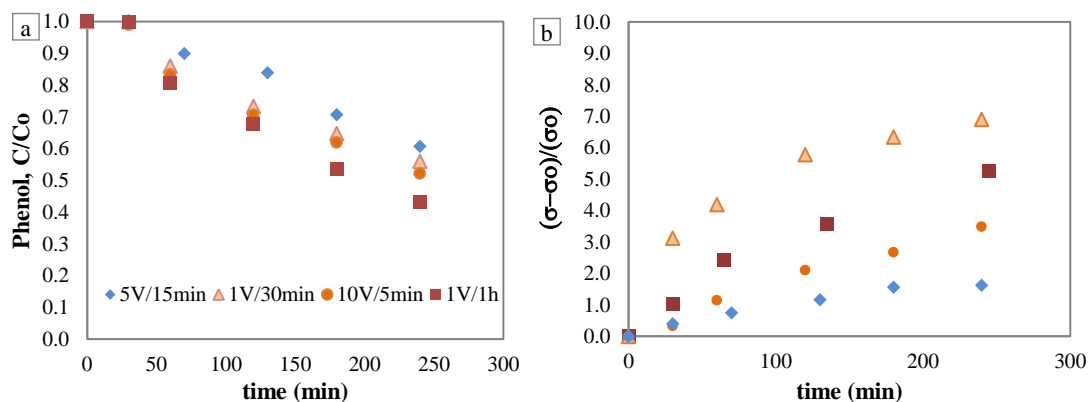


Figure 5.14 Comparison between phenol degradation with ZnO-NFs obtained at different anodization conditions (left) and their respectively conductivities (right)

5.2.3 Effect of Morphology on photocatalytic performance of ZnO-NFs: Different shapes of nanostructures

Photocatalytic experiments were conducted using ZnO-NFs with different surface morphologies (i.e. different shapes). All the films used herein were post-treated at 350 °C for 1 hour and 1 °C/min. As discussed in Sections 5.2.1 and 5.2.2 differences in crystalline size and the thickness of the ZnO-NFs do not affect the photocatalysis. Therefore, the differences in the degradation of phenol can be attributed to differences in the morphology of the ZnO-NFs. Figure 5.15 displays both the FESEM micrographs of the different morphologies used in this analysis, and the degradation of phenol obtained with the different ZnO-NFs (top and bottom respectively).

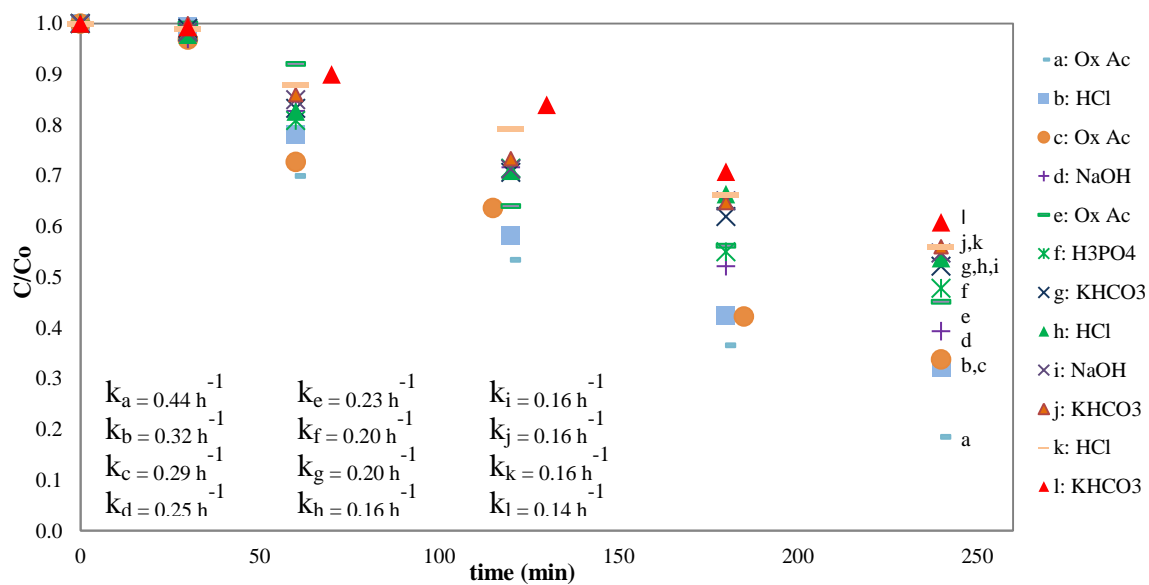
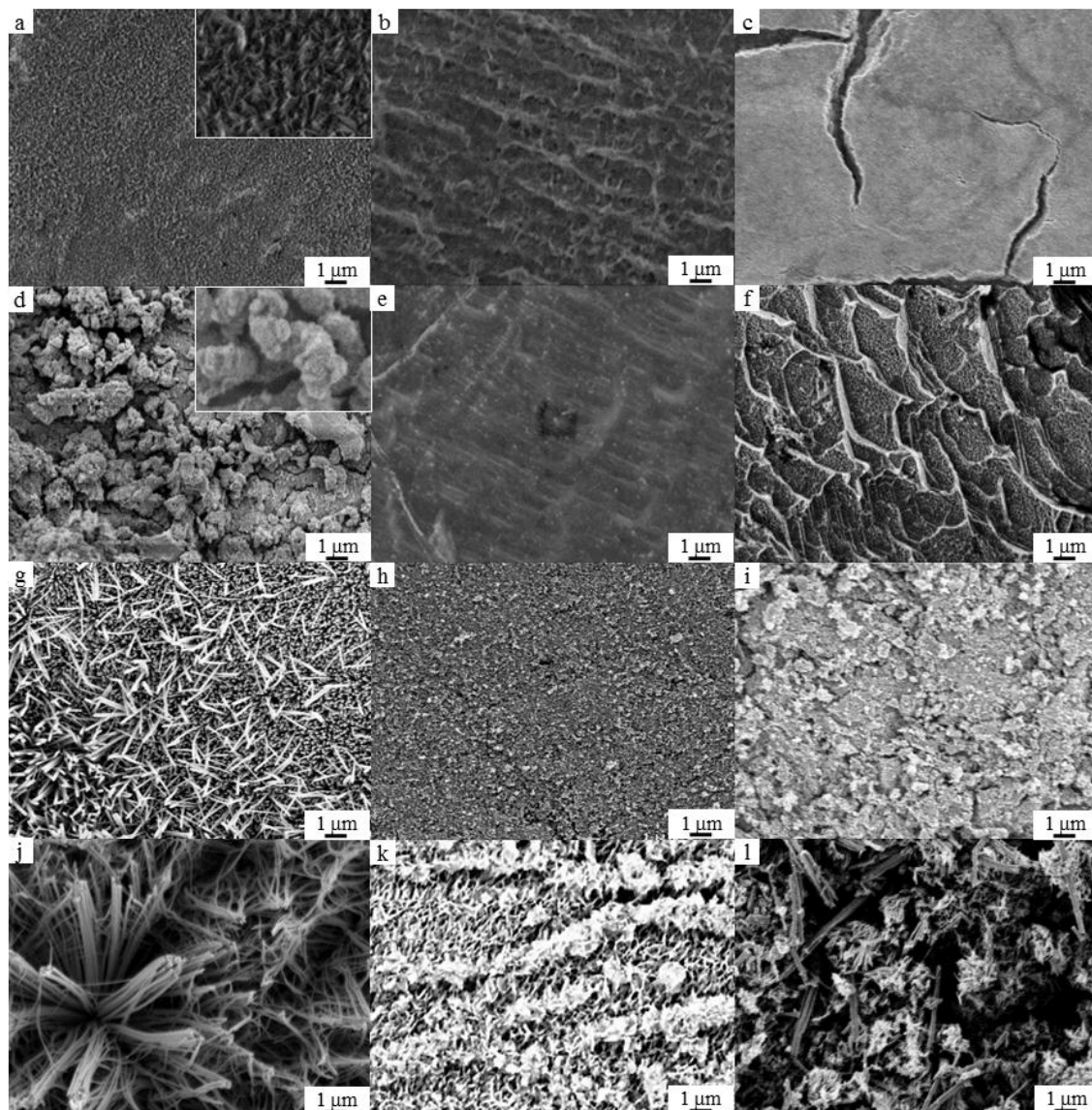


Figure 5.15 FESEM micrographs of ZnO-NF used for photocatalytic studies (top) and their photocatalytic activity in the (bottom)

In general, the rate of degradation of phenol varied with the shape of the nanostructures. As shown in Figure 5.15-b, a difference of 40% in phenol degradation was found between the lowest and highest degradation level observed after 4 hours of reaction. Although no direct relationship was found between the morphologies and degradation rate, some trends were identified. With some exceptions, large and complex nanostructures (with a potentially high surface areas) result in low degradation as the UV light might not be able to penetrate through the top surface and reach the total surface area of the photocatalyst. On the other hand, small nanostructures tend to scatter the light in smaller proportions and they are thus more likely to be reached by the UV light and therefore more photo-active surface area participates in the reaction.

The ZnO-NF that displayed the best photocatalytic performance (Figure 5.15-a) had a nano-flake like morphology; while the lowest degradation was obtained with the interpenetrated nanowire film (Figure 5.15-l). Films visualized in Figure 5.15-c and Figure 5.10-e displayed initial featureless surfaces and therefore a low surface area was expected, however their photocatalytic performances were better than ZnO-NFs with defined nanostructures such as those depicted in Figure 5.10(f-l). The latter result confirms that, in heterogeneous photocatalysis with a supported photocatalyst, surface area is not the only controlling factor.

As shown in Figure 5.16, for immobilised photocatalysts, the surface area does not determine the photocatalytic activity as some area cannot be reached by the light (Figure 5.16-b). Therefore, the property named in this work as photo-active surface area (which is function of the total surface area and morphology) plays an important role due to it defines the area that can be activated by light. Additionally, if the photon penetration length is taking into account, a new property named herein as photo-active surface volume can be established, and defined as the total volume of photocatalyst that can be activated by light at certain wavelength light. Since the photon penetration length is function of the wavelength light, the photo-active surface volume is function of the type of light applied (Figure 5.16-c). It is important to clarify that with thin films (which have a thickness lower than the photon penetration length) the photo-active surface volume is also function of the thickness.

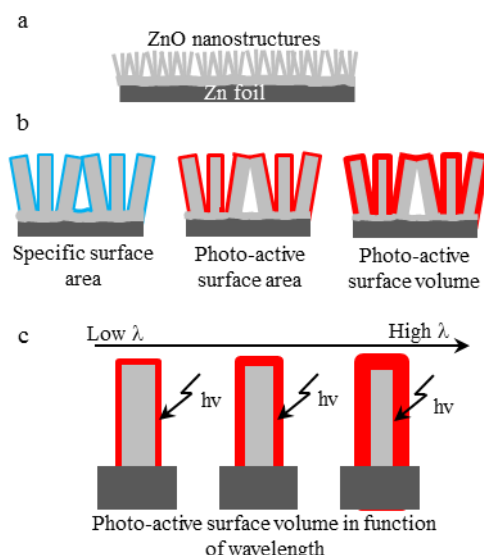


Figure 5.16 Schematic of photo-active surface area and photo-active surface volume for immobilised photocatalysts.

Other studies have also described some aspects of the relation between morphology, particle size and photocatalytic activity of ZnO films [308] without providing an analysis about the effect of morphology in photocatalysis. For instance, Li and Haneda [133] found a linear relationship between the amount of adsorbed substrate (Acetaldehyde) compare to the photocatalytic activity once the data is normalised (divided by BET surface area). In this study it is suggested that morphology has a higher influence on photocatalysis than the surface area. Other studies have also suggested that well aligned nanostructures displayed better photocatalytic degradation of different organic compounds and its by-products [134], [297], [309]. Herein no correlation between the alignments of the nanostructures and their photocatalytic performance was found.

Changes in conductivity, during the photocatalytic experiments, were not directly related to the dissolution of Zn in the water. Figure 5.17 shows the conductivities measured during each photocatalytic experiment and the final value of dissolved Zn (red font). Additionally, to facilitate a comparison between the degradation of phenol (Figure 5.15 bottom) and changes in conductivity (Figure 5.17), the same symbols were used and the codification (letters from 'a' to 'l') used for the FESEM micrographs in Figure 5.15-top was kept.

Different values of dissolved Zn were found regardless of the conductivity and the photocatalytic performance in terms of phenol degradation. For instance, ZnO-NFs named “a”, “b” and “c” (see arrows in Figure 5.17) displayed the 3 highest levels of photocatalytic degradation of phenol (Figure 5.15 bottom), however they displayed different changes in conductivity and different final values of dissolved Zn. As discussed previously, apart from Zn dissolution, differences in conductivity values are related to production of different by-products with different solubilities (see Table 5.1).

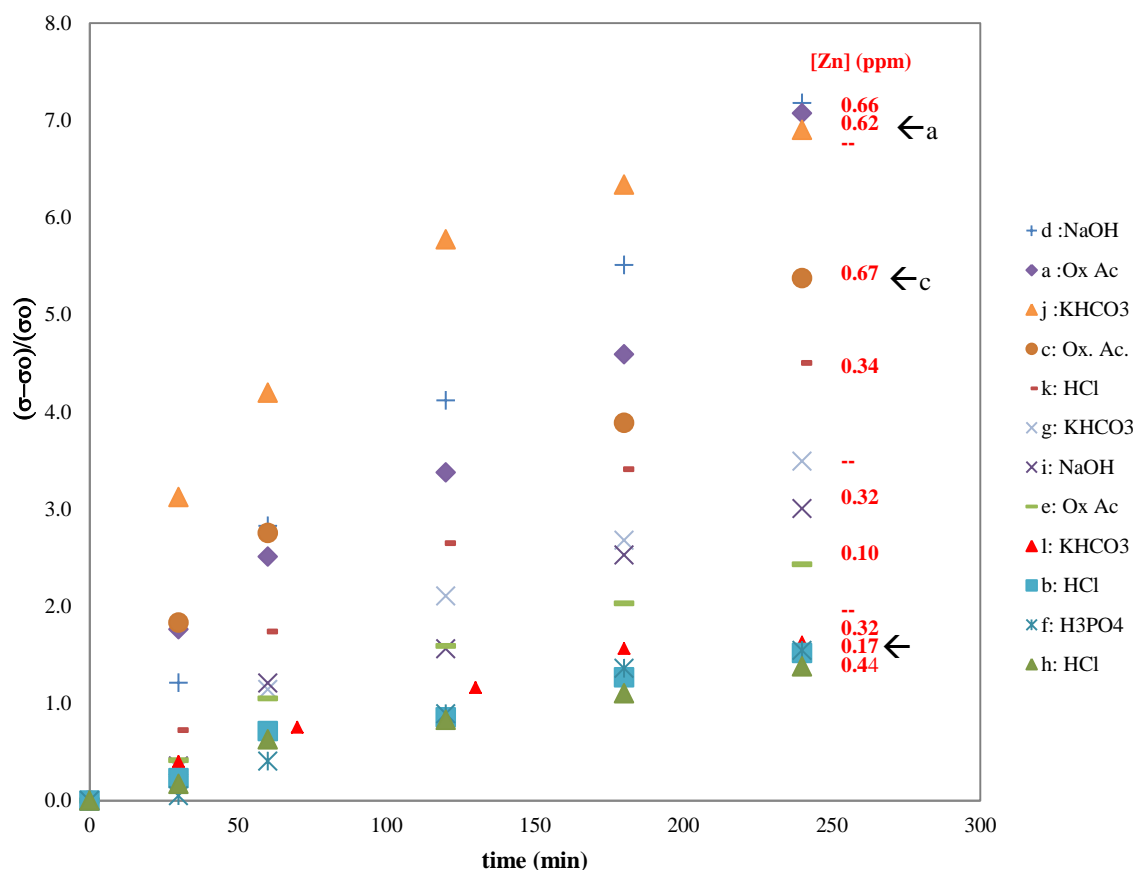
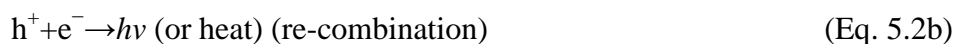


Figure 5.17 Changes in conductivity and final value of dissolved Zn produced during photocatalytic degradation of phenol with different ZnO-NFs. The nomenclature used in this figure is the same as Figure 5.10 and includes the electrolyte used during the production of the ZnO-NFs by anodization.

5.3 Stability of ZnO-NFs morphology during photocatalytic reactions.

The main constraint to the extensive use of ZnO as a photocatalyst is its instability in water and its photo-corrosion [127]. The erosion and deactivation of ZnO has been attributed to either the formation of Zn(OH)₂ once it is exposed to water [127], or to the changes in morphology from the use of its molecular oxygen (from the crystal lattice) during photocatalysis [153]. Therefore, external factors such as the oxygen level and pH

have an effect on the stability of the photocatalyst. In addition UV light accelerates the dissolution of ZnO. It has been suggested that residual photo-generated holes on the ZnO surface could attack the Zn-O bond dissociating Zn^{2+} as it is displayed in equations 5.2(a-c) [231].



The numbers of electron-holes are directly proportional to the number of photons that reach the ZnO surface which are also proportional to the intensity of the light. Therefore, higher intensities of incident light result in a higher ZnO dissolution rate [231].

This section, will discuss the stability of the ZnO-NFs under different oxygen levels, the formation of new nanostructures during the photocatalytic reaction and alternative post-treatments that might improve the stability of the ZnO-NF.

5.3.1 Effect of Oxygen level on the morphology of ZnO films during photocatalytic reactions

Oxygen plays an important role in photocatalysis as it is needed for the oxidation of compounds and for the formation of reactive oxygen species. During photocatalytic reactions, oxygen from different sources is present i.e. dissolved oxygen (DO) from the water solution, oxygen from the ZnO material and molecular oxygen from the dissociation of water. Despite some studies have reported the concentration of DO during photocatalytic experiments for depuration of water pollutants [310][153], it is still not clear the origin of oxygen that is used for the photocatalytic degradation of those contaminants (see Section 2.2.4). Although the effect of different levels of DO on the stability of the photo-catalyst morphology has been discussed before, to the authors knowledge, anoxic conditions in photocatalysis have not been reported yet. Therefore, the present section presents the first analysis of photocatalytic degradation of phenol under anoxic conditions.

The Photocatalytic degradation of phenol was performed at three different levels of dissolved oxygen including a non-saturated DO solution, a saturated DO solution and anoxic conditions. The phenol solution was saturated with DO by bubbling air continuously while the non-saturated DO conditions were obtained by natural absorption of oxygen from the environment in the open batch reactor. For the anoxic experiment, a minimal level of DO was obtained by flowing argon into the phenol solution before and during the 4 hours reaction; in addition, these experiment was carried out in a closed-bag inflated with argon to avoid potential dissolution of oxygen from the environment (Figure 5.18). All experiments were carried out using ZnO-NFs obtained with KHCO_3 [0.05M] at 10 °C 1V for 1 hour of anodization reaction and exposed to thermal post-treatment at 350 °C for 1 hour with heating rate of 1 °C/min.

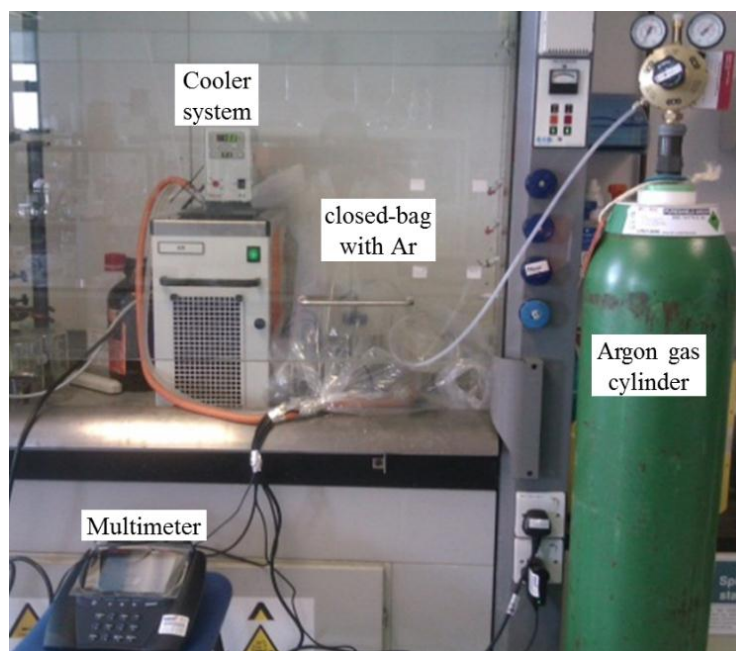


Figure 5.18 Set up of the photocatalytic experiment at anoxic conditions.

The concentration of DO was monitored throughout the reactions and the results are displayed in Figure 5.19-b. Experiments with and without air flow (saturated and unsaturated) displayed similar values of DO, it was due to a high absorption of oxygen by the phenol solution caused by the stirring. During the first hour of photocatalysis at anoxic conditions low levels of DO (less than 1 mg/mL) was observed in solution. Figure 5.19-a shows the degradation of phenol at different levels of DO. After the first hour, all the experiments showed similar degradation of phenol regardless of the level of DO.

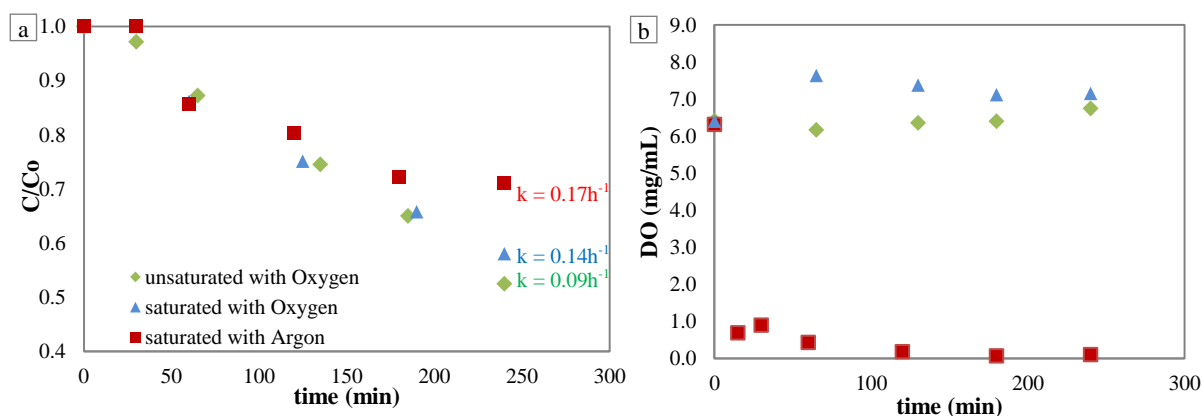


Figure 5.19 OD concentration measured throughout the photocatalytic reaction (a). Photocatalytic degradation of phenol under different oxygen dissolved conditions (b).

Phenol was partially degraded under anoxic conditions where the concentration of phenol decreased by 30%. In anoxic conditions, the reaction rate is mass-transfer-limited by the supply of oxidant, therefore, the reaction might follow the Mars-van Krevelen (MvK) mechanisms where the oxidation of phenol occurs using oxygen from the ZnO lattice (see Section 2.2.3). After 180 minutes, the reaction rate declines presumably due to the deficiency of available oxygen from the ZnO structure. A regeneration of the ZnO might occur when the lost surface oxygen from the lattice is replaced by dissolved oxygen [311]. However, as the DO was negligible in this experiment, this self-protective mechanism of regeneration becomes minimal leading to high corrosion of the photocatalyst or low degradation of phenol due to the lack of oxidant (electron acceptor).

Experiments with higher levels of oxygen displayed higher degradation of phenol due to the dissolved oxygen acting as an electron acceptor [312], [313]. The reaction conducted under saturated and unsaturated DO conditions showed similar results with values of degradation of phenol ranging between 50 and 55% after 4 hours of reaction. The latter results agreed with those from the study conducted by Ali *et al* [299] with ZnO films, where similar photocatalytic degradation of methylene blue was obtained under oxygen rich and oxygen-limited conditions. The results in the present study indicated that the requirement of oxygen for the oxidation of phenol is satisfied even at low concentrations of dissolved oxygen and therefore an excess of oxygen does not have any favourable effect on the reaction rate.

To study the effect of the DO on the morphology of the ZnO-NFs, FESEM micrographs were taken before and after photocatalytic degradation of phenol (Figure 5.15). The initial morphology of each ZnO-NF was a collection of nanowires distributed semi-homogeneously along the surface and with a star-like structures formed for the accumulation of nanowires in one area (Figure 5.20-a). After the reaction under anoxic conditions, the main features of the nanowire structures remained but the nanowires were partially covered with an extra layer of material presumably deposition of Zn(OH)₂ (Figure 5.20-b). It is assumed that ZnO nanostructures were preserved under anoxic conditions due to the minimal photocatalytic activity, suggesting that photo-corrosion of ZnO is higher when photocatalytic processes occur.

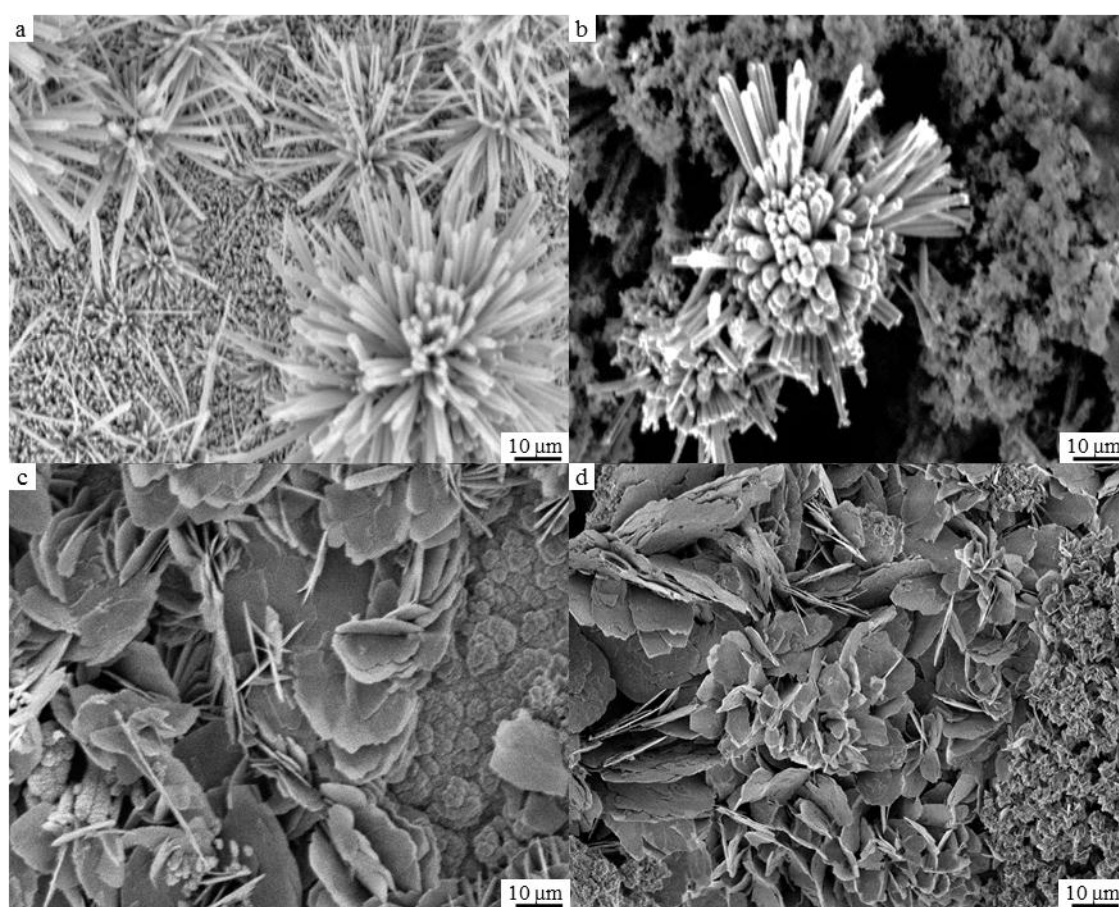


Figure 5.20 FESEM micrographs of ZnO morphologies before and after photocatalytic degradation of phenol. (a) Initial morphology; (b) reaction without Oxygen saturated with Argon; (c) unsaturated with oxygen; (d) saturated with oxygen.

On the other hand, reactions which occurred under unsaturated and saturated DO conditions showed a total alteration of the initial nanowire morphology shape (Figure 5.20-c and 5.20-d). It was found that during the photocatalytic degradation of phenol, new flake-like nanostructures were formed. Additionally, it was observed that a high

level of DO leads to the formation of bigger flake-like nanostructures. No similar results of variation of morphology produced during the photocatalytic reaction were found in the literature. Studies have reported that high levels of dissolved oxygen protect the ZnO nanostructures as it avoids the use of oxygen from the ZnO lattice during photocatalytic reactions[299], [309] which are not in accordance with the findings of the present study.

Further analysis of the flake-like nanostructures showed that their composition was a combination of ZnO and Zn(OH)₂ (Table 5.3). The composition of nanostructures formed during the experiments under unsaturated and saturated DO is similar, suggesting that the changes produced by different DO levels are mainly morphological. Additionally, about 25% of the composition resulted to be carbon. As the photocatalytic process involves adsorption of the organic pollutants, the carbon found is attributed to traces of phenol and phenolate intermediates adsorbed on the photo-catalyst. Finally, the composition analysis revealed traces of iron which are attributed to minimal dissolution of the cathode. These traces do not affect the photocatalytic performance of the ZnO, since the proportion of iron is minimal so no photo-Fenton effects were considered.

Table 5.3 Composition of ZnO films after photocatalytic degradation of phenol under different dissolved oxygen conditions

	C 1s %	Fe 2p %	O 1s %	Zn 2p %
Unsaturated DO	23.1	1.3	54.5	21.1
Saturated DO	26.5	1.0	52.3	20.1

Measurements of Zn concentration by atomic absorption confirmed the presence of Zn in the phenolic solution. Variations (increases and decreases) in the concentration of dissolved Zn(II) indicated that, during the photocatalytic reaction, some ZnO was dissolved. The Zn²⁺ ions then reacted with the dissolved oxygen forming fresh Zn(OH)₂ and ZnO which are re-deposited on the top of the film forming the new nanostructures.

An increase in the conductivity was observed for all the experiments (Figure 5.21). The experiments conducted under anoxic conditions display the lowest increase in conductivity followed by the experiment with air flow (saturated DO). Since the final concentrations of dissolved Zn in all the experiments were similar with values ranging

between 4.5 to 5.0 ppm; the differences of changes in conductivity are mainly attributed to level of degradation of phenol expressed in formation of ionic by-products and CO₂ as discussed before.

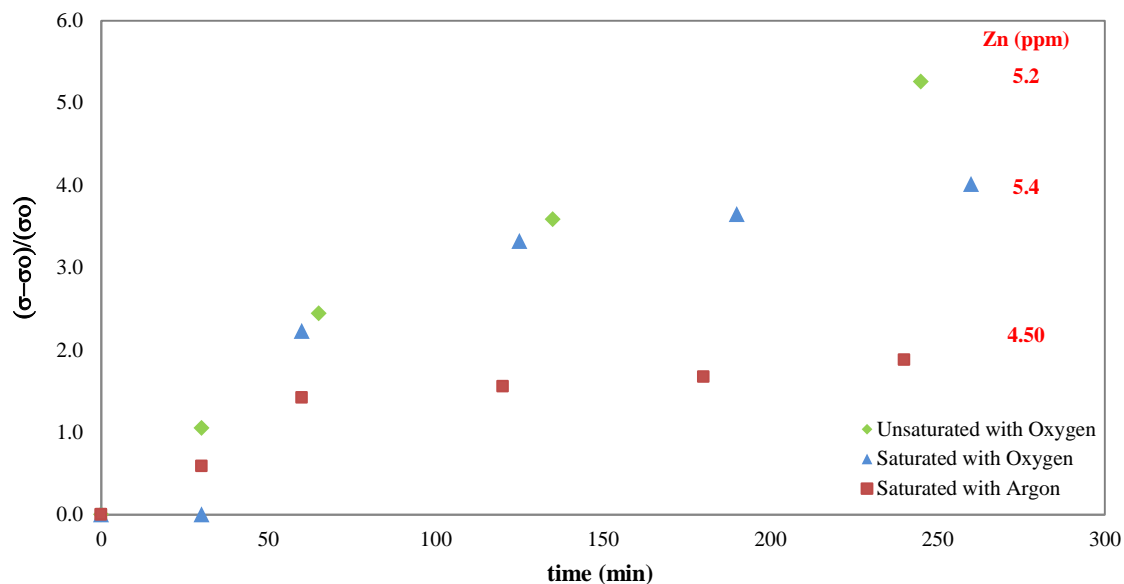


Figure 5.21 Changes in conductivity measured along the photo catalytic reactions with different oxygen dissolved conditions.

5.3.2 Formation of new ZnO nanostructures during photocatalytic reaction.

During the photocatalytic reactions at different DO levels (section 5.3.1) and with different morphologies (section 5.2.1), the formation of new nanostructures was observed on the film surface. To have a better understanding of the mechanism that controls this process, a new set of experiments and analysis was carried out. Initially, a piece of Zn foil was exposed to air for 24 hours leading to the formation of a natural ZnO layer; simultaneously two other pieces of Zn foil, with the same dimensions, were immersed in deionised water for 24 hours. One of the pieces immersed in water was irradiated with UV light. FESEM micrographs of the films were taken before and after of the water immersion and changes in the conductivity of the water during the first 5 hours of the experiment were recorded.

FESEM micrographs revealed that the initial Zn foil (Figure 5.22-a) was covered by a featureless ZnO layer. Zn foil immersed in water (Figure 5.22 b-c), on the other hand, showed a formation of particles on the top of the surface. The sizes of these particles varied between 0.20 μm and 0.50 μm and had quasi-spherical shapes. UV light did not

inhibit the formation of the particles in water, but it affected the number of particles per area and the texture of the nanostructures surface. Nanoparticles exposed to UV light (Figure 5.22-c) have a rougher surface compared to those without UV exposure (Figure 5.22-b). High values of conductivity for the experiment with UV light suggests a high dissolution of Zn ions caused by light, and therefore the difference in surface texture is likely to be caused by photocorrosion.



Figure 5.22 FESEM micrographs of Zn foil exposed to different external environments. Zn foil exposed to air (a); Zn foil immersed in deionised water (b); Zn foil immersed in deionised water with UV irradiation (c).

According to evidence about the corrosion mechanisms of Zn [239], and based on the thermodynamic speciation of Zn(II) presented in Figure 4.2, it is suggested that once the Zn foil is exposed to deionised water, the thin natural layer of ZnO and the Zn(II) itself dissolved forming Zn^{2+} ions which react with oxygen forming ZnO and $Zn(OH)_2$. Additionally, once the concentration of Zn(II) reaches a certain threshold concentration

a re-precipitation on the top of the foil occurs. Although the mechanism of dissolution of Zn^0 and deposition of ZnO and $Zn(OH)_2$ is similar to the one suggested in section 5.3.1 for the formation of flake-like nanostructures, the formation of nanostructures in pure deionized water is different as it does not involve redox reactions.

Similar experiments to the previous ones with Zn foil were conducted with ZnO-NFs immersed in water and phenol solution. In the presence of phenol, the morphology tends to varied dramatically, while in water ZnO-NFs were slightly modified with only a deposition of ZnO on the surface of the nanowires (this deposition will be extensively discussed in Section 5.3.3). ZnO-NFs appear to be more stable in water (even when are exposed to UV light) due to the absence of processes associated to photocatalytic reactions than occur on the surface of the photocatalyst.

The morphologies of different ZnO-NFs were analysed before and after being exposed to a photocatalytic experiment, and the micrographs are presented in Figure 5.23 and Figure 5.24. FESEM micrographs revealed that the initial morphology of the ZnO-NFs serves as a template for the final shape of the new nanostructures. As a result, flat ZnO layers tend to form small flake-like morphologies (Figure 5.23-c and 5.23-e); nano-wires tend to turn into nano-flakes like structures (Figure 5.24-g, 5.24-j and 5.24-l), and 2D morphologies such as flakes and flower-lake morphologies turn into highly dense, porous sponge-like structures as it can be observed in Figure 5.23-a, 5.23-b, 5.24-h, and 5.24-k. Amorphous structures observed in Figures 5.23-d and 5.23-i resulted in similar shapes but bigger nanostructures after the photocatalytic reaction.

It is evident that another factor that affected the initial morphology of the ZnO-NFs is the mechanical abrasion produced during the agitation process. Agitation plays an essential role during photocatalysis as it assures adequate mass transfer between the pollutant and oxygen present in the water and the photo-catalyst. Experiments that were carried out without any type of stirring resulted in a significantly lower degradation of the Phenol and in a lower modification of the initial morphology of the photocatalyst.

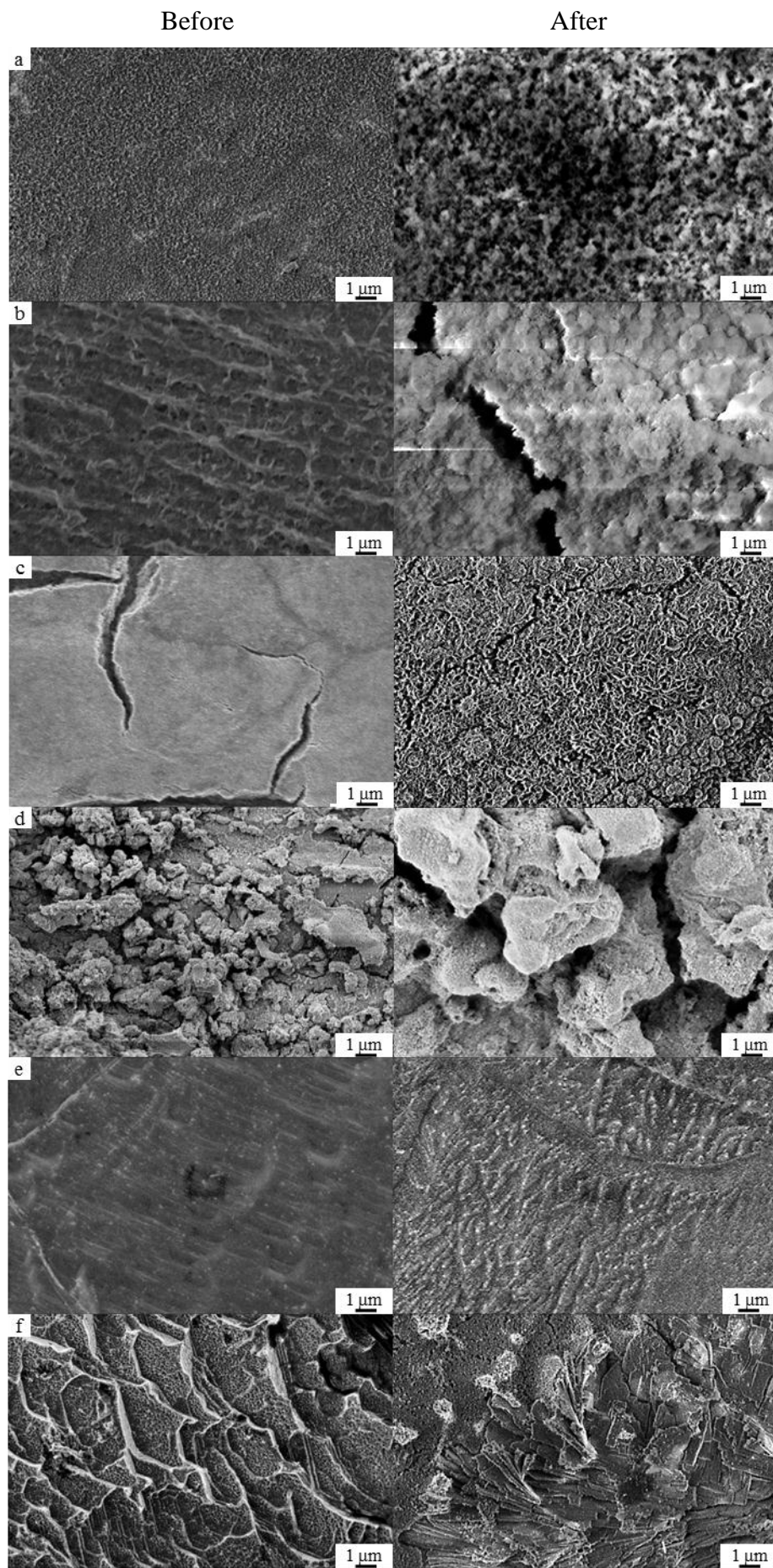


Figure 5.23 FESEM micrographs of ZnO-NF before (left) and after (right) photocatalytic experiments, showing the formation of new nanostructures.

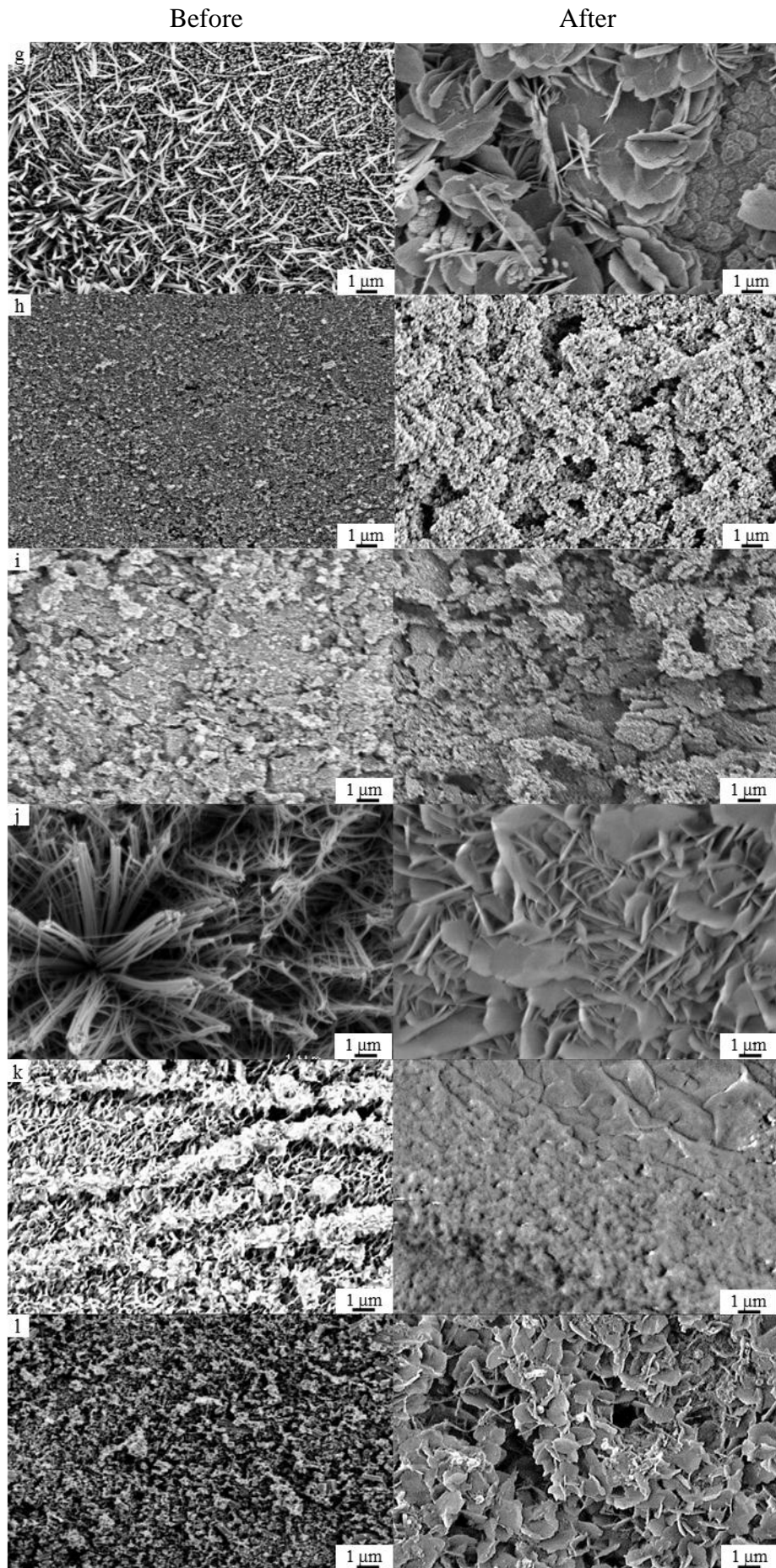


Figure 5.24 FESEM micrographs of ZnO-NF before (left) and after (right) photocatalytic experiments, showing the formation of new nanostructures.

The apparent “stability” of the ZnO-NF morphologies in those experiments is attributed to the lack of mechanical abrasion and the minimal use of the photo catalyst due to mass transfer limitation and lack of oxidation reactions.

5.3.3 Alternative post-treatments

Based on the results obtained by immersing Zn foils in deionised water (see Section 5.3.2) and with the aim of increasing both the surface area and the photo-active surface area of the ZnO-NF, additional ZnO nanostructures were deposited on the top of the initial nanowires. ZnO-NFs (nanowires) were immersed in water for 24 hours in darkness followed by a dry process and a thermal post-treatment at 350 °C for 1 hour in air. Figure 5.25-a shows the FESEM micrograph of the initial morphology with a nanowire configuration. Figures 5.25-b and Figure 5.25-c show the deposition of a new layer on the top of the initial nanostructures. EDX analysis confirmed that the new layer was composed of Zn and oxygen. Higher magnification of the FESEM micrographs (Figures 5.25 d-f) revealed a homogeneous deposition of new quasi-spherical nanostructures on the surface of the nanowires similar to those observed in Figure 5.22-b. As discussed before, the absence of redox reactions results in the deposition of new nanostructures without affecting the initial morphology of ZnO nanowires.

The ZnO-NFs treated with the new nanostructures were used as a photo catalyst for the degradation of phenol. Despite the potential increase in the surface area of the photo-catalyst caused by the new nanostructures, no significant improvement in the photocatalytic performance was achieved. The degradation of phenol after 4 hours was similar to the experiments using standard ZnO-NFs (not immersed in deionised water) as shown in Figure 5.26. This result supports the hypothesis of the limited effect of surface area in photocatalysis [133][299][300] and strengthens the hypothesis of the importance of the photo-active surface area. Since the new nanostructures deposited in the ZnO-NF showed a denser configuration, there was an effect of light scattering that limited the use of the total surface area of the photocatalyst. As a result, the potential enhancement in photocatalysis given by a larger surface area is negatively compensated by a lower photo-active surface area.

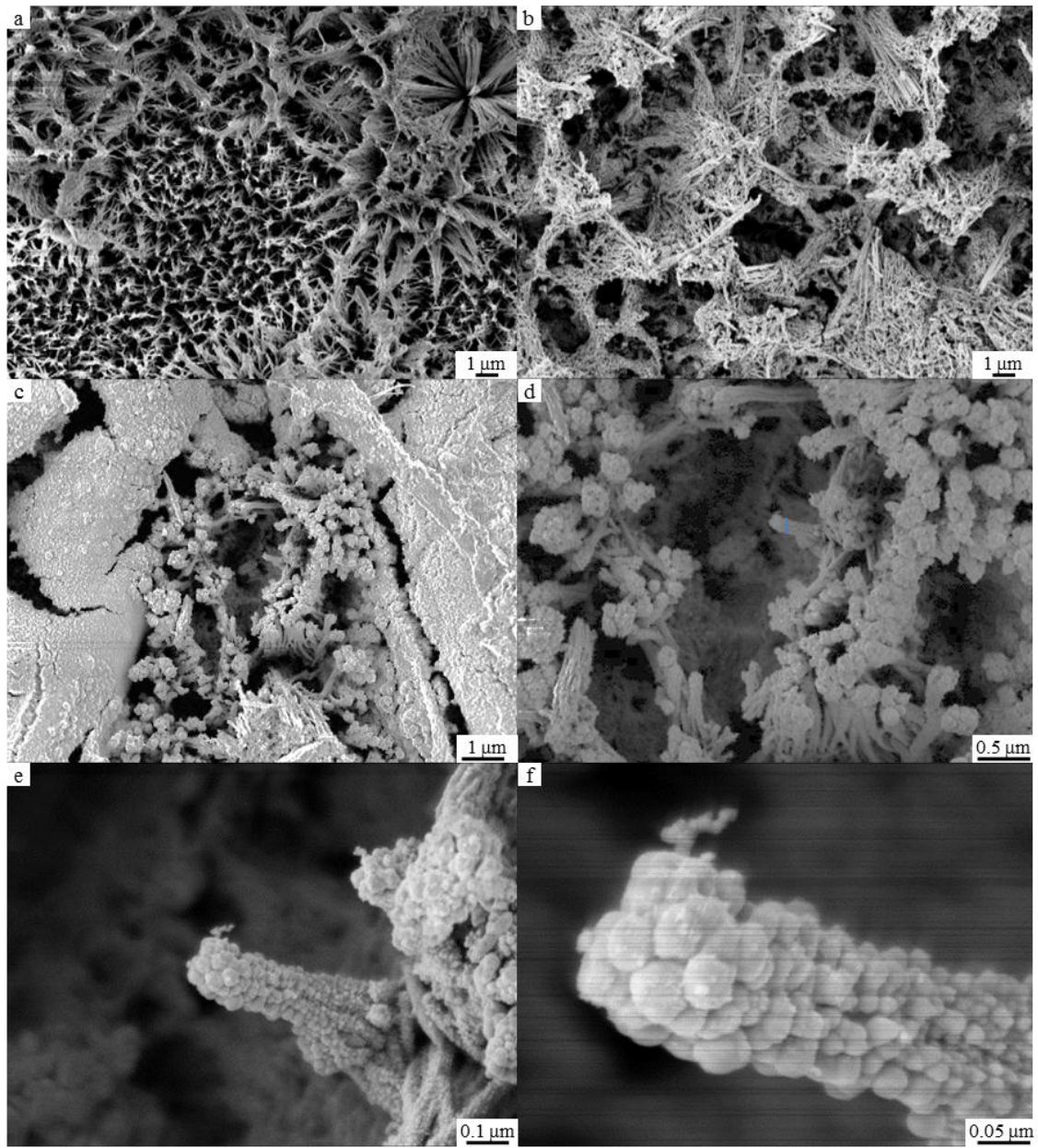


Figure 5.25 FESEM micrographs of Zn-NF before (a) and after (b-e) deposition of new nanostructures on the surface of nanowires. (The new nanostructures are shown at different magnifications)

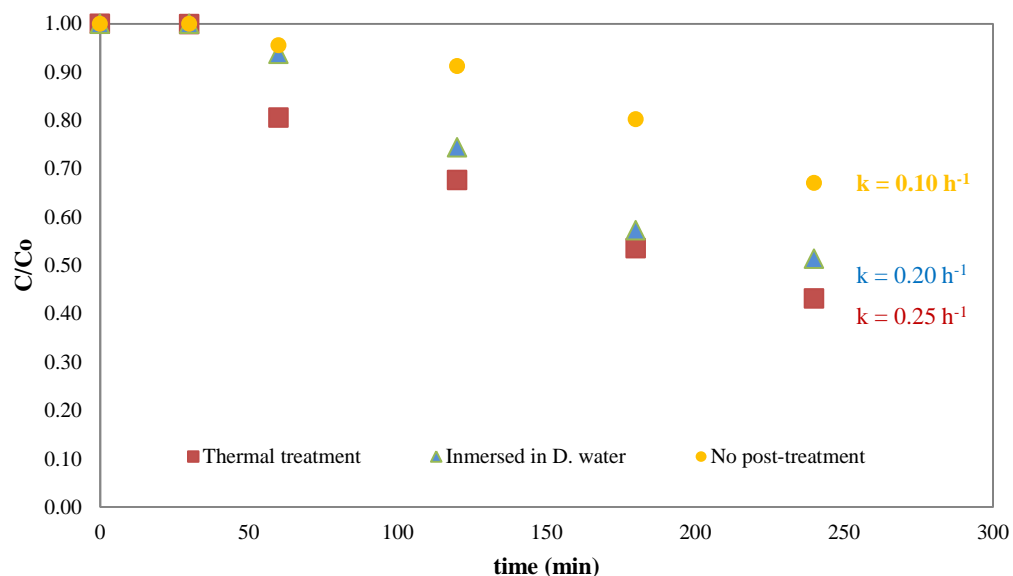


Figure 5.26 Comparison of the photocatalytic performance of ZnO-NFs with and without deposition of new nanostructures on the surface of the nanowires (photocatalytic degradation of phenol).

Another post-treatment investigated in this work was oxygen plasma. As discussed before, thermal post-treatments vary the crystallinity of photocatalyst and change the surface texture of the nanowire while improving the photocatalytic performance of the ZnO-NFs (see section 4.11). However, the post-annealing treatment involved some challenges that might limit the production of homogeneous ZnO layers: After post-annealing some of the ZnO-NFs displayed cracks in their surface and occasionally the ZnO layer peeled off exposing the Zn foil as shown in Figure 5.27. These issues were likely to be produced by the different linear thermal expansion coefficients of the two materials ($29.7 \times 10^{-6} \text{ m/(m K)}$ for Zinc and $7.47 \times 10^{-6} \text{ m/(m K)}$ for ZnO)[314] and the growth of the crystallites at high temperature. To overcome this issue, an oxygen plasma post-treatment was tested.

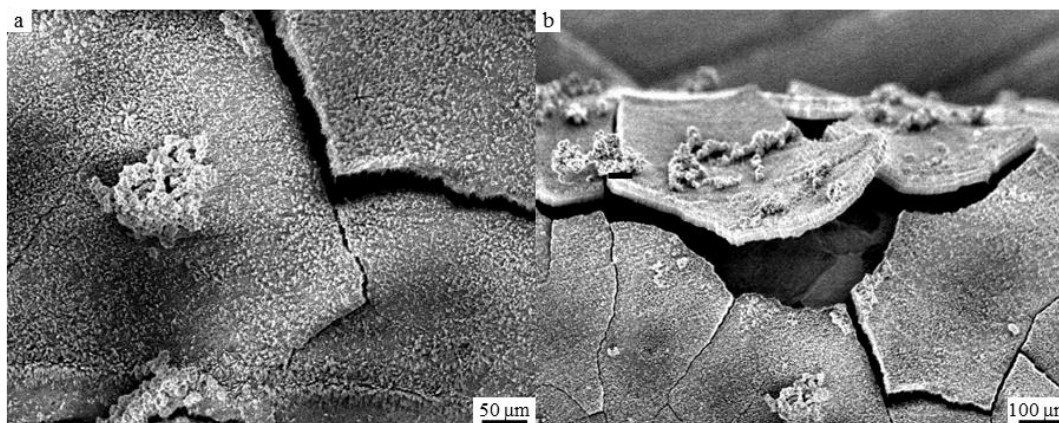


Figure 5.27 FESEM micrographs of Zn-NF displaying cracks (a) and loose of the ZnO layer (b) due to thermal post-treatment

ZnO-NFs were exposed to plasma-treatment with oxygen for 20 minutes. Regardless of the morphology or thickness of the ZnO-NFs, all the films displayed homogeneous ZnO layers after being exposed to the plasma treatment and neither visible cracks nor detachments of the ZnO layer were observed as shown in Figure 5.28 .

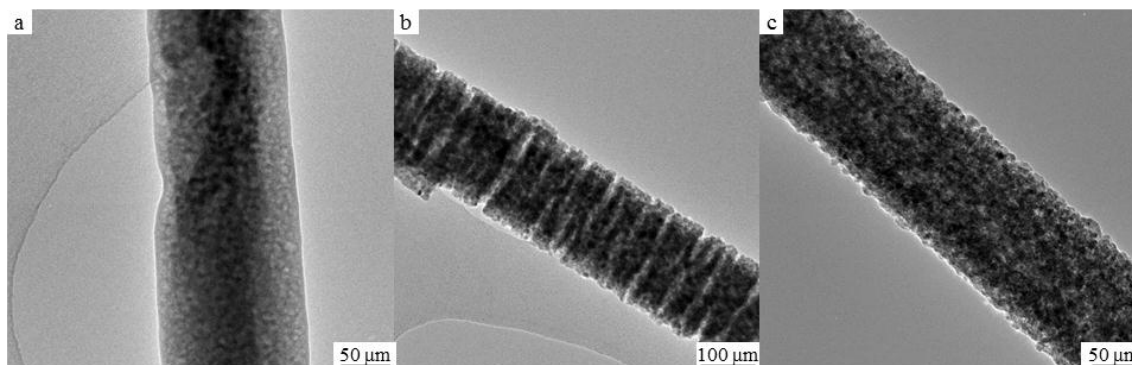


Figure 5.28 TEM micrographs of ZnO films obtained with KHCO_3 [0.05M], 1V, 10C, 1h exposed to different post-annealing: with not post treatment (a); thermal post-treatment at 350 °C for 1 h (b); oxygen plasma post-treatment (c).

In terms of morphology, no differences were found after the oxygen-plasma post-treatment. The photocatalytic degradation of phenol using the ZnO-NF treated with plasma result in 12% enhancement of the photocatalytic activity compared to similar films treated with heat, and 36% enhancement compared to ZnO-NFs with no post-treatment as shown in Figure 5.29.

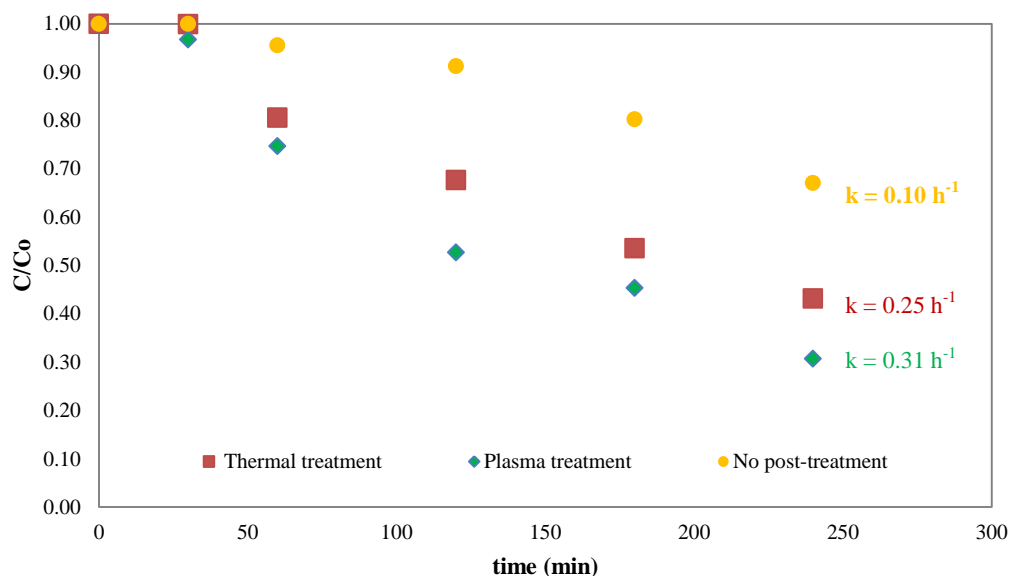


Figure 5.29 Comparison of the photocatalytic performance of ZnO-NFs exposed to thermal post-treatment and oxygen plasma post-treatment

After the photocatalytic reaction, the morphology of the ZnO-NF did not show strong variation apart from the deposition of a new ZnO layer on the top of the nano-wires. Unlike the homologous ZnO-NFs that were post-annealed, no formation of flakes-like nanostructures occurred, indicating that this post-treatment provides more stability to the photocatalyst (Figure 5.30).

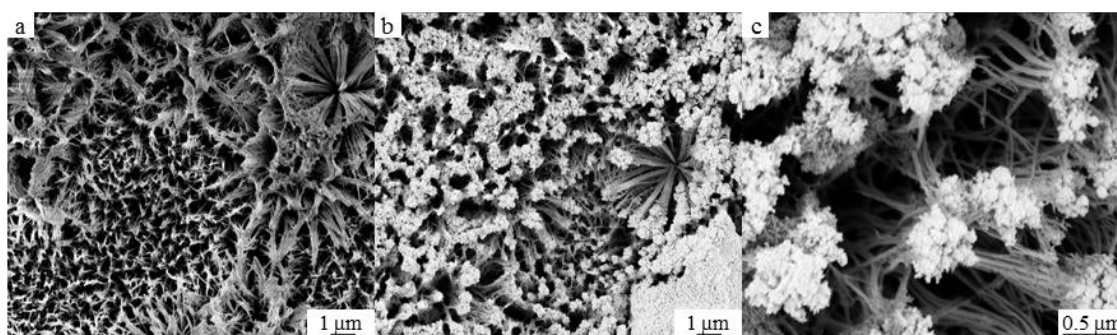


Figure 5.30 FESEM micrographs of Zn-NFs (post-treated with oxygen plasma) before (a) and after (b-c) photocatalytic degradation of phenol

During oxygen plasma treatment, the amount of photocatalyst increased as $\text{Zn}(\text{OH})_2$ turned into ZnO and changes in oxygen surface occurred varying the hydrophobicity of the ZnO-NFs [315]. Optical studies have also suggested that oxygen plasma suppresses the presence of chemisorption sites (oxygen deficiency sites) and oxygen

vacancies[316]. Based on this, the enhancement of the photocatalytic activity of the ZnO-NF is attributed to changes in crystallinity produced by oxygen plasma treatments as observed by XRD analysis (Figure 5.31). The increase in stability of the photocatalyst morphology occurred mainly due to the minimal thermal stress suffered by the material which results in low dissolution of the material. As observed in Figure 5.32, the final value of dissolved Zn in the reaction with film treated with oxygen plasma is considerable lower than the experiment with the post-annealed film, which agreed with the morphological stability discussed before.

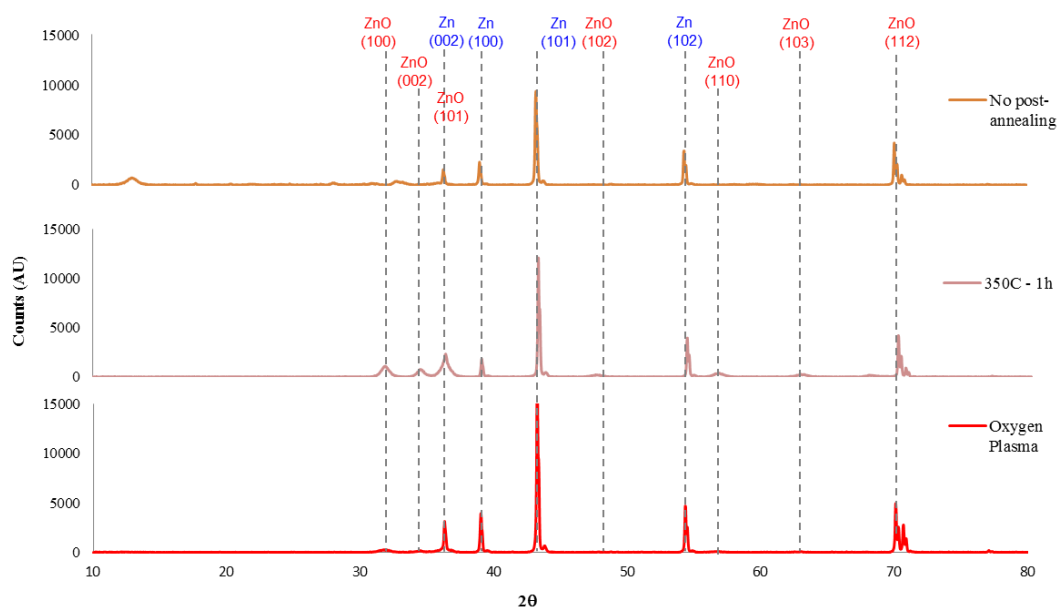


Figure 5.31 XRD of ZnO films obtained with KHCO_3 [0.05M], 1V, 10C, 1h exposed to different post-annealing: with not post treatment; thermal post-treatment at 350 °C for 1 h; oxygen plasma post-treatment.

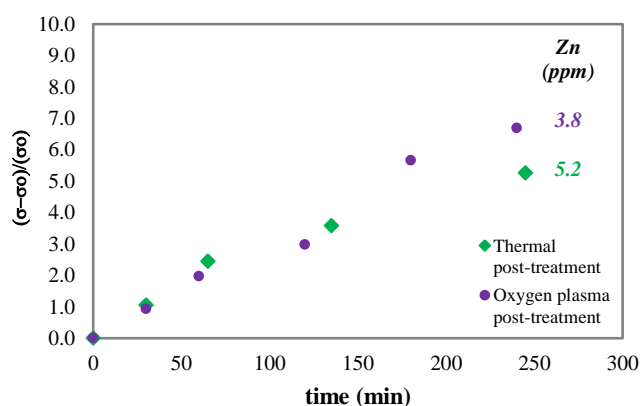


Figure 5.32 Changes in conductivity measured along the photo catalytic reactions with different post-treatment. (Colour font show the final concentration of dissolved Zn in the phenol solution)

5.4 Summary

This chapter investigated the photocatalytic performance and stability of ZnO-NFs produced by anodization of Zn, using phenol as a model compound and performing the reactions in a batch reactor. The first section discussed the preliminary experiments where the kinetic reactions of photolysis and photocatalysis of the phenol in the batch reactor were established. It was found that photolysis of phenol in this reactor was less than 10% and the main by-products identified during the photocatalytic degradation of phenol were catechol and benzoquinone. The reaction rate of phenol obeys pseudo-first order kinetics while the TOC degradation followed pseudo-zero order kinetics. In the second section, the effect of crystallinity and morphology of the ZnO-NFs was investigated. It was found that crystal size does not affect the photocatalytic performance of the films while the morphology has an important impact on the degradation of phenol. It was suggested that the main factor that influences the photocatalysis is the light absorbance capacity of the ZnO-NF, which determines the active photocatalytic surface area and it is function of films morphology. Finally, the stability of the ZnO-NFs was tested under different oxygen levels including anoxic conditions. Degradation of phenol occurred even at very low oxygen conditions where the degradation of phenol, according to other authors, follows the Mars-van Krevelen mechanism. Additionally, the formation of new nanostructures that were produced during the photocatalytic reaction was studied and a mechanism of formation was proposed. It was demonstrated that oxygen plasma post-treatment enhances the photocatalytic activity of the ZnO-NF by 36% while making the photocatalyst more stable for the photocatalytic degradation of phenol.

*“You never change things by fighting the
existing reality.
To change something, build a new model that
makes the existing model obsolete.”*
R. Buckminster Fuller

Chapter 6: Alternative reactors to study the photocatalytic performance of ZnO nanostructures.

As discussed in Chapter 5, the stirred batch reactor showed some limitations for photocatalytic processes resulting in low degradation of phenol (less than 70% after 4 hours of reaction). Variation of the batch system can enhance the degradation of organic compounds and provide alternatives to study the stability of the photocatalyst under different flow regimens [317]. This Chapter discusses the design of two alternative types of reactors used in a recirculated batch systems and their use with the supported ZnO nanostructures. The first type of reactor was a flat plate photocatalytic reactor (FP-PCR). For this type of reactor two models were built; one made with stainless steel and another with epoxy acrylic. The FP-PCRs were intended to study the photocatalytic performance of the ZnO-NFs under laminar and turbulent flow conditions. However, mass transfer limitations (discussed in this Chapter) prevented achieving this target. A tubular annular photocatalytic reactor (TA-PCR) was also designed and ZnO nanostructured wire (ZnO-NW) was used as photocatalyst. The photocatalytic activity and morphological stability of the ZnO-NFs and ZnO-NWs were tested during the photodegradation and photocatalytic degradation of phenol (used as a model compound). Additionally, in preliminary work, ZnO was deposited on optical fibers for future applications in photocatalysis. The experiments reported in this Chapter were carried out with the aim of studying the stability of the ZnO nanostructures and therefore no kinetic analysis were considered during the tests.

6.1 Photocatalytic reactors for ZnO-NF_(s) studies.

As discussed in Section 2.2.6 (*photocatalytic reactors*), the majority of the studies related to the design of photocatalytic reactors have been focused on slurry reactors and only few models have been proposed for supported photocatalysts. Slurry reactors (conventional and thin-film), where the catalyst is dispersed in the media, provide high surface to volume ratios that allow high contact between the photocatalyst and the molecules of pollutants facilitating the photocatalytic reaction [98]. However, light-related factors such as the optical thickness (τ) (known also as opacity of the photoreactor) and the scattering albedo (ω) given by the photocatalyst in suspension limit the use of larger amount of photocatalyst and make the radiation absorption-scattering modelling complex [100].

As discussed in Chapter 5, the photocatalytic degradation of phenol obtained with the stirred batch reactor was less than 70%, and the total degradation of organic compounds measured by TOC was only 50% after 4 hours of reaction. Additionally, the morphology of the ZnO-NFs suffered from photocorrosion and mechanical abrasion, and the formation of new nanostructures was also observed. Since photoreactions proceed rapidly in reactors with a small volume of irradiated solution, micro reactors are a good solution as they have a remarkably large surface-to-volume ratio compared with conventional batch reactors [107]. Therefore, for the design of the new photocatalytic reactors, small volumes were preferred.

Two flat plate photocatalytic reactors (FP-PCR) were designed and used in the photolysis and photocatalytic degradation of methyl orange and phenol. The reactors (one made on stainless steel and the other with an epoxy acrylic based material) were designed to work with constant recirculation of the model compound solutions. During the experiments the solution was kept in an external jacketed beaker (reservoir) provided with a magnetic stirrer where temperature was controlled using a water cooled cell (Thermo Scientific HAAKEC 10-K10). Oxygen was supplied by flowing air into the reservoir and additional measurements such as pH, conductivity and Dissolved oxygen (DO) were measured using a benchtop multiparameter (Meter set Versa Star®) (Figure 6.1).

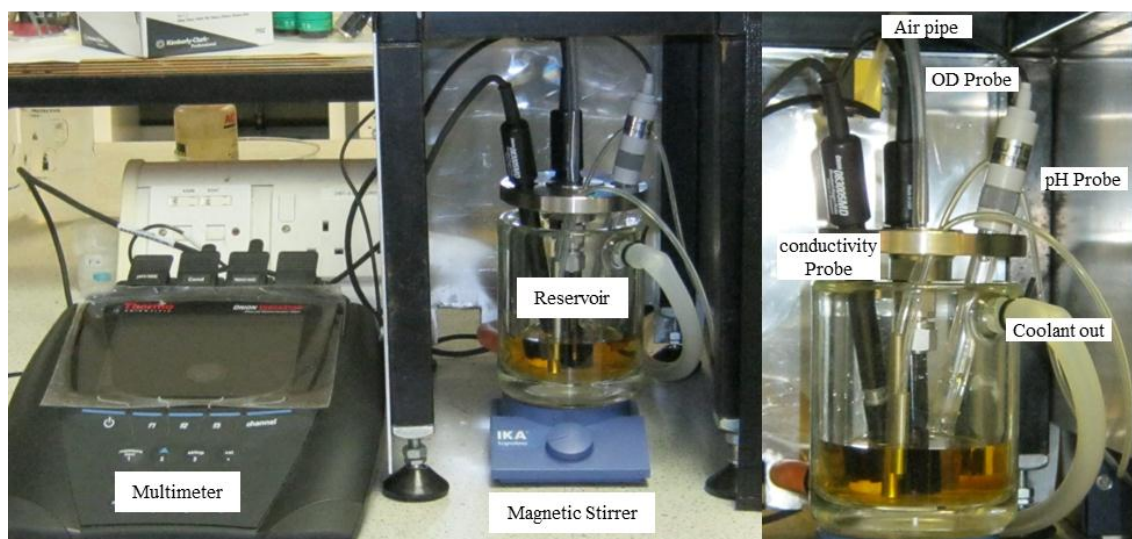


Figure 6.1 Reservoir and multi-meter used in the photocatalytic setup.

The whole setup was placed in a two chamber metallic box to avoid human exposure to the UV light. The largest chamber was used as the irradiation area where the photocatalytic reactor was placed. The small chamber was used to contain the reservoir with the oxygen supply and the probes for pH, OD and conductivity measurements. In this way the reservoir could be checked and samples could be taken without being exposed to UV light (Figure 6.2).

The model compound solutions were pumped into the reactor by means of a peristaltic pump (Micro-pump magnetically coupled gear pump head GJ series) with a range of flow rates from 30 to 1100 ml/min controlled by a gear pump driver (Ismatec gear pump drive Model MCP-Z Standard). UV light was provided using a UV-lamp (UVG- 54 Handheld UV lamp, 254 nm UV / 6 Watts) and Swagelok fittings were used for connecting the different parts of the set up.

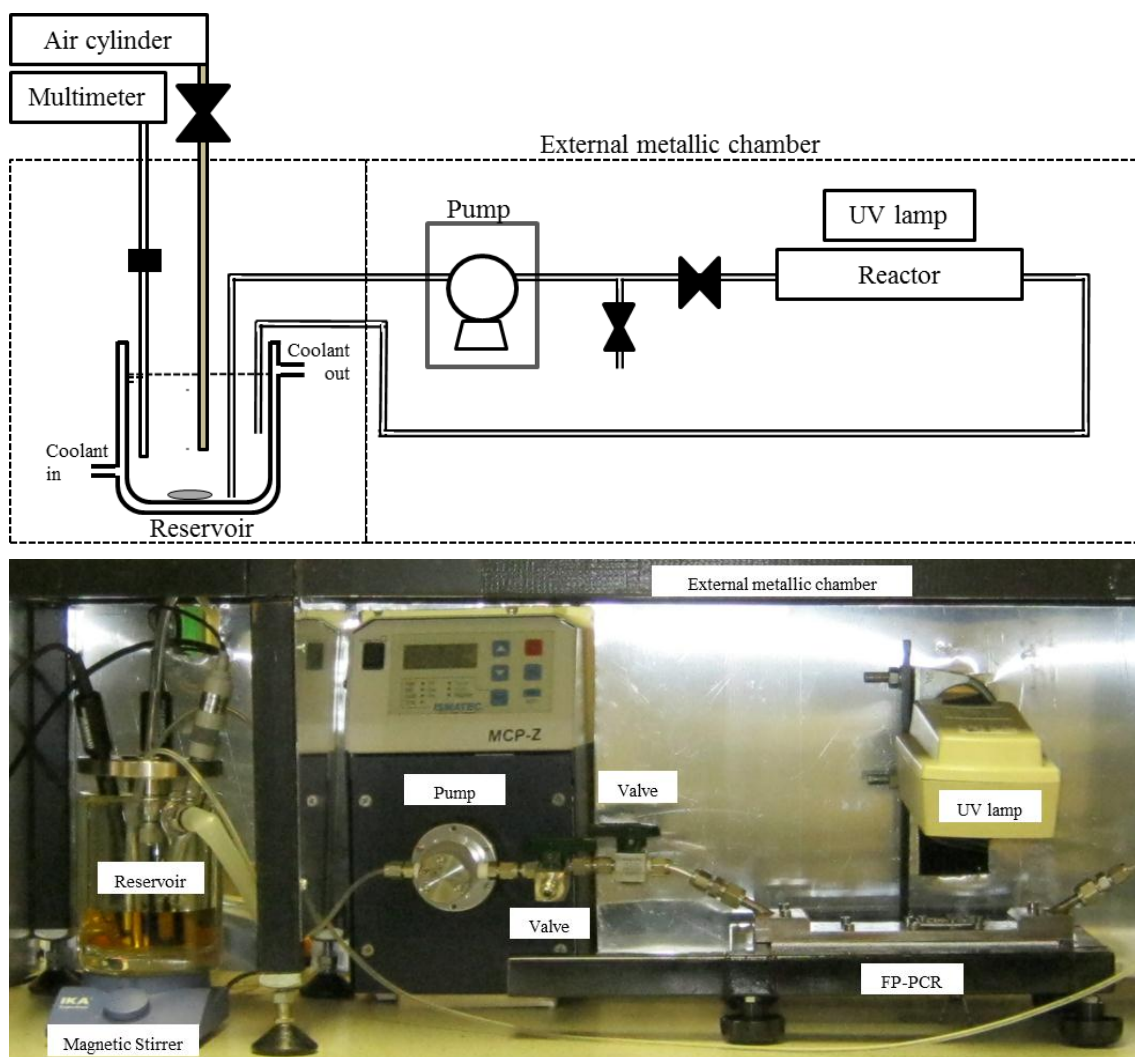


Figure 6.2 Schema (top) and picture (bottom) of the FP-PCR setup

The design guidelines selected for the photocatalytic reactors were:

- a) The reactors were designed to hold the ZnO-NFs produced in the lab (1cm diameter).
- b) Constant light exposition area, therefore all experiments with ZnO-NFs were run under similar conditions of light intensity. Also it guaranteed a constant photolysis area.
- c) Constant and minimal column of water over the catalyst, therefore a potential absorption of light produced by the model compounds was minimal.
- d) Plug-flow regime without dead zones. The reactors were designed to work under a wide range of Reynolds numbers (100-3500). For the range of laminar regime

the entrance length were calculated and used as a guide for the total length of the reactor and position of the catalyst.

- e) The materials of the reactors, pipes and connexions were chemically inert to the selected model compounds.

6.1.1 Stainless steel flat plate batch photocatalytic reactor design

The metallic FP-PR consists of two stainless steel plates with a single channel 1 cm in width, 17 cm in length, and 0.5 mm in depth allocated on the top plate. The bottom plate had a threaded hole with a diameter of 1 cm to screw the ZnO-NF holder. This system allowed installing and removing the ZnO films without opening the reactor which was closed by 8 screws allocated on both sides along the reactor. The entrance and exit of the channel was made of stainless steel pipe (1/4 in) with a slope of 30 degrees (Figure 6.3). A quartz glass 0.5 mm thick, 2 cm long and 1.5 cm wide was placed on the top of the reactor above the ZnO film holder section. The quartz window was sealed with silicone and the top of the frame was closed with screws. The intensity of the light was measured in the reactor with and without the quartz. The value obtained exposing the UV light meter probe directly to the light was 0.836 mW/cm^2 while the light intensity measured through the quartz was 0.824 mW/cm^2 with a reduction in the light intensity of only of 1.4 %.

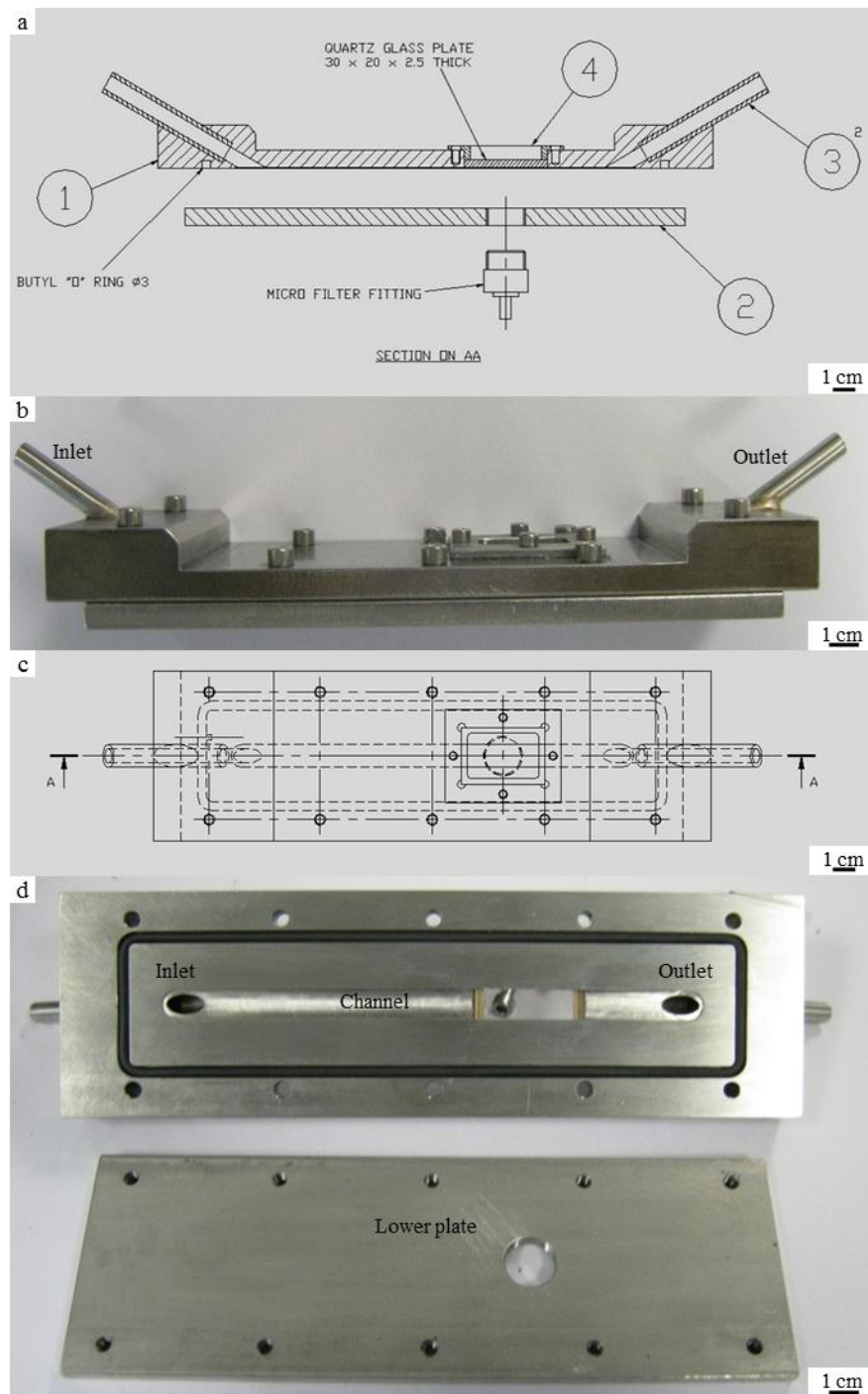


Figure 6.3 schema and picture of stainless steel flat plate batch photocatalytic reactor. Section AA (a); lateral view (b); Section BB (c); upper view (d). Top figure shows different parts of the reactor: top plate (1), bottom plate (2), outlet tubing (3) and quartz window (4)

To ensure a stable flow in the photocatalytic area (below the window), the entrance length (Le) was calculated for different flows and thus different Reynolds number (table 6.1). Le was calculated using Equation 6.1 for laminar flow and Equation 6.2 for turbulent flow where Re is Reynolds number and D_h is the hydraulic diameter [318].

$$Le = 0.06 Re D_h \quad (eq. 6.1)$$

$$Le = 4.4 Re^{1/6} D_h \quad (eq. 6.2)$$

For noncircular tubes and channels D_h is defined as the relationship between the cross sectional area (A) and the wet perimeter (WP) (Eq 6.3):

$$D_h = \frac{4A}{WP} \quad (eq. 6.3)$$

The Reynolds number is defined by the Manning formula (eq. 6.4) where ρ is the density of the fluid (water), v the velocity and μ the dynamic viscosity of the fluid.

$$Re = \frac{\rho v D_h}{\mu} \quad (eq. 6.4)$$

Table 6.1 Entrance length for the FP-PCR calculated at different Reynolds numbers.

Re	v (m/s)	Q (m^3/s)	Q (ml/min)	Le (cm)
3500	3.73	1.49E-05	895.18	1.61
3000	3.20	1.28E-05	767.30	1.57
2500	2.66	1.07E-05	639.41	1.53
2000	2.13	8.53E-06	511.53	11.29
1500	1.60	6.39E-06	383.65	8.47
1000	1.07	4.26E-06	255.77	5.65
500	0.53	2.13E-06	127.88	2.82
200	0.21	8.53E-07	51.15	1.13
150	0.16	6.39E-07	38.36	0.85
100	0.11	4.26E-07	25.58	0.56

In order to work at different laminar flows, the entrance length selected was 11.5 cm and the reactor was designed with a total length of 17 cm. The total residence time (t_{r-t}) of the fluid in the reactor (channel) and the residence time in the irradiation area (t_{r-p}) of the reactor were calculated using the total length of the channel (l_{ch}) and the length of the photolysis area (l_p) using Equation 6.5-a and 6.5-b respectively. The number of times that the total volume of the model compound is recirculated (N_r) after 4 hours varied with the flow rate (see Table 6.2). Additionally, the retention time of the pollutant on the illuminated area is inversely proportional to the flow rate. As a result, the total light exposition (t_{le}) is constant regardless of the flow rate. For instance,

experiments at low flow rates have high retention times and a small number of recirculations (N_r), while experiments at high flow rates have low retention times and a large number of recirculations.

$$t_{r-t} = \frac{l_{ch}}{v} \quad (eq. 6.5a)$$

$$t_{r-p} = \frac{l_p}{v} \quad (eq. 6.5b)$$

Table 6.2 Residences times for the FP-BR calculated at different Reynolds numbers.

Re	v (m/s)	Q (mL/min)	t_{ch} (s)	t_{rp} (s)	N_r (cicle/min)	Cumulative residence time(s)
3500	3.73	895.18	0.046	0.0040	36	0.14
3000	3.20	767.30	0.053	0.0047	31	0.14
2500	2.66	639.41	0.064	0.0056	25	0.14
2000	2.13	511.53	0.080	0.0070	20	0.14
1500	1.60	383.65	0.106	0.0094	15	0.14
1000	1.07	255.77	0.160	0.0141	10	0.14
500	0.53	127.88	0.319	0.0282	5	0.14
200	0.21	51.15	0.798	0.0704	2	0.14
100	0.11	25.58	1.595	0.1408	1	0.14

The head loss (h_f) for the reactor (channel) was calculated using the Darcy-Weisbach equation (Equation 6.6) which is considered valid for ducts regardless their cross section and for both laminar and turbulent flows [318]. In the Darcy-Weisbach Equation, L is the length, g refers to acceleration due to gravity, and f is the Darcy friction factor. For laminar flow $f = f_{lam}$ and is defined by equation 6.7.

$$h_f = f \frac{L}{D_h} \frac{v^2}{2g} \quad (eq. 6.6)$$

$$f_{lam} = \frac{64 \mu}{\rho v D_h} \quad (eq. 6.7)$$

The Pressure drop in the channel (ΔP_r) was calculated using equation 6.8 and results are displayed in Table 6.3.

$$\Delta P_r = \pi r^2 = \rho g h_f \quad (eq. 6.8)$$

The frictional losses (h_{fa}) along the photocatalytic set up were calculated for each section of the circuit (Valves, elbows, and pipes that connect the reactor with the reservoir) using Equation 6.9. The total pressure drop was calculated as the sum of all the pressure drops of the segments (ΔP_a) (Equation 6.10) and the pressure drop in the reactor or channel (ΔP_r) (Table 6.4).

$$h_{fa} = \frac{k v^2}{2g} \quad (\text{eq. 6.9})$$

$$\Delta P_a = \rho g \sum h_{fa} \quad (\text{eq. 6.10})$$

Table 6.3 Head loss and pressure drop for the FP-PCR calculated at different Reynold number

Re	f_{lam}	$h_f (m)$	$\Delta P_r (Pa)$	$\Delta P_r (bar)$
2500	0.04	1.52	14917.61	0.149
2000	0.04	1.22	11934.09	0.119
1500	0.06	0.91	8950.57	0.090
1000	0.09	0.61	5967.05	0.060
500	0.18	0.30	2983.52	0.030
200	0.45	0.12	1193.41	0.012
150	0.60	0.09	895.06	0.009
100	0.90	0.06	596.70	0.006

Table 6.4 Total head loss and pressure drop for the photocatalytic setup calculated at different Reynolds number

Re	Total $h_f (m)$	Total $\Delta P (bar)$
2500	2.22	0.22
2000	1.41	0.14
1500	0.78	0.08
1000	0.34	0.03
500	0.080	0.008
200	0.010	0.001
150	0.0051	0.0005
100	0.0017	0.0002

6.1.2 Preliminary experiments with FP-PCR - Photolysis of Methyl Orange

Methyl orange (MO) was used as model compound for an initial scan to establish the experimental conditions in the FP-PCR and to pre-evaluate the photocatalytic

performance of the ZnO-NFs in this type of reactor. MO, among other azo-dyes, represents an environmental risk due to its bio-recalcitrant nature and toxicity, and therefore degradation studies are important from an environmental point of view [46]. However, the main reason to use MO was the feasibility to measure changes in concentration using a spectrophotometer. Since MO has high capability of light absorption, some of the changes in colour might be produced by decomposition (decolouration) while others might be produced by degradation as will be discussed in this section. As a result, after the preliminary experiments with MO, phenol was used with the selected experimental conditions (results will be discussed in Section 6.5.1). As no analytical studies were performed with MO, changes produced are generically indicated as “decomposition” of the MO.

The photolysis of MO was tested at 123.8 mL/min for different initial concentrations and results are displayed in Figure 6.4. Initial low concentrations resulted in higher decolouration of MO after 4 hours of reaction; as shown in Figure 6.4-a the lowest concentration used in the experiment (1.25 ppm) resulted in a final decomposition of about 40% while the photodegradation of MO at 10 ppm was only 10%. There was no linear relationship between initial concentration and the final decomposition after 4 hours (Figure 6.4-b red dots).

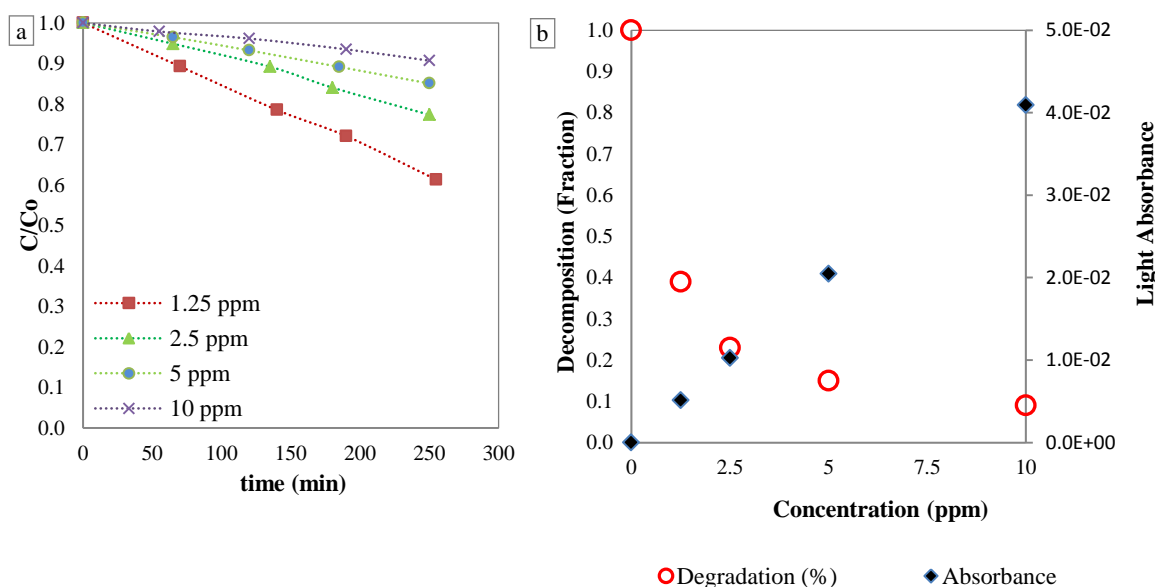


Figure 6.4 Photolysis of MO at different initial concentration (a). Final Photodecomposition of MO after 240 min for different flows and light absorbance at the different MO concentrations (b) (lines in Figure 6.4-a are used as a guide to facilitate visualization of the trends)

The total absorbance of light by MO in the fluid column was calculated for the different concentrations (M) using Beer-Lambert law with a pathway of 0.05 cm and a coefficient extinction of $2.68 \times 10^4 \text{ cm}^{-1}\text{M}^{-1}$. As shown in Figure 6.4b, the total absorbance decreased with concentration. Although the total absorbance is directly proportional to the MO concentration, the final decomposition of MO decreased exponentially.

In a laminar flow, with high volumes of liquid, molecules located in the upper layer absorbed a large amount of the UV light, reducing the potential degradation of molecules located in lower layers. By increasing the concentration, the absorption of light in the upper layers increases and the intensity of light in the lower layers decreases, reducing the level of degradation on the total system (Figure 6.5). On the other hand, with small volumes of liquid and low concentration, the effect of light absorption is lower and the penetration of light for the different layers can be similar.

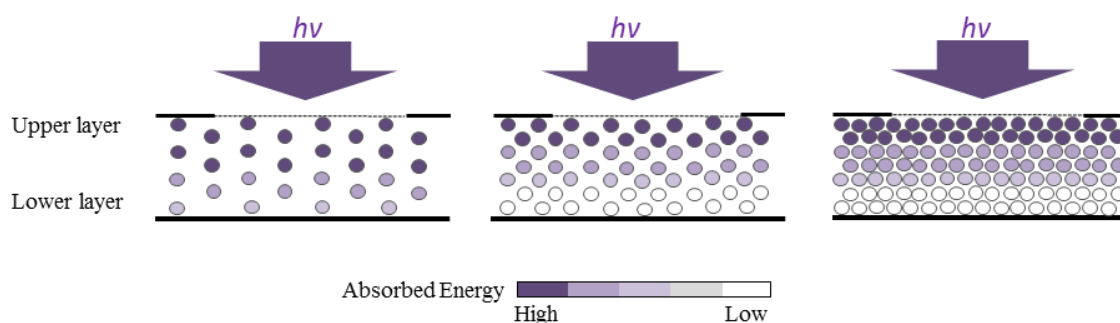


Figure 6.5 Schema of light absorbance at different concentrations on the model compound in the illuminated zone of the FP-PCR

Beer-Lambert law was also used to calculate the absorbance and transmittance of light at different depths in the illuminated zone of the FP-PCR. As shown in Figure 6.6a, the absorption of light increased with concentration and with optical thickness. However, values of transmittance (Figure 6.6b) indicated that more than 90% of the light passed through the liquid column and therefore the lower layers were also illuminated. This result indicates that the differences in the photolytic degradation of MO in the reactor were due to the kinetic reactions rather than light absorption limitations.

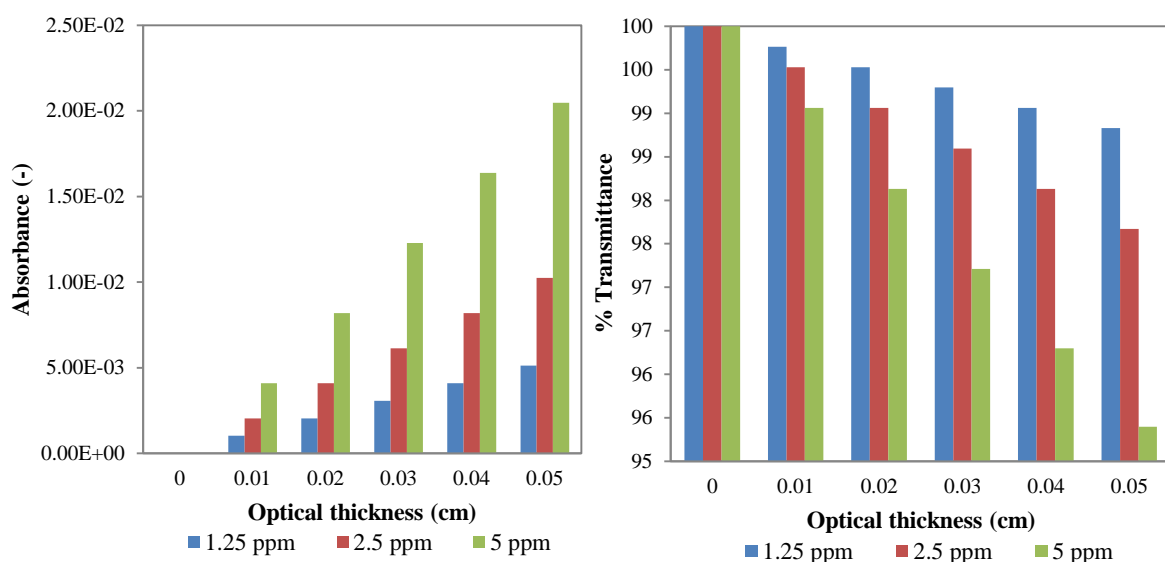


Figure 6.6 MO absorbance (a) and MO transmittance (b) of light at different optical thickness in the illuminated zone of the FP-PCR

MO solutions were flowed at different rates through the reactor. Different flows result in different levels of decomposition of the dye as displayed in Figure 6.7-a. The photodegradation of MO was considerably higher with a total degradation of 65% obtained at the highest flows that were tested (250 ml/min). The degradation of the MO by light is directly related to the flow as it is shown in Figure 6.7-b. To the author's knowledge the information related to the photolysis of MO is very limited: Photocatalytic studies that have used it as a model compound mentioned negligible photolysis under UV (350 nm) and solar light illumination after 2 hours of reaction in a stirred batch reactor [47], while another study displayed decolouration of less than 10% after 2 hours of reaction in a Pyrex reaction cell [157]. Moreover no information of photolysis of dyes under different flow rates in the same photocatalytic reactor was found in the literature.

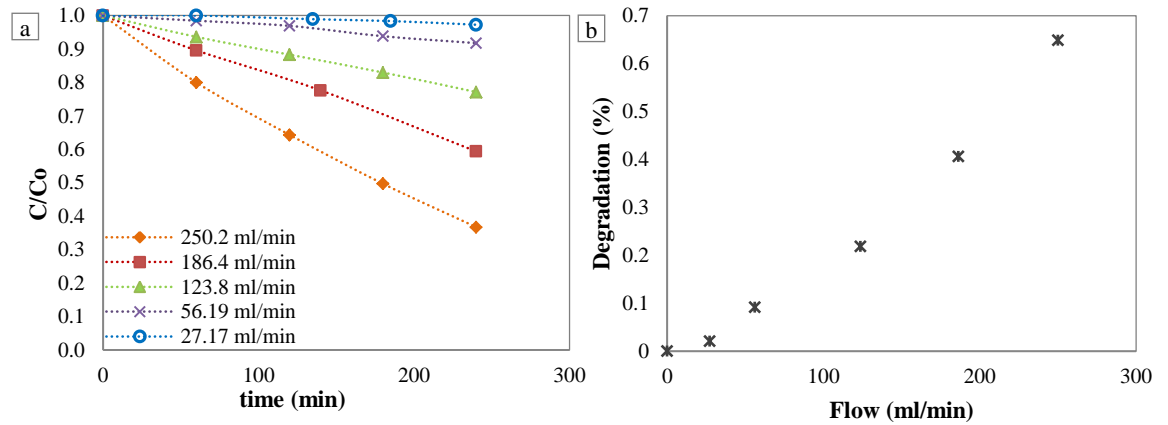


Figure 6.7 Photolysis of MO at different flows (a). Final photodecomposition of MO after 240 min at different flows (b) (lines in Figure 6.6-a are used as a guide to facilitate visualization of the trends)

The relationship between the flow-rate and the rate of decomposition of the MO was analysed by conducting a mass balance analysis of the system. For this analysis, it was assumed that (i) the reaction only occurred in the UV irradiated volume and (ii) the reservoir was perfectly mixed. The initial concentration of MO that entered the reactor (C_0) corresponded to the concentration of MO at the outlet of the reservoir (g/mL). Similarly, the concentration in the outlet (C_1) in the reactor was similar to the concentration in the entrance of the reservoir, as shown in Figure 6.7.

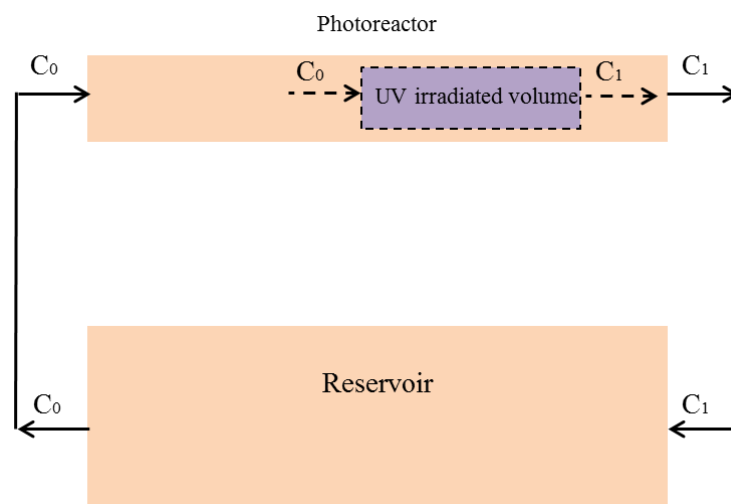


Figure 6.8 Reactor modelling of the FP-PCR for photolysis

As reported by Pickett [319], changes in concentration within the system is given by Equation 6.11 and 6.12, where \mathcal{Q} is the volumetric flow rate (mL/s), V_R is the volume in

the reservoir (mL) and V_p is the volume in the photoreactor (mL) which also corresponds to the volume in the illuminated zone.

In the photoreactor

$$\vartheta C_0 = \vartheta C_1 + V_p \frac{dC_1}{dt} \quad (\text{Eq. 6.11})$$

In the reservoir where mixing took place

$$\vartheta C_1 = \vartheta C_0 + V_R \frac{dC_0}{dt} \quad (\text{Eq. 6.12})$$

Assuming a differential reactor (with a conversion lower than 5% in each time), the resulting differential equation is [81] given by Equation 6.13, where R_p is the photocatalytic reaction rate and V_p and V_R remain constant:

$$\frac{dC_0}{dt} = -R_p \left(\frac{V_p}{V_R + V_p} \right) \quad (\text{Eq. 6.13})$$

From Equation 6.13 it can be observed that changes in concentration of MO in the reservoir are directly proportional to R_p . At high flow rates, the reaction rate in the photoreactor is higher due to the dye being recirculated more times through the reactor, resulting in high degradation of MO (measured in the reservoir). As other dyes, MO can be degraded via direct photolysis when the MO molecules absorb light [320]. The absorption of photons results in a transition from an electronic ground state to an electronically excited state. If the absorbed energy is sufficient, a molecular transformation occurs via bond cleavage, rearrangement, oxidation, or reduction [320]. Additionally, electron transfer within the molecule might result in the destruction of conjugated bonds causing decolouration [321].

The high decomposition of MO by photolysis represented an issue for the study of photocatalysis. Even in short reactions, the photolysis was high and therefore it was difficult to distinguish which portion of decomposition of the pollutant is caused by the exposure to UV light (photolysis), by the photocatalytic effect or by a potential synergy between both processes. Therefore, the lowest flow (27.2 ml/min) with the lowest photolysis effect was selected for further analysis with MO, and the value of photolysis was displayed in all the plots as a reference.

6.1.3 FP-PCR used as a slurry photocatalytic reactor for the decomposition of MO.

As discussed in Section 2.3.2, the use of powder photocatalysts provides not only a high photocatalytic active area but also minimizes mass transfer limitations as the pollutant is perfectly mixed with the catalyst. The FP-PCR was used as a slurry reactor for the degradation of MO [2.5 ppm] with two different amounts of commercial ZnO powder (Particle Size: 44 μm , BET specific surface area: $5.3 \pm 0.5 \text{ m}^2 \text{ g}^{-1}$) dispersed in the MO solution. The experiments were carried out at 27.2 mL/min (Figure 6.9).

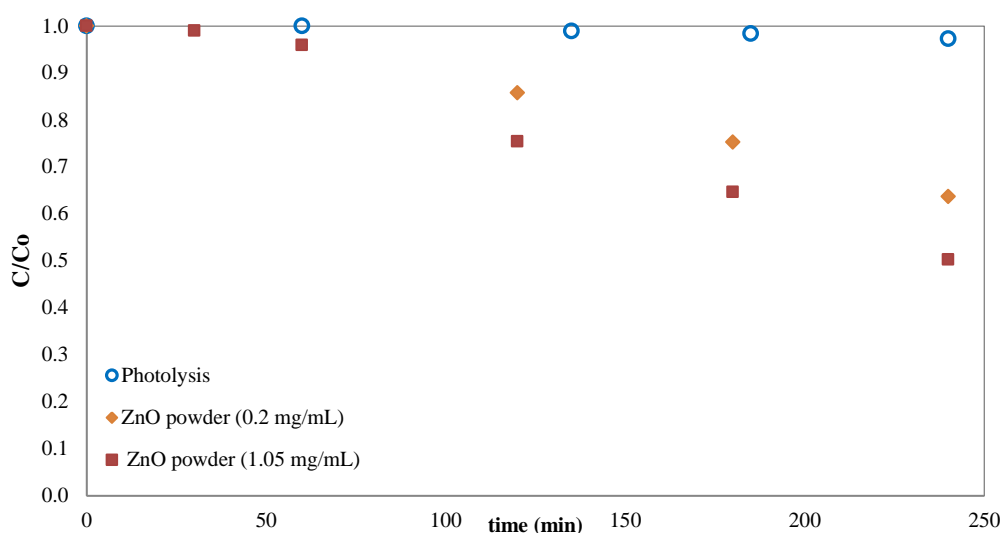


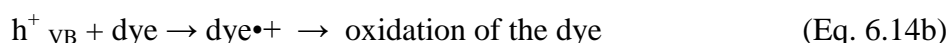
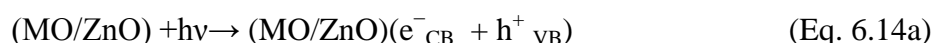
Figure 6.9 Photocatalysis of MO [2.5 ppm] with ZnO powder (Flow: 27.2 ml/min)

The use of powdered ZnO results in an enhancement of the MO photodecomposition suggesting the occurrence of photocatalytic degradation in addition to photolysis as shown by comparing the curves with and without ZnO powder in Figure 6.9. Larger doses of photocatalyst lead to a higher degradation of MO. For 0.2 mg/mL of ZnO powder there was a total reduction on the concentration of MO of 36 %. By increasing the catalyst loading to 1.05 mg/mL, the decomposition after 4 hours reached 50 %. Large amounts of photocatalyst result in higher degradation of dyes due to the increment in the photo-active surface area. However, as discussed in the literature [47], the increase of catalyst loading also results in higher scattering of light produced by the ZnO particles suspended in the solution (scattering albedo), and therefore further increases in the photocatalyst doses do not have any enhancement effects.

In the presence of photocatalyst, the reaction of MO degradation initiates by the photoexcitation of the ZnO powder and the formation of an electron-hole pair. The high

oxidative potential of the hole (h^+_{VB}) leads to the direct oxidation of the dye to reactive intermediates (as shown in Equations 6.14) and to the degradation by the hydroxyl radical ($\bullet\text{OH}$) as shown in Equations 6.15 and depicted in Figure 6.10 [47]. The direct oxidation shown by the Equation 6.12 differs from the direct photolysis described in Section 6.1.2. In the former case, there is the participation of the h^+_{VB} (formed during the photo activation of the ZnO) with the formation of the reactive dye during photocatalysis as shown in Equations 6.14 and 6.15.

Direct oxidation:



Oxidation by hydroxyl radical:

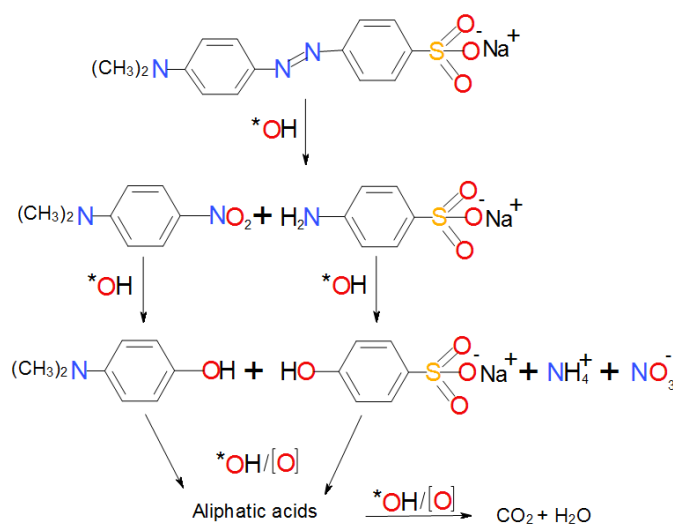
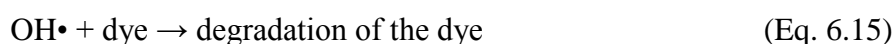
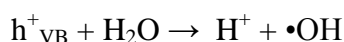


Figure 6.10 Degradation pathway for methyl orange (adapted from L. Gomathi Devi *et al* [322] and Wang *et al* [323])

6.1.4 ZnO-NFs as a photocatalytic material in FP-PCR.

The photocatalytic performances of the ZnO-NFs were tested in the FP-PCR for the photocatalytic degradation of MO [2.5 ppm] at 27.2 mL/min and 250 mL/min. The ZnO-NFs used herein were obtained by anodization with KHCO_3 at 1V, 10 °C and 1 hour and post-annealed at 350 °C for 1 hour at 1 °C/min. To avoid dead zones on the

FP-PR and potential restrictions of the flow made by the ZnO-NF, the film was placed on the reactor assuring an even level with the base of the channel as shown in Figure 6.11.

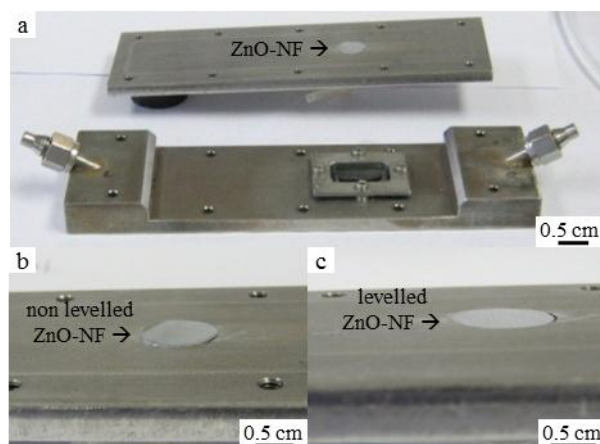


Figure 6.11 Pictures of the ZnO-NF placed in FP-PCR. General view of the reactor (a); non-levelled ZnO-NF (b), levelled ZnO-NF (c)

Figure 6.12 displays the photolysis and photocatalytic results obtained at the lowest and highest tested flows. Results show no significant enhancement of the decomposition of MO regardless the flow. The experiment run at the lowest flow rate (27.2 mL/min) showed an enhancement of only 10% in the decomposition; while at high flow (250.2 mL/min) it was less than 5%. As the photocatalytic activity of the ZnO-NF was already tested in the degradation of phenol (see Section 5.1) and the photocatalytic degradation of MO was already tested with ZnO powder, it was assumed that the low photocatalytic degradation observed was produced by a low diffusion of the MO molecules in the reactor. Changes in the initial MO concentration might improve the mass transfer between the MO and the ZnO-NF and therefore higher photocatalytic decomposition could be reached.

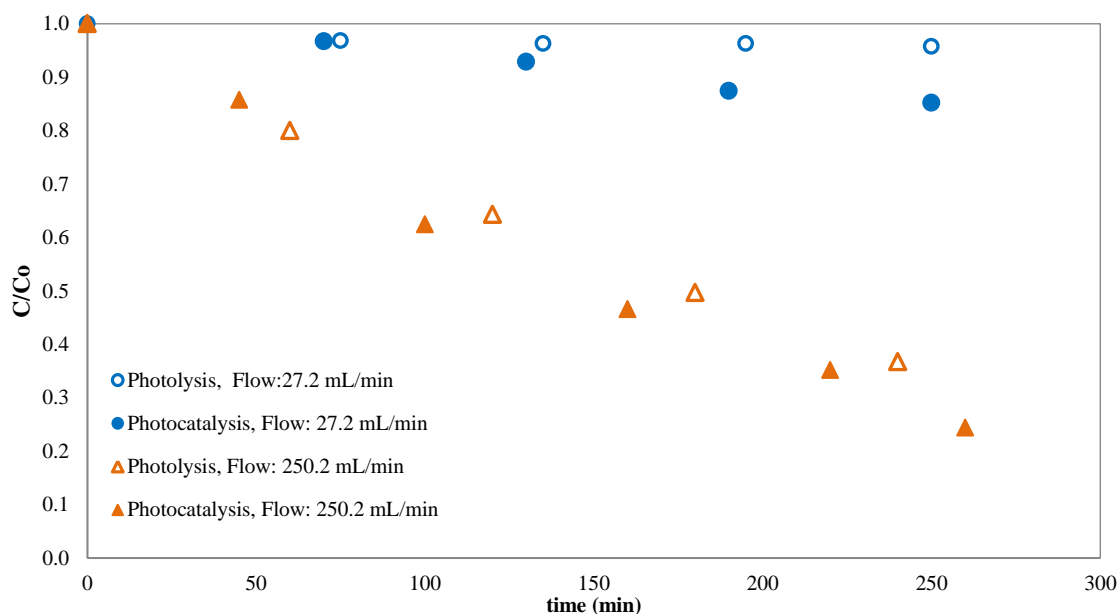


Figure 6.12 Photolysis and photocatalysis of MO [2.5 ppm] with ZnO-NFs at the highest and lowest tested flow.

Minimal concentrations of substrate (MO) results in a lower absorption rate on the photocatalyst and therefore a low overall degradation rate. By increasing the concentration of substrate, still below saturation of the photocatalytic surface, more molecules are likely to be absorbed. As the reaction at low concentration of substrate is not limited by the photocatalyst active sites, the reaction obeys apparent first-order kinetics [324]. In contrast, at high concentrations, the majority of the photocatalytic active area is occupied by the substrate and its by-products; the demand of reactive species is higher but the formation of $\text{OH}\cdot$ and $\text{O}_2\cdot^-$ remains constant, resulting in a constant reaction rate. On the other hand, a reduction in the reaction rate occurs when slow diffusion of by-products reduces the photocatalyst absorption capacity, or when the high concentration of dissolved substrate affects the absorption of light [325].

For the test of the films in the FP-PCR, three different concentrations of MO were tested at the lowest flow rate. All the experiments displayed similar results with no enhancement on the degradation produced by photocatalysis (Figure 6.13). The fact that different initial concentrations resulted in similar degradations suggested that issues other than the initial concentration of the substrate, and related to the absorption-desorption of the pollutant on the photocatalyst surface, affected the process in this reactor.

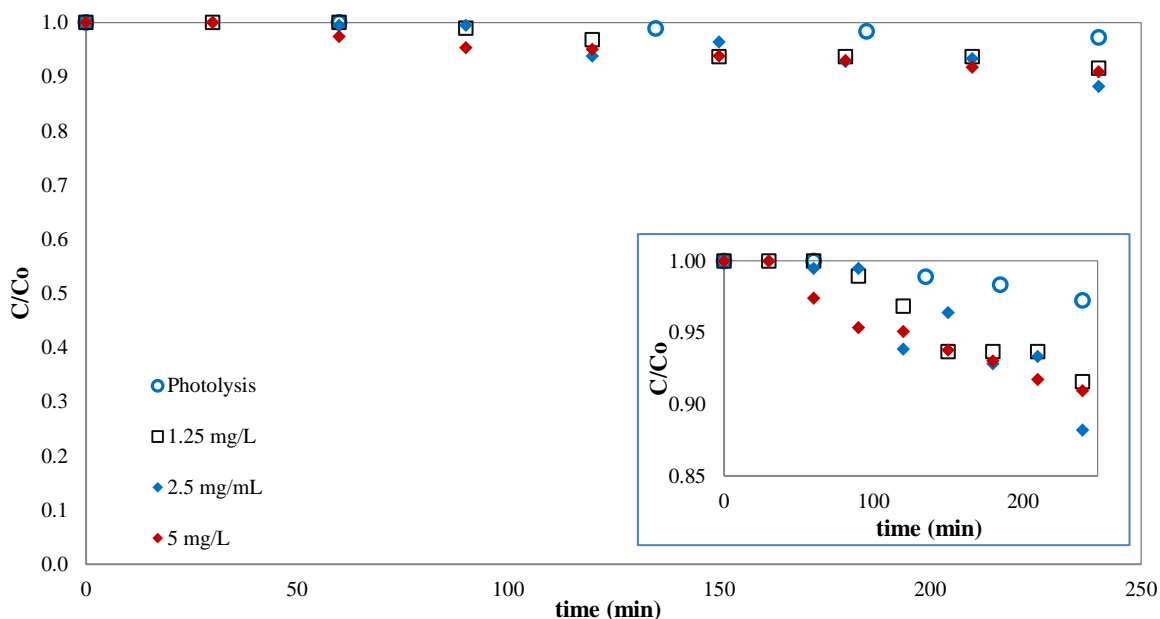


Figure 6.13 Photocatalysis at different concentration of MO at 27.2 mL/min. (Inset: enlarged Figure)

With the aim of understanding the low photocatalysis of MO in this type of reactor, selected experimental conditions from this section were used in the photocatalytic degradation of phenol in the FP-PCR. Additionally, a non-metallic reactor was built and the ZnO-NFs were tested using phenol as a model compound.

6.1.5 Turning to a more stable model compound

Although several studies have used dyes as model compounds to study photocatalysis [144], [145], [326]–[329], the use of these molecules is still a matter of debate as they can be degraded in the presence of light by different routes including the injection of photoexcited electrons on the photocatalyst (see Section 6.1.4). In addition, dyes are susceptible to decolouration caused by the destruction of their conjugated bonds [53] and due to their large extinction coefficient, the absolute molar amount of dye can be significantly smaller than the total amount of the photocatalyst [52]. Therefore, dyes are an excellent model compound for preliminary photocatalytic tests (especially when photolysis studies are performed) but present several limitations when conducting a rigorous study of the photocatalytic performance of materials or for kinetic studies.

Phenol has a low extinction coefficient ($\epsilon = 2.34 \times 10^3 \text{ cm}^{-1} \text{ M}^{-1}$) [284] compared to MO ($\epsilon = 2.68 \times 10^4 \text{ cm}^{-1} \text{ M}^{-1}$) and thus its capacity of absorbing light is minimal. Therefore, this compound is suitable for photocatalytic studies as discussed in Section 5.1. Although UVC light can directly degrade it by breaking its conjugated bonds, the molecules do not have the capacity of injecting photoexcited electrons on the photocatalyst. Therefore, after the photolysis of phenol is established at certain experimental conditions, further changes in its concentration can be attributed to photocatalysis. As a part of the analysis carried out with the metallic FP-PCR, photolysis and photocatalytic experiments were carried out with phenol [20 ppm] at 27.2 mL/min and at 250 mL/min.

As shown in Figure 6.14, the photolysis of phenol in the FP-PCR was minimal. Phenol exposed to UV light (in absence of the photocatalyst) with a flow rate of 27.2 mL/min displayed a photolysis of 12 % while the degradation of phenol at 250 mL/min was only 2 %. On the other hand, no photocatalytic degradation of phenol occurred regardless of the flow rate. For the experiment run at 27.2 mL/min, the experiment including a ZnO-NF (photocatalysis) resulted in lower total degradation compared to the photolysis at a similar flow rate. The latter result could indicate a potential radical scavenger effect given by the metallic material of the reactor.

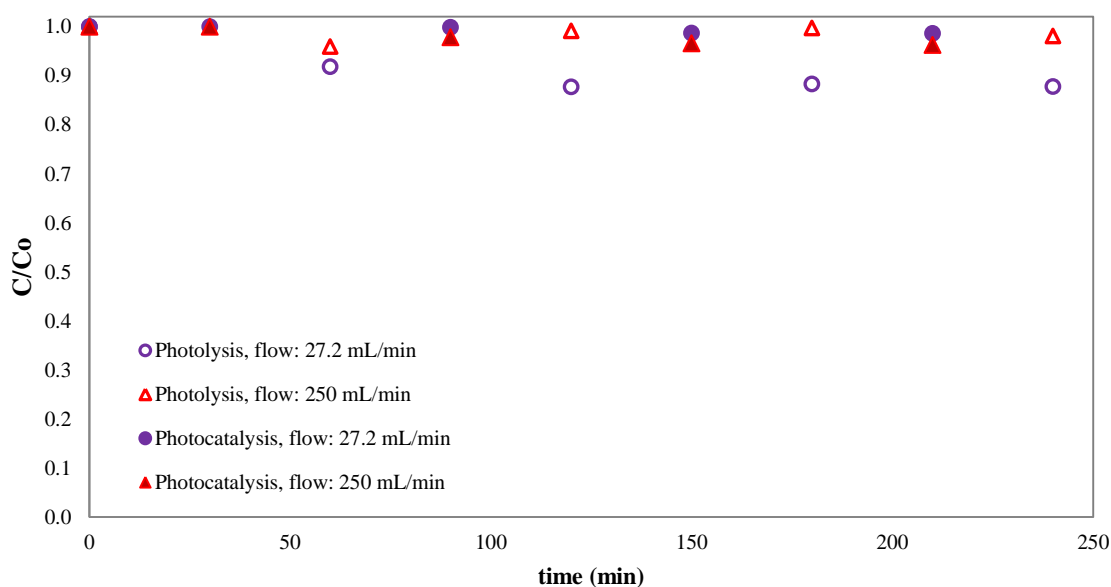
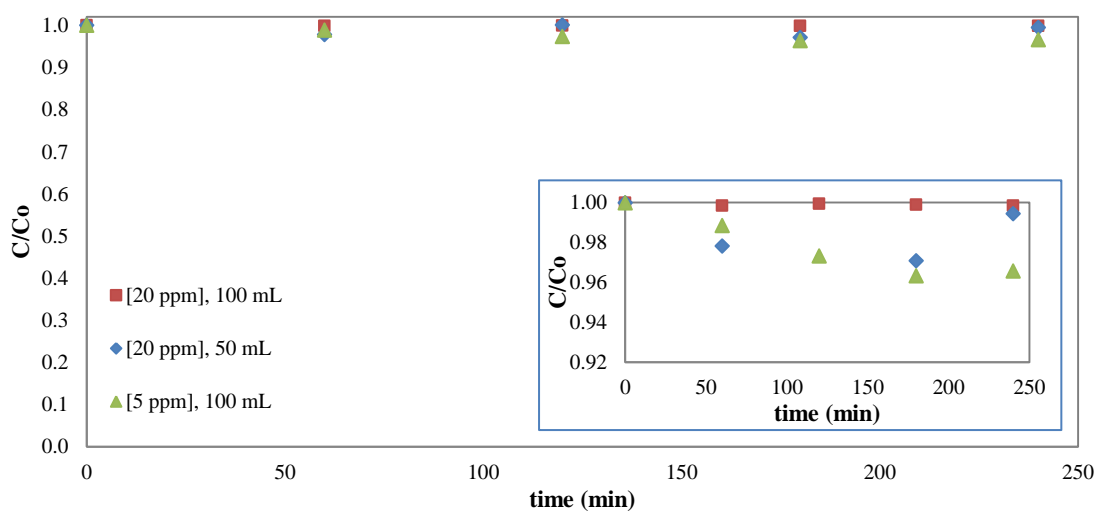


Figure 6.14 Photolysis and photocatalysis of phenol [20 ppm] at different flows

The negligible photocatalysis observed in the FP-PCR can be also attributed to external mass transfer limitations. In heterogeneous photocatalysis, these limitations occur when one or more of the basic steps related to absorption or desorption of the reactants do not take place in the system (see Section 2.2). External mass transfer limitations are a common issue in photocatalytic reactors that use immobilised photocatalyst [330]–[332]. Different comparative studies, most of them carried out in annular reactors, have found a mass transfer rate for laminar flow in the order of 10^{-3} mm.s⁻¹ with a considerable increase in the mass transfer rate for turbulent flow.

In order to increase the mass transfer rate, a set of experiments were carried out at higher flow rates (700 mL/min) where turbulent flow is fully developed (see Table 6.2). In addition to increasing the flow rate, a lower concentration of phenol was used and the amount of phenol was reduced by half. Results displayed in Figure 6.15 showed that turbulent flow did not improve the photocatalytic degradation of phenol under the selected conditions.



. **Figure 6.15** Photocatalysis of phenol at two different initial concentration and two volumes of solution in the FP-PCR at flow rate of 700 mL/min (Inset: enlarged Figure)

Studies with phenols and dyes have demonstrated the relationship between the degradation rate and the initial concentration in photocatalytic reactions using different reactor configurations [46]. However this dependence was not observed in the FP-PCR

due to the lack of photodegradation produced by the mass transfer limitations discussed before.

Although mass transfer limitations are a common issue in photocatalytic reactors that use immobilised photocatalysts, there is limited information available about this phenomena, in particular in reactors that work in recirculated flow mode [81]. Other studies with alternative reactors have also reported mass transport limitations. For instance, the spinning disk reactor (SDR) has been recommended under specific flow regimes in order to minimise a drop in reaction rate [106]. A comparative study between this reactor and the annular one highlights the advantages of the SDR where the high photocatalytic performance was mainly attributed to the higher average photonic efficiency and the large average volumetric flow rate due to the small volume of substrate treated per second in the reactor [333].

6.1.6 Epoxy acrylic flat plate batch photocatalytic reactor.

In order to eliminate the potential radical scavenger effect given by the metallic FP-PCR, a non-metallic material was used in a new design of a flat plate photocatalytic reactor obtained via 3D printing. The epoxy acrylic FP-PCR was designed based on the hydraulic calculations made for the metallic FP-PCR. It consisted in a monolithic structure with a rectangular internal channel of 17 cm length, 0.8 cm width and 1mm depth. The inlet and outlet sections were in parallel to the flow without any slope and with connections for stainless steel tubing (1/4 in.) as shown in Figure 6.16. The irradiation section has a UVC transparent quartz window situated 11.3 cm from the entrance (*Le*) assuring a stable flow in the photocatalytic area (see Table 6.1).

Similar photolytic and photocatalytic experiments to the ones carried out with the metallic FP-PCR were performed with the epoxy acrylic FP-PCR (see section 6.1.5). As for reactions run in the metallic FP-PCR, no degradation of the phenol by photolysis or photocatalysis was obtained with the epoxy acrylic FP-PCR. Since the epoxy acrylic material of the reactor does not interact with the ions or the electrons generated during the activation of the photocatalyst, it was established that radical scavengers did not affect the reaction. Therefore, the external mass transfer limitation was assumed to be the main issue responsible for the absence of photocatalysis in this type of reactor. Another limitations found in photocatalytic processes is the slow electron transfer

between the photocatalyst and the absorbed oxygen or hydroxyl groups produced by the slow adsorption kinetics of these species [334]–[336].

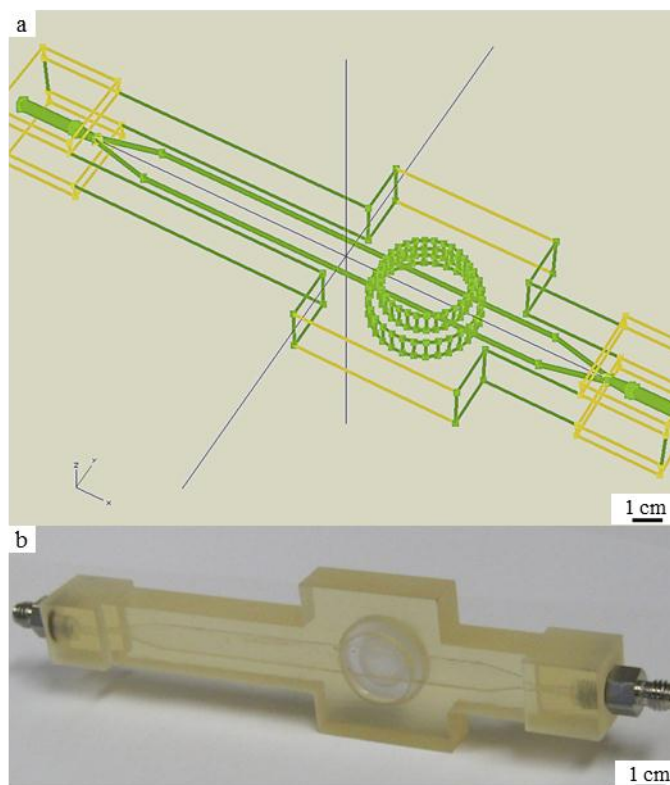


Figure 6.16 CAD-drawing (a) and picture (b) of the epoxy acrylic flat plate batch photocatalytic reactor.

6.2 Exploring new shapes of photo catalyst substrate: From flat shape to cylindrical shapes

The fluid dynamics in non-cylindrical systems such channels or a ducts with non-uniform geometries is complex. In catalytic processes and in particular in photocatalytic reactions, the variation of dynamic properties when a liquid flows through a system might cause serious issues of mass transfer. Therefore, the probability of having limited absorption-desorption of the pollutants on the surface of the catalyst increases.

Since part of this study was aimed at testing the supported ZnO nanostructures in reactors with different configurations, (and due to the technical issues with the FP-PCRs previously discussed) it was decided to explore alternative shapes of supported ZnO nanostructures and reactor configurations. As a result, a single tubular annular photocatalytic reactor (TA-PCR) was designed and the supported photo catalyst was

obtained using Zn wire as the starter material for the anodization process. After anodization of the Zn wire, ZnO nanostructures were formed on the surface of the wire. This type of photocatalyst was named Nanostructured-ZnO-Wire (ZnO-NW).

6.2.1 Tubular annular photocatalytic reactor (TA-PCR) design.

The tubular annular photocatalytic reactor (TA-PCR) consisted of a 25 cm long-UVC transparent-quartz tubing, with an internal diameter of 0.4 cm. The ZnO-NW was placed inside of the tubing along its length as shown in Figure 6.17. The reactor has an annulus configuration where the model compound solution (i.e. phenol) flowed between the quartz tubing and the ZnO-NW. The external part consists of a set of 6 UVC lamps (TUV 6W T5 UVC 22cm tube Phillips®) placed around the quartz tubing at a distance of 1.5 cm. The UVC lamps were also contained by a polycarbonate tube that acts as a jacket protecting the lamps from scratches and mechanical damage while providing a support for them. During operation, the polycarbonate jacket was wrapped with aluminium foil to minimize UV exposure to people.

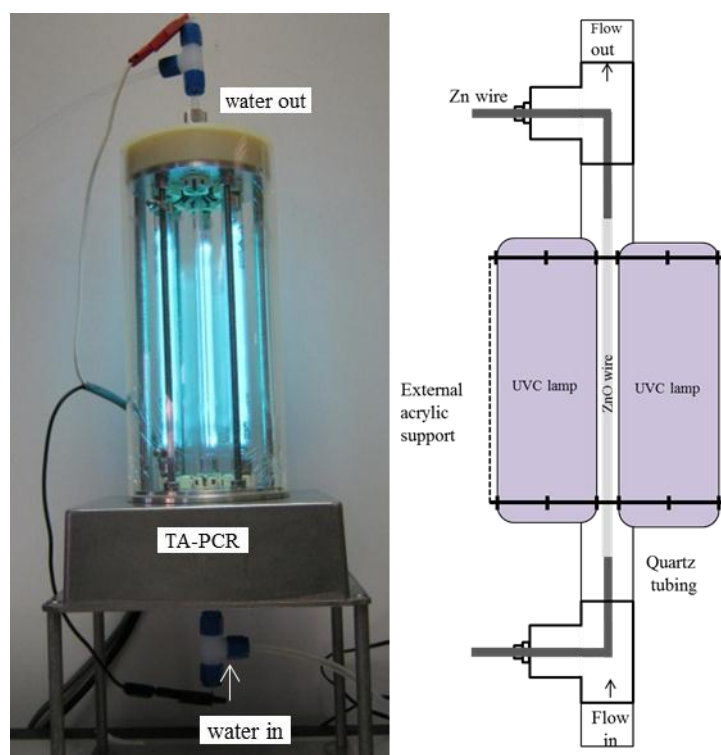


Figure 6.17 Tubular annular batch photocatalytic reactor (TA-PCR)

The TA-PCR was connected to the FP-PCR set up by using a three way valve (Figure 6.18) and therefore the pump, reservoir and two-chamber metallic box displayed in

Figure 6.1 was used for all the reactors. Sampling and the measurements of conductivity and pH took place in the reservoir. Additionally, by using a “T” connection in the inlet and outlet of the quartz tubing it was possible to apply a current directly to the wire and perform electric assisted photocatalysis (EAPC).

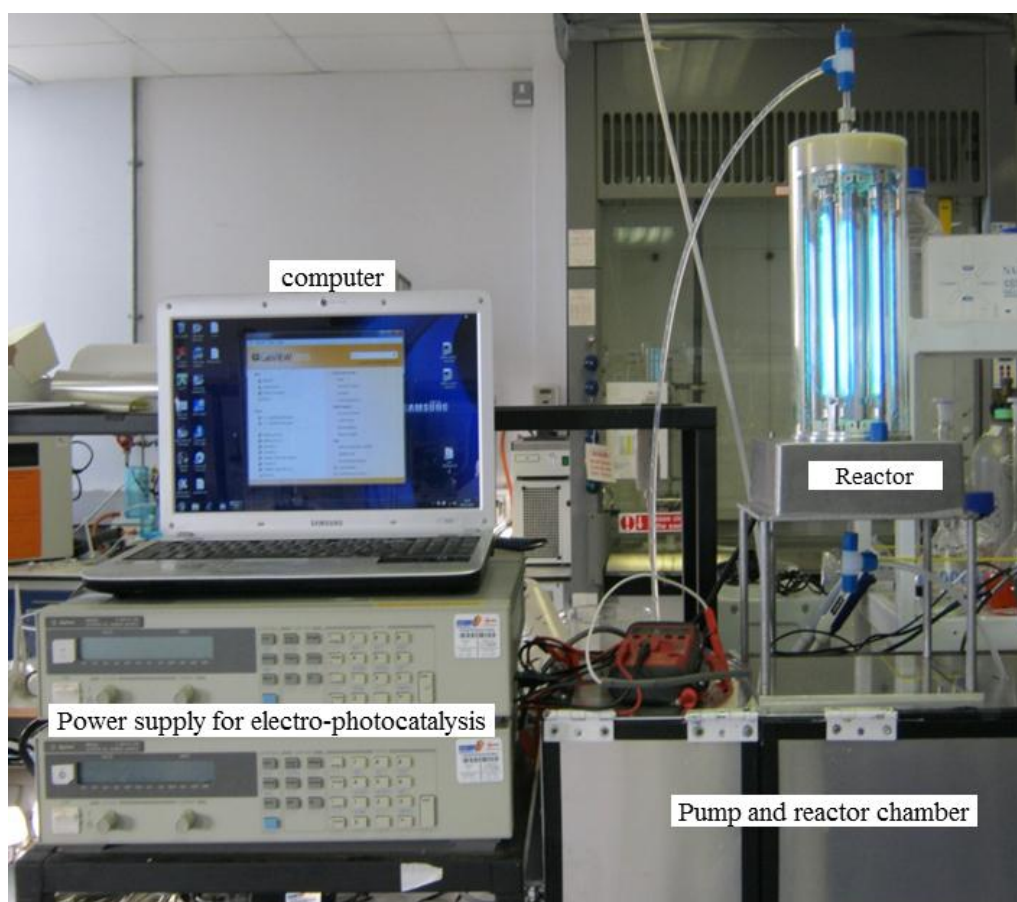
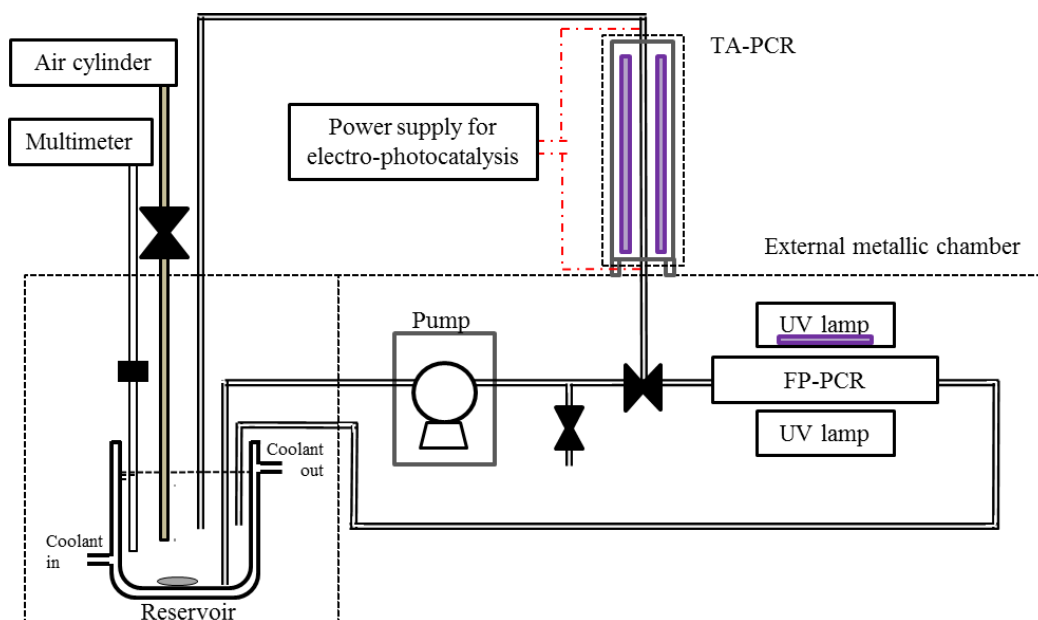


Figure 6.18 Schematic (top) and picture (bottom) of the TA-PCR setup

For the TA-PCR, velocity and flow were calculated for different Reynolds number using Equation 6.4. The hydraulic diameter (Dh) was calculated for an annular configuration using Equation 6.16, where D_o is the internal diameter of the quartz tube (4 mm) and D_i is the diameter of the Zn wire (1 mm). The entrance lengths for laminar and turbulent flows were calculated with Equation 6.1 and Equation 6.2 respectively. Retention time in the quartz pipe (t_{r-q}) was calculated using Equation 6.17 where l_q is the length of the quartz pipe. Results of these calculations are displayed in Table 6.5.

$$Dh = \frac{4 \cdot 0.25\pi (D_o^2 - D_i^2)}{\pi (D_o + D_i)} \quad (\text{Eq. 6.16})$$

$$t_{r-q} = \frac{l_q}{v} \quad (\text{Eq. 6.17})$$

Table 6.5 Entrance length and retention times for the TA-PCR.

Re	v (m/s)	Q (ml/min)	Le (cm)	t_{pi} (s)	t_{pp} (s)	N_r (cycle/min)
4000	0.67	1890.6	10.5	0.37	0.30	38
3000	0.50	1418.0	10.0	0.50	0.40	28
2500	0.42	1181.6	9.7	0.60	0.48	24
2300	0.38	1087.1	82.8	0.65	0.52	22
2000	0.33	945.3	72.0	0.75	0.60	19
1000	0.17	472.7	36.0	1.50	1.20	10
600	0.10	283.6	21.6	2.49	1.99	6
500	0.08	236.3	18.0	2.99	2.39	5
200	0.03	94.5	7.2	7.48	5.98	2
100	0.02	47.3	3.6	14.96	11.96	1
50	0.01	23.6	1.8	29.91	23.93	1

The TA-PCR contained a set of six UVC tubes, 212.1 mm in length and with a diameter of 16 mm, with the following electric characteristics: 6 W, 42 V and 0.16 A and a theoretical UV-C irradiation of 1.7 W as shown in Figure 6.19 .

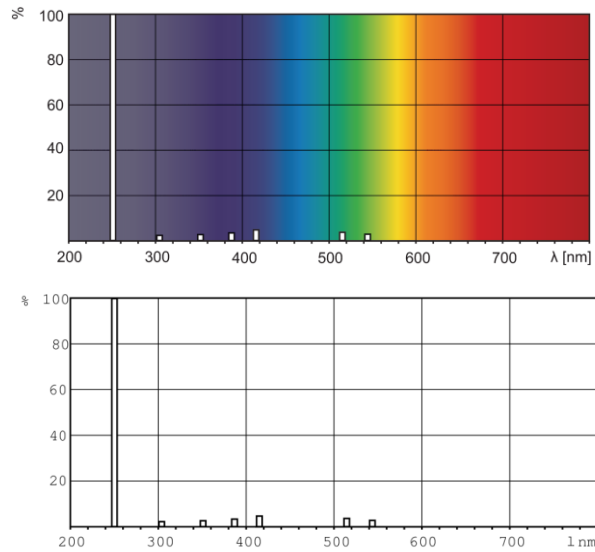


Figure 6.19 Photometric data, UVC lamps 6 W phillips used for the TA-PCR [337].

6.2.2 Nano-structured photocatalytic wires (ZnO-NW) for photocatalytic applications

The anodization of the Zn wires with KHCO_3 has been described in detail in Section 3.1.3. Changes to the morphology of the wires after electro-polishing were analysed by FESEM (Figure 6.20). After electro-polishing, the surface of the wires becomes more even and smooth. However, defects such as creases on the wire surface remained even after prolonged electro polishing.

Anodization of Zn wire using KHCO_3 as electrolyte resulted in the formation of a homogeneous layer of nanowires on the Zn wire surface (Figure 6.21). The growth of ZnO-NW is considered to follow the proposed mechanism for the formation of ZnO nanostructures by anodization at neutral pH discussed in Section 4.2.1 (*Proposed mechanism for formation of ZnO nanostructures by anodization*). However, given the radial configuration of the substrate the ZnO film is exposed to different tensions during the anodization process as will be discussed later.

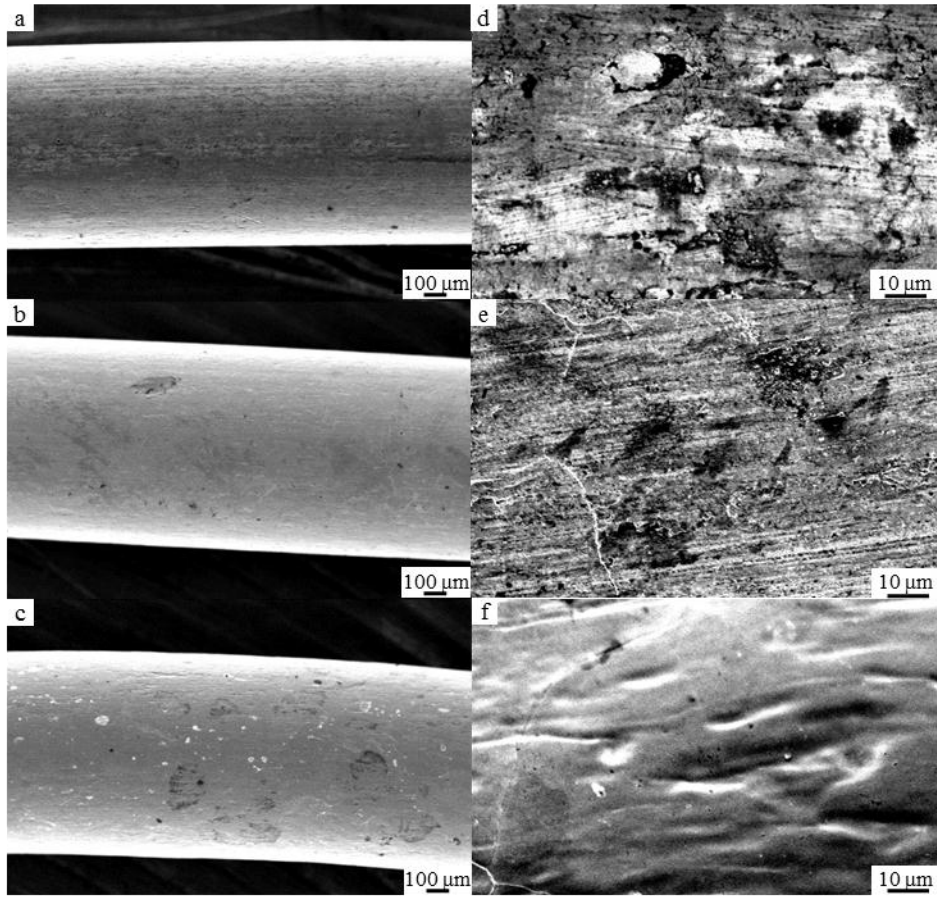


Figure 6.20 FESEM micrographs of 1 mm wire. Zn wire (a,d); annealed Zn wire (b,e) and electro polished Zn wire in Perchloric acid – Ethanol [1:2] at 20v, -70C for 15 min (c,f).

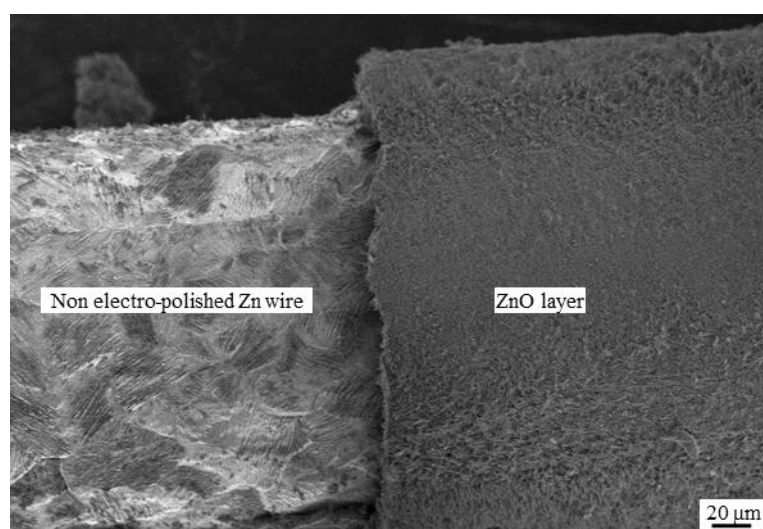


Figure 6.21 FESEM micrographs of ZnO-NW showing area with and without ZnO layer

Similar to the anodization of Zn foil (see Section 4.4), variation of the anodization time affected the morphology of the ZnO-NWs (Figure 6.22). As shown in Figure 6.21-a, Zn wire anodized for only 1 minute showed minimal nanostructure formation. Wires exposed to anodization for 5 minutes (Figure 6.22-b) and 15 minutes (Figure 6.22-c) resulted in a denser layer with more nanowires per unit area; both ZnO-NWs displayed axial formation of nanowires homogeneously distributed along the surface as shown in Figures 6.21(e-f). On the other hand, anodization run for 1 hour (Figure 6.22-d) resulted in different arrangement where the nanowires form flower-like structures (Figure 6.22-g).

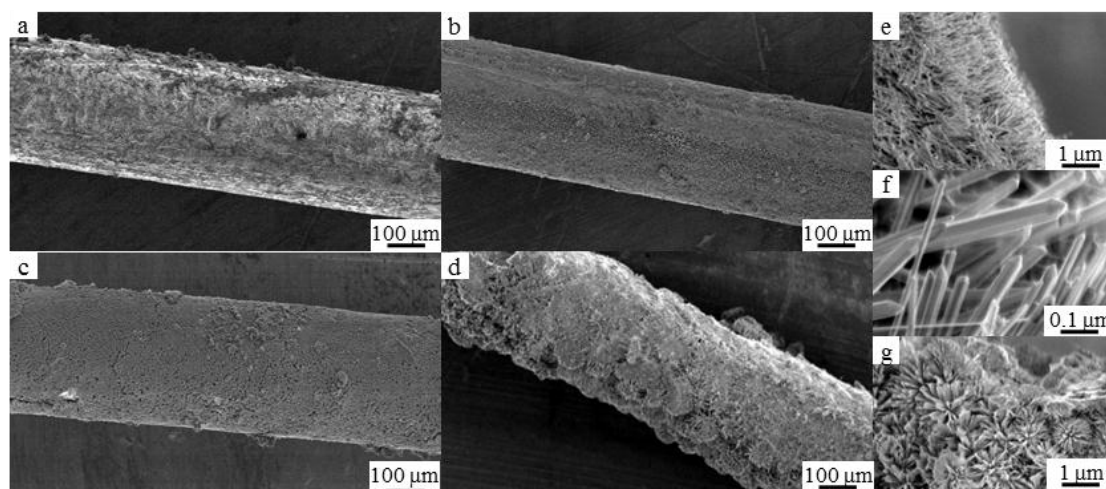


Figure 6.22 Anodization of Zn wire at 0.1M, 1 V, 10 C and 1 min (a), 5 min (b), 15 min (c,e,f) and 45 min (d,g).

Longer anodization leads to the formation of thicker ZnO films. In general, thick ZnO films obtained for more than 1 hour at 1V and 10 °C were more likely to crack and peeled off during the formation of the ZnO layer (Figure 6.23). This is the result of a potential radial tension produced during the over-growth of the ZnO nanowires in the inner part of the film, which stresses the ZnO layer causing cracks. As shown in Figure 6.24, ZnO nanostructures formed in a radial configuration have a restrained space at the base of the film (at the interconnection between the Zn substrate and the ZnO layer) generating tension between the growing nanostructures. In the outer or external area of the film, on the other hand, the ZnO nanostructures have more space to grow and therefore minimal tension occurs in that zone.

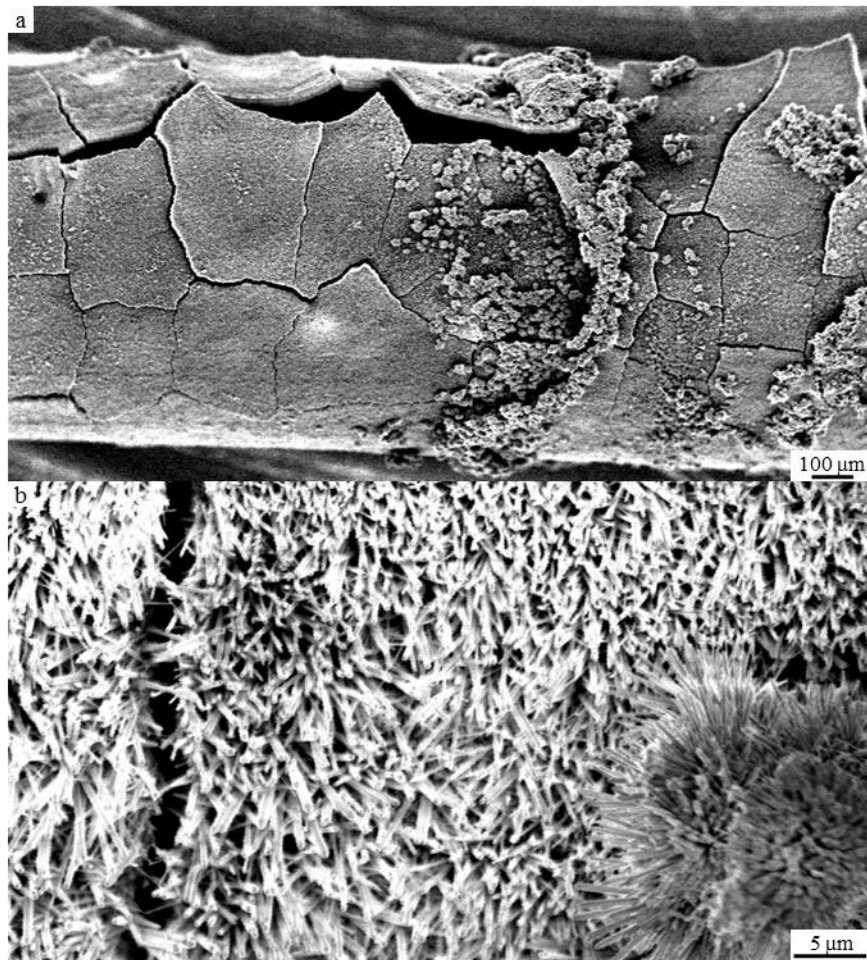


Figure 6.23 Cracks formed as a result of anodization of Zn wire at 0.1M, 1 V, 10 C and 70 min (a-b)

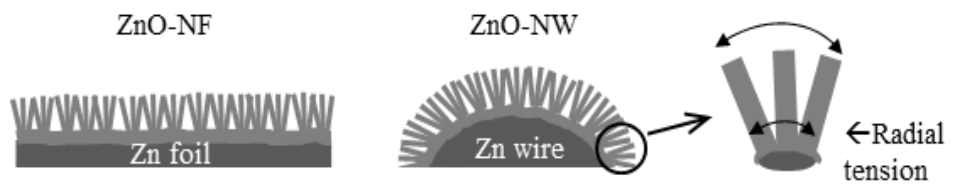


Figure 6.24 Schema of ZnO-NF and ZnO-NW showing radial tension.

ZnO-NWs were post-annealed at 350 °C for 1 hour at a heating rate of 1 °C /min. Thin ZnO-NWs were less likely to crack during the thermal post-treatment compared to the flat ZnO-NFs. The radial configuration of the ZnO-NW with minimal tension in the outer areas of the film might help release tension produced during thermal treatment (see Figure 6.24). A set of ZnO-NWs produced with non-electro polished Zn wires displayed higher stability of the ZnO layer. It is suggested that the initial roughness of the non-electro polished wires (See Figure 6.19-b) helps the attachment of the ZnO film to the substrate.

6.2.3 ZnO-NW as photocatalytic material TA-PCR

The photolysis of 50 mL of a phenol solution [5 ppm] was tested at 10 °C in the TA-PCR at two different flow rates, 38.4 ml/min and 255 ml/min, for 4 hours (Figure 6.25). The photodegradation of phenol was discussed in Section 5.1.1. Unlike the flat plate reactor (FP-PCR), the configuration of the TA-PCR allowed high degradation of the phenol by photolysis. 38% of the phenol was degraded during the first hour, followed by a 20% degradation during the second hour and 5% in the last hour of reaction. This result suggests that the concentration of the pollutants affect the rate of photodegradation.

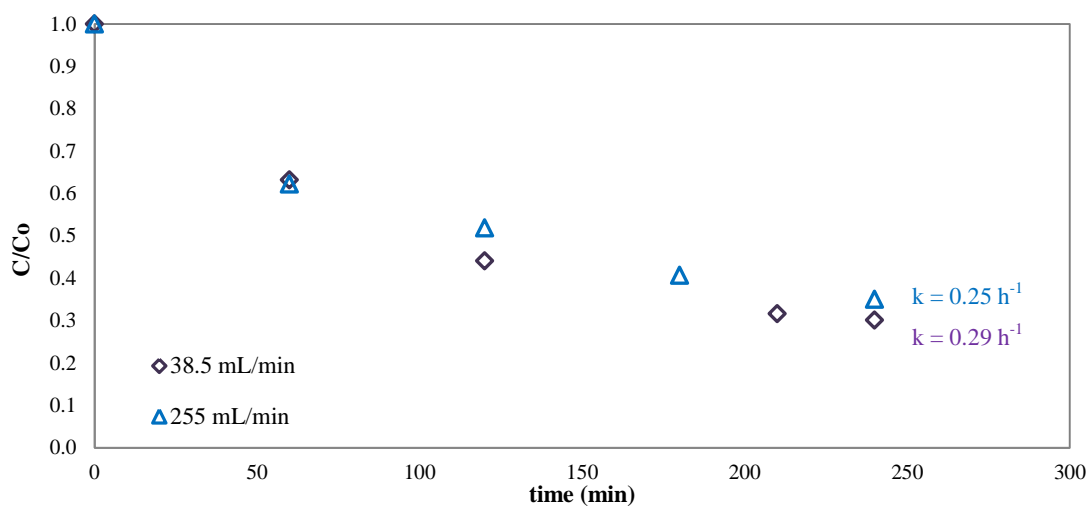


Figure 6.25 Photolysis of phenol [5 ppm], at two different flow rates and 10 °C.

There was no significant difference in the photodegradation of phenol for different flow rates (Figure 6.25). Since the total light exposure time after 4 hours of reaction is constant regardless of the flow rate (see Table 6.7), and with no parallel reactions outside of the illuminated area (see Section 6.1.2.), the degradation of phenol occurs

only in the illuminated area. Therefore, similar photodegradation is obtained when molecules had a long retention time in the reactor but is only recirculated a few times (low flow rates) compared to molecules that have short residence time but are recirculated more times, as is the case with high flow rates.

In an attempt to minimize the effect of the photolysis in the tubular reactor, the numbers of UV lamps was decreased to 3 instead of 6 lamps. Results of photolysis with 3 UV lamps around the quartz tubing resulted in similar effects to those experiments carried out with 6 lamps indicating an optimal radiation in both cases. Further experiments were carried out using only 3 UV lamps. As the photolysis in the AT-PCR resulted in a high degradation of phenol, the potential photocatalysis will be determined by the enhancement of the photolysis process, with base photolysis depicted as reference.

To test the photocatalytic performance of the ZnO-NWs in the tubular reactor, 3 types of experiments were performed at 255 ml/min. The first experiment consisted of using a Zn wire within the reactor. By doing this it was possible to determine any potential photocatalysis produced by the natural ZnO layer formed on the Zn wire surface. For the second experiment, a ZnO-NW was produced with KHCO_3 at 1 V for 1 hour at 10 °C and used as photocatalytic material. The last experiment involved applying a voltage of 0.02 V to the system by connecting the ends of the Zn wire, and connecting them to a current supplier (see Figure 6.18). Changes in morphology of the Zn wire and the ZnO-NWs were studied. Additionally, the conductivity and concentration of dissolved Zn in the phenol solution were recorded during the experiments.

With the tubular configuration, the main mass transfer limitations discussed in Sections 6.15 and 6.16 was minimised, and after 2 hours 65% of the phenol was degraded. Results displayed in Figure 6.26 show that the natural ZnO layer formed on the surface of the Zn wire acts as a photocatalytic material. After the first hour an enhancement of 13% of the degradation of phenol occurred. This difference increased after the second hour where the degradation of phenol was 20% higher compared to photolysis degradation. The Photocatalytic degradation of phenol using the ZnO-NW showed an enhancement of phenol degradation of 35% during the first hour and 50% during the second hour, resulting in almost total degradation of phenol after three hours of reaction. By applying electricity (0.2 V / 0.9 Amps) to the Zn wire, the electric assisted

photocatalysis (EAPC) results in a similar degradation to that obtained with ZnO-NW with an enhancement of 45% after 2 hours.

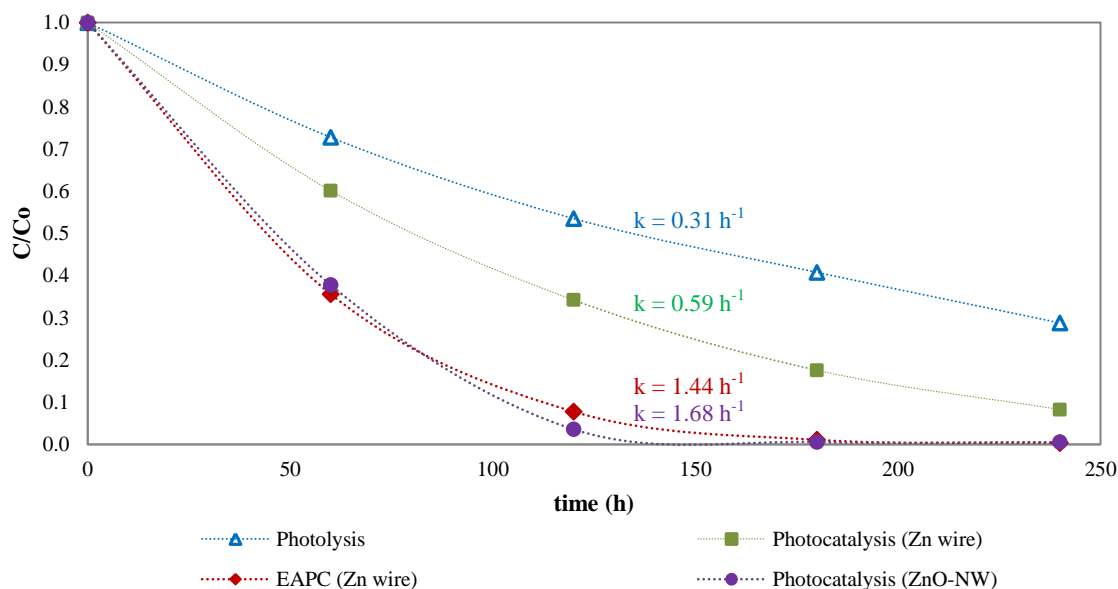


Figure 6.26 Photolysis, photocatalytic and electrical assisted photocatalysis (EAPC) degradation of phenol [5 ppm], 10 °C, in the TA-PCR

By comparing the two experiments carried out with zinc wire (covered by a natural layer of oxide) with and without electricity it was observed that the small current applied to the system has a substantial impact on the photocatalytic degradation of phenol. The role that electricity played in the enhancement of phenol degradation is not yet clear and further studies are needed. It is suggested herein that phenomena such as changes in wettability of the material, minimization of the electron-hole recombination and a potential direct electro-catalytic oxidation might occur during the EAPC.

Although the electro-wetting performance of nanostructured metal oxides has not been widely studied [250], it has been demonstrated by different studies that by applying an external electric field the hydrophobicity of films change (electro-wetting) [338]. These changes are related to the absorbed species on the surface that varied the total charge of the material. During the EAPC, the charge of the surface of the wire covered by thin ZnO layer might vary improving the absorption of chemical species, resulting in a higher degradation of phenol.

The EAPC process can be mistaken as a photo-electro-catalysis and electro-catalytic oxidation. Photo-electro-catalytic studies for water treatment are performed in an

electrochemical cell where the photocatalyst material is used as a working electrode and an external counter is usually placed parallel (see Section 2.2.7) while in the EAPC an electric field was applied directly to the substrate of photocatalyst material. Despite the differences between the two processes, the reduction on the electron-hole recombination given by the electrons during electro-photo-catalysis and discussed by different studies [339], [340] is also likely to occur in the EAPC. As discussed in Section 2.2 the minimization of the electron-hole recombination results in a higher number of reactive species and therefore improves the photocatalytic degradation of phenol.

As discussed in Section 5.1.2, changes in conductivity occur for different reasons such as the formation of ions (dissociation of by-products), formation of soluble CO_2 and dissolution of Zn(II) ions. The phenol degradation obtained during the EAPC reaction showed the highest changes in conductivity followed by the ZnO-NW photocatalysis, the Zn-wire photocatalysis and photolysis respectively (Figure 6.27-a). Changes in conductivity produced during the photolysis of phenol are mainly attributed to the formation of by-products and the CO_2 . The conductivity registered during the EAPC experiment displayed higher values compared to the other reactions. Unlike electro-photo-catalysis, a reduction on the conductivity rate was observed during photolysis and photocatalysis after 2 hours of reaction.

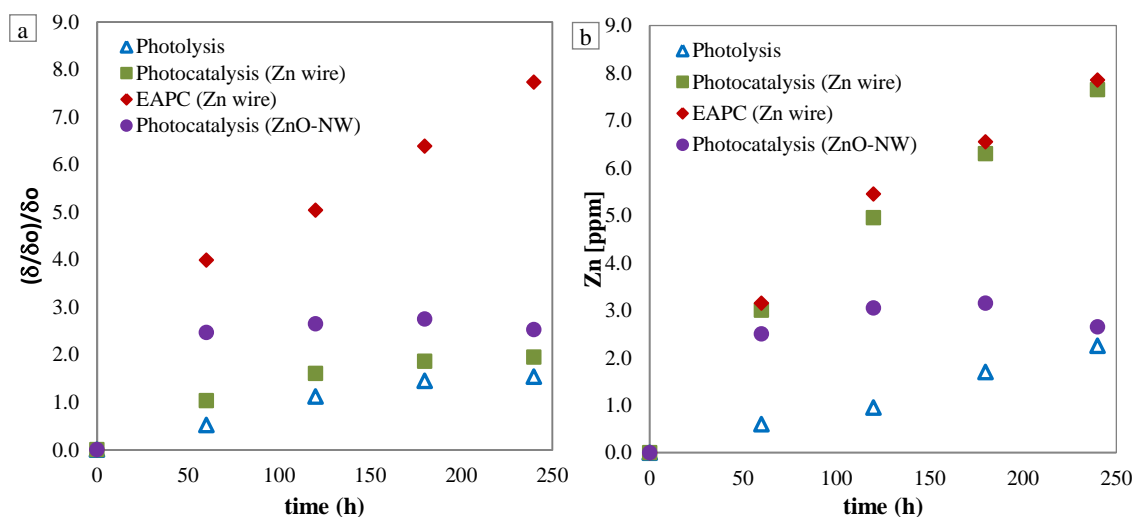


Figure 6.27 changes in conductivity (a) and concentration of dissolved Zn (b) in the TA-PCR

The concentration of soluble Zn was recorded for the different reactions and the results are displayed in Figure 6.27-b. Values of dissolved Zn were similar for the reactions with the Zn wire (i.e. electro-photocatalysis and photocatalysis). The highest values of

dissolved Zn in these reactions occurred for the formation and further dissolution of ZnO and Zn(OH)₂ during the reaction, as it was discussed throughout Chapter 5. During photocatalysis with the ZnO-NW, the dissolved Zn tended to decrease after 3 hours of reaction indicating the potential precipitation of the Zn(II) species. Additionally, the concentration of dissolved Zn obtained during the photocatalytic degradation of phenol with ZnO-NW is considerably lower than those obtained with the ZnO-NF in the batch reactor and discussed in Chapter 5. The latter results indicate a higher stability of the ZnO-NW produced either due to the arrangement of the ZnO-NWs themselves, or due to the configuration of the reactor. The stability of the morphology of the ZnO-NW and changes in the Zn wire was studied by FESEM.

Figure 6.28 shows the FESEM micrographs of the Zn wire used in the photocatalytic and electro-photocatalytic experiments. After the photocatalytic reaction, the Zn wire was found to be covered by a thin layer of ZnO, and the surface was relatively homogeneous with no formation of well-defined nanostructures (Figures 6.28-a and 6.28-b). On the other hand, after the EAPC reaction the formation of clustered nanostructures was observed on the surface of the Zn wire (Figures 6.28-c and 6.28-d). The fact that the formation of these nanostructures only occurred in the electro-photocatalytic experiment indicates that the applied voltage played an essential role in the formation of the new nanostructures. This process is also related to the high conductivity and dissolved Zn measured in the solution.

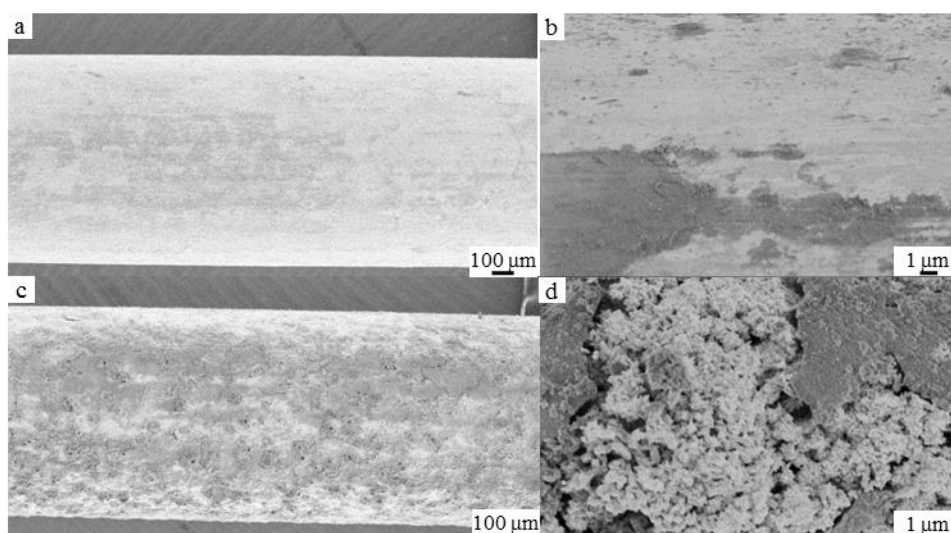


Figure 6.28 FESEM of Zn wire after photocatalytic (a-b) and EAPC (c-d) reaction.

Unlike experiments carried out with ZnO-NF in the batch reactor (see Section 5.3.2), the initial morphology of the ZnO-NW (Figures 6.28-a and 6.28-b) suffered minor changes, with only a slightly deposition of new ZnO and Zn(OH)₂ material observed on the top of the nanowires (Figure 6.29-c and 6.29-d). As depicted in Figure 6.30, the flow and recirculation of the solution minimized accumulation of dissolved Zn near to the nanostructures and further re-deposition. As a result no formation of new nanostructures occurred. It is suggested herein that the radial configuration of the photo catalyst provides higher stability to dissolution. This stability of the material agreed with the low concentration of Zn found in the experiment with ZnO-NW (Figure 6.27-b) compared to the FP-PCR case.

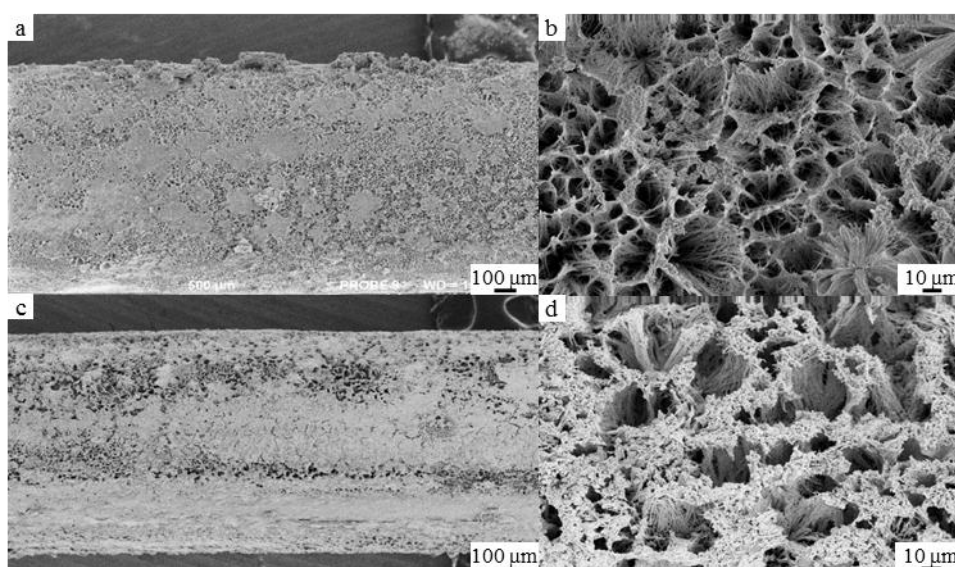


Figure 6.29 FESEM of Zn-NW before (a,b) and after (c,d) photocatalytic reaction.

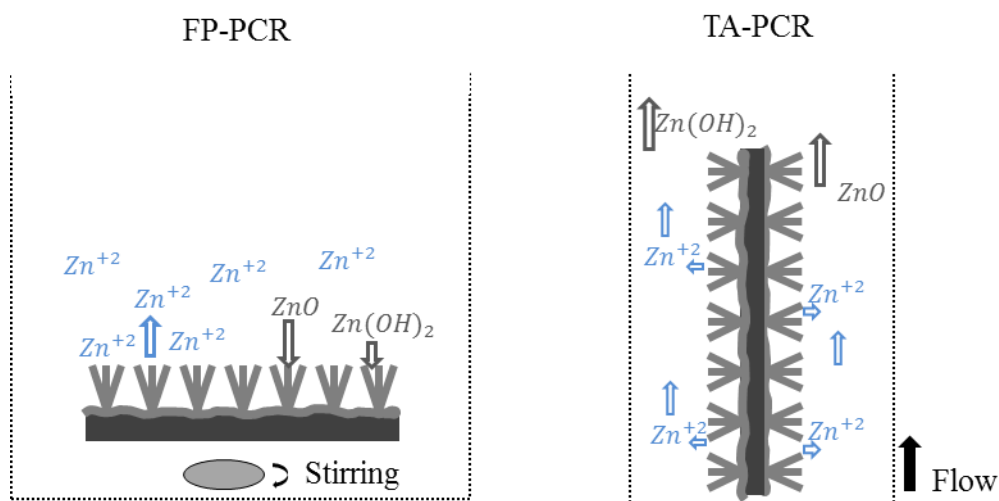


Figure 6.30 Proposed schema of the dissolution and precipitation of Zn(II) in the FP-PCR and TA-PCR.

It is noted that the volume of the phenol solution treated with TA-PCR (50 mL) was double the one used in batch experiments (25 mL) and thus the degradation obtained with the ZnO-NW and the TA-PCR appears to be much higher than the one obtained with batch reactor. Furthermore, differences in the experimental conditions made it impossible to compare the two systems for several reasons. For example: (i) Though ZnO-NWs and ZnO-NFs were obtained under similar anodization conditions, the total area of anodization in the wire was higher and thus a larger surface area of the photocatalyst was obtained. (ii) The ratio of the area of the photo catalyst to the volume of solution of the pollutant was also different for each system. For instance, by comparing only the area of the Zn foil and Zn wire, the area-volume ratio was 2.3 times higher in the TA-PCR (experiments performed in the batch reactor (see Chapter 5) with the ZnO-NF had a ratio of 0.08 cm²/mL while the one for the experiment performed with the tubular reactor and the ZnO-NW was 0.19 cm²/mL). Finally, (iii) the total UV light exposure was higher in the TA-PCR, and the scattering of light produced by the water column in the batch reactor could decrease the intensity of light that reached the surface of the photo catalyst.

Results obtained with the TA-PCR were inconclusive, and thus further experimentation is required to study not only the ZnO-NWs but also the effect of electricity applied directly to the photocatalyst. This future work will be further discussed in Chapter 7.

6.3 Deposition of ZnO on optical fibers

To complement the exploration of new photocatalyst substrates, ZnO was supported on optical fibers. In addition to the potential uses of optical fibers coated with ZnO for environmental photocatalytic applications (i.e. photocatalytic reactors), the potential development of active devices such as phase modulators, wavelength modulators, electric field sensors and field sensors make this composite material attractive for further studies [341].

6.3.1 Preparation of the sol-gels

Sol gel deposition can be used as a low cost method to produce solid materials using a sol-gel as an intermediate step, giving the possibility of developing films or fibers directly from the solution [42]. Often the precursors are involved in a sequence of reactions such as hydrolysis of the molecular precursor, polymerization, condensation by dehydration, nucleation and growth, producing oxides networks [43]. A variety of ZnO films obtained by sol-gel deposition at different conditions of pre and post heat treatment with a vast variety of precursors, solvents, additives and substrates has been reported in the literature [44]. The simplicity, potential uses of low temperatures and low cost makes this method ideal for the production of thin and transparent ZnO films in glass and optical fibers.

In this project, two different methods of Sol gel deposition were used for coating optical fibers with a ZnO layer [45], [46]. The first sol-gel, named SGA, was obtained by mixing Zinc acetate dehydrated with ethylene glycol (99% *Alfa Aesar*) in three different proportions. The mixture was dropped in a round bottom single neck flask provided with a water jacketed reflux column on top and heated in a water ethylene glycol bath to 150 °C (Figure 6.31). The temperature was kept constant for 15 minutes, during this time the formation of a transparent solution was observed. The obtained liquid was left to cool to room temperature where a semi-transparent brittle solid was formed. The solid was dissolved in a mixture of glycerol and propanol, and a drop of triethylamine (99.9%, *Sigma Aldrich*) was added. The mixture was kept at room temperature and left overnight with constant stirring. The Sol-gel had a precipitate associated to the excess of zinc acetate; therefore a further filtration took place using a SPE Supelco Visiprep® and a hydrophilic-lipophilic balanced (HLB) adsorbent (3 ml cartridge). The filtrated sol-gel was collected in a glass vessel and stored in darkness. As the proportion of Zinc acetate dehydrate and ethylene glycol for the preparation of the sol-gels varied, the

obtained samples were labelled as a SGA1, SGA2 and SGA3. Quantities of the compounds used to obtain the different sol-gels are reported in table 6.6.

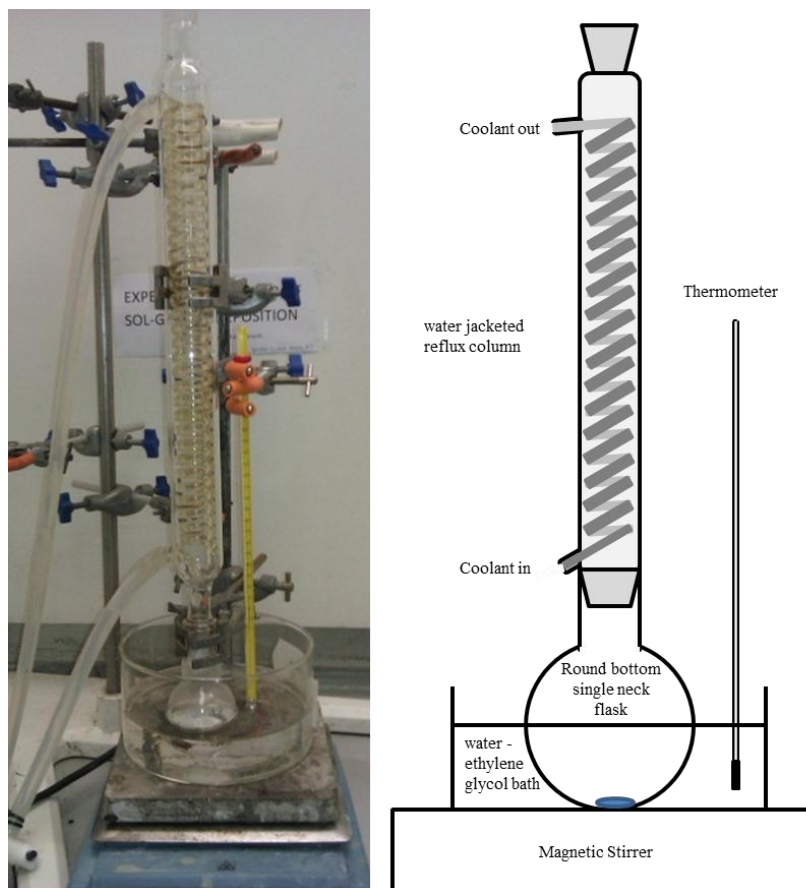


Figure 6.31 Schema of the set-up for the production of Sol-gel

Table 6.6 Composition of the Sol-Gel samples for ZnO deposition experiments

Compound	SGA1	SGA2	SGA3	SGB4	SGB5
Zinc acetate dehydrate	5.0 g	1.0 g	0.50 g	0.52 g	0.53 g
Ethylene glycol	1.5 ml	0.25 ml	0.20 ml	-	-
n-propil alcohol	10 ml	2 ml	1 ml	-	-
glycerol	0.25 ml	0.05 ml	0.025ml	-	-
Ethanol	-	-	-	25 ml	25 ml
water	-	-	-	0.2 ml	0.2 ml
Triethylamine	3 drop	1 drop	1 drop	-	-
PVP	-	-	-	2 g	1 g

For the second Sol-gel method named SGB, zinc acetate was dissolved in ethanol (>99.8%, *Sigma Aldrich*) under vigorous stirring; deionised water was added drop by drop. After 15 minutes polyvinylpyrrolidone (PVP) was added drop wise and after 20 minutes the sol-gel became clear. The Sol-gel was left overnight under stirring at room temperature to allow stabilization. The proportion of glycerol, propanol, and PVP added was varied to obtain different sol-gels which were labelled as a SGB4 and SGB5. (Table 6.6).

6.3.2 Coating of glass and optical fibers

Glass slides that were 5 cm long and 2.5 cm wide (*VWR International*) were washed with detergent and rinsed extensively with deionised water, followed by a degreasing process with Ethanol (>99.8%, *Sigma Aldrich*) in an ultrasonic bath (Fisher Scientific, FB 15048) for 10 minutes. The glass slides were also dried at 30 °C for 1 hour and left to cool in air at room temperature. Slides were tilted 45° and coated by dropping sol-gels from the top and left to spread along the surface. Two slides (SGB4a, SGB5a) were immersed a second time in order to obtain thicker films. After 15 minutes the glass slides were dried in air at 500 °C (CWF1100, Carbolite) for one hour at heating rate of 1 °C/min.

White and transparent films were obtained over the glass as shown in Figure 6.32. Layers formed with the SGA displayed a white and non-homogeneous deposit of ZnO with a rough surface. On the other hand, layers obtained with SGB were homogeneous and translucent. The slides that were coated twice displayed a less homogeneous layer compared to the single-coated ones. Additionally, the adherence of the layer to the glass was higher with SGB. The PVP used in the production of SGB played an important role improving the adherence between the glass and the ZnO layer making it less susceptible to peel off.

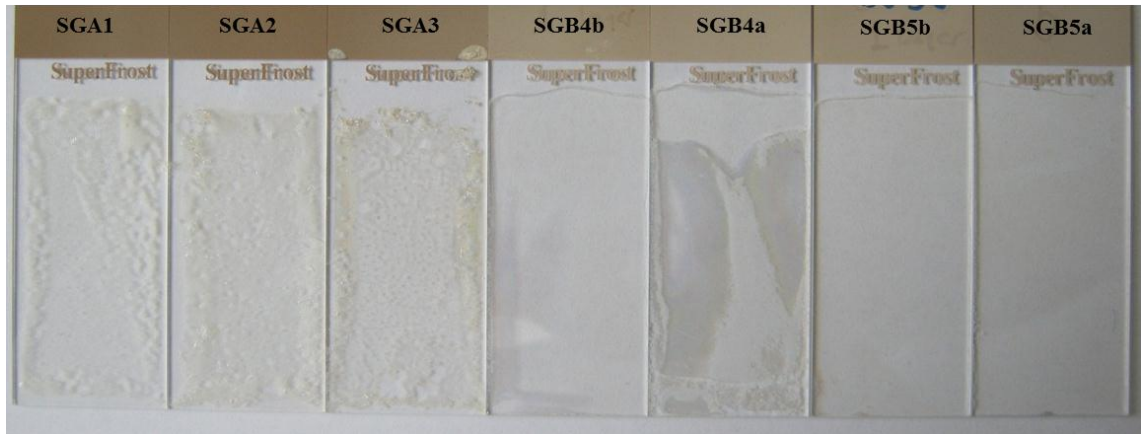


Figure 6.32 Sol-gel depositions over glass slides

The Photonic Crystals fibers (PCF) used in this project were developed by the centre for photonics and photonic materials of the department of physics at the University of Bath. The PCFs showed different internal configurations (Table 6.7) and were labelled as PCF01, PCF02, and PCF03. The PCFs were cut to be 5 cm long and the external polymer was removed from the PCFs with a razor blade and cleaned with cotton buds impregnated with acetone. The fibers were immersed in SGA and SGB for 1 minute. Samples were removed from the sol-gels, hung from one end (allowing the removal of the excess of sol-gel), and then left to dry at room temperature for 1h. Some samples were immersed a second time in order to obtain a thicker layer. All samples were dried in air at 500 °C for 1 hour with a heating rate of 1 °C/min. Samples were stored in darkness in a desiccator cabinet for future analysis.

Table 6.7 PCF internal configurations[342]

Code	Internal configuration
PCF01	Non “endlessly single mode” ESM fiber (microscope)
PCF02	19 cell Hollow-core photonic bandgap fibers (HC PBGF) with large holes
PCF03	Hollow-core HC 1550-01 with Large holes

Similar to the layers obtained with the glass slides, the ZnO coating obtained with SGB resulted in a homogeneous layer while samples coated with SGA were less homogeneous (Figure 6.33). PCFs that were immersed twice in the SGB displayed a thicker homogeneous layer. As shown in Figure 6.34, the use of SGA results in ZnO layers with accumulation of particles in the surface (6.34c). On the other hand, FESEM

revealed that the surfaces of the fibers coated with the SGB were smooth and no nanostructures were observed on the surface. The composition of the layers obtained with SGA and SGB was analysed by XRD.

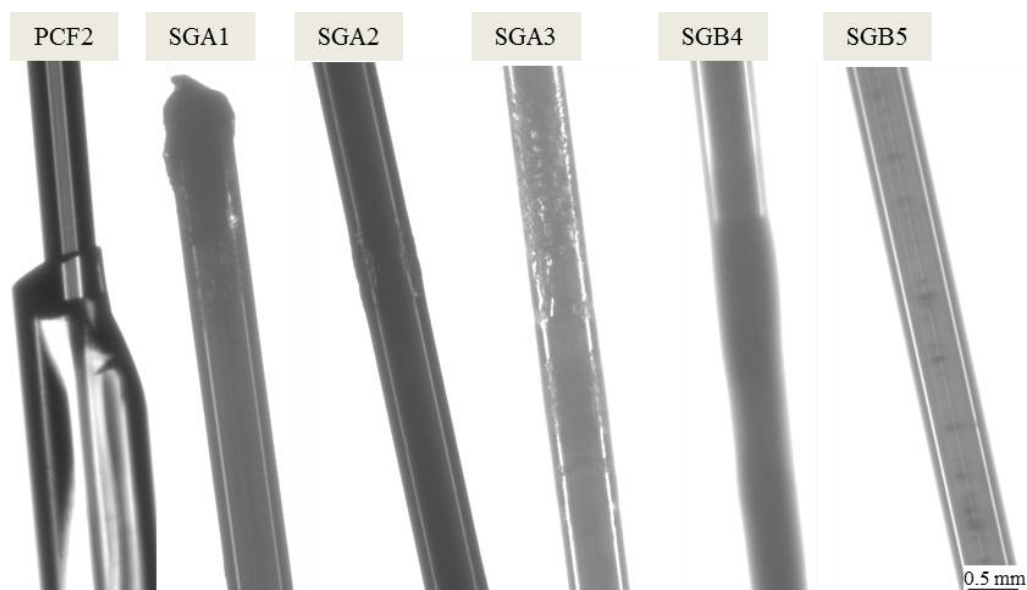


Figure 6.33 PCF2 coated with SGA and SGB

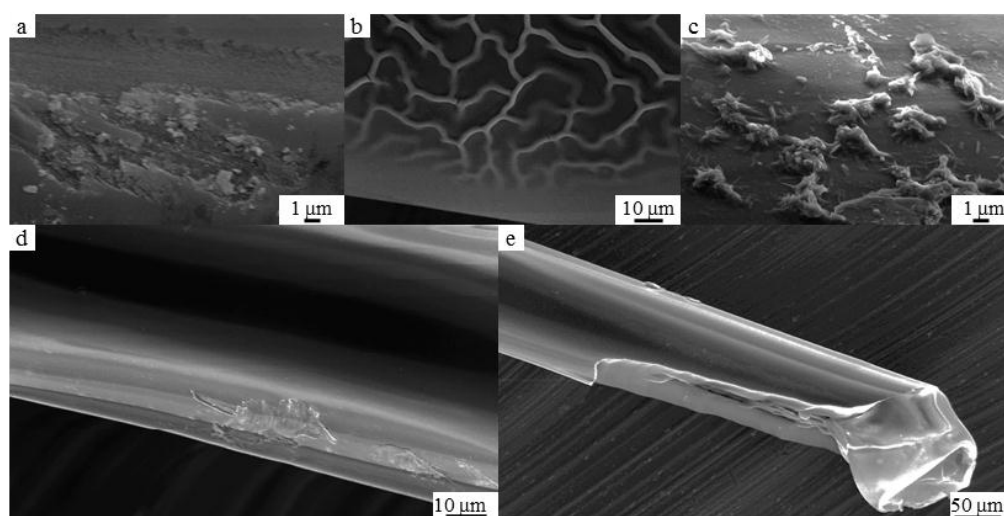
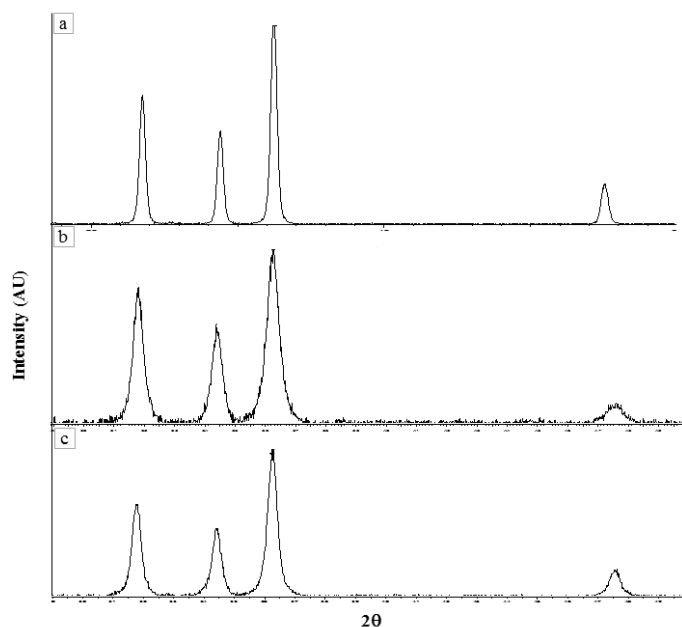


Figure 6.34 FESEM micrographs of PCF2 coated with SGA1 (a), SGA2 (b), SGA3 (c), SGB4 (d), SGB5(e).

The XRD analysis was carried out in a Philips X-ray generator – PW 1710 diffractometer set in powder mode. ZnO powder was extracted by scraping the layer from the glass slides. Both methods of sol-gel production led to the production of polycrystalline ZnO (Figure 6.35). The XRD patterns coincided with the crystallographic phase of the ZnO (JCPDS36-1451). The peaks with the strongest

intensity were (101), (100) and (002) and (103) while peaks (102), (110) were not detected. The preferential orientation after the post-treatment was (101) and (100) for both methods. The FWHM obtained from the XRD peaks revealed that the ZnO produced by SGB lead to the formation of bigger crystals.



6.35 XRD of ZnO powder (a), SGA (b), SGB (c).

Since the coating of optical fibers was conducted as a proof of concept and with an associated project with the Centre for Photonics and Photonics Material of the University of Bath, no further analysis was performed.

6.4 Decolouration of MO by ZnO-NF in darkness

Two ZnO-NFs produced with HCl and KHCO_3 were immersed in 10 mL of MO. The vessels were totally covered with aluminium foil and left in darkness for 24 hours with a constant agitation made by an electrical orbital shaker. As a control, the same amount of MO was used in similar conditions. Changes in concentration were registered before and after using an UV-Vis spectrophotometer to measure the absorbance of the MO. After 24 hour, the MO solutions with ZnO-NW showed high decolouration while the control remained unchanged as shown in Figure 6.36-a and 6.36-b. MO was decolourised in about 90% by the ZnO-NF produced with HCl and 80% by the ZnO-NF produced with KHCO_3 respectively as shown in Figure 6.36-c.

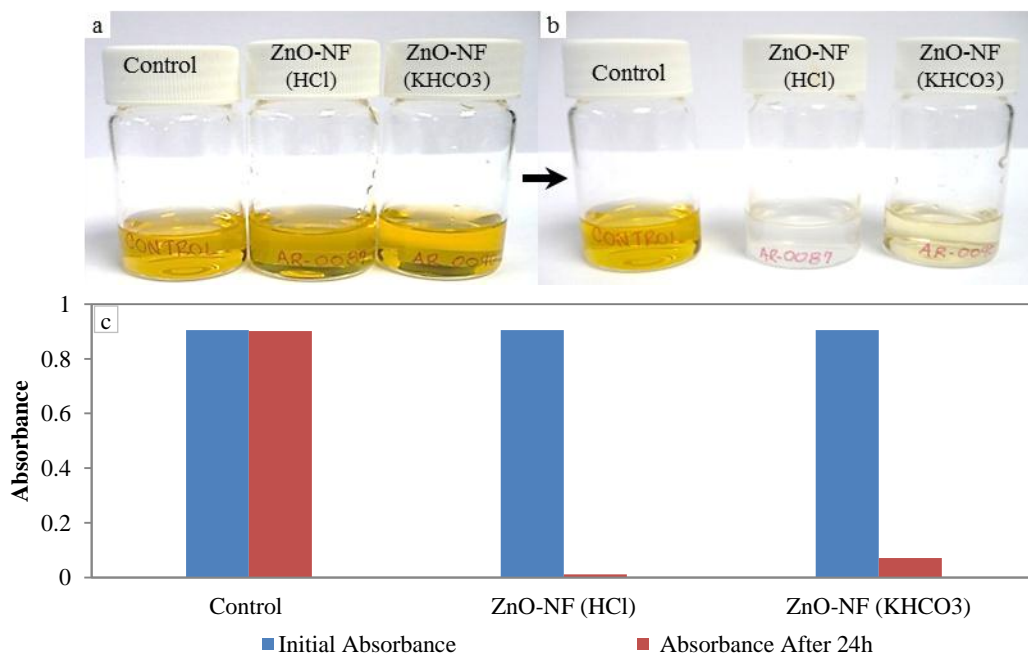


Figure 6.36 Changes in colour produced by ZnO-NF in darkness after 24 hours. Initial samples (a), samples after 24 hours (b), Changes in MO absorbance (c). The anodization conditions of the ZnO-NF were: HCl [0.1M], 1h, 1V, 10 °C and HKCO₃ [0.1M], 1min, 40V, 10 °C.

The MO solutions with the ZnO-NFs were left in darkness for another period of 24 hours. The final absorbance was measured and the ZnONFs were removed from the solution. After this extra 24 hours in darkness, an extra-decolouration of about 1% and 6% occurred for the films produced with HCl and KHCO₃ respectively. The ZnO-NF produced with KHCO₃ was found to be coloured by the dye indicating absorption of the MO on the surface. However, the surface of the ZnO-NF produced with HCl did not change in colour and a white ZnO layer was observed as shown in Figure 6.37.

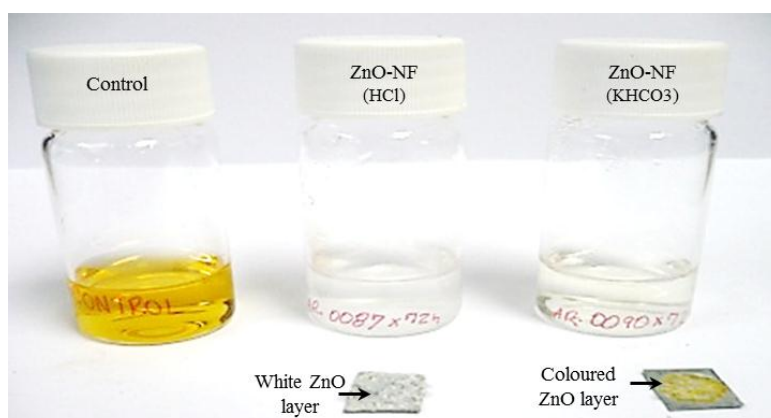


Figure 6.37 Final decolouration of MO produced by ZnO-NF in darkness after 48 hours and their respective ZnO-NFs. The anodization conditions of the ZnO-NF were: HCl [0.1M], 1h, 1V, 10 °C and HKCO₃ [0.1M], 1min, 40V, 10 °C.

Similar experiments were carried out with different ZnO-NF morphologies and with 2 doses of ZnO powder (0.8 and 1.2 mg) for 15 hours. As displayed in Figure 6.38, with ZnO powder the MO absorbance decreased 5% for the lower doses (0.8 mg) and 10% for the highest doses (1.2 mg). These changes are attributed to an absorption process of the MO in the ZnO surface. On the other hand, a MO decolouration of 70 to 80% was obtained with the ZnO-NFs. Since the majority of the ZnO-NFs did not show visible yellow colour on their surface, it is presumed that changes in the absorbance (measured on the solution) are not caused by a simple adsorption of the dye on the ZnO surface. Similar experiments where photocatalytic materials have been immersed in MO solutions and left in darkness have reported no changes in the concentration or colour of the dye [47]. For instance, Madhab C *et al* [343] used a doubly interpenetrated porous semiconductor metal-organic framework in the decomposition of MO, the study reported no “changes in the UV spectra of the MO” in absence of light.

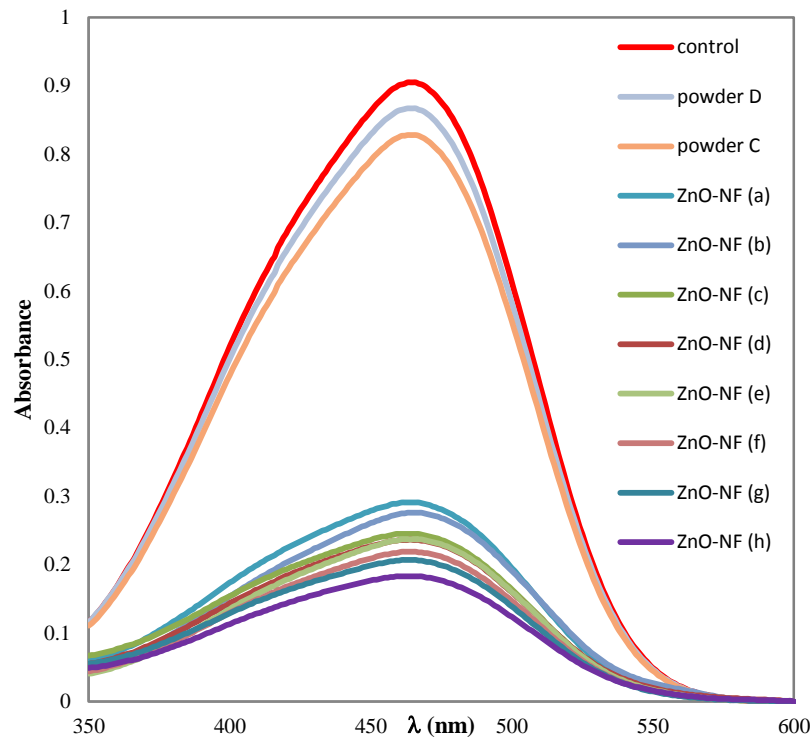


Figure 6.38 Final decolouration of MO produced by ZnO powder and by ZnO-NF with different morphologies and obtained at different anodization conditions.

Herein, it is not clear if the changes in the MO absorbance were due to degradation or decolouration of the dye. As discussed in section 6.1.2 and 6.1.3, MO suffers structural changes produced either by photolysis (mainly by the destruction of conjugated bond

caused by either absorption of photons [320] or by electron transfer [321]) or by photocatalysis where highly reactive species induce direct oxidation or oxidation by hydroxyl radicals (See Equations 6.11 to 6.12) [47]. These structural changes can lead to either decolouration of the dye (by reduction of conjugated bonds) or to degradation of the molecule.

Since the experiments carried out here did not involve exposure to light, it is suggested that a non-well established mechanism occurred in darkness. It is hypothesized herein that the decolouration of the dye could have occurred in different ways: (i) by a previous photo activation of the ZnO-NF by white light (From the laboratory), (ii) by a activation of the ZnO-NF given by photons absorbed by the dye before the darkness conditions happened (this can occur due to the high capacity of dyes of absorbing photon from the visible light [52]), (iii) by a catalyst decolouration produced by the Zn or by the combination of Zn/ZnO and (iv) by an electron transfer mechanism from the media to the dye induced by internal reactions such as the dissolution and precipitation of Zn(II) species. The latter hypothesis is based on the morphological changes observed and discussed in Section 5.3.2.

Very limited literature about these phenomena or similar ones was found. Pradhan *et al* [73], have reported degradation of MO [10^{-5} M] in darkness produced by ZnO doped with Al. In this study ZnO and ZnO-Al films were produced by spray-pyrolysis and supported on Pyrex glass. ZnO-Al showed better performance for the degradation of MO after 3 hours of photocatalysis with 80% of the MO degraded. Authors suggested that the degradation of MO in darkness can be due to a migration of electrons from the aluminium atoms to the surface producing $O_2^{\bullet-}$ radicals favouring decomposition even in darkness. As this study measured the MO changes only by monitoring its decolouration using a UV-vis spectrophotometer, it is not clear which type of decomposition MO suffered. Scott, *et al* [344], examined the role of UV-light pre-treatment and time relaxation on Pt/TiO₂ particles for the catalytic and photocatalytic degradation of formic acid. In this study, formic acid was partially mineralised by Pt/TiO₂ in darkness. This degradation increased with a pre-illuminated treatment. Additionally, the catalytic degradation of formic acid by Pt/TiO₂ in absence of light due to the catalytic action of the Pt is discussed. It is also suggested that the presence of metal in the metal oxide photocatalysts improve the electron-hole separation due to the photogenerated electrons accumulating in the metal which can also mediate the

reduction of the molecular oxygen. The two latter studies have observed similar phenomena (degradation in darkness) with doped materials. Herein, the ZnO-NFs were not doped. However, a potential catalytic role of the Zn foils should be considered in further studies.

By comparing the changes in the final absorbance spectrums with the ZnO-NF morphologies, a relationship was found between morphology and decolouration (Figure 6.39). Featureless morphologies such as the depicted in Figure 6.39-a and 6.39-b result in lower MO decolouration compared to the films that display more complex morphologies (Figure 6.39-c to 6.39-h). As the nanostructures arrangement became more complex and the size of the nanostructures appears to be larger, the decolouration of MO increases. For instance, The ZnO-NF in Figure 6.39-a produced the lowest MO decolouration (70%) and no nanostructures can be observed in the FESEM micrograph, Figure 6.39-e displays visible nanostructures and a final decolouration of 75%, while Figure 6.39-f has the largest nanostructures with a nanowire arrangement and display the highest MO decolouration (80%). These results suggest that the mechanism of MO decolouration occur on the surface of the ZnO layer and therefore morphology and in particular surface area plays an important role.

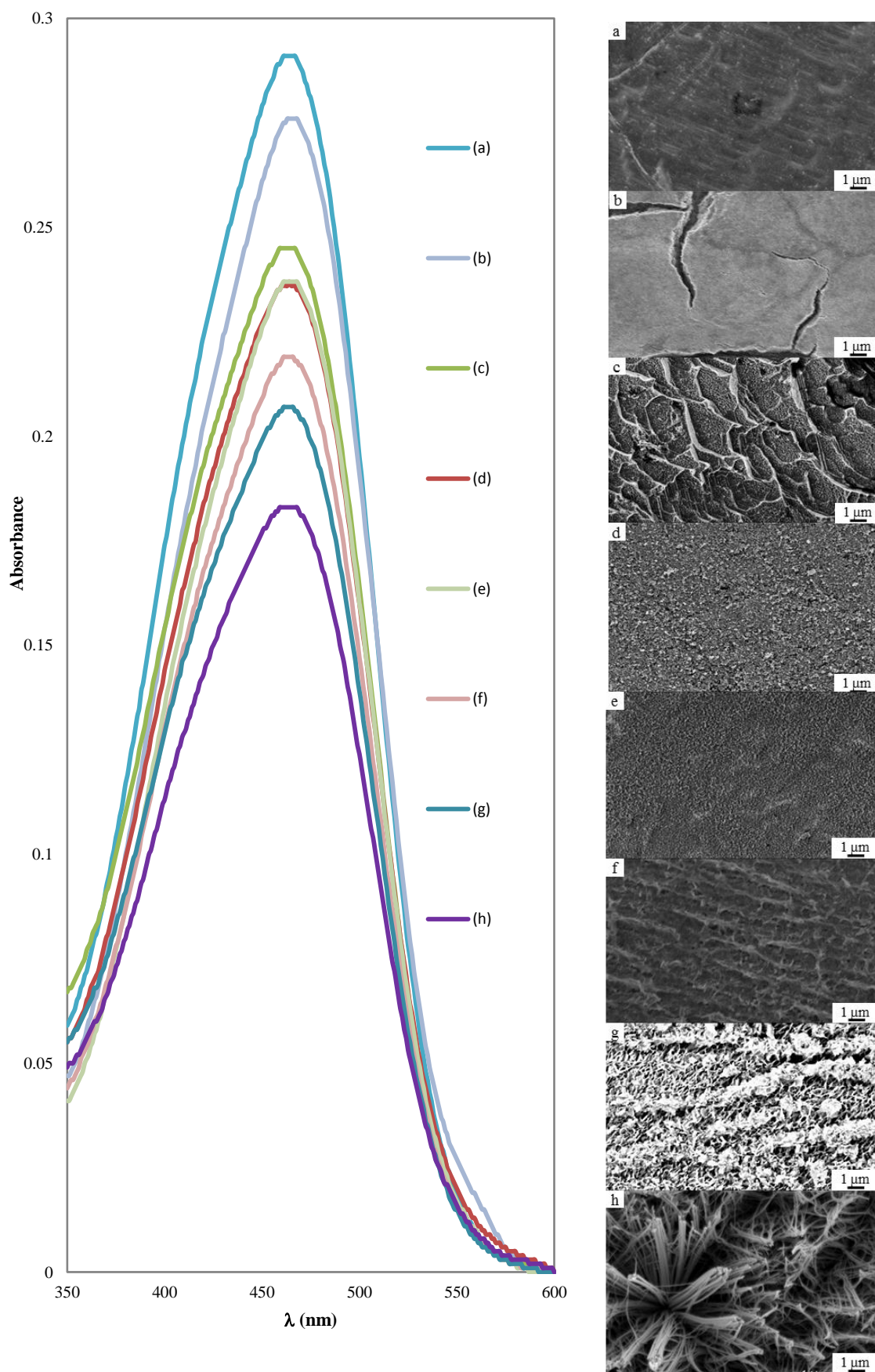


Figure 6.39 Comparison between final decolouration of MO produced by different ZnO-NFs and their morphology.

6.5 Summary

In this chapter alternative reactors and shapes of supported materials were explored for the study of the ZnO nanostructures. In the first section, the design and use of the flat plate photocatalytic reactor was discussed. A preliminary test of the FP-PCR using MO and phenol as a model compounds showed a mass transfer limitation of the reactor which resulted in minimal degradation of the compounds. It was found that the changes in concentration of MO observed during the experiments were due to decolouration produced by UV light rather than degradation. The second section presented the work carried out with the tubular annular photocatalytic reactor and a brief analysis on the production and properties of the ZnO-NW was presented. Photolysis, photocatalysis and EAPC was studied for the degradation of phenol in the TA-PCR reactor. ZnO-NW used in this reactor showed higher morphological stability and no formation of new nanostructures were observed. The current applied during the EAPC was found to improve the degradation of phenol and to participate in the formation of nanostructures on the Zn wire. The coating of glass and optical fibers by sol-gel deposition was discussed as a proof of concept for further studies. Finally, in the last section, the degradation of MO by ZnO-NF in darkness and the relationship between the decolouration of MO and morphology of the ZnO-NW was presented.

“An expert is a person who has made all the mistakes that can be made in a very narrow field.”

Niels Bohr

Chapter 7: Conclusions and future work.

The aim of the work presented throughout this thesis was to conduct a systematic study of the correlation between anodization variables, the physicochemical properties of the obtained nanostructured ZnO films and the photocatalytic activity of the films, paying considerable attention to morphology and its stability under reactions degradation of pollutants in water. The project was divided in three stages. (i) Production of ZnO-NFs, their characterisation as photocatalytic materials and an analysis of the correlation between anodization parameters and intrinsic ZnO-NFs properties which were presented in Chapter 4. (ii) ZnO-NFs were used as a photocatalyst for the degradation of phenol in a batch reactor. The photocatalytic activity, morphological stability and the effect of the ZnO-NFs properties on the photocatalytic degradation of phenol was discussed in Chapter 5. (iii) Two types of reactors were designed and tested to study the photocatalytic performance and morphological stability of the ZnO nanostructures under different mixing conditions. The design, preliminary test, and the production of ZnO-NWs were presented in Chapter 6. Additionally, the decomposition of methyl orange in darkness with ZnO-NFs was discussed and preliminary work on the deposition of ZnO on optical fibres was discussed. This chapter will conclude the main findings obtained from the result of the present work and propose possible future work. Conclusions presented in this section will follow the schematic order of the previous chapters.

7.1. Conclusions

7.1.1. Production of ZnO-NF for photocatalytic applications

Nanostructured ZnO films were obtained via the anodization of Zn foil. It was found that the initial annealing and electropolishing does not have any effect on the formation of the nanostructures as similar morphologies were obtained regardless of the annealing

and electropolishing conditions, however, in order to standardize the initial appearance of the zinc surface, these processes are highly recommended before anodization.

7.1.2. Mechanism of anodization of ZnO and formation of nanostructures

A mechanism of ZnO nanostructure formation was proposed based on: (i) theoretical data of speciation of Zn(II), (ii) measurements of pH, conductivity, dissolved Zn and current density during anodization and (iii) by comparing current density plots of the well-studied anodization of alumina with the ones of anodization of zinc. The proposed mechanism suggests that the formation of ZnO nanostructures result from the competition between dissolution of the initial Zn and ZnO and the deposition of different species of Zn(II) such as ZnO, Zn(OH)₂ and zincates produced by the reaction between the Zn⁺² with the dissociated electrolyte. It is also postulated that, as the pH of the electrolyte determines the predominant Zn(II) species present in the solution, and the dissolution rate of the Zn and ZnO, pH has a strong effect on the formation of nanostructures and, therefore, its effect has to be accounted in anodization studies. The formation of nanowires with KHCO₃ initiate with a formation of a ZnO layer followed by an initial nucleation of the ZnO layer, similar to the one formed during the production of alumina pores by anodization of Al. Afterward, the process follows the mechanism of dissolution and precipitation explained before with a higher rate of deposition compared to dissolution that results in the formation of nanostructures rather than pore-like structures.

7.1.3. Anodization conditions and its effect in ZnO properties

From the morphological analysis of the ZnO-NFs and its correlation to anodization parameters, the following conclusions were found:

- a) The shape of the nanostructures is determined mainly by the type of electrolyte which also determines the pH of the process. The nanostructure surface density increases with concentration, voltage and time. The latter experimental condition also determines the size of nanostructures, leading to the formation of 3D interpenetrated nanostructures once the nanostructures reach a certain length.
- b) The effect of temperature varies with the electrolyte used and the voltage applied.

- c) Dense and well-aligned nanostructures with high aspect ratios display high contact angles, while low aspect ratios and less ordered surfaces show smaller contact angles, forming hydrophilic surfaces.
- d) Changes in time and in the applied voltage result in similar size distribution of the wire diameters.
- e) Nanowires with different crystal size distribution are produced by varying voltage and anodization times. This result provides great opportunities for further studies where samples with different crystal sizes are required for optical and photocatalytic properties.

7.1.4. Guidelines for controlled formation of ZnO nanostructures via anodization

From results obtained during the study of the correlation between anodization parameters and ZnO nanostructure properties, the following design guidelines can be devised:

- a) 1D aligned arrays, usually with super-hydrophobic surfaces, are mainly obtained at near neutral pH regardless of voltage and time.
- b) 3D arrays (hydrophobic and hydrophilic) are formed for long reaction times, regardless of the pH and the voltage.
- c) 2D arrays can be formed at low and high pH regardless of the voltage and time. However, 2D arrays formed at high pH display hydrophobic behaviour only at high voltage.
- d) The anodization conditions where corrosion and pitting are more common are low pH, high voltage and long-time reactions.

7.1.5. ZnO-NF as a photocatalytic material for the degradation of phenol in batch reactor

Phenol was successfully degraded by the ZnO-NFs in a batch reactor. Among the analysed by-products, benzoquinone was found at the highest concentration followed by catechol and hydroquinone. After 12 hours of photocatalytic reaction with the ZnO-NFs, 90 % of the phenol was degraded but some by-products still remained in the solution. Since the concentration of benzoquinone increased parallel to the degradation

of other by-products and phenol, a proposed degradation pathway was given, showing a preferential formation of this compound.

The size of the ZnO crystals does not have a major effect on the photocatalytic degradation of phenol. The thickness of the ZnO layer used for photocatalytic experiments was found to be higher than the photon penetration depth of the polycrystalline ZnO and therefore similar degradation of phenol was observed at different ZnO layer thickness.

The shape and the arrangement of the nanostructures are correlated to the photocatalytic performance of the ZnO-NFs. Although no direct measurements of the BET specific surface areas were carried out, visual analysis made using FESEM micrographs and with adsorption of metal (Mg) suggested significant differences of surface area between the ZnO-NFs used in photocatalytic experiments. For instance, ZnO-NFs that displayed an apparent high surface area did not show the highest rate of phenol degradation. In contrast, some ZnO-NFs with hardly any formation of nanostructures degraded phenol in a higher rate. As a result, a clear trend between morphology and photocatalysis was not found. In contrast to other studies where the total surface area is categorised as the main key factor for improving photocatalysis; this study added valuable work to the essential role of the total photo- active surface area in photocatalyst which appears to be directly related to the morphology of the photocatalyst. Additionally, a new property named herein photo- active surface volume is proposed to describe the total volume of catalyst that can be activated by light at certain wavelength.

Acidification of the phenol solution, found during photocatalysis, is produced by the formation of acidic by-products while the increase in conductivity and changes in dissolved Zn are related to the dissolution of the ZnO layer and the formation of ions and CO₂ during the degradation of phenol.

7.1.6. Stability of ZnO-NF during photocatalytic reactions

Phenol can be degraded by photocatalysis even at minimal concentrations of dissolved oxygen. Oxygen saturated and unsaturated solutions of phenol resulted in similar degradation rates. Under anoxic conditions absorbed dissociated hydroxyl groups from

water, and oxygen from the ZnO lattice, are used in the production of reactive species and degradation of phenol.

During the photocatalytic degradation of phenol in the batch reactor, the formation of new nanostructures was observed. High levels of oxygen contribute to the formation of the new nanostructures due to the increase of the production and precipitation of ZnO and Zn(OH)₂. On the other hand, under anoxic conditions this phenomena was minimal and the initial morphology of the ZnO-NFs remained.

The formation of the new morphologies appears to be related to oxidation process occurring during the photocatalytic degradation of phenol. ZnO-NFs exposed to water without being exposed to UV light maintained their initial morphologies but a layer of ZnO and Zn(OH)₂ was deposited on the top of the nanowires. During the photocatalytic reaction, on the other hand, the initial morphology of the ZnO-NF varied dramatically. It appears that the initial morphology of the nanostructures serves as a template for the new morphologies.

7.1.7. Effect of Post-treatment of ZnO-NF in photocatalytic activity

The thermal post-treatment lead to the formation of cracks on the ZnO nanowire surfaces and changed the crystallinity of the nanostructures without affecting the general morphology of the ZnO-NFs. The crystallinity of the ZnO nanostructures vary with post-annealing time, however, after a certain period of post-treatment, no further changes are produced. ZnO-NFs exposed to post-annealing displayed higher degradation of phenol due to the changes in crystallinity and in the ZnO content.

Hierarchical nanostructures produced by immersion of ZnO-NFs in deionised water did not enhance the photocatalytic degradation of phenol. On the other hand, oxygen plasma treatment appears to be a promising post-treatment. ZnO-NFs treated by oxygen plasma displayed an enhancement in the degradation of phenol by 40% and 10% compared to the untreated films and post-annealed films respectively. Additionally to the positive effect on phenol degradation, ZnO-NFs treated with oxygen plasma were more stable during the photocatalytic reaction, the dissolution of Zn was lower and the final morphology remained similar to the initial. The higher stability produced by the oxygen

plasma treatment appears to be related to a minimal thermal stress during the post-treatment where no cracks were produced on the surface of the nanowires.

7.1.8. Photocatalytic experiments with FP-PCR

Photocatalytic experiments in the FP-PCR with MO and phenol revealed a mass transfer limitation. This minimizes internal and external mass transfer processes between the model pollutants and the photocatalyst resulting in no photocatalytic degradation. Changes in the initial concentration of the MO and phenol and variation of the flow rate did not improve the mass transfer and no degradation of the model pollutants was observed.

7.1.9. ZnO-NW and cylindrical reactor

ZnO nanowires were grown on the Zn wire surface by anodization using KHCO_3 as electrolyte. The anodization of a Zn wire follows similar mechanisms to the anodization with Zn foil. Thick ZnO layers growing in a radial shapes were more susceptible to display cracks on the surface due to a radial tension on the base of the nanostructures. On the other hand, after thermal post-treatment, thin ZnO layers grown on the wire were more stable than the ones grown on the Zn foil as the former ones did not display cracks.

Phenol was successfully degraded by the ZnO-NWs in the TA-PCR. Mass transfer limitations in this type of reactor were minimal compared to the FP-PCR with 65% of phenol degradation reached after 2 hours of reaction using the TA-PCR. As the total illumination exposition time was constant for all the experiments, phenol exhibited similar photolytic degradation regardless the flow rate.

A natural oxide layer formed on the surface of the Zn wire acted as a photocatalyst enhancing the degradation of phenol by 20% after the second hour compared to photolysis. Furthermore, ZnO-NWs enhance the degradation by 35% during the first hour and 50% during the second hour of reaction. By applying a low current to the Zn wire, the phenol degradation rates were found similar to the ones obtained with nanostructured materials. This process, named herein as electric assisted photocatalysis (EAPC), differs from the photo-electro-catalysis in the way that electricity is applied to the system; however the reduction on the electron-hole recombination given by the

electrons during electro-photo-catalysis is also likely to occur during the EAPC and is likely to be the responsible for the enhancement of the phenol degradation.

The radial configuration of the ZnO-NW appears to be more stable against photo corrosion and mechanical abrasion. The initial and final morphology of the ZnO-NWs used in photocatalytic reactions were similar and no modification on the shape of the nanowires was observed. The flow in the TA-PCR, which acts as a stirring process, improved the mass transfer between phenol molecules and the photocatalyst, and also minimised the re-deposition of ZnO on the nanowires. On the other hand, It was found that the low current applied to the Zn wire during the EAPC induced the formation of nanostructures on the Zn wire surface.

7.1.10. Decomposition of MO with ZnO-NF in darkness

ZnO-NFs decolourised methyl orange in dark conditions. The process appears to be related to the morphology of the ZnO-NF and in particular to the surface area. A trend between decolouration of MO and morphology was found.

7.1.11. Deposition of ZnO on optical fibers surface.

ZnO was successfully deposited on the surface of optical fibres; the most homogeneous ZnO layer was obtained with the sol-gel labelled as SGB4 and SGB5. These two sol-gels were obtained using PVP which appear to improve the adherence of the sol-gel on the optical fibre and to the formation of a smooth ZnO layer without affecting the final composition of the layer.

7.1.12. Concluding Remarks

This thesis has addressed some of the gaps in knowledge about the relationship between the production of ZnO photocatalytic nanostructures by anodization, their photocatalyst properties and their photocatalytic activity. It postulated a mechanism for the formation of the ZnO nanostructures and provides a useful guideline for the control of the morphology of nanostructures during their production by anodization. Conclusions obtained from the correlation between morphology and photocatalytic activity contributes to the understanding of the factors that control photocatalysis and in particular gives strong evidence of the photo-active surface which no necessarily are

correlated to the surface area. The latter contribution represents a significant step towards to the development of nanostructured photocatalysts based on efficient morphologies rather than only large specific surface areas. It also provides information about the stability of the ZnO material as a photocatalyst and evidences the formation of new nanostructures during photocatalysis which have not been reported before. Finally, three not-well-known processes and phenomena were identified: The advantages of using oxygen plasma as a post-treatment during the production of ZnO nanostructures, the phenomena of decomposition of dyes in darkness by the ZnO-NFs and the enhancement of photocatalysis made by EAPC with a small voltage applied directly across the photocatalyst substrate.

7.2. Future work.

Proposed future work presented in this section cover (i) further experiments that might contribute to a better understanding of the work discussed throughout this thesis and (ii) new projects based on the results obtained in this project.

7.2.1. Mechanism of nanostructures formation via anodization of Zn.

Although a mechanism for the ZnO nanostructures formation was proposed in this thesis, subsequent analysis is recommended to fully understand the physiochemical changes involved in this process. Some of the analyses suggested are: A chemical identification of each Zn(II) species formed during anodization and a comparison of the different changes of current density, pH, conductivity and dissolved Zn during anodization reactions for different electrolytes is needed.

7.2.2. Further study of crystal size and crystal defects produced during anodization.

Although it was found that crystal size distribution was affected by anodization voltage and anodization time, no further studies correlating these parameters were carried out. A further analysis will provide higher support to control the crystal size of the ZnO nanostructures.

ZnO-NF obtained at different anodization conditions displayed different band-gap energies. Although hypotheses explaining the reason of these differences were postulated, no further analysis was performed. An analysis of crystal defects in films

with different band gap energies used in a photocatalytic reaction will contribute to understanding its effect on the photocatalytic activity.

7.2.3. An alternative post-treatment to enhance the photocatalytic activity and morphological stability of ZnO nanostructures.

Oxygen plasma post-treatment was explored in this work. Results showed an improvement in the photocatalytic performance and stability of the ZnO-NFs. However, the different experimental conditions such as irradiation time and intensity of this treatment were not tested and only a morphological analysis of the ZnO-NFs exposed to oxygen plasma was carried out. Further analysis will add major understanding on the effect of the treatment on the material properties and its potential use for improvement photocatalytic materials. Some of the aspects that can be studied are: (i) changes in crystallinity, composition and lattice defects produced by the oxygen plasma post-treatment on the ZnO-NFs (ii) effect of oxygen plasma irradiation time on the photocatalytic performance of ZnO-NFs and (iii) analysis of stability of the ZnO-NFs morphology under different oxygen plasma irradiation conditions. Additionally, other types of plasma such as Hydrogen plasma and argon plasma can be explored.

7.2.4. Further analysis on the photocatalyst in anoxic photocatalytic reactions.

In this work, it was shown that photocatalytic degradation of phenol occurs under anoxic conditions suggesting that the reaction followed the Mars-van Krevelen mechanism. Additionally, it was shown that the composition of the ZnO-NFs were similar after reactions under saturated and unsaturated oxygen conditions. However, the composition of the ZnO-NFs used at anoxic conditions was not studied and no studies related to oxygen vacancies in the ZnO lattice were conducted. A study of the crystallinity of the ZnO nanostructures before and after photocatalytic reactions and, in particular, on the lattice defects and oxygen vacancies might allow for better understanding of the mechanism of the photocatalytic reactions under anoxic conditions.

7.2.5. ZnO-NW and TA-PCR

Results obtained in this work showed the potential use of the TA-PCR to study different aspects of the stability of the supported photocatalyst among other photocatalytic

aspects and the electro assisted photocatalysis. A set of experiments and analysis proposed herein are:

- a) Effect of flow rate on the mass transfer between supported photocatalyst and substrate, including the effect on the photocatalytic degradation of phenol at different flow rates.
- b) Analysis of morphological stability of ZnO-NWs under different flow rate conditions.
- c) Study of the effect of applied voltage and flow rate on the potential electro-oxidation reaction (in absence of UV light) and on the electric assisted photocatalysis.
- d) Study of the effect of applied current on the stability of the ZnO-NWs in electro assisted photocatalysis.

7.2.6. Further studies of the degradation of dyes by ZnO-NFs in darkness conditions.

Results obtained in this work showed the potential use of ZnO-NFs for the decolouration of dyes with a minimal use of energy. Further analytical studies about degradation of MO including detection of by-products and reduction of the total organic carbon can provide more information about the mechanism of the decolouration. A further morphological analysis of the ZnO-NFs is recommended, as it can show structural changes (similar to those observed in this thesis). Potential formation of ZnO layer produced during the process in dark can produce internal reactions with transfer of electrons from the media to the absorbed dye inducing molecular transformation of the dye.

References

- [1] H. Ternes, Thomas . Joss, Adriano. Siegrist, "Scrutinizing pharmaceuticals and personal care products in waste water treatment," *Environ. Sci. Technol.*, 2004.
- [2] B. Kasprzyk-Hordern, R. M. Dinsdale, and A. J. Guwy, "The occurrence of pharmaceuticals, personal care products, endocrine disruptors and illicit drugs in surface water in South Wales, UK.," *Water Res.*, vol. 42, no. 13, pp. 3498–518, Jul. 2008.
- [3] M. a Shannon, P. W. Bohn, M. Elimelech, J. G. Georgiadis, B. J. Mariñas, and A. M. Mayes, "Science and technology for water purification in the coming decades.," *Nature*, vol. 452, no. 7185, pp. 301–10, Mar. 2008.
- [4] S. a. Avlonitis, K. Kouroumbas, and N. Vlachakis, "Energy consumption and membrane replacement cost for seawater RO desalination plants," *Desalination*, vol. 157, no. 1–3, pp. 151–158, Aug. 2003.
- [5] C. McCullagh, N. Skillen, M. Adams, and P. K. J. Robertson, "Photocatalytic reactors for environmental remediation: a review," *J. Chem. Technol. Biotechnol.*, vol. 86, no. 8, pp. 1002–1017, Aug. 2011.
- [6] Z. H. Ma N, Zhang Y, Quan X, Fan X, "Performing a microfiltration integrated with photocatalysis using an Ag-TiO(2)/HAP/Al(2)O(3) composite membrane for water treatment: Evaluating effectiveness for humic acid removal and anti-fouling properties.," *Water Res.*, vol. 44, no. 20, pp. 6104–6114, 2010.
- [7] R. Munter, "Advanced Oxidation Processes - Current status and prospects," *Proc. Est. Acad. Sci. Chem*, vol. 50, no. 2, pp. 59–80, 2001.
- [8] H. F. Lin, R. Ravikrishna, and K. . Valsaraj, "Reusable adsorbents for dilute solution separation. 6. Batch and continuous reactors for the adsorption and degradation of 1,2-dichlorobenzene from dilute wastewater streams using titania as a photocatalyst," *Sep. Purif. Technol.*, vol. 28, no. 2, pp. 87–102, Aug. 2002.
- [9] et al. Alfano, O.M., "Photocatalysis in water environments using artificial and solar light," *Catal. Today*, vol. 58(2–3), pp. 199–230, 2000.
- [10] D. Beydoun, R. Amal, G. Low, and S. Mcevoy, "Role of nanoparticles in photocatalysis," pp. 439–458, 2000.
- [11] A. B. F. Martinson, J. W. Elam, J. T. Hupp, and M. J. Pellin, "ZnO nanotube based dye-sensitized solar cells," *Nano Lett.*, vol. 7, no. 8, pp. 2183–7, Aug. 2007.
- [12] Z. L. Wang, "Zinc oxide nanostructures: growth, properties and applications," *J. Phys. Condens. Matter*, vol. 16, no. 25, pp. R829–R858, Jun. 2004.
- [13] M. Alhamed and W. Abdullah, "Structural and Optical Properties of ZnO: Al Films Prepared by the Sol-Gel Method," *J. Electron Devices*, vol. 7, pp. 246–252, 2010.
- [14] M. Kobayashi and W. Kalriess, "Photocatalytic Activity of Titanium Dioxide and Zinc Oxide," vol. 112, no. June, pp. 83–85, 1997.
- [15] L. historical Society, "Un Millenium Goals," 2010. [Online]. Available: http://www.lewishistoricalsociety.com/wiki/tiki-read_article.php?articleId=114.
- [16] A. Brown, M. D. Matlock, and D. Ph, "A Review of Water Scarcity Indices and Methodologies," 2011.
- [17] A. Singh and J. Van Woerden, "Review of Data Needs," pp. 215–230.
- [18] F. and A. O. of the U. N. FAO, "Water-scarcity." FAO, Food and Agriculture Organization of the Unted Nations, 2012.
- [19] T. H. E. United and N. World, *Managing Water under Uncertainty and Risk*, vol. 1. .

- [20] World Meteorological Organization, "(IPCC), Intergovernmental Panel on Climate Change.," *Intergovernmental Panel on Climate Change*, 2012. [Online]. Available: <http://www.wmo.int/pages/themes/climate>.
- [21] U. Nations, "United Nations Statistics Division," 2012. [Online]. Available: <http://unstats.un.org/unsd/default.htm>.
- [22] G. E. Outlook, "GEO 4 environment for development," 2007.
- [23] W. B. C. F. S. D. Wbcsd, "Business solutions for a sustainable world," 2012. [Online]. Available: <http://www.wbcsd.org/home.aspx>.
- [24] S. and C. O. U. UN water; United Nation Educational, "World Water Assessment Programme," 2012. [Online]. Available: <http://www.unesco.org/new/en/natural-sciences/environment/water/wwap/>.
- [25] F. Méndez-Arriaga, S. Esplugas, and J. Giménez, "Degradation of the emerging contaminant ibuprofen in water by photo-Fenton.," *Water Res.*, vol. 44, no. 2, pp. 589–95, Jan. 2010.
- [26] N. a Doerr-MacEwen and M. E. Haight, "Expert stakeholders' views on the management of human pharmaceuticals in the environment.," *Environ. Manage.*, vol. 38, no. 5, pp. 853–66, Nov. 2006.
- [27] K. Hirsch, R., Ternes, T. A., Haberer, K., Mehlich, A., Ballwanz, F., Kratz, "Determination of antibiotics in different water compartments via liquid chromatography-electrospray tandem mass spectrometry.," *J. Chromatogr.*, vol. 815, no. 2, pp. 213–223., 1998.
- [28] T. a Ternes, M. Meisenheimer, D. McDowell, F. Sacher, H.-J. Brauch, B. Haist-Gulde, G. Preuss, U. Wilme, and N. Zulei-Seibert, "Removal of pharmaceuticals during drinking water treatment.," *Environ. Sci. Technol.*, vol. 36, no. 17, pp. 3855–63, Sep. 2002.
- [29] G. R. Boyd, H. Reemtsma, D. a Grimm, and S. Mitra, "Pharmaceuticals and personal care products (PPCPs) in surface and treated waters of Louisiana, USA and Ontario, Canada.," *Sci. Total Environ.*, vol. 311, no. 1–3, pp. 135–49, Jul. 2003.
- [30] D. D. Glassmeyer, S. T., Furlong, E. T., Kolpin, D. W., Cahill, J. D., Zaugg, S. D., Werner, S. L., Meyer, M. T., Kryak, "Transport of chemical and microbial compounds from known wastewater discharges: Potential for use as indicators of human fecal contamination.," *Environ. Sci. Technol.*, vol. 39, no. 14, pp. 5157–5169., 2005.
- [31] M. R. Birgit Gross, John Montgomery-Brown, Anneke Naumann, "Occurrence and fate of pharmaceuticals and alkylphenol ethoxylate metabolites in an effluent-dominated river and wetland," *Environ. Toxicol. Chem.*, vol. 23, no. 9, pp. 2074–2083, 2004.
- [32] W. Ayscough, N. J., Fawell, J., Franklin, G., Young, *Review of human pharmaceuticals in the environment. Review of Human Pharmaceuticals in the Environment. R & D technical report*. 2000.
- [33] P. K. Jjemba, "Excretion and ecotoxicity of pharmaceutical and personal care products in the environment.," *Ecotoxicol. Environ. Saf.*, vol. 63, no. 1, pp. 113–30, Jan. 2006.
- [34] D. van der Kooij, *The significance of HPCs for water quality and human health*. Geneva: IWA Publishing, World Health Organization, 2003.
- [35] D. Metcalf & Eddy. Tchobanoglous, George. Burton, Franklin L and Stensel, "wastewater engineering: An overview," in *Wastewater engineering, treatment and reuse.*, Fouth., New York: Mc Graw Hill International editions, 2003, pp. 1–24.
- [36] C. B. Coyne and J. M. Bergelson, "CAR: a virus receptor within the tight junction.," *Adv. Drug Deliv. Rev.*, vol. 57, no. 6, pp. 869–82, May 2005.

- [37] D. Metcalf & Eddy. Tchobanoglous, George. Burton, Franklin L. Stensel, "Advanced wastewater treatments," in *Wastewater Engineering, Treatment and Reuse*, Fourth., New York: Mc Graw Hill International editions, 2003, pp. 1035–1205.
- [38] Water Environment Federation, "Membrane Equipment and System Overview," in *Membrane Systems for Wastewater treatment*, Alexandria USA: Mc Graw Hill, 1994, pp. 16–53.
- [39] Y. Zhou, "Evaluating the costs of desalination and water transport," *Water Resour. Res.*, vol. 41, no. 3, pp. 1–10, 2005.
- [40] K. P. Lee, T. C. Arnot, and D. Mattia, "A review of reverse osmosis membrane materials for desalination—Development to date and future potential," *J. Memb. Sci.*, vol. 370, no. 1–2, pp. 1–22, Mar. 2011.
- [41] W. treatment solutions LENNTECH, "Membrane technology." [Online]. Available: <http://www.lenntech.com/membrane-technology.htm>. [Accessed: 04-May-2015].
- [42] W. E. F. (WEF), "Membrane systems for wastewater treatment," in *Membrane systems for wastewater treatment*, 2006, pp. 58–109.
- [43] A. Ibadon and P. Fitzpatrick, "Heterogeneous Photocatalysis: Recent Advances and Applications," *Catalysts*, vol. 3, no. 1, pp. 189–218, Mar. 2013.
- [44] M. N. Chong, B. Jin, C. W. K. Chow, and C. Saint, "Recent developments in photocatalytic water treatment technology: a review.," *Water Res.*, vol. 44, no. 10, pp. 2997–3027, May 2010.
- [45] M. Anne, "Heterogeneous Photocatalysis," 1993.
- [46] S. Ahmed, M. G. Rasul, W. N. Martens, R. Brown, and M. a. Hashib, "Advances in Heterogeneous Photocatalytic Degradation of Phenols and Dyes in Wastewater: A Review," *Water, Air, Soil Pollut.*, vol. 215, no. 1–4, pp. 3–29, May 2010.
- [47] S. K. Kansal, M. Singh, and D. Sud, "Studies on photodegradation of two commercial dyes in aqueous phase using different photocatalysts.," *J. Hazard. Mater.*, vol. 141, no. 3, pp. 581–90, Mar. 2007.
- [48] G. G. De Oliveira, N. R. C. F. Machado, and O. A. A. Santos, "DECOLOURIZATION OF VARIOUS DYES BY PHOTOCATALYSIS USING ZNO AS AN ALTERNATIVE CATALYST TO TIO₂," pp. 1–10, 2002.
- [49] G. Li Puma, V. Puddu, H. K. Tsang, A. Gora, and B. Toepfer, "Photocatalytic oxidation of multicomponent mixtures of estrogens (estrone (E1), 17 β -estradiol (E2), 17 α -ethynylestradiol (EE2) and estriol (E3)) under UVA and UVC radiation: Photon absorption, quantum yields and rate constants independent of photon absorp," *Appl. Catal. B Environ.*, vol. 99, no. 3–4, pp. 388–397, Sep. 2010.
- [50] D. Dolat, N. Quici, E. Kusiak-Nejman, a. W. Morawski, and G. Li Puma, "One-step, hydrothermal synthesis of nitrogen, carbon co-doped titanium dioxide (N,CTiO₂) photocatalysts. Effect of alcohol degree and chain length as carbon dopant precursors on photocatalytic activity and catalyst deactivation," *Appl. Catal. B Environ.*, vol. 115–116, pp. 81–89, Apr. 2012.
- [51] R. Andreozzi, "Advanced oxidation processes (AOP) for water purification and recovery," *Catal. Today*, vol. 53, no. 1, pp. 51–59, 1999.
- [52] B. Ohtani, "Preparing Articles on Photocatalysis—Beyond the Illusions, Misconceptions, and Speculation," *Chem. Lett.*, vol. 37, no. 3, pp. 216–229, 2008.
- [53] J.-M. Herrmann, "Fundamentals and misconceptions in photocatalysis," *J. Photochem. Photobiol. A Chem.*, vol. 216, no. 2–3, pp. 85–93, Dec. 2010.

- [54] K. Fujishima, Akira and Honda, "Electrochemical Photolysis of Water at a Semiconductor Electrode," *Nature*, vol. 238, pp. 37–38, 1972.
- [55] Corpous, "No Title," 2014. [Online]. Available: <http://www.scopus.com>. [Accessed: 17-Apr-2014].
- [56] J. Herrmann, "Heterogeneous photocatalysis: fundamentals and applications to the removal of various types of aqueous pollutants," *Catal. Today*, vol. 53, no. 1, pp. 115–129, Oct. 1999.
- [57] A. E. Cassano and O. M. Alfano, "Reaction engineering of suspended solid heterogeneous photocatalytic reactors," *Catal. Today*, vol. 58, no. 2–3, pp. 167–197, May 2000.
- [58] J. F. Richard, C. Bosquet, F. Pilichowski, "Photocatalytic transformation of aromatic compounds in aqueous zinc oxide suspensions" effect of substrate concentration on the distribution of products," *J. Photochem. Photobiol. A Chem.*, vol. 108, pp. 45–49, 1997.
- [59] A. Houas, H. Lachheb, M. Ksibi, E. Elaloui, C. Guillard, and J. Herrmann, "Photocatalytic degradation pathway of methylene blue in water," vol. 31, pp. 145–157, 2001.
- [60] I. R. Bellobono, R. Scotti, M. D'Arienzo, F. Morazzoni, R. Bianchi, R. Stanescu, C. Costache, L. Bobirica, G. Cobzaru, P. M. Tozzi, M. Rossi, M. L. Bonardi, F. Groppi, and L. Gini, "Nonlinear Modelling of Kinetic Data Obtained from Photocatalytic Mineralisation of 2,4-Dichlorophenol on a Titanium Dioxide Membrane," *Int. J. Photoenergy*, vol. 2009, pp. 1–10, 2009.
- [61] S. L. Pechenyuk and M. R. Materials, "Reviews The use of the pH at the point of zero charge for characterizing the properties of oxide hydroxides," vol. 48, no. 6, pp. 1017–1023, 1999.
- [62] X. E. Styliidi, M., Kondarides, D.I., Verykios, "Pathways of solar light-induced photocatalytic degradation of azo dyes in aqueous TiO₂ suspensions," *Appl. Catal. B Environ.*, vol. 40, pp. 271–286, 2003.
- [63] W. Malato, S., Fernandez-Ibanez, P., Maldonado, M.I., Blanco, J., Gernjak, "Decontamination and disinfection of water by solar photocatalysis: recent overview and trends," *Catal. Today*, vol. 147, pp. 1–59, 2009.
- [64] C. Minero, "Kinetic analysis of photoinduced reactions at the water semiconductor interface," *Catal. Today*, vol. 54, pp. 205–216, 1999.
- [65] N. Serpone, "Some remarks on so-called heterogenous photocatalysis and on the mechanical application of the Langmuir–Hinshelwood kinetic model," *J. Adv. Oxid. Technol.*, vol. 10, pp. 111–115, 2007.
- [66] C. Doornkamp and V. Ponec, "The universal character of the Mars and Van Krevelen mechanism," *J. Mol. Catal. A Chem.*, vol. 162, no. 1–2, pp. 19–32, Nov. 2000.
- [67] M. Litter, "Heterogeneous photocatalysis Transition metal ions in photocatalytic systems," *Appl. Catal. B Environ.*, vol. 23, no. 2–3, pp. 89–114, Nov. 1999.
- [68] J. Moreira, B. Serrano, A. Ortiz, and H. de Lasa, "A unified kinetic model for phenol photocatalytic degradation over TiO₂ photocatalysts," *Chem. Eng. Sci.*, vol. 78, pp. 186–203, Aug. 2012.
- [69] G. Li Puma, B. Toepfer, and A. Gora, "Photocatalytic oxidation of multicomponent systems of herbicides: Scale-up of laboratory kinetics rate data to plant scale," *Catal. Today*, vol. 124, no. 3–4, pp. 124–132, Jun. 2007.
- [70] M. A. Mueses, F. Machuca-Martinez, and G. Li Puma, "Effective quantum yield and reaction rate model for evaluation of photocatalytic degradation of water contaminants in heterogeneous pilot-scale solar photoreactors," *Chem. Eng. J.*, vol. 215–216, pp. 937–947, Jan. 2013.

- [71] a. Cabrera Reina, L. Santos-Juanes, J. L. García Sánchez, J. L. Casas López, M. I. Maldonado Rubio, G. Li Puma, and J. a. Sánchez Pérez, “Modelling the photo-Fenton oxidation of the pharmaceutical paracetamol in water including the effect of photon absorption (VRPA),” *Appl. Catal. B Environ.*, vol. 166–167, pp. 295–301, May 2015.
- [72] and A. R. O. Carp, C. L. Huisman, “Photoinduced reactivity of titanium dioxide,” *Prog. solid state Chem.*, vol. 32, pp. 33–177, 2004.
- [73] P. Pradhan, J. C. Alonso, and M. Bizarro, “Photocatalytic Performance of ZnO: Al Films under Different Light Sources,” *Int. J. Photoenergy*, vol. 2012, pp. 1–7, 2012.
- [74] J.-M. Herrmann, “Heterogeneous photocatalysis: an emerging discipline involving multiphase systems,” *Catal. Today*, vol. 24, pp. 157–164, 1995.
- [75] V. K. and A. A. A. Pareek, “Analysis of photocatalytically reactive systems: kinetic modeling and reactor design via computational fluid dynamics,” *Photochem. Photobiol. A Chem.*, vol. 1, pp. 345–412, 2003.
- [76] R. Article, “Light intensity distribution in heterogenous photocatalytic,” pp. 171–201, 2008.
- [77] M. Hill, “Dictionary of scientific & technical terms,” *6E. S.v.*, 2003. [Online]. Available: <http://encyclopedia2.thefreedictionary.com>. [Accessed: 14-Apr-2015].
- [78] T. Egerton, “UV-Absorption—The Primary Process in Photocatalysis and Some Practical Consequences,” *Molecules*, vol. 19, no. 11, pp. 18192–18214, 2014.
- [79] I. Salvado and D. M. Hargreaves, “Evaluation of the Intrinsic Photocatalytic Oxidation Kinetics of Indoor Air Pollutants,” vol. 41, no. 6, pp. 2028–2035, 2007.
- [80] and G. L. P. Salvado-Estivill, I., A. Brucato, “Two-Dimensional Modeling of a Flat-Plate Photocatalytic Reactor for Oxidation of Indoor Air Pollutants,” *Ind. Eng. Chem.*, vol. 46, no. 23, pp. 7489–7496, 2007.
- [81] M. Vezzoli, W. N. Martens, and J. M. Bell, “Investigation of phenol degradation: True reaction kinetics on fixed film titanium dioxide photocatalyst,” *Appl. Catal. A Gen.*, vol. 404, no. 1–2, pp. 155–163, Sep. 2011.
- [82] et al Dijkstra, M.F.J., “Modelling the photocatalytic degradation of formic acid in a reactor with immobilized catalyst,” *Chem. Eng. Sci.*, vol. 57, pp. 22–23, 2002.
- [83] et al. Goetz, V., “Modelling aqueous heterogeneous photocatalytic degradation of organic pollutants with immobilized TiO₂,” *Chem. Eng. Process. Process Intensif.*, vol. 48, no. 1, pp. 532–537, 2009.
- [84] R. Dillert, A. E. Cassano, R. Goslich, and D. Bahnemann, “Large scale studies in solar catalytic wastewater treatment,” *Catal. Today*, vol. 54, no. 2–3, pp. 267–282, 1999.
- [85] A. E. and O. M. A. Cassano, “Reaction engineering of suspended solid heterogeneous photocatalytic reactors,” *Catal. Today*, vol. 58, no. 2–3, pp. 167–197, 2000.
- [86] C. M. Ling, A. R. Mohamed, and S. Bhatia, “Performance of photocatalytic reactors using immobilized TiO₂ film for the degradation of phenol and methylene blue dye present in water stream.,” *Chemosphere*, vol. 57, no. 7, pp. 547–54, Nov. 2004.
- [87] and H. D. L. Romero-Vargas Castrillon, S., H. Ibrahim, “Flow field investigation in a photocatalytic reactor for air treatment (Photo-CREC-air),” *Chem. Eng. Sci.*, vol. 61, no. 10, pp. 3343–3361, 2006.
- [88] et al Esterkin, C.R., “Radiation field inside a reactor of glass-fiber meshes coated with TiO₂,” *AIChE J.*, vol. 48, no. 4, pp. 832–845, 2002.
- [89] et al Imoberdorf, G.E., “Monte Carlo model of UV-Radiation interaction with TiO₂-Coated spheres,” *AIChE J.*, vol. 53, no. 10, pp. 2688–2703, 2007.

- [90] and C. W. aghipour, F., N. Ellis, "Experimental and computational study of gas-solid fluidized bed hydrodynamics," *Chem. Eng. Sci.*, vol. 60, no. 24, pp. 6857–6867, 2005.
- [91] A. L. L. Zazueta, H. Destailats, and G. Li Puma, "Radiation field modeling and optimization of a compact and modular multi-plate photocatalytic reactor (MPPR) for air/water purification by Monte Carlo method," *Chem. Eng. J.*, vol. 217, pp. 475–485, Feb. 2013.
- [92] G. L. Puma and P. L. Yue, "A laminar falling film slurry photocatalytic reactor. Part I—model development," *Chem. Eng. Sci.*, vol. 53, no. 16, pp. 2993–3006, Aug. 1998.
- [93] G. L. Puma and P. L. Yue, "A laminar falling film slurry photocatalytic reactor. Part II—experimental validation of the model," *Chem. Eng. Sci.*, vol. 53, no. 16, pp. 3007–3021, Aug. 1998.
- [94] G. Li Puma and P. L. Yue, "A Novel Fountain Photocatalytic Reactor for Water Treatment and Purification: Modeling and Design," *Ind. Eng. Chem. Res.*, vol. 40, no. 23, pp. 5162–5169, Nov. 2001.
- [95] G. L. Puma and P. L. Yue, "The modeling of a fountain photocatalytic reactor with a parabolic profile," vol. 56, pp. 721–726, 2001.
- [96] G. Li Puma and P. L. Yue, "A novel fountain photocatalytic reactor: model development and experimental validation," *Chem. Eng. Sci.*, vol. 56, no. 8, pp. 2733–2744, Apr. 2001.
- [97] G. Li Puma, J. N. Khor, and A. Brucato, "Modeling of an Annular Photocatalytic Reactor for Water Purification: Oxidation of Pesticides," *Environ. Sci. Technol.*, vol. 38, no. 13, pp. 3737–3745, Jul. 2004.
- [98] G. Li Puma and P. L. Yue, "Modelling and design of thin-film slurry photocatalytic reactors for water purification," *Chem. Eng. Sci.*, vol. 58, no. 11, pp. 2269–2281, Jun. 2003.
- [99] G. Li Puma, "Modeling of Thin-Film Slurry Photocatalytic Reactors Affected by Radiation Scattering," *Environ. Sci. Technol.*, vol. 37, no. 24, pp. 5783–5791, Dec. 2003.
- [100] G. Li Puma and A. Brucato, "Dimensionless analysis of slurry photocatalytic reactors using two-flux and six-flux radiation absorption–scattering models," *Catal. Today*, vol. 122, no. 1–2, pp. 78–90, Apr. 2007.
- [101] A. Górak and A. Stankiewicz, "Intensified Reaction and Separation Systems," *Annu. Rev. Chem. Biomol. Eng.*, vol. 2, no. 1, pp. 431–451, 2011.
- [102] C. Engineering, "A TAYLOR VORTEX REACTOR FOR HETEROGENEOUS," vol. 50, no. 20, 1995.
- [103] A. K. and A. A. C. M. B. Ray, "Novel swirl-flow reactor for kinetic studies of semiconductor photocatalysis," *AIChE J.*, vol. 43, no. 10, pp. 2571–2578, 1997.
- [104] M. R. Hoffmann and M. M. K. Laboratories, "Development and Optimization of a TiO₂-Coated FiberOptic Cable Photocatalytic Degradation of 4-Chlorophenol," vol. 29, no. 12, pp. 2974–2981, 1995.
- [105] M. Dionysiou, D. Balasubramanian, G. Suidan, M. Khodadoust, A. Baudin, I. Laine, "Rotating disk photocatalytic reactor: Development, characterization, and evaluation for the destruction of organic pollutants in water," *Water Res.*, vol. 34, no. 11, pp. 2927–2940, 2000.
- [106] I. Boiarkina, S. Pedron, and D. Patterson, "experimental and modelling investigation of the effect of the flow regime on the photocatalytic degradation of methylene blue on a thin film coated ultraviolet irradiated spinning disc reactor. Opus : University of Bath Online Publication Store An Experiment," vol. 110, pp. 14–24, 2011.

- [107] T. S. Tejiro Ichimura, Yoshihisa Matsushita, Kosaku Sakeda, "Photoreactions," in *Microchemical Engineering in Practice*, London: John Wiley & Sons, Inc, 2009, pp. 385–402.
- [108] Y. Inoue, "Photocatalytic water splitting by RuO₂-loaded metal oxides and nitrides with d⁰- and d¹⁰ -related electronic configurations," *Energy Environ. Sci.*, vol. 2, no. 4, p. 364, 2009.
- [109] M. R. Hoffmann, S. T. Martin, W. Choi, and D. W. Bahnemann, "Environmental Applications of Semiconductor Photocatalysis," pp. 69–96, 1995.
- [110] A. A. B. Dhananjay S Bhaskhande, Vishwas G Pangarkar, "Photocatalytic degradation for environmental applications - a review," *J. Chem. Technol. Biotechnol.*, vol. 77, no. 1, pp. 102–116, 2001.
- [111] J. Schneider, M. Matsuoka, M. Takeuchi, J. Zhang, Y. Horiuchi, M. Anpo, and D. W. Bahnemann, "Understanding TiO₂ Photocatalysis: Mechanisms and Materials," *Chem. Rev.*, vol. 114, pp. 9919–9986, 2014.
- [112] S. M. Gupta and M. Tripathi, "A review of TiO₂ nanoparticles," *Chinese Sci. Bull.*, vol. 56, no. 16, pp. 1639–1657, 2011.
- [113] H. T. Tanaka K, Capule M F V, "Effect of crystallinity of TiO₂ on its photocatalytic action," *Chem Phys Lett*, no. 187, pp. 73–76, 1991.
- [114] S. A., "Anatase shows its reactive side," *Nat. Mater.*, no. 7, pp. 613–615, 2008.
- [115] K. Nakata and A. Fujishima, "TiO₂ photocatalysis: Design and applications," *J. Photochem. Photobiol. C Photochem. Rev.*, vol. 13, no. 3, pp. 169–189, 2012.
- [116] H. M. R. Choi Y, Termin A, "The role of metal ion dopants in quantum-sized TiO₂ Charge, : Correlation between photoreactivity and carrier recombination dynamics," *J Phys Chem*, vol. 98, pp. 13669– 13679, 1994.
- [117] G. E. G. Diwald O, Thompson T L, "The effect of nitrogen ion implantation on the photoactivity of TiO₂ J, rutile single crystals.," *Phys Chem B*, vol. 108, pp. 52–57, 2004.
- [118] K. Hashimoto, H. Irie, and A. Fujishima, "TiO₂ Photocatalysis: A Historical Overview and Future Prospects," vol. 44, no. 12, pp. 8269–8285, 2006.
- [119] and M. A. H. J. M. White ,Janos Szanyi, "The Photon-Driven Hydrophilicity of Titania: A Model Study Using TiO₂(110) and Adsorbed Trimethyl Acetate," *J. Phys. Chem. B*, vol. 107, no. 34, pp. 9029–9033, 2003.
- [120] S. Singh, P. Thiyagarajan, K. Mohan Kant, D. Anita, S. Thirupathiah, N. Rama, B. Tiwari, M. Kottaisamy, and M. S. Ramachandra Rao, "Structure, microstructure and physical properties of ZnO based materials in various forms: bulk, thin film and nano," *J. Phys. D. Appl. Phys.*, vol. 40, no. 20, pp. 6312–6327, Oct. 2007.
- [121] R. Blossey, "Self-cleaning surfaces--virtual realities.," *Nat. Mater.*, vol. 2, no. 5, pp. 301–6, May 2003.
- [122] Z. Meng and Z. Juan, "Wastewater treatment by photocatalytic oxidation of Nano-ZnO 2 principles of photocatalytic oxidation (Cui (2001), Lei (2001)) Synthesization of Nano-ZnO," *Glob. Environ. Policy Japan*, vol. 12, no. 12, pp. 1–9, 2008.
- [123] Y. C. Wang, I. C. Leu, and M. H. Hon, "Preparation and characterization of nanosized ZnO arrays by electrophoretic deposition," *J. Cryst. Growth*, vol. 237–239, pp. 564–568, Apr. 2002.
- [124] C. J. S. J. Pearton, *Zinc Oxide Bulk, Thin Films and Nanostructures: Processing, Properties and Applications*. London: Burlington Elsevier, 2006.
- [125] P. K. Basu, E. Bontempi, S. Maji, H. Saha, and S. Basu, "Variation of optical band gap in anodically grown nanocrystalline ZnO thin films at room temperature—effect of electrolyte concentrations," *J. Mater. Sci. Mater. Electron.*, vol. 20, no. 12, pp. 1203–1207, Feb. 2009.

- [126] H. Chen, A. Du Pasquier, G. Saraf, J. Zhong, and Y. Lu, "Dye-sensitized solar cells using ZnO nanotips and Ga-doped ZnO films," *Semicond. Sci. Technol.*, vol. 23, no. 4, p. 045004, Apr. 2008.
- [127] P. Spathis and I. Poulios, "THE CORROSION AND PHOTOCORROSION AND ZINC OXIDE COATINGS," vol. 37, no. 5, 1995.
- [128] Hadis Morkoç and Ümit Özgür, "General Properties of ZnO," in *Zinc Oxide: Fundamentals, Materials and Device Technology.*, 2009.
- [129] S. J. Pearton, D. P. Norton, K. Ip, Y. W. Heo, and T. Steiner, "Recent progress in processing and properties of ZnO," *Prog. Mater. Sci.*, vol. 50, no. 3, pp. 293–340, 2005.
- [130] A. L. Rudd and C. B. Breslin, "Photo-induced dissolution of zinc in alkaline solutions," *Electrochim. Acta*, vol. 45, no. 10, pp. 1571–1579, Jan. 2000.
- [131] E. a. Meulenkamp, "Size Dependence of the Dissolution of ZnO Nanoparticles," *J. Phys. Chem. B*, vol. 102, no. 40, pp. 7764–7769, 1998.
- [132] P. Kalinauskas, I. Valsiūnas, M. Samulevičienė, and E. Juzeliūnas, "Zinc photocorrosion in neutral solutions," *Corros. Sci.*, vol. 43, no. 11, pp. 2083–2092, Nov. 2001.
- [133] D. Li and H. Haneda, "Morphologies of zinc oxide particles and their effects on photocatalysis," *Chemosphere*, vol. 51, no. 2, pp. 129–37, Apr. 2003.
- [134] S. Park, J. C. Lee, and D. W. Lee, "Photocatalytic ZnO nanopowders prepared by solution combustion method for noble metal recovery," *J. Mater. Sci.*, vol. 8, no. 38, pp. 4493–4497, 2003.
- [135] L. Jing, Z. Xu, X. Sun, and J. Shang, "The surface properties and photocatalytic activities of ZnO ultra ® ne particles," *Appl. Surf. Sci.*, vol. 180, pp. 308–314, 2001.
- [136] Z. B. Shao, C. Y. Wang, S. D. Geng, X. D. Sun, and S. J. Geng, "Fabrication of nanometer-sized zinc oxide at low decomposing temperature," *J. Mater. Process. Technol.*, vol. 178, no. 1–3, pp. 247–250, 2006.
- [137] S. P. Devipriya and S. Yesodharan, "Photocatalytic degradation of phenol in water using TiO_2 and ZnO ," *J. Environ. Biol.*, vol. 31, no. 3, pp. 247–9, May 2010.
- [138] M. Qamar and M. Muneer, "A comparative photocatalytic activity of titanium dioxide and zinc oxide by investigating the degradation of vanillin," *Desalination*, vol. 249, no. 2, pp. 535–540, Dec. 2009.
- [139] J. J. Vora, S. K. Chauhan, K. C. Parmar, S. B. Vasava, S. Sharma, and L. S. Bhutadiya, "Kinetic Study of Application of ZnO as a Photocatalyst in Heterogeneous Medium," *E-Journal Chem.*, vol. 6, no. 2, pp. 531–536, 2009.
- [140] P. P.-Z. C.A.K. Gouvêa, F. Wypych, S.G. Moraes, N. Durán, N. Nagata, "Semiconductor-assisted photocatalytic degradation of reactive dyes in aqueous solution," *Chemosphere*, vol. 40, pp. 433–440, 2000.
- [141] M. B. A. Akyol, H.C. Yatmaz, "Photocatalytic decolorization of Remazol Red RR in aqueous ZnO suspensions," *Appl. Catal. B Environ.*, vol. 54, pp. 19–24, 2004.
- [142] V. M. S. Sakthivel, B. Neppolian, M.V. Shankar, B. Arabindoo, M. Palanichamy, "Solar photocatalytic degradation of azo dye: comparison of photocatalytic efficiency of ZnO and TiO_2 ," *Sol. Energy Mater. Sol. Cells*, vol. 77, pp. 65–82, 2003.
- [143] K. Byrappa, a. K. Subramani, S. Ananda, K. M. L. Rai, R. Dinesh, and M. Yoshimura, "Photocatalytic degradation of rhodamine B dye using hydrothermally synthesized ZnO," *Bull. Mater. Sci.*, vol. 29, no. 5, pp. 433–438, Oct. 2006.

- [144] N. Daneshvar, D. Salari, and a. . Khataee, "Photocatalytic degradation of azo dye acid red 14 in water on ZnO as an alternative catalyst to TiO₂," *J. Photochem. Photobiol. A Chem.*, vol. 162, no. 2–3, pp. 317–322, Mar. 2004.
- [145] C. a Gouvêa, F. Wypych, S. G. Moraes, N. Durán, N. Nagata, and P. Peralta-Zamora, "Semiconductor-assisted photocatalytic degradation of reactive dyes in aqueous solution.," *Chemosphere*, vol. 40, no. 4, pp. 433–40, Feb. 2000.
- [146] S. Sakthivel, B. Neppolian, M. V Shankar, B. Arabindoo, M. Palanichamy, and V. Murugesan, "Solar photocatalytic degradation of azo dye: comparison of photocatalytic efficiency of ZnO and TiO₂," vol. 77, no. 3, pp. 65–82, 2003.
- [147] P. B. A.A. Khodja, T. Sehili, J.F. Pihichowski, "Photocatalytic degradation of 2-phenylphenol on TiO₂ and ZnO in aqueous suspensions," *J. Photochem. Photobiol. A Chem.*, vol. 141, pp. 231–239, 2001.
- [148] A. Amine, T. Sehili, J. Pilichowski, and P. Boule, "Photocatalytic degradation of 2-phenylphenol on TiO₂ and ZnO in aqueous suspensions," vol. 141, pp. 231–239, 2001.
- [149] C. Lizama, J. Freer, J. Baeza, and H. D. Mansilla, "Optimized photodegradation of Reactive Blue 19 on TiO₂ and ZnO suspensions," vol. 76, pp. 235–246, 2002.
- [150] M. a Behnajady, N. Modirshahla, and R. Hamzavi, "Kinetic study on photocatalytic degradation of C.I. Acid Yellow 23 by ZnO photocatalyst.," *J. Hazard. Mater.*, vol. 133, no. 1–3, pp. 226–32, May 2006.
- [151] D. Deng, S. T. Martin, and S. Ramanathan, "Synthesis and characterization of one-dimensional flat ZnO nanotower arrays as high-efficiency adsorbents for the photocatalytic remediation of water pollutants †," pp. 2685–2691, 2010.
- [152] N. Daneshvar, S. Aber, M. S. S. Dorraji, A. R. Khataee, and M. H. Rasoulifard, "Preparation and Investigation of Photocatalytic Properties of ZnO Nanocrystals: Effect of Operational Parameters and Kinetic Study," pp. 23–28, 2008.
- [153] A. M. Ali, E. a. C. Emanuelsson, and D. a. Patterson, "Conventional versus lattice photocatalysed reactions: Implications of the lattice oxygen participation in the liquid phase photocatalytic oxidation with nanostructured ZnO thin films on reaction products and mechanism at both 254nm and 340nm," *Appl. Catal. B Environ.*, vol. 106, no. 3–4, pp. 323–336, Aug. 2011.
- [154] C. J. Mcfarlane, E. A. C. Emanuelsson, A. M. Ali, W. Gao, and D. A. Patterson, "Understanding the rate, mechanism and reuseability of zinc oxide nanostructured films as photocatalysts for industrial wastewater treatment," vol. 2, no. 2, pp. 63–79, 2009.
- [155] A. M. Ali, E. a. C. Emanuelsson, and D. a. Patterson, "Photocatalysis with nanostructured zinc oxide thin films: The relationship between morphology and photocatalytic activity under oxygen limited and oxygen rich conditions and evidence for a Mars Van Krevelen mechanism," *Appl. Catal. B Environ.*, vol. 97, no. 1–2, pp. 168–181, Jun. 2010.
- [156] A. A. Yawalkar, D. S. Bhatkhande, V. G. Pangarkar, and A. A. C. M. Beenackers, "Solar-assisted photochemical and photocatalytic degradation of phenol," vol. 370, no. November 2000, pp. 363–370, 2001.
- [157] T. A. Saleh and V. K. Gupta, "Journal of Colloid and Interface Science Photocatalyzed degradation of hazardous dye methyl orange by use of a composite catalyst consisting of multi-walled carbon nanotubes and titanium dioxide," *J. Colloid Interface Sci.*, vol. 371, no. 1, pp. 101–106, 2012.
- [158] S. Baruah, M. A. Mahmood, M. T. Z. Myint, T. Bora, and J. Dutta, "Enhanced visible light photocatalysis through fast crystallization of zinc oxide nanorods.," *Beilstein J. Nanotechnol.*, vol. 1, pp. 14–20, Jan. 2010.
- [159] S. Bakardjieva, V. Stengl, L. Szatmary, J. Subrt, J. Lukac, N. Murafa, D. Niznansky, K. Cizek, J. Jirkovsky, and N. Petrova, "Transformation of brookite-

- type TiO₂ nanocrystals to rutile: correlation between microstructure and photoactivity,” *J. Mater. Chem.*, vol. 16, no. 18, p. 1709, 2006.
- [160] M. Ali, Y. Khan, S. Hussain, O. Nur, and M. Willander, “Anions effect on the low temperature growth of ZnO nanostructures,” *Vaccum*, vol. 86, no. 12, pp. 1998–2001, 2012.
- [161] J. Zhang, L. Sun, J. Yin, H. Su, C. Liao, and C. Yan, “Control of ZnO morphology via a simple solution route,” *Chem. Mater.*, vol. 14, no. 10, pp. 4172–4177, 2002.
- [162] G. Huey-Shya, R. Adnan, and M. Farrukh, “ZnO nanoflake arrays prepared via anodization and their performance in the photodegradation of methyl orange,” *Turk J Chem*, vol. 35, pp. 375–391, 2011.
- [163] P. K. Basu, N. Saha, S. Maji, H. Saha, and S. Basu, “Nanoporous ZnO thin films deposited by electrochemical anodization: effect of UV light,” *J. Mater. Sci. Mater. Electron.*, vol. 19, no. 6, pp. 493–499, Feb. 2008.
- [164] B. Engineering and P. Studies, “Jesus Moreira del Rio Doctor of Philosophy The University of Western Ontario Jesus Moreira del Rio,” 2011.
- [165] S. C. A. A. Sharma, P. Rao, R.P. Mathur, “Photocatalytic reactions of xylydine ponceau on semiconducting zinc oxide powder,” *J. Photochem. Photobiol. A Chem.*, vol. 86, pp. 197–200, 1995.
- [166] S. C. L. F.D. Mai, C.C. Chen, J.L. Chen, “Photodegradation of methyl green using visible irradiation in ZnO suspensions. Determination of the reaction pathway and identification of intermediates by a high-performance liquid chromatography–photodiode array-electrospray ionization-mass spectrometry,” *J. Chromatogr. A*, vol. 1189, pp. 355–365, 2008.
- [167] C. C. C. Lu, Y. Wu, F. Mai, W. Chung, C. Wu, W. Lin, “Degradation efficiencies and mechanisms of the ZnO-mediated photocatalytic degradation of Basic Blue 11 under visible light irradiation,” *J. Mol. Catal. A Chem.*, vol. 310, pp. 159–165, 2009.
- [168] S. Baruah, M. Jaisai, and J. Dutta, “Development of a visible light active photocatalytic portable water purification unit using ZnO nanorods,” *Catal. Sci. Technol.*, vol. 2, no. 5, p. 918, 2012.
- [169] S. K. Pardeshi and a. B. Patil, “A simple route for photocatalytic degradation of phenol in aqueous zinc oxide suspension using solar energy,” *Sol. Energy*, vol. 82, no. 8, pp. 700–705, Aug. 2008.
- [170] A. Di Paola, E. García-López, G. Marci, and L. Palmisano, “A survey of photocatalytic materials for environmental remediation,” *J. Hazard. Mater.*, vol. 211–212, pp. 3–29, Apr. 2012.
- [171] L. K. Adams, D. Y. Lyon, and P. J. J. Alvarez, “Comparative eco-toxicity of nanoscale TiO₂, SiO₂, and ZnO water suspensions,” *Water Res.*, vol. 40, no. 19, pp. 3527–32, Nov. 2006.
- [172] C. Wang, L. Liu, A. Zhang, P. Xie, J. Lu, and X. Zou, “Antibacterial effects of zinc oxide nanoparticles on Escherichia coli K88,” *African J. Biotechnol.*, vol. 11, no. 44, pp. 10248–10254, May 2012.
- [173] C. a. David, J. Galceran, C. Rey-Castro, J. Puy, E. Companys, J. Salvador, J. Monné, R. Wallace, and A. Vakourov, “Dissolution kinetics and solubility of ZnO nanoparticles followed by AGNES,” *J. Phys. Chem. C*, vol. 116, no. 21, pp. 11758–11767, 2012.
- [174] Y. Yu, J. C. Yu, C. Y. Chan, Y. K. Che, J. C. Zhao, L. Ding, W. K. Ge, and P. K. Wong, “Enhancement of adsorption and photocatalytic activity of TiO₂ by using carbon nanotubes for the treatment of azo dye,” *Appl. Catal. B Environ.*, vol. 61, no. 1–2, pp. 1–11, 2005.

- [175] X. Liu, "Growth mechanism and properties of ZnO nanorods synthesized by plasma-enhanced chemical vapor deposition," *J. Appl. Phys.*, vol. 95, no. 6, p. 3141, 2004.
- [176] J. L. Yang, S. J. An, W. I. Park, G.-C. Yi, and W. Choi, "Photocatalysis Using ZnO Thin Films and Nanoneedles Grown by Metal-Organic Chemical Vapor Deposition," *Adv. Mater.*, vol. 16, no. 18, pp. 1661–1664, Sep. 2004.
- [177] T. Kawano, H. Uchiyama, T. Kiguchi, S. Wada, and H. Imai, "Epitaxial growth of winding ZnO nanowires on a single-crystalline substrate," *J. Ceram. Soc. Japan*, vol. 117, no. 1363, pp. 255–257, 2009.
- [178] J. Choi, J. E. Yoo, J. H. Lim, I. S. Jung, and Y. Jo, "Fabrication of zinc oxide nanostructures by chemical and electrochemical methods," vol. 10, no. c, p. 7941, 2008.
- [179] S. He, M. Zheng, L. Yao, X. Yuan, M. Li, L. Ma, and W. Shen, "Preparation and properties of ZnO nanostructures by electrochemical anodization method," *Appl. Surf. Sci.*, vol. 256, no. 8, pp. 2557–2562, Feb. 2010.
- [180] O. O. F. Piezoelectricity, F. Formed, B. Y. Anodization, and C. Sciences, "OBSERVATION OF PIEZOELECTRICITY IN THIN FILMS FORMED BY ANODIZATION," pp. 434–437, 1980.
- [181] X. Wu, G. Lu, C. Li, and G. Shi, "Room-temperature fabrication of highly oriented ZnO nanoneedle arrays by anodization of zinc foil," *Nanotechnology*, vol. 17, no. 19, pp. 4936–4940, Oct. 2006.
- [182] C. Y. Kuan, J. M. Chou, I. C. Leu, and M. H. Hon, "Formation and field emission property of single-crystalline Zn microtip arrays by anodization," *Electrochem. commun.*, vol. 9, no. 8, pp. 2093–2097, Aug. 2007.
- [183] S. J. Kim and J. Choi, "Self-assembled arrays of ZnO stripes by anodization," *Electrochem. commun.*, vol. 10, no. 1, pp. 175–179, Jan. 2008.
- [184] Z. Wang, "Nanostructures of zinc oxide," *Mater. today*, no. June, pp. 26–33, 2004.
- [185] F. Edwards, J. D. & Keller, "Formation of anodic coatings on aluminum," *Trans. Electrochem. Soc.*, vol. 79, pp. 135–144, 1941.
- [186] A. J. P. O. Sullivan and G. C. Wood, "The morphology and mechanism of formation of porous anodic films on aluminium," vol. 317, no. 1531, pp. 511–543, 2011.
- [187] M. Wang, Y. Liu, and H. Yang, "A unified thermodynamic theory for the formation of anodized metal oxide structures," *Electrochim. Acta*, vol. 62, pp. 424–432, Feb. 2012.
- [188] D. L. Keller, F., Hunter, M. S. & Robinson, "Structural features of oxide coatings on aluminum," *J. Electrochem. Soc.*, vol. 100, pp. 411–419, 1953.
- [189] A. Shetty and K. K. Nanda, "Synthesis of zinc oxide porous structures by anodization with water as an electrolyte," *Appl. Phys. A*, vol. 109, no. 1, pp. 151–157, Jun. 2012.
- [190] T. Aerts, T. Dimogerontakis, I. De Graeve, J. Fransaer, and H. Terryn, "Influence of the anodizing temperature on the porosity and the mechanical properties of the porous anodic oxide film," *Surf. Coatings Technol.*, vol. 201, no. 16–17, pp. 7310–7317, May 2007.
- [191] S. J. Kim, J. Lee, and J. Choi, "Understanding of anodization of zinc in an electrolyte containing fluoride ions," *Electrochim. Acta*, vol. 53, no. 27, pp. 7941–7945, Nov. 2008.
- [192] Z. L. Srimala Sreekantan, Lee Ren Gee, "Room temperature anodic deposition and shape control of one dimensional nanostructure zinc oxide," *J. Alloys Compd.*, vol. 476, pp. 513–518, 2009.

- [193] G. S. Huang, X. L. Wu, Y. C. Cheng, J. C. Shen, A. P. Huang, and P. K. Chu, "Fabrication and characterization of anodic ZnO nanoparticles," *Appl. Phys. A*, vol. 86, no. 4, pp. 463–467, Dec. 2006.
- [194] L.-M. P. Zhudong Hu, Qing Chen, Zhen Li, Yuan Yu, "Large-Scale and Rapid Synthesis of Ultralong ZnO Nanowire Films via Anodization," *J. Phys. Chem. C- J PHYS CHEM C*, vol. 114, pp. 881–889, 2010.
- [195] M. T. M. Koper and Y. Iwasawa, "Electrocatalysis.," *Phys. Chem. Chem. Phys.*, vol. 16, no. 27, p. 13567, Jul. 2014.
- [196] "Instrumental Methods in Electrochemistry," 2010.
- [197] T. A. Egerton, "Photoelectrocatalysis," *UNESCO - EOLSS*.
- [198] T. T. G. and M. V. B. Z. Guilherme Garcia Bessegato, "Enhancement of Photoelectrocatalysis Efficiency by Using Nanostructured Electrodes," in *modern electrochemical methods in nano surface and corrosion science*, M. Aliofkhazraei, Ed. 2014.
- [199] a. . Vlyssides, D. Papaioannou, M. Loizidou, P. . Karlis, and a. . Zorpas, "Testing an electrochemical method for treatment of textile dye wastewater," *Waste Manag.*, vol. 20, no. 7, pp. 569–574, Nov. 2000.
- [200] C. . Murphy, OJ. Hitchens, GD. Kaba, L. Verostko, "Direct electrochemical oxidation of organics for wastewater treatment," *Water Res.*, vol. 26, no. 4, pp. 443–451, 1992.
- [201] Y. Yang, J. Li, H. Wang, X. Song, T. Wang, B. He, X. Liang, and H. H. Ngo, "An electrocatalytic membrane reactor with self-cleaning function for industrial wastewater treatment.," *Angew. Chem. Int. Ed. Engl.*, vol. 50, no. 9, pp. 2148–50, Feb. 2011.
- [202] E. K. M. Daghri R, Drogui P, Dimboukou-Mpira A, "Photoelectrocatalytic degradation of carbamazepine using Ti/TiO₂ nanostructured electrodes deposited by means of a pulsed laser deposition process," *Chemosphere*, vol. 93(11), pp. 2756–2766, 2013.
- [203] P. I. Philippidis N, Sotiropoulos S, Efstathiou A, "Photoelectrocatalytic degradation of the insecticide imidacloprid using TiO₂/Ti electrodes," *Photochem. Photobiol. A Chem.*, vol. 204(2–3), pp. 129–136, 2009.
- [204] B. Z. M. Cardoso JC, Lizier TM, "Highly ordered TiO₂ nanotube arrays and photoelectrocatalytic oxidation of aromatic amine," *Appl. Catal. B Environ.*, vol. 99(1–2), pp. 96–102, 2010.
- [205] R. T. Sapkal, S. S. Shinde, M. a Mahadik, V. S. Mohite, T. R. Waghmode, S. P. Govindwar, K. Y. Rajpure, and C. H. Bhosale, "Photoelectrocatalytic decolorization and degradation of textile effluent using ZnO thin films.," *J. Photochem. Photobiol. B.*, vol. 114, pp. 102–7, Sep. 2012.
- [206] Y. Shaogui, Q. Xie, L. Xinyong, L. Yazhi, C. Guohua, B. Science, C. W. Bay, and H. Kong, "Preparation, characterization and photoelectrocatalytic properties of nanocrystalline Fe₂O₃/TiO₂ , ZnO/TiO₂ , and Fe₂O₃/ZnO/TiO₂ composite film electrodes towards pentachlorophenol degradation Yang," *PhysChemComm*, vol. 6, pp. 659–664, 2004.
- [207] B. E. Martinez-Huitle CA, "Decontamination of wastewaters containing synthetic organic dyes by electrochemical methods: A general review," *Appl. Catal. B Environ.*, vol. 87(3–4), pp. 105–145, 2009.
- [208] Z. Y. Quan X, Ruan X, Zhao H, Chen S, "Photoelectrocatalytic degradation of pentachlorophenol in aqueous solution using a TiO₂ nanotube film electrode," *Environ. Pollut.*, vol. 147, no. 2, pp. 409–414, 2007.
- [209] R. Sheasby, P. G.; Pinner, *The Surface Treatment and Finishing of Aluminum and its Alloys 2*, Sixth. ASM International & Finishing Publications, 2001.

- [210] D. L. Keller, F. Hunter, M. S. Robinson, "Structural features of oxide coatings on aluminum," *J. Electrochem. Soc.*, vol. 100, pp. 411–419, 1953.
- [211] A. K. Vijh, "Sparking voltages and side reactions during anodization of valve metals in terms of electron tunnelling," *corr*, vol. 11, no. 6, pp. 411–417, 1971.
- [212] A. Ramirez-Canon, D. O. Miles, P. J. Cameron, and D. Mattia, "Zinc oxide nanostructured films produced via anodization: a rational design approach," *RSC Adv.*, vol. 3, no. 47, p. 25323, 2013.
- [213] H. Aluminium and T. Norwegian, "EFFECT OF PRECIPITATION ON THE EVOLUTION CUBE RECRYSTALLISATION TEXTURE," vol. 45, no. I, pp. 4593–4602, 1997.
- [214] M. Mhaede, "Influence of surface treatments on surface layer properties, fatigue and corrosion fatigue performance of AA7075 T73," *Mater. Des.*, vol. 41, pp. 61–66, Oct. 2012.
- [215] P. Pendyala, M. S. Bobji, and G. Madras, "Evolution of Surface Roughness During Electropolishing," *Tribol. Lett.*, vol. 55, no. 1, pp. 93–101, Apr. 2014.
- [216] P.-H. Shih, H.-J. Hung, Y.-R. Ma, and S.-Y. Wu, "Tuning the dimensionality of ZnO nanowires through thermal treatment: An investigation of growth mechanism," *Nanoscale Res. Lett.*, vol. 7, no. 1, p. 354, Jan. 2012.
- [217] Z. B. Fang, Z. J. Yan, Y. S. Tan, X. Q. Liu, and Y. Y. Wang, "Influence of post-annealing treatment on the structure properties of ZnO films," *Appl. Surf. Sci.*, vol. 241, no. 3–4, pp. 303–308, Mar. 2005.
- [218] R. Flewit, PEJ. Wild, "Electron Sources," in *Physical methods for materials characterisation methods for materials characterisation*, First., Bristol UK: Institute of Physics Publishing, 2002, pp. 244–359.
- [219] Y. Yuan and T. R. Lee, *Surface Science Techniques*, vol. 51. Berlin, Heidelberg: Springer Berlin Heidelberg, 2013.
- [220] X. Chen, X.-P. Wang, and X. Xu, "Effective contact angle for rough boundary," *Phys. D Nonlinear Phenom.*, vol. 242, no. 1, pp. 54–64, Jan. 2013.
- [221] L. Gao and T. J. McCarthy, "How Wenzel and Cassie were wrong," *Langmuir*, vol. 23, no. 7, pp. 3762–5, Mar. 2007.
- [222] L. Gao and T. J. McCarthy, "Contact angle hysteresis explained," *Langmuir*, vol. 22, no. 14, pp. 6234–7, Jul. 2006.
- [223] C. W. Extrand, "Contact Angles and Hysteresis on Surfaces with Chemically Heterogeneous Islands," *Langmuir*, vol. 19, no. 9, pp. 3793–3796, Apr. 2003.
- [224] A. Marmur and E. Bittoun, "When Wenzel and Cassie are right: reconciling local and global considerations," *Langmuir*, vol. 25, no. 3, pp. 1277–81, Mar. 2009.
- [225] G. Alberti and a. DeSimone, "Wetting of rough surfaces: a homogenization approach," *Proc. R. Soc. A Math. Phys. Eng. Sci.*, vol. 461, no. 2053, pp. 79–97, Jan. 2005.
- [226] G. Whyman, E. Bormashenko, and T. Stein, "The rigorous derivation of Young, Cassie–Baxter and Wenzel equations and the analysis of the contact angle hysteresis phenomenon," *Chem. Phys. Lett.*, vol. 450, no. 4–6, pp. 355–359, Jan. 2008.
- [227] W. Laws, P. S. Swain, and R. Lipowsky, "Contact Angles on Heterogeneous Surfaces : A New Look at," no. 10, pp. 6772–6780, 1998.
- [228] P. S. Lipowski, R.; Lenz, P.; Swain, "Wetting and dewetting of structured and imprinted surfaces," *Colloids Surfaces A Physicochem. Eng. Asp.*, vol. 161, no. 1, pp. 3–22, 2000.
- [229] J. Drelich, "Guidelines to measurements of reproducible contact angles using a sessile-drop technique," *Surf. Innov.*, vol. 1, Jun. 2013.

- [230] Z. Zhang, H. Chen, J. Zhong, G. Saraf, and Y. Lu, "Fast and Reversible Wettability Transitions on ZnO Nanostructures," *J. Electron. Mater.*, vol. 36, no. 8, pp. 895–899, May 2007.
- [231] J. Han, W. Qiu, and W. Gao, "Potential dissolution and photo-dissolution of ZnO thin films.," *J. Hazard. Mater.*, vol. 178, no. 1–3, pp. 115–22, Jun. 2010.
- [232] B. Pal and M. Sharon, "Enhanced photocatalytic activity of highly porous ZnO thin films prepared by sol–gel process," *Mater. Chem. Phys.*, vol. 76, no. 1, pp. 82–87, Jul. 2002.
- [233] F. Lu, W. Cai, and Y. Zhang, "ZnO Hierarchical Micro/Nanoarchitectures: Solvothermal Synthesis and Structurally Enhanced Photocatalytic Performance," *Adv. Funct. Mater.*, vol. 18, no. 7, pp. 1047–1056, Apr. 2008.
- [234] N. Serpone, P. Maruthamuthu, P. Pichat, E. Pelizzetti, and H. Hidaka, "Exploiting the interparticle electron transfer process in the photocatalysed oxidation of phenol, 2-chlorophenol and pentachlorophenol: chemical evidence for electron and hole transfer between coupled semiconductors," *J. Photochem. Photobiol. A Chem.*, vol. 85, no. 3, pp. 247–255, Jan. 1995.
- [235] F. Bentahar and D. Technologie, "The degradation of phenol in water solution by TiO₂ photocatalysis in a helical reactor," *Glob. NEST J.*, vol. 10, no. 3, pp. 404–418, 2008.
- [236] M. Humphreys, F. J. Hatherly, "Recrystallization and related annealing phenomena," in *Recrystallization and related annealing phenomena*, Second., Oxford: Elsevier Ltd, 2002, pp. 1–10.
- [237] D. Landolt, "Fundamental aspects of electropolishing," *Electrochim. Acta*, vol. 32, no. 1, pp. 1–11, 1987.
- [238] G. D. Sulka, "Highly ordered anodic porous alumina formation by self-organized anodizing," in *Nanostructured Materials in Electrochemistry*, Ali Eftekh., W. Wiley-VCH Verlag GmbH & Co. KGaA, Ed. 2008.
- [239] T. William, J. Albrecht, J. Addai-mensah, and D. Fornasiero, "Effect of pH , Concentration and Temperature on Copper and Zinc Hydroxide Formation / Precipitation in Solution," pp. 1–10.
- [240] L. G. . Fokkink, a de Keizer, and J. Lyklema, "Temperature dependence of the electrical double layer on oxides: Rutile and hematite," *J. Colloid Interface Sci.*, vol. 127, no. 1, pp. 116–131, Jan. 1989.
- [241] I. I. I. A. Thermodynamic, "Adsorption of Hydrolyzable Metal Ions at the Oxide-Water Interface," vol. 40, no. 1, 1972.
- [242] T. W. J. Albrecht and D. Addai-Mensah, Jonas, Fornaciero, *Effect of pH, Concentration and Temperature on Copper and Zinc Hydroxide Formation/Precipitation in Solutio*. 2011.
- [243] W. Stumm and J. J. Morgan, *Aquatic Chemistry: Chemical Equilibria and Rates in Natural Waters*, Third. New York: Hoboken : Wiley, 1996.
- [244] Grzegorz D. Sulka, "Highly ordered anodic porous alumina formation by self-organized anodizing," in *Nanostructured Materials in Electrochemistry*, G. Wiley-VCH Verlag GmbH & Co. KGaA, Weinheim, Ed. Germany, 2008.
- [245] R. Wahab, Y.-S. Kim, and H.-S. Shin, "Synthesis, Characterization and Effect of pH Variation on Zinc Oxide Nanostructures," *Mater. Trans.*, vol. 50, no. 8, pp. 2092–2097, 2009.
- [246] R. F. Egerton, P. Li, and M. Malac, "Radiation damage in the TEM and SEM.," *Micron*, vol. 35, no. 6, pp. 399–409, Jan. 2004.
- [247] J. Zhang, W. Huang, and Y. Han, "Wettability of zinc oxide surfaces with controllable structures.," *Langmuir*, vol. 22, no. 7, pp. 2946–50, Mar. 2006.
- [248] I. I. I. Mogyorósi, Károly. Kun, Róbert. Szabó, Tamás. Dékány, "Preparation and Photocatalytic Application of Different TiO₂ and Zn(OH)₂/ZnO Nanoparticles

- and Hydrophilic/Hydrophobic Layered Silicates,” in *Role of Interfaces in Environmental Protection*, 2003, pp. 425–443.
- [249] J. Han and W. Gao, “Surface Wettability of Nanostructured Zinc Oxide Films,” *J. Electron. Mater.*, vol. 38, no. 4, pp. 601–608, Dec. 2008.
- [250] J. L. Campbell, M. Breedon, K. Latham, and K. Kalantar-zadeh, “Electrowetting of superhydrophobic ZnO nanorods,” *Langmuir*, vol. 24, no. 9, pp. 5091–8, May 2008.
- [251] S. Cassie, A.B.D., Baxter, “Wettability of porous surface,” *Trans. Faraday Soc.*, vol. 40, pp. 546–551, 1944.
- [252] R. N. Wenzel, “Resistance of solid surfaces to wetting by water,” *Ind. Eng. Chem.*, vol. 28, p. 988, 1936.
- [253] D. Quéré, “Non-sticking drops,” *Reports Prog. Phys.*, vol. 68, no. 11, pp. 2495–2532, Nov. 2005.
- [254] S. Gogte, P. Vorobieff, R. Truesdell, A. Mammoli, F. van Swol, P. Shah, and C. J. Brinker, “Effective slip on textured superhydrophobic surfaces,” *Phys. Fluids*, vol. 17, no. 5, p. 051701, 2005.
- [255] M. Sakai, J. Song, N. Yoshida, S. Suzuki, Y. Kameshima, and A. Nakajima, “Direct Observation of Internal Fluidity in a Water Droplet during Sliding on Hydrophobic Surfaces,” no. 10, pp. 4906–4909, 2006.
- [256] L. Mahadevan and Y. Pomeau, “Rolling droplets,” *Phys. Fluids*, vol. 11, no. 9, pp. 2449–2453, Sep. 1999.
- [257] M. Sakai, H. Kono, A. Nakajima, X. Zhang, H. Sakai, M. Abe, and A. Fujishima, “Sliding of water droplets on the superhydrophobic surface with ZnO nanorods,” *Langmuir*, vol. 25, no. 24, pp. 14182–6, Dec. 2009.
- [258] A. B. Gurav, S. S. Lathe, R. S. Vhatkar, J. G. Lee, D. Y. Kim, J. J. Park, and S. S. Yoon, “Superhydrophobic surface decorated with vertical ZnO nanorods modified by stearic acid,” *Ceram. Int.*, vol. 40, no. 5, pp. 7151–7160, 2014.
- [259] X. Feng, L. Feng, M. Jin, J. Zhai, L. Jiang, and D. Zhu, “Reversible superhydrophobicity to super-hydrophilicity transition of aligned ZnO nanorod films,” *J. Am. Chem. Soc.*, vol. 126, no. 1, pp. 62–3, Jan. 2004.
- [260] Y. Li, W. Cai, G. Duan, B. Cao, F. Sun, and F. Lu, “Superhydrophobicity of 2D ZnO ordered pore arrays formed by solution-dipping template method,” *J. Colloid Interface Sci.*, vol. 287, no. 2, pp. 634–9, Jul. 2005.
- [261] D. a L. Leelamanie, J. Karube, and A. Yoshida, “Relative humidity effects on contact angle and water drop penetration time of hydrophobized fine sand,” *Soil Sci. Plant Nutr.*, vol. 54, no. 5, pp. 695–700, 2008.
- [262] M. Gong, X. Xu, Z. Yang, Y. Liu, H. Lv, and L. Lv, “A reticulate superhydrophobic self-assembly structure prepared by ZnO nanowires,” *Nanotechnology*, vol. 20, no. 16, p. 165602, Apr. 2009.
- [263] Z. R. Tian, J. a Voigt, J. Liu, B. McKenzie, M. J. McDermott, M. a Rodriguez, H. Konishi, and H. Xu, “Complex and oriented ZnO nanostructures,” *Nat. Mater.*, vol. 2, no. 12, pp. 821–6, Dec. 2003.
- [264] S.-H. Yi, S.-K. Choi, J.-M. Jang, J.-A. Kim, and W.-G. Jung, “Low-temperature growth of ZnO nanorods by chemical bath deposition,” *J. Colloid Interface Sci.*, vol. 313, no. 2, pp. 705–10, Sep. 2007.
- [265] A. Janotti and C. G. Van de Walle, “Fundamentals of zinc oxide as a semiconductor,” *Reports Prog. Phys.*, vol. 72, no. 12, p. 126501, Dec. 2009.
- [266] S. Rahmane, B. Abdallah, a. Soussou, E. Gautron, P.-Y. Jouan, L. Le Brizoual, N. Barreau, a. Soltani, and M. a. Djouadi, “Epitaxial growth of ZnO thin films on AlN substrates deposited at low temperature by magnetron sputtering,” *Phys. Status Solidi*, vol. 207, no. 7, pp. 1604–1608, May 2010.

- [267] L. Schmidt-Mende and J. L. MacManus-Driscoll, "ZnO – nanostructures, defects, and devices," *Mater. Today*, vol. 10, no. 5, pp. 40–48, May 2007.
- [268] L. . Kukreja, S. Barik, and P. Misra, "Variable band gap ZnO nanostructures grown by pulsed laser deposition," *J. Cryst. Growth*, vol. 268, no. 3–4, pp. 531–535, Aug. 2004.
- [269] L. Qin, C. Shing, S. Sawyer, and P. S. Dutta, "Enhanced ultraviolet sensitivity of zinc oxide nanoparticle photoconductors by surface passivation," *Opt. Mater. (Amst.)*, vol. 33, no. 3, pp. 359–362, Jan. 2011.
- [270] C. Chen, Y. Lu, H. He, M. Xiao, Z. Wang, L. Chen, and Z. Ye, "Violet emission in ZnO nanorods treated with high-energy hydrogen plasma.," *ACS Appl. Mater. Interfaces*, vol. 5, no. 20, pp. 10274–9, Oct. 2013.
- [271] C. Li, G. Fang, F. Su, G. Li, X. Wu, and X. Zhao, "Synthesis and photoluminescence properties of vertically aligned ZnO nanorod–nanowall junction arrays on a ZnO-coated silicon substrate," *Nanotechnology*, vol. 17, no. 15, pp. 3740–3744, 2006.
- [272] S. Y. Ma, X. H. Yang, X. L. Huang, a. M. Sun, H. S. Song, and H. B. Zhu, "Effect of post-annealing treatment on the microstructure and optical properties of ZnO/PS nanocomposite films," *J. Alloys Compd.*, vol. 566, pp. 9–15, Jul. 2013.
- [273] J. H. P. Tyman, *Synthetic and natural phenols*. Elsevier, 1996.
- [274] R. Guerra, "Ecotoxicological and chemical evaluation of phenolic compounds in industrial e , uents," vol. 44, pp. 1737–1747, 2001.
- [275] F. Gnudi, "TECHNICAL NOTE PHENOLIC COMPOUNDS IN SURFACE WATER," vol. 33, no. 14, pp. 3213–3219, 1999.
- [276] G. L. Puma and P. L. Yue, "Effect of the Radiation Wavelength on the Rate of Photocatalytic Oxidation of Organic Pollutants," *Ind. Eng. Chem. Res.*, vol. 41, pp. 5594–5600, 2002.
- [277] S. Novalle, "New Reactor Design for Photocatalytic Wastewater Treatment with TiO₂ Immobilized on Fused-Silica Glass Fibers: Photomineralization of 4-Chlorophenol," vol. 28, no. 4, pp. 670–674, 1994.
- [278] R. W. Matthews and S. R. McEvoy, "A comparison of 254 nm and 350 nm excitation of TiO₂ in simple photocatalytic reactors," *J. Photochem. Photobiol. A Chem.*, vol. 66, pp. 355–366, 1992.
- [279] W. Chu and C. C. Wong, "The photocatalytic degradation of dicamba in TiO₂ suspensions with the help of hydrogen peroxide by different near UV irradiations.," *Water Res.*, vol. 38, no. 4, pp. 1037–43, Feb. 2004.
- [280] B. Bayarri, M. N. Abellán, J. Giménez, and S. Esplugas, "Study of the wavelength effect in the photolysis and heterogeneous photocatalysis," *Catal. Today*, vol. 129, no. 1–2, pp. 231–239, Nov. 2007.
- [281] R. S. Thakur, R. Chaudhary, and C. Singh, "Fundamentals and applications of the photocatalytic treatment for the removal of industrial organic pollutants and effects of operational parameters: A review," *J. Renew. Sustain. Energy*, vol. 2, no. 4, p. 042701, 2010.
- [282] C. G. Joseph, G. L. Puma, A. Bono, Y. H. Taufiq-Yap, and D. Krishnaiah, "Sonolysis, Photolysis and Sequential Sonophotolysis for the Degradation of 2,4,6-trichlorophenol: The Effect of Solution Concentration," *Chem. Eng. Commun.*, no. February 2015, p. 141217104822009, Jul. 2014.
- [283] S. Lathasree, a. N. Rao, B. SivaSankar, V. Sadasivam, and K. Rengaraj, "Heterogeneous photocatalytic mineralisation of phenols in aqueous solutions," *J. Mol. Catal. A Chem.*, vol. 223, no. 1–2, pp. 101–105, Dec. 2004.
- [284] I. B. Berlman, *Handbook of fluorescence spectra of aromatic molecules*, Second. Academic Press, 1971.

- [285] Shimadzu Corporation, "UV Talk Letter," 2009.
- [286] E. Grabowska, J. Reszczyńska, and A. Zaleska, "Mechanism of phenol photodegradation in the presence of pure and modified-TiO₂: A review.," *Water Res.*, vol. 46, no. 17, pp. 5453–71, Nov. 2012.
- [287] W. M. Wijekoon, M. K. P. Zonh, Z. Ho. Hetherington, "Phenol Adsorption on ZnO (0001) probed by Coherent Anti-Stokes Raman Scattering Spectroscopy using Guided Waves," *J. Chem. Soc. Faraday Trans.*, vol. 89, no. 7, pp. 1067–1069, 1993.
- [288] L. Octave, "Kinetics of Homogeneous Reactions," in *Chemical Reaction engineering*, Third., New York: John Wiley & Sons, Inc, 1999.
- [289] S. Contreras, E. Pascual, S. Esplugas, J. Gim, and M. Rodri, "Comparison of different advanced oxidation processes for phenol degradation," vol. 36, pp. 1034–1042, 2002.
- [290] T. Luenloi, B. Chalermssinsuwan, T. Sreethawong, and N. Hinchiranan, "Photodegradation of phenol catalyzed by TiO₂ coated on acrylic sheets: Kinetics and factorial design analysis," *Desalination*, vol. 274, no. 1–3, pp. 192–199, Jul. 2011.
- [291] H. Benhebal, M. Chaib, T. Salmon, J. Geens, A. Leonard, S. D. Lambert, M. Crine, and B. Heinrichs, "Photocatalytic degradation of phenol and benzoic acid using zinc oxide powders prepared by the sol-gel process," *Alexandria Eng. J.*, vol. 52, no. 3, pp. 517–523, 2013.
- [292] M. C. Lu, G.-D. Roam, J.-N. Chen, and C. P. Huangb, "Factors affecting the photocatalytic degradation of dichlorvos over titanium dioxide supported on glass," *J. Photochem. Photobiol. A Chem.*, vol. 76, no. 1–2, pp. 103–110, 1993.
- [293] M. D. L. M. Ballari, R. Brandi, O. Alfano, and A. Cassano, "Mass transfer limitations in photocatalytic reactors employing titanium dioxide suspensions. II. External and internal particle constrains for the reaction," *Chem. Eng. J.*, vol. 136, no. 2–3, pp. 242–255, 2008.
- [294] D. Chen, F. Li, and A. K. Ray, "Effect of mass transfer and catalyst layer thickness on photocatalytic reaction," *AIChE J.*, vol. 46, no. 5, pp. 1034–1045, 2000.
- [295] H. Li, Z. Bian, J. Zhu, D. Zhang, G. Li, Y. Huo, H. Li, and Y. Lu, "Mesoporous Titania Spheres with Tunable Chamber Structure and Enhanced Photocatalytic Activity," *J. AM. CHEM. soc.*, no. 129, pp. 8406–8407, 2007.
- [296] L. Xu, Y.-L. Hu, C. Pelligra, C.-H. Chen, L. Jin, H. Huang, S. Sithambaram, M. Aindow, R. Joesten, and S. L. Suib, "ZnO with Different Morphologies Synthesized by Solvothermal Methods for Enhanced Photocatalytic Activity," *Chem. Mater.*, vol. 21, no. 13, pp. 2875–2885, Jul. 2009.
- [297] C. Hariharan, "Photocatalytic degradation of organic contaminants in water by ZnO nanoparticles: Revisited," *Appl. Catal. A Gen.*, vol. 304, pp. 55–61, May 2006.
- [298] F. M. Moghaddam and H. Saeidian, "Controlled microwave-assisted synthesis of ZnO nanopowder and its catalytic activity for O-acylation of alcohol and phenol," *Mater. Sci. Eng. B*, vol. 139, no. 2–3, pp. 265–269, May 2007.
- [299] A. M. Ali, E. a. C. Emanuelsson, and D. a. Patterson, "Photocatalysis with nanostructured zinc oxide thin films: The relationship between morphology and photocatalytic activity under oxygen limited and oxygen rich conditions and evidence for a Mars Van Krevelen mechanism," *Appl. Catal. B Environ.*, vol. 97, no. 1–2, pp. 168–181, Jun. 2010.
- [300] R. Ohtani, Bunsho; Prieto Mahaney, Orlando Omar; Amano, Fumiaki; Murakami, Naoya; Abe, "What Are Titania Photocatalysts?—An Exploratory

- Correlation of Photocatalytic Activity with Structural and Physical Properties,” *J. Adv. Oxid. Technol.*, vol. 13, no. 3, pp. 247–261, 2010.
- [301] O.-O. Prieto-Mahaney, N. Murakami, R. Abe, and B. Ohtani, “Correlation between Photocatalytic Activities and Structural and Physical Properties of Titanium(IV) Oxide Powders,” *Chem. Lett.*, vol. 38, no. 3, pp. 238–239, 2009.
- [302] S. K. Pardeshi and a. B. Patil, “Effect of morphology and crystallite size on solar photocatalytic activity of zinc oxide synthesized by solution free mechanochemical method,” *J. Mol. Catal. A Chem.*, vol. 308, no. 1–2, pp. 32–40, Aug. 2009.
- [303] R. K. Wahi, W. W. Yu, Y. Liu, M. L. Mejia, J. C. Falkner, W. Nolte, and V. L. Colvin, “Photodegradation of Congo Red catalyzed by nanosized TiO₂,” *J. Mol. Catal. A Chem.*, vol. 242, no. 1–2, pp. 48–56, Dec. 2005.
- [304] B. Otheni, “Photocatalysis A to Z — What We Know and What We Don ’ t Know in A Scientific Sense,” *J. Photochem. Photobiol. C, Photochem. Rev.*, 2010.
- [305] G. Leofanti, M. Padovan, G. Tozzola, and B. Venturelli, “Surface area and pore texture of catalysts,” *Catal. Today*, vol. 41, no. 1–3, pp. 207–219, 1998.
- [306] S. Mahdavi, M. Jalali, and A. Afkhami, “Removal of heavy metals from aqueous solutions using Fe₃O₄, ZnO, and CuO nanoparticles,” *J. Nanoparticle Res.*, vol. 14, no. 8, 2012.
- [307] R. a. Rosenberg, M. Abu Haija, K. Vijayalakshmi, J. Zhou, S. Xu, and Z. L. Wang, “Depth resolved luminescence from oriented ZnO nanowires,” *Appl. Phys. Lett.*, vol. 95, no. 24, pp. 2009–2011, 2009.
- [308] K. M. Parida and S. Parija, “Photocatalytic degradation of phenol under solar radiation using microwave irradiated zinc oxide,” *Sol. Energy*, vol. 80, no. 8, pp. 1048–1054, Aug. 2006.
- [309] A. M. Ali, E. a. C. Emanuelsson, and D. a. Patterson, “Conventional versus lattice photocatalysed reactions: Implications of the lattice oxygen participation in the liquid phase photocatalytic oxidation with nanostructured ZnO thin films on reaction products and mechanism at both 254nm and 340nm,” *Appl. Catal. B Environ.*, vol. 106, no. 3–4, pp. 323–336, Aug. 2011.
- [310] V. Iliev, D. Tomova, S. Rakovsky, a. Eliyas, and G. L. Puma, “Enhancement of photocatalytic oxidation of oxalic acid by gold modified WO₃/TiO₂ photocatalysts under UV and visible light irradiation,” *J. Mol. Catal. A Chem.*, vol. 327, no. 1–2, pp. 51–57, Jul. 2010.
- [311] G. D. Lee and J. L. Falconer, “Transient measurements of lattice oxygen in photocatalytic decomposition of formic acid on TiO₂,” vol. 70, pp. 145–148, 2000.
- [312] C. V Ovesen, B. S. Clausen, J. Schiøtz, P. Stoltze, H. Topsøe, and J. K. Nørskov, “Kinetic Implications of Dynamical Changes in Catalyst Morphology during Methanol Synthesis over Cu / ZnO Catalysts,” vol. 142, pp. 133–142, 1997.
- [313] D. Li, H. Haneda, N. Ohashi, N. Saito, and S. Hishita, “Morphological reform of ZnO particles induced by coupling with MO_x (M=V,W,Ce) and the effects on photocatalytic activity,” *Thin Solid Films*, vol. 486, no. 1–2, pp. 20–23, Aug. 2005.
- [314] T. Hanada, “Basic Properties of ZnO, GaN, and Related Materials,” *Oxide Nitride Semicond.*, pp. 1–19, 2009.
- [315] X. Q. Meng, D. X. Zhao, J. Y. Zhang, D. Z. Shen, Y. M. Lu, L. Dong, Z. Y. Xiao, Y. C. Liu, and X. W. Fan, “Wettability conversion on ZnO nanowire arrays surface modified by oxygen plasma treatment and annealing,” *Chem. Phys. Lett.*, vol. 413, no. 4–6, pp. 450–453, Sep. 2005.

- [316] M. Liu and H. K. Kim, "Ultraviolet detection with ultrathin ZnO epitaxial films treated with oxygen plasma," *Appl. Phys. Lett.*, vol. 84, no. 2, p. 173, 2004.
- [317] M. de Lasa, Hugo. Serrano, Benito. Salas, *Photocatalytic Reaction Engineering*. Springer, 2005.
- [318] F. M. White, *Fluid Mechanics*. Mc Graw Hill International editions, 2003.
- [319] D. J. Pickett, "The analysis of a batch electrochemical reactor with continuously recirculating electrolyte," *Electrochim. Acta*, vol. 18, no. 11, pp. 835–837, 1973.
- [320] OECD Publishing, "Test No. 316: Photo-transformation of Chemicals in Water – Direct Photolysis," 2008.
- [321] J.-M. Herrmann, "Photocatalysis fundamentals revisited to avoid several misconceptions," *Appl. Catal. B Environ.*, vol. 99, no. 3–4, pp. 461–468, Sep. 2010.
- [322] L. Gomathi Devi, S. Girish Kumar, K. Mohan Reddy, and C. Munikrishnappa, "Photo degradation of methyl orange an azo dye by advanced Fenton process using zero valent metallic iron: influence of various reaction parameters and its degradation mechanism," *J. Hazard. Mater.*, vol. 164, no. 2–3, pp. 459–67, May 2009.
- [323] C.-C. Wang, J.-R. Li, X.-L. Lv, Y.-Q. Zhang, and G. Guo, "Photocatalytic organic pollutants degradation in metal–organic frameworks," *Energy Environ. Sci.*, vol. 7, no. 9, p. 2831, Jul. 2014.
- [324] M. Selvam, K. Muruganandham, M. Muthuvel, I. Swaminathan, "The influence of inorganic oxidants and metal ions on semiconductor sensitized photodegradation of 4-fluorophenol," *Chem. Eng. J.*, vol. 128, pp. 51–57, 2007.
- [325] M. M. Bahnemann, W. Muneer, M. Haque, "Titanium dioxide-mediated photocatalysed degradation of few selected organic pollutants in aqueous suspensions, Catalysis Today," *Catal. Today*, vol. 124, pp. 133–148, 2007.
- [326] R. Shidpour, A. Simchi, F. Ghanbari, and M. Vossoughi, "Photo-degradation of organic dye by zinc oxide nanosystems with special defect structure: Effect of the morphology and annealing temperature," *Appl. Catal. A Gen.*, vol. 472, pp. 198–204, Feb. 2014.
- [327] S.-M. Lam, J.-C. Sin, A. Z. Abdullah, and A. R. Mohamed, "Degradation of wastewaters containing organic dyes photocatalysed by zinc oxide: a review," *Desalin. Water Treat.*, vol. 41, no. 1–3, pp. 131–169, Mar. 2012.
- [328] H. Lachheb, E. Puzenat, A. Houas, M. Ksibi, E. Elaloui, C. Guillard, and J.-M. Herrmann, "Photocatalytic degradation of various types of dyes (Alizarin S, Crocein Orange G, Methyl Red, Congo Red, Methylene Blue) in water by UV-irradiated titania," *Appl. Catal. B Environ.*, vol. 39, no. 1, pp. 75–90, Nov. 2002.
- [329] C. Guillard, H. Lachheb, A. Houas, M. Ksibi, E. Elaloui, and J.-M. Herrmann, "Influence of chemical structure of dyes, of pH and of inorganic salts on their photocatalytic degradation by TiO₂ comparison of the efficiency of powder and supported TiO₂," *J. Photochem. Photobiol. A Chem.*, vol. 158, no. 1, pp. 27–36, May 2003.
- [330] A. M. and S. Le Hunte, "An overview of semiconductor photocatalysis," *J. Photochem. Photobiol. A Chem.*, vol. 108, no. 1, pp. 1–35, 1997.
- [331] et al. Ballari, M.d.l.M., "Mass transfer limitations in photocatalytic reactors employing titanium dioxide suspensions: I. Concentration profiles in the bulk," *Chem. Eng. J.*, vol. 136(1), pp. 50–65, 2008.
- [332] et al. Ballari, M.D., "Mass transfer limitations in photocatalytic reactors employing titanium dioxide suspensions - II. External and internal particle constrains for the reaction," *Chem. Eng. J.*, vol. 136(2–3), pp. 242–255, 2008.
- [333] C. Engineering, I. Boiarkina, S. Norris, and D. Alec, "photocatalytic spinning disc reactor as a process intensification technology: Comparison to an annular

- reactor for the Opus : University of Bath Online Publication Store The Case for the Photocatalytic Spinning Disc Reactor as a Process Intensification T,” pp. 752–765, 2013.
- [334] and D. F. O. A. Mills, J. Wang, “Dependence of the kinetics of liquid-phase photocatalysed reactions on oxygen concentration and light intensity,” *J. Catal.*, vol. 243, pp. 1–6, 2006.
- [335] D. F. Ollis, “Photocatalytic purification and remediation of contaminated air and water,” *Surf. Chem. Catal.*, vol. 3, pp. 405–411, 2000.
- [336] and P. S. D. Monllor-Satoca, R. Gomez, M. Gonzalez-Hidalgo, “The ‘direct-indirect’ model: An alternative kinetic approach in heterogeneous photocatalysis based on the degree of interaction of dissolved pollutant species with the semiconductor surface,” *Catal. Today*, vol. 129, pp. 247–255, 2007.
- [337] Phillips, “Photometric data, UVC lamps 6W phillips,” 2005.
- [338] A. Evie L. Papadopoulou, Alexios Pagkozidis, Marios Barberoglou, Costas Fotakis and E. Stratakis, “Electrowetting Properties of ZnO and TiO₂ Nanostructured Thin Films,” *J. Phys. Chem. C- J PHYS CHEM C*, vol. 114, pp. 10249–10253, 2010.
- [339] Y. Su, Y. Yang, H. Zhang, Y. Xie, Z. Wu, Y. Jiang, N. Fukata, Y. Bando, and Z. L. Wang, “Enhanced photodegradation of methyl orange with TiO₂ nanoparticles using a triboelectric nanogenerator.,” *Nanotechnology*, vol. 24, no. 29, p. 295401, Jul. 2013.
- [340] Z. Li, B. Gao, G. Z. Chen, R. Mokaya, S. Sotiropoulos, and G. Li Puma, “Carbon nanotube/titanium dioxide (CNT/TiO₂) core–shell nanocomposites with tailored shell thickness, CNT content and photocatalytic/photoelectrocatalytic properties,” *Appl. Catal. B Environ.*, vol. 110, pp. 50–57, Nov. 2011.
- [341] L. Sagalowicz, G. R. Fox, and I, “Planar defects in ZnO thin films deposited on optical fibers and flat substrates,” *J. Mater. Res.*, vol. 14, no. 5, pp. 1876 – 1885, 1999.
- [342] P. News, “State-of-the-Art Phot,” vol. 23, pp. 24–31, 2012.
- [343] M. C. Das, H. Xu, Z. Wang, G. Srinivas, W. Zhou, Y.-F. Yue, V. N. Nesterov, G. Qian, and B. Chen, “A ZnO-containing doubly interpenetrated porous metal-organic framework for photocatalytic decomposition of methyl orange,” *Chem. Commun. (Camb)*, vol. 47, no. 42, pp. 11715–7, Nov. 2011.
- [344] J. Scott, W. Irawaty, G. Low, and R. Amal, “Enhancing the catalytic oxidation capacity of Pt/TiO₂ using a light pre-treatment approach,” *Appl. Catal. B Environ.*, vol. 164, pp. 10–17, Mar. 2015.